



# Revisiting the chemistry of star formation

Thomas Vidal

## ► To cite this version:

Thomas Vidal. Revisiting the chemistry of star formation. Astrophysics [astro-ph]. Université de Bordeaux, 2018. English. NNT : 2018BORD0151 . tel-01949526

**HAL Id: tel-01949526**

**<https://theses.hal.science/tel-01949526>**

Submitted on 10 Dec 2018

**HAL** is a multi-disciplinary open access archive for the deposit and dissemination of scientific research documents, whether they are published or not. The documents may come from teaching and research institutions in France or abroad, or from public or private research centers.

L'archive ouverte pluridisciplinaire **HAL**, est destinée au dépôt et à la diffusion de documents scientifiques de niveau recherche, publiés ou non, émanant des établissements d'enseignement et de recherche français ou étrangers, des laboratoires publics ou privés.

THÈSE PRÉSENTÉE PAR  
**THOMAS VIDAL**  
POUR OBTENIR LE GRADE DE  
**DOCTEUR DE**  
**L'UNIVERSITÉ DE BORDEAUX**

ÉCOLE DOCTORALE: SCIENCES PHYSIQUES ET DE L'INGÉNIEUR

SPÉCIALITÉ: ASTROPHYSIQUE

---

**REVISITING THE CHEMISTRY OF STAR FORMATION**

---

SOUS LA DIRECTION DE: VALENTINE WAKELAM

SOUTENUE LE : 25/09/2018

**MEMBRES DU JURY:**

Mme Serena Viti	Professor, UCL, London	Rapportrice
M. Bertrand Lefloch	Directeur de recherche, IPAG, Grenoble	Rapporteur
Mme Stéphanie Cazaux	Assistant professor, Delft University	Examinatrice
M. François Dulieu	Professeur, Univ. Cergy-Pontoise	Examineur
M. Marcelino Agundez	Chercheur, CSIC, Madrid	Examineur
M. Fabrice Herpin	Astronome, Univ. Bordeaux	Examineur
Mme Valentine Wakelam	Directeur de recherche, Univ. Bordeaux	Directrice de thèse



# REVISITING THE CHEMISTRY OF STAR FORMATION

## Abstract

Astrochemical studies of star formation are of particular interest because they provide a better understanding of how the chemical composition of the Universe has evolved, from the diffuse interstellar medium to the formation of stellar systems and the life they can shelter. Recent advances in chemical modeling, and particularly a better understanding of grains chemistry, now allow to bring new hints on the chemistry of the star formation process, as well as the structures it involves.

In that context, the objective of my thesis was to give a new look at the chemistry of star formation using the recent enhancements of the NAUTILUS chemical model.

To that aim, I focused on the sulphur chemistry throughout star formation, from its evolution in dark clouds to hot cores and corinos, attempting to tackle the sulphur depletion problem. I first carried out a review of the sulphur chemical network before studying its effects on the modeling of sulphur in dark clouds. By comparison with observations, I showed that the NAUTILUS chemical model was the first able to reproduce the abundances of S-bearing species in dark clouds using as elemental abundance of sulphur its cosmic one. This result allowed me to bring new insights on the reservoirs of sulphur in dark clouds. I then conducted an extensive study of sulphur chemistry in hot cores and corinos, focusing on the effects of their pre-collapse compositions on the evolution of their chemistries. I also studied the consequences of the use of the common simplifications made on hot core models. My results show that the pre-collapse composition is a key parameter for the evolution of hot cores which could explain the variety of sulphur composition observed in such objects. Moreover, I highlighted the importance of standardizing the chemical modeling of hot cores in astrochemical studies. For my last study, I developed an efficient method for the derivation of the initial parameters of collapse of dark clouds via the use of a physico-chemical database of collapse models, and comparison with observations of Class 0 protostars. From this method, and based on a sample of 12 sources, I was able to derive probabilities on the possible initial parameters of collapse of low-mass star formation.

**Keywords:** Astrochemistry - Star formation - Chemical model - Dark clouds - Collapse - Hot cores

---

### Unité de recherche

Laboratoire d'Astrophysique de Bordeaux (LAB - UMR 5804)

B18N, allée Geoffroy Saint-Hilaire

33615 Pessac, France





# REVISITER LA CHIMIE DE LA FORMATION STELLAIRE

## Résumé

Les études astrochimiques de la formation stellaire sont particulièrement importantes pour la compréhension de l'évolution de l'Univers, du milieu interstellaire diffus à la formation des systèmes stellaires. Les récentes avancées en matière de modélisation chimique permettent d'apporter de nouveaux résultats sur le processus de formation stellaire et les structures mises en jeu.

L'objectif de ma thèse était donc d'apporter un regard neuf sur la chimie de la formation stellaire en utilisant les récentes avancées sur le modèle chimique NAUTILUS.

J'ai pour cela étudié l'évolution de la chimie du soufre durant la formation stellaire pour tenter d'apporter de nouvelles réponses au problème de déplétion du soufre. J'ai d'abord effectué une révision du réseau chimique soufré et étudié son effet sur la modélisation du soufre dans les nuages denses. En comparant aux observations, j'ai montré que le modèle NAUTILUS était capable de reproduire les abondances des espèces soufrées dans les nuages denses en utilisant comme abondance élémentaire de soufre son abondance cosmique. Ce résultat m'a permis d'apporter de nouveaux indices sur les réservoirs de soufre dans ces objets. Puis j'ai effectué une étude complète de la chimie du soufre dans les coeurs chauds en me concentrant sur les effets sur la chimie de la composition pre-effondrement. J'ai également étudié les conséquences des différentes simplifications couramment faites pour la modélisation des coeurs chauds. Mes résultats montrent que la composition pre-effondrement est un paramètre majeur de l'évolution chimique des coeurs chauds, fournissant de nouveaux indices pour expliquer la variété de compositions en espèces soufrées observée dans ces objets. De plus, ma recherche a mis en évidence la nécessité d'uniformiser les modèles de chimie utilisés pour les coeurs chauds. Enfin, j'ai développé une méthode efficace pour inverser les paramètres initiaux d'effondrement de nuages denses en me basant sur une base de données de modèles physico-chimiques d'effondrement, ainsi que sur l'observation d'enveloppes de protoétoiles de Classe 0. A partir d'un échantillon de 12 sources, j'ai pu en déduire des probabilités concernant les possibles paramètres initiaux d'effondrement de la formation d'étoiles de faible masse.

**Mots clés:** Astrochimie - Formation stellaire - Modèle chimique - Nuages denses - Effondrement - Coeur chauds

---

### Unité de recherche

Laboratoire d'Astrophysique de Bordeaux (LAB - UMR 5804)

B18N, allée Geoffroy Saint-Hilaire

33615 Pessac, France



# REMERCIEMENTS

Je tiens en premier lieu à remercier ma directrice de thèse, Valentine Wakelam. Merci de m'avoir accordé ta confiance sur un sujet de thèse dans un domaine qui n'était initialement pas mon domaine de formation, et de m'avoir permis de réaliser mon rêve de devenir astrophysicien. Tu es la directrice de thèse et chef d'équipe idéale par ta disponibilité, ton sens de l'écoute, la confiance que tu as en ton équipe, la liberté de réflexion que tu nous laisse tout en sachant nous remettre dans le droit chemin si nécessaire, et j'en passe. Merci pour le cadre de travail que tu m'as offert. Merci pour les multiples "Je te fais confiance" que tu m'as adressé lorsque tu savais que je pouvais me débrouiller seul, moi qui avait souvent tendance à demander de l'aide au moindre doute. Merci aussi d'avoir su me recadrer lorsque j'ai commencé l'enseignement et que j'ai eu du mal à organiser mon travail en conséquence. Enfin, merci pour ta compréhension et ton soutien pour la suite de mon parcours professionnel. Tu es devenue pour moi un modèle de réussite et d'exemplarité au travail.

Je remercie également les membres de mon jury. Merci à Serena Viti et Bertrand Lefloch d'avoir accepté de rapporter mon travail, ainsi que pour leur précieux conseils pour l'amélioration de ce manuscrit. Je remercie également Stéphanie Cazaux, François Dulieu, Fabrice Herpin et Marcelino Agundez d'avoir accepté de prendre part à ce jury.

Je remercie Jean-Christophe Loison et Neil Vaytet, dont le travail et la collaboration ont permis l'aboutissement de mes travaux.

Merci à Pierre Gratier pour ta contribution majeure à la réussite de ma thèse. Sans ta patience et ton expertise je n'aurais pu mener à bien mon dernier travail de thèse qui me tenait tant à cœur de réussir. Tu es une des personnes les plus brillantes qu'il m'a été donné de rencontrer.

Merci à Maxime Ruaud pour ta camaraderie et ton soutien. Merci de m'avoir permis de me sentir bien dans l'équipe à mon arrivée au laboratoire. Grâce à toi j'ai des souvenirs mémorable de la conférence PCMI à Lille, et je sais que l'on peut faire un barbecue avec une pièce de boeuf de 500g dans une cheminée. Enfin merci pour le lit qui a permis à Sandrine de mieux dormir à la fin de sa grossesse.

Je remercie également tout les membres de l'équipe AMOR, Anne Dutrey, Stéphane Guilloteau, Emmanuel Di Folco, Jessica Pericaud, et plus particulièrement de l'équipe 3DICE : Audrey Coutens, Liton Majumdar, Wasim Iqbal et Benjamin Pavone.

---

Merci également à Franck Selsis et Jérémy Leconte pour votre soutien et vos conseils, mais également pour les débats cinématographiques qui ont ponctué mon séjour au laboratoire et m'ont permis de garder le moral quand tout n'allait pas forcément très bien.

Merci à Arnaud Collioud et Géraldine Bourda pour m'avoir redonné goût au sport, ainsi que pour votre gentillesse et soutien moral indéfectible.

Merci à Grégoire Pique et Antsa Randriamanantena pour toutes les pauses faites ensembles.

Je tiens à remercier tout particulièrement Annick Caperan, Odile Derouaisne et Nathalie Le Roux pour nos innombrables débats du déjeuner qui ont franchement enrichi ma vie au laboratoire. Merci pour votre ouverture d'esprits, votre aide pour les entretiens et votre bonne humeur à toute épreuve. Merci également pour toutes les pistes de réflexions qui sont nées de nos discussions. Vous avez été mon bol d'oxygène quotidien lors des moments les plus difficiles de ma thèse.

Je remercie également les membres du laboratoire qui sont ponctuellement venus enrichir ces débats : Pascal Bordé, Caroline Soubiran, Sylvain Bontemps, Cécile Arnaudin, et tous les autres pour leur accueil et pour avoir rendu mon séjour au LAB aussi mémorable.

Merci à William Lefrançois et Christine Grauby-Heywang pour m'avoir donné l'opportunité d'enseigner à l'université, notamment de m'avoir fait confiance pour les cours et TDs. Un grand merci également aux deux promotions d'élèves de L1 Bio dont j'ai eu la chance d'être le professeur de Physique. Merci à tous pour votre indulgence et votre application au travail, j'espère avoir réussi à vous transmettre un peu de ma passion.

Un grand merci à Pierre-Yves Foucher pour mon stage de fin d'études qui m'a certainement permis d'obtenir cette thèse. Merci également de m'avoir donné l'opportunité d'avoir une publication avant même le début de ma thèse. Enfin merci pour ton soutien continu dans mon projet professionnel.

Je souhaite bien évidemment remercier mon enseignant de physique de classe préparatoire Monsieur Jean-Marc Reverdy. Merci d'avoir transmis, à moi et à tant d'autres, votre immense passion pour la Physique. Vous êtes à l'origine même de mon parcours professionnel, et je suis extrêmement fier de vous considérer comme mon mentor et ami.

---

Je souhaite également remercier mon professeur de philosophie de lycée, Monsieur Chemin, pour avoir noté dans mon dossier d'application en classes préparatoires que je n'avais "pas les capacités pour réussir en classes préparatoires".

Merci à mes grand-pères Hervé Vidal et Guy Ringenbach, l'un pour être un modèle de vie, l'autre pour avoir été le premier à me faire lever les yeux vers les étoiles.

Je remercie de tout mon cœur mes parents sans qui je ne serais pas arrivé jusqu'ici. Merci pour m'avoir toujours poussé à donner le meilleur de moi-même et pour votre soutien tout le long de mes études, tant concernant ma vie professionnelle que personnelle. Un grand merci également à mes deux sœurs, votre réussite professionnelle est une vraie source d'inspiration. Merci pour votre soutien et vos précieux conseils durant ces trois années de thèse.

Merci à mes amis Marion, Anne et Jean-Elie, Karim, Alexandre, Valentin et Emmanuel à qui je dois en grande partie ma réussite à l'ENAC. Merci à Gilles, Jean-François et Vincent d'être mes plus vieux soutiens et amis. Merci à Guillaume, pour tout. Merci à tous pour tous les moments partagés à Montpellier, Toulouse ou Bordeaux. Chacun et chacune d'entre vous avez participé à faire de moi la personne que je suis aujourd'hui.

Merci à Laetitia pour ton amitié à travers les drames, joies et réussites de nos vies depuis plus de 16 ans. C'était chouette de pouvoir vivre nos expériences en thèses respectives en parallèle.

Enfin, merci à toi Sandrine. Merci de m'avoir dit "oui" pour me supporter au quotidien, dans les meilleurs et les pires moments. Merci de m'avoir soutenu dans ma vie professionnelle ces 5 dernières années, je ne serais jamais arrivé jusqu'ici sans toi. Merci également d'avoir sublimé mon expérience de la thèse en une véritable aventure, avec notre mariage et la naissance d'Hector.



*"The atoms of our bodies are traceable to stars that manufactured them in their cores [...] We are not figuratively, but literally stardust."*

*"Kids are born scientists [...] An adult scientist is a kid that never grew up."*

Neil deGrasse Tyson

*"Why do we fall, sir ? So that we can learn to pick ourselves up."*

Alfred Pennyworth





# CONTENTS

<b>1</b>	<b>INTRODUCTION</b>	<b>25</b>
1.1	REVISITING THE CHEMISTRY ...	27
1.1.1	Spectroscopy's principle	28
1.1.2	Chemical modeling and laboratory experiments	29
1.1.2.1	Chemistry in the interstellar gas	30
1.1.2.2	Chemistry on dust grains	31
1.1.2.3	Generalities on chemical modeling	33
1.1.2.4	A word about laboratory experiments	34
1.1.3	The NAUTILUS chemical model	34
1.1.3.1	Gas phase chemistry	34
1.1.3.2	Grains chemistry	35
1.2	... OF STAR FORMATION	39
1.2.1	From diffuse clouds to dense clouds	39
1.2.2	Cloud collapse and star formation	40
1.2.3	The death of stars	42
1.3	OBJECTIVES AND ORGANIZATION OF THE THESIS	42
<b>2</b>	<b>SULPHUR CHEMISTRY IN DARK CLOUDS</b>	<b>45</b>
2.1	INTRODUCTION	47
2.1.1	The sulphur depletion problem	47
2.1.2	Current hypothesis on the reservoirs of sulphur in dark clouds	48
2.2	PRESENTATION OF THE ENHANCED CHEMICAL NETWORK	49
2.2.1	Modification of the sulphur network	49
2.2.2	Effects of the new network on the chemical model of dark clouds	51
2.2.2.1	The main sulphur bearing species	51
2.2.2.2	The newly implemented sulphur bearing species	54
2.2.2.3	Comparison with the previous network	58
2.3	COMPARISON WITH OBSERVATIONS IN THE DARK CLOUD TMC-1	63
2.3.1	Comparison with models A and B	64
2.3.2	Variation of the elemental sulphur abundance	65
2.3.2.1	Comparison with all observed gas phase species	66
2.3.2.2	Comparison with observed sulphur bearing gas phase species	67
2.3.2.3	The new species HNCS and HSCN	68

2.3.2.4	Sulphur bearing species on grains towards W33A . . . . .	69
2.3.3	Sulphur reservoirs in dark clouds . . . . .	70
2.4	<b>DISCUSSIONS AND SUMMARY . . . . .</b>	73
2.4.1	About the elemental abundance of sulphur . . . . .	73
2.4.2	About the reservoirs of sulphur in dark clouds . . . . .	73
2.4.3	About the observability of HCS . . . . .	74
2.4.4	Summary . . . . .	74
3	<b>A NEW LOOK AT SULPHUR CHEMISTRY IN HOT CORES AND CORINOS . . . . .</b>	77
3.1	<b>INTRODUCTION . . . . .</b>	79
3.2	<b>MODELS PARAMETERS . . . . .</b>	80
3.2.1	H <sub>2</sub> <i>ad hoc</i> formation mechanism . . . . .	81
3.2.2	Parent dark cloud parameters . . . . .	81
3.2.3	Hot core models parameters . . . . .	83
3.2.3.1	The 0D static model parameters . . . . .	83
3.2.3.2	The 1D static model parameters . . . . .	83
3.2.3.3	The 0D dynamic model parameters . . . . .	84
3.3	<b>HOT CORE CHEMISTRY . . . . .</b>	85
3.3.1	0D models . . . . .	85
3.3.1.1	Oxygen chemistry . . . . .	85
3.3.1.2	Sulphur chemistry . . . . .	89
3.3.1.3	Comparisons to observations . . . . .	98
3.3.2	1D static models . . . . .	99
3.3.3	0D dynamic models . . . . .	101
3.4	<b>DISCUSSIONS AND SUMMARY . . . . .</b>	102
3.4.1	About the modification of the density profile of the dynamic model . . . . .	102
3.4.2	About H <sub>2</sub> S and the initial abundance of sulphur . . . . .	103
3.4.3	About the sensitivity to the type of model . . . . .	104
3.4.4	About the importance of the pre-collapse chemical composition . . . . .	104
3.4.5	Summary . . . . .	105
4	<b>CONSTRAINING THE IPPC OF COLLAPSING PRESTELLAR CORES . . . . .</b>	107
4.1	<b>INTRODUCTION . . . . .</b>	109
4.2	<b>RHD CHEMICAL COLLAPSE MODELS OF LOW-MASS STAR FORMATION . . . . .</b>	109
4.2.1	The database . . . . .	109
4.2.1.1	Bonnor-Ebert spheres . . . . .	110
4.2.1.2	The Lagrangian grid . . . . .	111
4.2.1.3	Initial setup of the collapse models . . . . .	113
4.2.2	Chemical modeling . . . . .	114
4.2.2.1	Selection of the reference dataset for chemical modeling . . . . .	114
4.2.2.2	Parameters of the chemical modeling . . . . .	115
4.3	<b>POST-TREATMENT OF THE CHEMICAL OUTPUTS AND RESULTS . . . . .</b>	116
4.3.1	Search for tracers of initial physical parameters of collapse . . . . .	116

4.3.1.1	Definition of the regions of study . . . . .	116
4.3.1.2	Correlations in the Hot Corinos Region . . . . .	119
4.3.2	Constraints on the envelope of Class 0 protostars . . . . .	126
4.3.2.1	Presentation of the method . . . . .	127
4.3.2.2	Results on the envelope of IRAS 16293-2422 . . . . .	129
4.3.2.3	Summary of the results on the source sample . . . . .	132
4.4	DISCUSSIONS AND SUMMARY . . . . .	139
4.4.1	About the modeling bias . . . . .	140
4.4.2	About the applicability of the method on the HCR dataset . . . . .	141
4.4.3	Summary . . . . .	142
5	CONCLUSIONS AND PERSPECTIVES	145
A	SUMMARY OF SULPHUR COMPOUNDS REACTIONS REVIEW	151
B	INITIAL PARAMETERS OF THE RADIATION HYDRODYNAMIC MODELS	167
C	CORRELATIONS IN THE HOT CORE REGION	173
D	CONSTRAINTS ON THE IPPC FOR EACH SOURCES	179
E	ACRONYMS AND SYMBOLS	185
F	INTRODUCTION	189
F.1	REVISITER LA CHIMIE ... . . . .	189
F.1.1	Généralités . . . . .	189
F.1.2	Le modèle de chimie NAUTILUS . . . . .	189
F.1.2.1	Chimie en phase gazeuse . . . . .	190
F.1.2.2	Chimie sur les grains . . . . .	191
F.2	...DE LA FORMATION STELLAIRE . . . . .	194
F.2.1	Des nuages diffus aux nuages denses . . . . .	195
F.2.2	Effondrement et formation stellaire . . . . .	196
F.3	OBJECTIFS ET ORGANISATION DE LA THÈSE . . . . .	198
G	RÉSUMÉ, CONCLUSIONS ET PERSPECTIVES	199
H	PUBLICATIONS	207
	BIBLIOGRAPHIE	236



# LIST OF FIGURES

1.1	The "astronomer's periodic table" (McCall, 2001) . . . . .	27
1.2	Illustration of the principle of spectroscopy. The emitted spectra of CH <sub>3</sub> CN (in blue) and HCOOH (in red) are superimposed on the total observed spectrum. Credits: <a href="http://www.herschel.fr/">http://www.herschel.fr/</a> . . . . .	29
1.3	Barnard 68 at different wavelengths (clockwise). This molecular cloud is at a distance of 160 pc in the Ophiuchus constellation. At visible (0.4 to 0.8 $\mu$ m) and near-infrared (0.8 to 1.4 $\mu$ m) wavelengths, it appears as a dark "hole" in the stellar population around it. The hole vanishes at longer wavelength ( $\approx$ 2 $\mu$ m) because of interstellar reddening due to the presence of grains in the line of sight. Credits: ESO . . . . .	32
1.4	Representation of an interstellar grain as modeled by the NAUTILUS chemical model. . . . .	36
1.5	Summary of the chemical processes taken into account in the NAUTILUS 3-phases chemical model (from Ruaud et al., 2016). . . . .	38
1.6	The cycle of interstellar matter. Credits: Bill Saxton, NRAO/AUI/NSF. .	39
1.7	Steps of star formation. The figure can be seen as the detail of the right part of the cycle in figure 1.6, between the dark cloud and the solar system phases. The terms FHSC and SHSC mean respectively first and second hydrostatic core. . . . .	41
2.1	Abundances relative to H of the main gas phase S-bearing species S, CS and SO as a function of time for dark cloud physical conditions. The dotted line represents the elemental abundance of sulphur (here, $[S]_{\text{ini}} = 8 \times 10^{-8}$ ). . . . .	52
2.2	Abundances relative to H of the main S-bearing species on the grains HS and H <sub>2</sub> S as a function of time for dark cloud physical conditions, on the surfaces (solid line) and in the bulks (dashed line). The dotted line represents the elemental abundance of sulphur (here, $[S]_{\text{ini}} = 8 \times 10^{-8}$ ). .	53
2.3	Abundances of HNCS (blue) and HSCN (red) relative to H as a function of time for dark cloud physical conditions in the gas phase (solid line), on the grains surface (dotted line) and in the grains bulk (dashed line). .	55
2.4	Abundances of CH <sub>3</sub> SH relative to H as a function of time for dark cloud physical conditions in the gas phase (solid line), on the grains surface (dotted line) and in the grains bulk (dashed line). . . . .	57

2.5	Comparison between models A (blue) and B (red) abundances of $C_3S$ relative to H as a function of time for dark cloud physical conditions in the gas phase (solid line) and in the grains bulk (long-dashed line). . . . .	58
2.6	Comparison between models A (blue) and B (red) abundances of $H_2CS$ relative to H as a function of time for dark cloud physical conditions in the gas phase (solid line) and on the grains surface (dotted line). . . . .	60
2.7	Comparison between models A (blue) and B (red) abundances of HCS relative to H as a function of time for dark cloud physical conditions in the gas phase (solid line) and on the grains surface (dotted line). . . . .	61
2.8	Comparison between models A (blue) and B (red) abundances of HS relative to H as a function of time for dark cloud physical conditions in the gas phase (solid line) and on the grains surface (dotted line). . . . .	62
2.9	Comparison between models A (blue) and B (red) abundances of $H_2S$ relative to H as a function of time for dark cloud physical conditions in the gas phase (solid line) and on the grains surface (dotted line). . . . .	62
2.10	Comparison between models A (blue) and B (red) abundances of SO relative to H as a function of time for dark cloud physical conditions in the gas phase (solid line) and on the grains surface (dotted line). . . . .	63
2.11	Distances of disagreement for models 1, 2, 3 and 4 considering 62 detected species in TMC-1 (CP). . . . .	66
2.12	Distances of disagreement for models 1, 2, 3 and 4 considering only the 11 detected S-bearing species in TMC-1 (CP). . . . .	68
2.13	Comparison of the simulated gas phase abundances of HNCS and HSCN with the observed ones in TMC-1 (CP) (horizontal dashed lines). . . . .	69
2.14	Comparison of the computed abundances of solid OCS (a) and $SO_2$ (b) for models 1, 2, 3 and 4 (solid lines) with the observed one towards W33A (black dashed lines). . . . .	70
2.15	Abundances of the sulphur reservoirs relative to H as a function of time for dark cloud physical conditions : (a) in the gas phase, (b) on the grains surface (solid line) and bulk (dashed line). The dotted line represents the elemental abundance of sulphur (here, $[S]_{ini} = 1.5 \times 10^{-5}$ ). . . . .	71
2.16	Percentage of the total amount of sulphur contained in the reservoirs as a function of time for dark cloud physical condition using a cosmic elemental abundance of sulphur $[S]_{ini} = 1.5 \times 10^{-5}$ . . . . .	72
3.1	Radial structure of the 1D static and 0D dynamic models at final time for: (a) density, for which I plot the initial structure from Aikawa et al. (2008) as reference, (b) temperature, for which I plot the limit of the hot core ( $T > 100$ K) for the 1D static ( $R_{HC}^{1D} = 80$ AU, solid black vertical line) and 0D dynamic ( $R_{HC}^{0D} = 135$ AU, dashed black vertical line). . . . .	84

3.2	Abundances of O, O <sub>2</sub> , and OH relative to H as a function of time for hot core conditions: $n_H = 2 \times 10^7 \text{ cm}^{-3}$ and $T = 100 \text{ K}$ (blue line) or $300 \text{ K}$ (red line), and for LEDC (top panel) and EDC (bottom panel) pre-collapse compositions. . . . .	86
3.3	Abundances of SO, SO <sub>2</sub> , and OCS relative to H as a function of time for hot core conditions: $n_H = 2 \times 10^7 \text{ cm}^{-3}$ and $T = 100 \text{ K}$ (blue line) or $300 \text{ K}$ (red line), and for LEDC (top panel) and EDC (bottom panel) pre-collapse compositions. . . . .	90
3.4	Abundances of H <sub>2</sub> S, H <sub>2</sub> CS, and CS relative to H as a function of time for hot core conditions: $n_H = 2 \times 10^7 \text{ cm}^{-3}$ and $T = 100 \text{ K}$ (blue line) or $300 \text{ K}$ (red line), and for LEDC (top panel) and EDC (bottom panel) pre-collapse compositions. . . . .	94
3.5	Abundances of SO, SO <sub>2</sub> , and OCS (top panel) and H <sub>2</sub> S, H <sub>2</sub> CS, and CS (bottom panel), relative to H as a function of the radius to the star IRAS 16293-2422 according to the 1D structure of Crimier et al. (2010), for the LEDC (blue line) and EDC (red line) pre-collapse compositions. Both models were run for a period of $3.5 \times 10^5$ years so the results would be comparable to those of the 0D dynamic models. The black dotted line represent the hot core spatial limit $R_{R_{\text{HC}}\text{HC}} = 80 \text{ AU}$ , $T > 100 \text{ K}$ . . . . .	99
3.6	Abundances of SO, SO <sub>2</sub> , and OCS (top panel) and H <sub>2</sub> S, H <sub>2</sub> CS, and CS (bottom panel), relative to H as a function of the radius to the star IRAS 16293-2422 according to the modified structure of Aikawa et al. (2008), for the LEDC (blue line) and EDC (red dashed line) pre-collapse compositions. The vertical black dashed line represents the hot core spatial limit $R_{\text{HC}} = 135 \text{ AU}$ , $T > 100 \text{ K}$ . . . . .	101
3.7	Abundances of SO, SO <sub>2</sub> , and OCS (top panel) and H <sub>2</sub> S, H <sub>2</sub> CS, and CS (bottom panel), relative to H as a function of the radius to the star IRAS 16293-2422 according to the original structure of Aikawa et al. (2008), for the LEDC (blue line) and EDC (red dashed line) pre-collapse compositions. The vertical black dashed line represents the hot core spatial limit $R_{\text{HC}} = 135 \text{ AU}$ , $T > 100 \text{ K}$ . . . . .	102
4.1	Example of a typical density profile of Bonnor-Ebert sphere. . . . .	111
4.2	Representation of the one-dimensional Lagrangian grid used in the RHD models. . . . .	112
4.3	Distribution of the abundances of H <sub>2</sub> O relative to H at the final time of the collapse as a function of the initial densities of the collapsing prestellar cores. The color coding represents the final temperatures of the cells. . . . .	117
4.4	Distribution of the abundances of H <sub>2</sub> O relative to H at the final time of the collapse as a function of the final temperatures. The color coding represents the final radii of the cells. The blue and red vertical bars delimit the three temperature intervals defined above. . . . .	118



4.5	Distribution of the abundances of $\text{CH}_3\text{CN}$ relative to H at the final time of the collapse as a function of the initial temperature. . . . .	120
4.6	Distribution of the abundances of $\text{H}_2\text{CS}$ relative to H at the final time of the collapse as a function of the free-fall time (left panel) and the initial density (right panel). . . . .	122
4.7	Distribution of the abundances of NS relative to H at the final time of the collapse as a function of the initial temperature. . . . .	123
4.8	Distribution of the abundances of OCS relative to H at the final time of the collapse as a function of the initial temperatures. . . . .	125
4.9	Example of the 3 possible cases of constraints that can be derived from the method with the distribution of the abundances of $\text{H}_2\text{CO}$ relative to H at the final time of the collapse as a function of the free-fall time. The blue line represents the TH case, the red one the case when constraints can be derived, and the green one the inconclusive case. . . . .	127
4.10	Comprehensive example of the application of the method on observed $\text{SO}_2$ in IRAS 16293-2422. The horizontal red line represents the observed abundance relative to H of $2.25 \times 10^{-10}$ and the dashed ones its uncertainty factor of 3. The light and dark green horizontal lines respectively represent the minimal and maximal values of the initial density $\rho_0$ that are constrained by the observed abundance. . . . .	130
4.11	Abundances distribution of $\text{N}_2\text{H}^+$ relative to H in the ER as a function of $T_0$ . . . . .	133
4.12	Correlation figure between $R_0$ and $\rho_0$ . . . . .	135
4.13	Probability mass function on the sample of 12 sources obtained for $M_0$ . . . . .	136
4.14	Probability mass function on the sample of 12 sources obtained for $R_0$ . . . . .	138
4.15	Probability mass function on the sample of 12 sources obtained for $\rho_0$ and $t_{\text{ff}}$ . . . . .	139
4.16	Probability mass function on the sample of 12 sources obtained for $T_0$ . . . . .	140
F.1	Le "tableau périodique de l'astronome" (McCall, 2001) . . . . .	190
F.2	Résumé des processus chimiques pris en compte dans le modèle 3 phases NAUTILUS (Ruaud et al., 2016). . . . .	194
F.3	Le cycle de la matière interstellaire. Credits: Bill Saxton, NRAO/AUI/NSF. . . . .	195
F.4	Les étapes de la formation stellaire. . . . .	196

# LIST OF TABLES

2.1	List of the sulphur bearing species firmly detected in dark clouds, in the gas phase and in grain ices. . . . .	48
2.2	Table of the 46 sulphur bearing species added to the network. . . . .	50
2.3	Initial abundances. $*a(b)$ stands for $a \times 10^b$ . . . . .	51
2.4	Description of the total amount of sulphur contained in HS and H <sub>2</sub> S in the grains bulk for times $\geq 6 \times 10^5$ years. The prefix "b-" is for the bulk species. . . . .	54
2.5	Observed abundances of sulphur bearing species in TMC-1 (CP) . $*a(b)$ stands for $a \times 10^b$ . . . . .	64
2.6	Results of the comparison of models A and B with observations in the dark cloud TMC-1 (CP) . . . . .	65
2.7	Set of elemental sulphur abundances. $*a(b)$ stands for $a \times 10^b$ . . . . .	66
3.1	Initial abundances. $*a(b)$ stands for $a \times 10^b$ . . . . .	82
3.2	Oxygen and sulphur reservoirs in both LEDC and EDC cases. The prefix "b-" is for the bulk species. . . . .	82
3.3	Summary of the models designations and physical parameters. . . . .	85
3.4	Description of the reactive oxygen composition in the gas phase at the first time step of the hot core models (post-collapse composition). The values display the percentage relative to the total abundance of oxygen. . . . .	92
3.5	Comparison of the abundances obtained in the LEDC case for the 1D static and 0D dynamic models. $a(b)$ stands for $a \times 10^b$ . . . . .	104
4.1	Initial physical parameters ranges for the original dataset and the reference dataset for chemical modeling . . . . .	114
4.2	Summary of the calculated Spearman's coefficients between the abundances at final time of the 482 gaseous species of the chemical network and the IPPC. . . . .	119
4.3	Summary of the observational dataset used for the method. $N_{\text{obs}}$ is the number of observed species used. . . . .	128

4.4	Summary of the application of the method to Schöier et al. (2002)'s observations of IRAS 16293-2422. IC stands for InConclusive and ND means that no data were available. Upper and lower limits are only defined within their corresponding IPPC range of values (see table 4.1). In red are contradictory results, and in blue the final constraints on the IPPC of the source. $e$ is the uncertainty factor. . . . .	131
4.5	Constraints given by HCO <sup>+</sup> with slightly increased uncertainty factors (compared to the one used in table 4.4). . . . .	131
4.6	Summary of the constraints on the IPPC obtained with the method on the 12 studied sources. The percentage of agreement (noted PA) displayed in the last column represents the number of species agreeing with the final constraints. . . . .	132
4.7	Summary of the corresponding collapse models for each source within the reference dataset, as well as their respective parent molecular clouds (noted PMC, when relevant). . . . .	136
A.1	Table of the sulphur compounds reactions added or reviewed in the network studied in chapter 2 . . . . .	152
B.1	Summary of the dataset of RHD models and their respective IPPC. . . .	167
C.1	Summary of the species in the HCR which are best correlated with the IPPC $T_0$ , $R_0$ , $\rho_0$ and $t_{\text{ff}}$ , ie with a Spearman's coefficient of $ \rho_S  > 0.6$ . . . .	173
D.1	Summary of the application of the method to Jørgensen et al. (2004)'s observations of L1448-I2. . . . .	179
D.2	Summary of the application of the method to Jørgensen et al. (2004, 2005)'s observations of L1448-C. . . . .	180
D.3	Summary of the application of the method to Jørgensen et al. (2004, 2005)'s observations of N1333-I2. . . . .	180
D.4	Summary of the application of the method to Jørgensen et al. (2004, 2005)'s observations of N1333-I4A. . . . .	180
D.5	Summary of the application of the method to Jørgensen et al. (2004, 2005)'s observations of N1333-I4B. . . . .	181
D.6	Summary of the application of the method to Jørgensen et al. (2004, 2005)'s observations of L1527. . . . .	181
D.7	Summary of the application of the method to Jørgensen et al. (2004, 2005)'s observations of VLA1623. . . . .	181
D.8	Summary of the application of the method to Jørgensen et al. (2004, 2005)'s observations of L483. . . . .	182
D.9	Summary of the application of the method to Jørgensen et al. (2004, 2005)'s observations of L723. . . . .	182
D.10	Summary of the application of the method to Jørgensen et al. (2004, 2005)'s observations of L1157. . . . .	182

D.11 Summary of the application of the method to Jørgensen et al. (2004)’s  
observations of L1551-I5. . . . . 183

E.1 Table of acronyms . . . . . 185

E.2 Table of symbols . . . . . 186



# 1 | INTRODUCTION

## Contents

---

<b>1.1</b>	<b>REVISITING THE CHEMISTRY ...</b>	<b>27</b>
1.1.1	Spectroscopy's principle	28
1.1.2	Chemical modeling and laboratory experiments	29
1.1.2.1	Chemistry in the interstellar gas	30
1.1.2.2	Chemistry on dust grains	31
1.1.2.3	Generalities on chemical modeling	33
1.1.2.4	A word about laboratory experiments	34
1.1.3	The NAUTILUS chemical model	34
1.1.3.1	Gas phase chemistry	34
1.1.3.2	Grains chemistry	35
<b>1.2</b>	<b>... OF STAR FORMATION</b>	<b>39</b>
1.2.1	From diffuse clouds to dense clouds	39
1.2.2	Cloud collapse and star formation	40
1.2.3	The death of stars	42
<b>1.3</b>	<b>OBJECTIVES AND ORGANIZATION OF THE THESIS</b>	<b>42</b>

---



## 1.1 REVISITING THE CHEMISTRY ...

Space is not empty. Even the least dense medium of our galaxy which fills the space between stars, called the interstellar medium (hereafter ISM), is actually composed of gas and dust, which mass fractions represent respectively 99% and 1% of the total ISM mass (Lequeux, 2005; Draine, 2011). The interstellar gas is under ionic, atomic and molecular form and is mainly constituted of the lightest elements in the Universe, namely hydrogen (H) and helium (He), representing respectively 70% and 28% of the total ISM mass. Heavier elements such as carbon (C), nitrogen (N), oxygen (O), sulphur (S), magnesium (Mg), iron (Fe), silicium (Si), or argon (Ar) account for only 2% of the total ISM mass (see figure 1.1). As for the interstellar dust, it is mainly composed of silicates, amorphous carbon and ices. This composition evolves through different phases, characterized by the state of its constituting matter, as well as the pressure and temperature it sustains. The discipline dedicated to the study of this chemical evolution of the ISM is called astrochemistry.

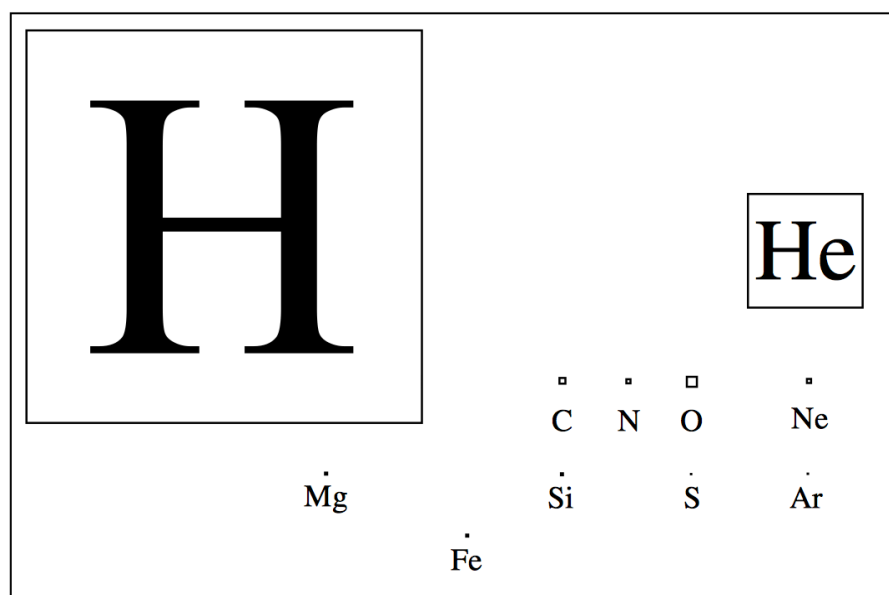


Figure 1.1: The "astronomer's periodic table" (McCall, 2001)

Astrochemistry, or molecular astrophysics, is one of the many branches of astrophysics, which consists in the study of the chemical elements in the Universe, at the crossroads of astronomy and chemistry. Especially, it focuses on the molecules' formation and destruction, as well as their interactions with radiations, interstellar dust grains, and each other. Astrochemistry fits in the more general context of astrobiology, which investigates the origin of the molecular components of Life in extraterrestrial



environments. In this context, astrochemical studies mainly focus on the several structures of the formation process of stellar systems, using three primary areas or research: spectroscopy, laboratory experiments and chemical models.

### 1.1.1 Spectroscopy's principle

Spectroscopy is the astrochemist's tool to extract chemical information from a given source. Using the spectra obtained when pointing towards a source with radio-telescopes and/or interferometers, one can infer information on the characteristics of a specific chemical element. Indeed, the chemical bonds between atoms of a given molecule are not rigid. Depending on the type of bonds, the number of atoms as well as the physical conditions, these chemical bonds can vibrate or rotate, emitting radiation at frequencies which are specific to the molecule. Hence, each chemical species emits its own "spectral print", or lines, which allows to determine its presence towards the pointed source. As illustrated in figure 1.2, when observing several chemical elements, the obtained spectrum is the superposition of each element's observed lines. This spectrum is then used to derive several physico-chemical information about the observed medium, such as the gas temperature  $T_{\text{gas}}$ , the total proton density (or density)  $n_H$ , and the observed abundance of each observed chemical species (hereafter noted  $[X]_{\text{obs}}$ , where  $X$  is the species), which is expressed as a fraction of  $n_H$ .

However, the identification of molecules from an observed spectrum suffers a few pitfalls:

- The characteristic spectrum of a molecule must be known in order to identify its different lines. This implies to be able to synthesize the molecule in laboratory within a similar physical environment as the one observed, so that its lines can be measured. This task is particularly complex because of the extreme physical condition of the ISM. This complexity is mainly due to the lack of knowledge on how to synthesize several molecules, as well as the fact that some of them, such as radicals, are very reactive and therefore tricky to manipulate. Moreover, the complexity increases with the size of the molecule, as well as its possible physical properties or danger for human health (hydrogen sulfide  $\text{H}_2\text{S}$  is for instance a highly poisonous, corrosive and flammable gas at atmospheric temperature and pressure). Only a few laboratories such as the Jet Propulsion Laboratory (JPL) or the Laboratoire de Physique des Lasers, Atomes et Molécules (PhLAM), are able to do such experiments.
- Some species emit at similar frequencies, which causes their lines to blend on the observed spectra. In that case, distinguishing the contribution of each species to the line can be complicated, especially if the spectral resolution is not high enough.

Nevertheless, astrochemists have detected more than 200 species in the ISM, from simple radicals such as OH, to complex organic molecules (COMs) such as methanol

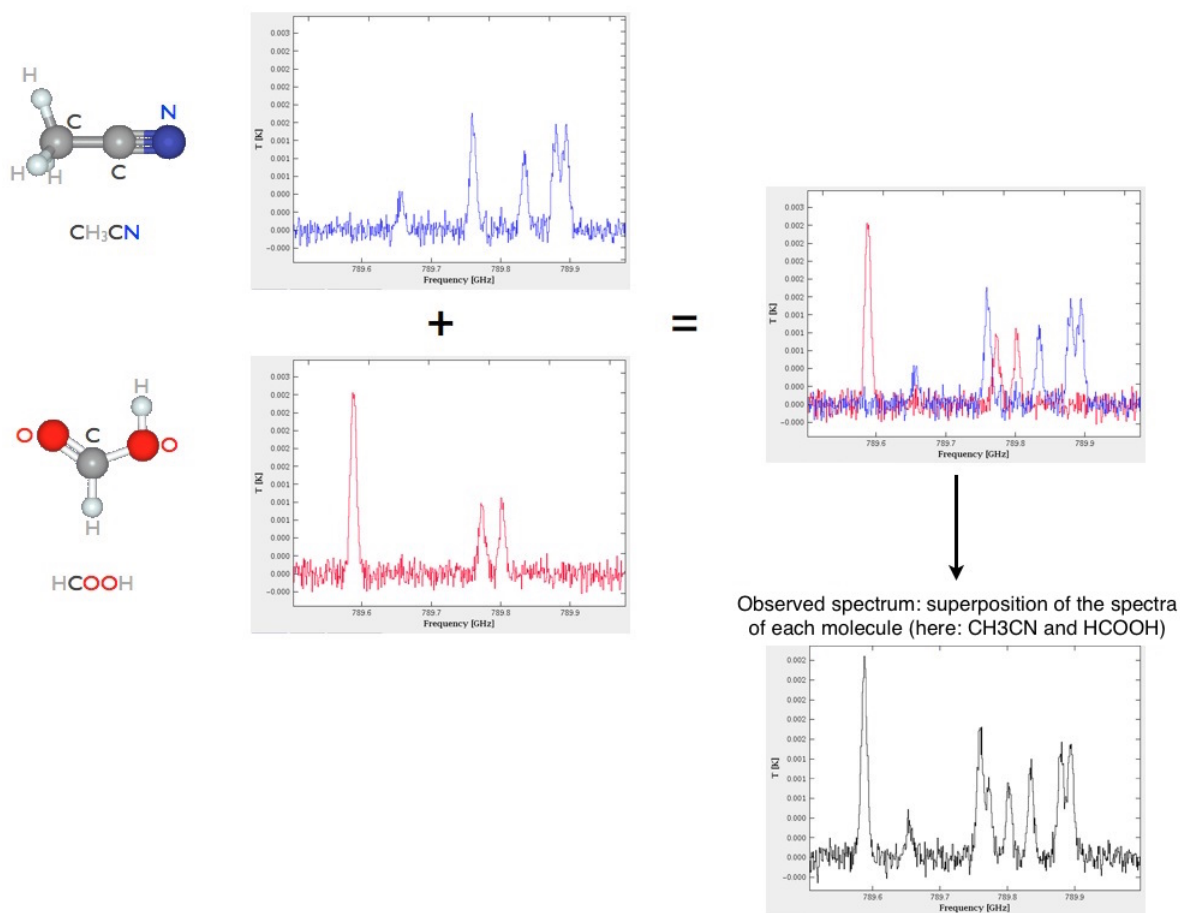


Figure 1.2: Illustration of the principle of spectroscopy. The emitted spectra of  $\text{CH}_3\text{CN}$  (in blue) and  $\text{HCOOH}$  (in red) are superimposed on the total observed spectrum. Credits: <http://www.herschel.fr/>

$\text{CH}_3\text{OH}$ . They keep on finding new ones, especially since the commissioning of powerful interferometers such as the Plateau de Bure Interferometer (PdBI) or the Atacama Large Millimeter Array (ALMA).

### 1.1.2 Chemical modeling and laboratory experiments

Another major aspect of astrochemistry is the chemical modeling. Indeed, it allows, by comparison to observations, to get a better understanding of the physical phenomena of the ISM, such as the formation of stars and planets. Moreover, it allows to bring constraints on the physical parameters of the ISM with the use of tracers, *ie* chemical species whose abundances trace particular environments. For instance, sulphur monoxide  $\text{SO}$  is used to trace small scale heating processes such as shocks. Chemical models therefore rely on a good comprehension of the physico-chemical processes that rule both phases of the ISM: the gas phase and the dust grains.

### 1.1.2.1 Chemistry in the interstellar gas

#### 1.1.2.1.1 Chemical processes

As the most abundant initial ingredients of all the physical structures of the Universe, interstellar gas plays a key role in the evolution of the ISM. From a chemical point of view, interstellar gas presents a rich and complex chemistry due to reactive collisions, despite the fact that it is characterized by low densities ( $< 100 \text{ part.cm}^{-3}$ ) and temperatures ( $< 100 \text{ K}$ ). Indeed, in this physical environment, reactive collisions are scarce. However, the interstellar gas evolves with characteristic time and space scales high enough to allow the formation of multiple chemical compounds (Lequeux, 2005; Draine, 2011). This chemistry is mainly ruled by the following processes (Herbst, 2006):

- ion-neutral reactions,
- radiative associations,
- dissociative recombinations,
- neutral-neutral reactions,
- photodissociation and photoionization reactions.

Apart from the ISM chemical composition, gas phase chemistry is also important for the physical evolution of the medium. Especially, the cooling of the gas is insured by the chemical species it contains via collisional excitations.

#### 1.1.2.1.2 Thermal processes

In the interstellar gas, the cooling processes are basically due to the conversion of kinetic energy to radiant energy, under the form of photons, which can escape from the system. These collisional excitations typically occur through inelastic collisions between the several compounds of the ISM, such as atoms, molecules, ions, electrons, and grains (Lequeux, 2005; Draine, 2011). The transmitted kinetic energy of the colliding compound allows to excite the targeted one, which then relaxes via the emission of an InfraRed (IR) photon, which easily escapes from the medium. Since hydrogen and helium require rather high energies for collisional excitations from their respective ground states, the cooling of the interstellar gas is mainly ensured by the metal lines. Hence, in the most diffuse part of the ISM, the most effective coolants are C II (158  $\mu\text{m}$  transition) and O I (63  $\mu\text{m}$  transition). In the denser molecular clouds, the cooling of the gas is mainly assured by the fine-structure transition of C I and by the ro-vibrational emission lines of  $\text{H}_2$ , CO,  $\text{O}_2$ ,  $\text{H}_2\text{O}$ , and some molecular ions.

### 1.1.2.2 Chemistry on dust grains

Interstellar dust grains find their origin in the material ejected from stars. They form in dense environment such as the atmosphere of evolved stars, from which they are released in the ISM via radiation pressure, stellar winds, or novae and supernovae explosions. The size of the grains can go from a few nanometers to several micrometers for the biggest ones, and they are composed of either silicates or amorphous carbon (Lequeux, 2005; Draine, 2011).

Before the advent of IR spectroscopy, interstellar grains were merely an annoyance for astronomers because of the phenomenon called interstellar extinction, namely that they efficiently absorb light within wavelengths from UltraViolet (UV) to the visible. However, thanks to IR observations, the interstellar grains population appeared to be a significant compound of astrophysical processes despite the fact that it represents only 1% of the ISM mass. Indeed, the light absorbed by the grains is reemitted at IR and sub-millimeter wavelength via the process called interstellar reddening, allowing astrophysicists to study the grains' role and properties in the ISM. The interstellar reddening phenomenon is illustrated in figure 1.3.

#### 1.1.2.2.1 Thermal processes

Interstellar grains participate actively in the heating of the gas, especially in regions prone to intense UV radiations. In fact, the incident UV photons tear electrons off the grains surface via photoelectric effects. The freed electrons then furnish energy to the surrounding gas via thermalization.

#### 1.1.2.2.2 Surface chemistry

The grains also participate actively to the ISM chemistry, notably as a catalyst for chemical reactions. As such, they allow the efficient formation of  $H_2$ , the most abundant molecule of the universe (Lequeux, 2005; Draine, 2011). Surface reactions happen via the following process:

1. The adsorption of gas phase species onto the grains surface via physisorption, *ie* via van der Waals interactions, which depends mainly on the collision rate between molecules and grains, and therefore the density of the medium,
2. The diffusion of the species on the grains surface, which depends mainly on the grains temperature, the nature of its core, as well as its porosity,
3. The reaction of the species upon encounter with another one,

The product species can then either keep on diffusing on the surface, or desorb back into the gas phase.

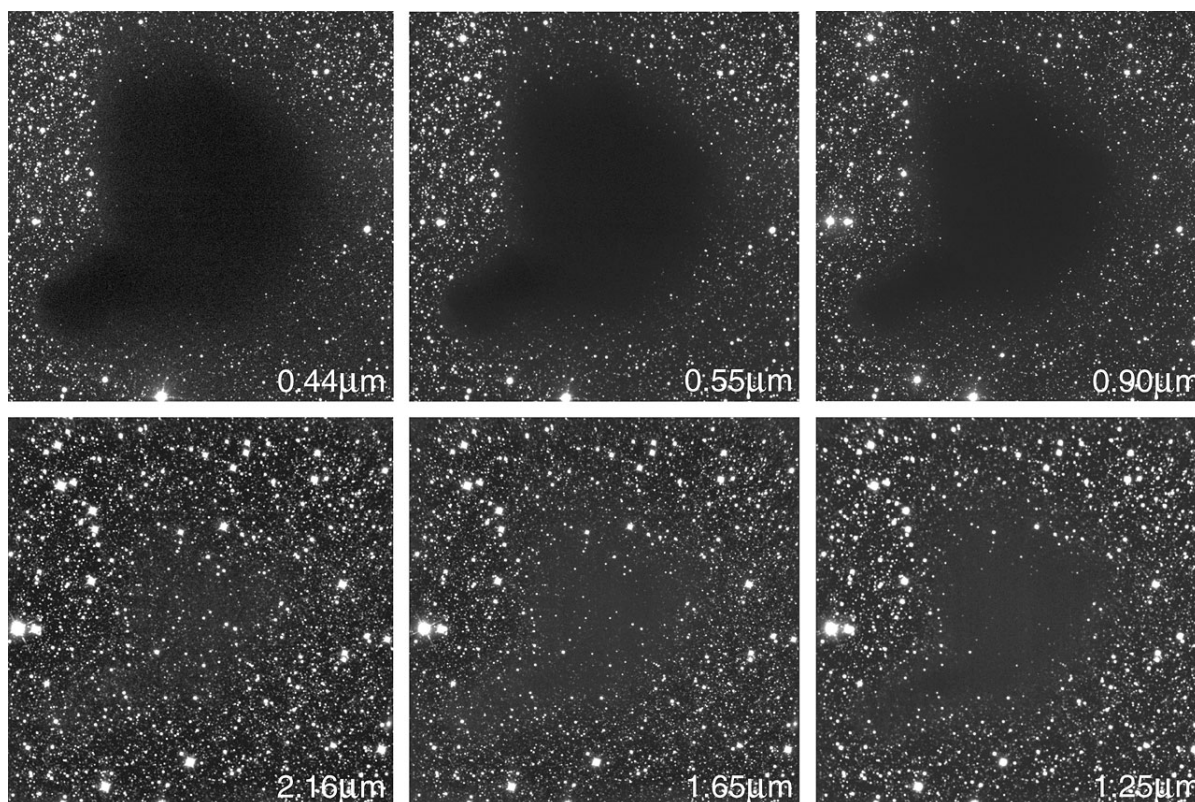


Figure 1.3: Barnard 68 at different wavelengths (clockwise). This molecular cloud is at a distance of 160 pc in the Ophiuchus constellation. At visible (0.4 to 0.8  $\mu\text{m}$ ) and near-infrared (0.8 to 1.4  $\mu\text{m}$ ) wavelengths, it appears as a dark "hole" in the stellar population around it. The hole vanishes at longer wavelength ( $\approx 2 \mu\text{m}$ ) because of interstellar reddening due to the presence of grains in the line of sight. Credits: ESO

Surface chemistry is especially efficient in dense regions of the ISM, where the temperature is cold enough for adsorbed species to spend a significant time on the grains surface. In such regions, the accumulation of adsorbed species on grains surface allows numerous reactions, as well as the stack of layers of "ices", forming the grains bulk. These "ices" are mainly a blend of water ( $\text{H}_2\text{O}$ ), carbon monoxide ( $\text{CO}$ ), and carbon dioxide ( $\text{CO}_2$ ). Species in the bulks are "trapped", since they have limited diffusivity and cannot desorb back into the gas phase, but can still react upon encounter with surrounding species. The complex chemistry of grains in these dense regions is notably believed to be mainly responsible for the formation of complex organic molecules, observed in star forming regions and which are of prime interest in the search for the origin of Life.

As the extreme dimensions and physical conditions of the ISM forbid *in situ* experimentations, the study of the aforementioned processes requires the use of chemical modeling coupled with laboratory experiments.



## 1.1.2.3 Generalities on chemical modeling

For a gas phase reaction such as the following one:



where  $X_1$  and  $X_2$  are the reactants, and  $X_3$  and  $X_4$  are the products, the reaction rate can be expressed as, in  $\text{part.cm}^{-3}.\text{s}^{-1}$ :

$$v = -\frac{dn(X_1)}{dt} = -\frac{dn(X_2)}{dt} = \frac{dn(X_3)}{dt} = \frac{dn(X_4)}{dt} \quad (1.2)$$

where  $n(X_i)$  is the concentration of species  $X_i$ , in  $\text{part.cm}^{-3}$ . If the reaction is elementary, *ie* happens directly without intermediaries, the reaction rate can be written as:

$$v = kn(X_1)n(X_2) \quad (1.3)$$

where  $k$  is the rate constant of the reaction, in  $\text{cm}^3.\text{s}^{-1}$ .

This approach can be generalized to model the evolution of the concentration  $n(X_i)$  of a species  $X_i$  by taking into account all the processes that participate to the formation and destruction of this species. The corresponding equation is a simple first order differential equation:

$$\frac{dn(X_i)}{dt} = \text{Formation} - \text{Destruction} \quad (1.4)$$

Hence, for  $N$  species  $X_i, i = \{1, \dots, N\}$ , the following system is obtained:

$$\begin{aligned} \frac{dn(X_1)}{dt} &= f_1(X_1, \dots, X_N) \\ \frac{dn(X_2)}{dt} &= f_2(X_1, \dots, X_N) \\ &\dots \\ \frac{dn(X_N)}{dt} &= f_N(X_1, \dots, X_N) \end{aligned} \quad (1.5)$$

where  $f_i$  depends on the rate constants  $k_j, j = \{1, \dots, M\}$  of the  $M$  chemical reactions of the network as well as the concentrations  $n(X_i)$  of the  $N$  species considered. The solution of this system of differential equations then gives the evolution of the

concentration of the  $N$  species as a function of time.

#### 1.1.2.4 A word about laboratory experiments

As seen in section 1.1.1, laboratory experiments play a significant role in the spectroscopy aspect of astrochemistry, namely by measuring the emission spectra of interstellar species. Another paramount role of laboratory experiment is to measure and calculate the parameters needed to correctly model chemical reactions. Equation (1.3) shows for example the importance of a good determination of the rate constant  $k$ , which mainly depends on parameters of the reactions that can only be measured in laboratory, such as its activation energy.

### 1.1.3 The NAUTILUS chemical model

The NAUTILUS chemical model computes the evolution of chemical abundances by solving a system of differential equations similar to (1.5). The model uses the "rate equation" approach, which consists in considering that the system evolution is continuous and deterministic, *ie* the state of the system at any given time can be inferred from its initial state. It can simulate a 3-phases chemistry including gas phase, grains surface and grains bulk chemistry, along with the possible exchanges between the different phases (Ruaud et al., 2016). The processes taken into account in the model are described in the following.

#### 1.1.3.1 Gas phase chemistry

##### 1.1.3.1.1 Bimolecular reactions

For a gas phase reaction between species  $i$  and  $j$ , the corresponding rate constant  $k_{ij}$  is calculated via the Arrhenius-Kooij law:

$$k_{ij} = \alpha_{ij} \left( \frac{T_{\text{gas}}}{300\text{K}} \right)^{\beta} \exp\left( \frac{-E_{A,ij}}{T_{\text{gas}}} \right) \quad (1.6)$$

where  $\alpha_{ij}$  and  $\beta$  are constants of the reaction,  $T_{\text{gas}}$  is the gas temperature, in K, and  $E_{A,ij}$  is the activation energy of the reaction, in K. The latter is the energy that the system needs for the reaction to overcome the barrier. Hence, only collisions that imply a sufficient kinetic energy can overcome the barrier and result in a reaction.  $\alpha_{ij}$ ,  $\beta$ , and  $E_{A,ij}$  are obtained by fitting laboratory measurements at different temperatures. In several cases, equation (1.6) can be simplified because  $\beta = 0$ , or because, as it is the case for most ion-neutral reactions, the reactions do not have a barrier, *ie*  $E_{A,ij} = 0$ .

### 1.1.3.1.2 Photodissociation and photoionization

The model takes into account the two main phenomenons responsible for the photodissociation and photoionization of gas phase species:

- the direct interaction between species and cosmic rays (CR),
- the direct interaction with UV photons, either coming from the interstellar radiation field or induced by CR (see [Prasad and Tarafdar, 1983](#)).

The efficiency of these phenomenons depends mainly on the CR ionization rate  $\zeta_{\text{CR}}$ , in  $\text{s}^{-1}$ , and the visual extinction  $A_V$ , in mag. The latter quantifies the absorption and scattering of the electromagnetic field by the gas and the dust grains, *ie* it determines the opacity of the considered medium to radiation.

### 1.1.3.2 Grains chemistry

Figure 1.4 displays the representation of an interstellar grain as modeled by the NAUTILUS chemical model. It considers grains with silicate cores and a radius of  $r_g = 0.1 \mu\text{m}$ . The adsorption of molecules on a bare grain forms mono-layers of ice, which consequently pile up to form the total icy grain coverage. The total number of mono-layer is  $N_{\text{ML}} = N_{\text{surf}} + N_{\text{bulk}}$  where  $N_{\text{surf}}$  is the number of surface mono-layers, *ie* the outer ones which can interact with the gas phase, and  $N_{\text{bulk}}$  the number of mono-layers in the bulk. The total maximum of mono-layers on the surface is set to  $N_{\text{surf,max}} = 2$ . On the outer mono-layers are considered sites called binding sites, which represents the small areas on grains where species can adsorb and chemical reactions can happen. A density of  $d_s = 1.5 \times 10^{15}$  sites per  $\text{cm}^2$  is considered in the model. In the following is explained how grains chemistry is modeled in NAUTILUS, and all the processes described are summarized in figure 1.5.

#### 1.1.3.2.1 Accretion and diffusion

Accretion onto grains surface is implemented in the model from [Hasegawa et al. \(1992\)](#). The corresponding accretion rate for a species depends mainly on the grains density in the medium, their geometrical cross section as well as the sticking coefficient. The latter is taken equal to 1 for all species except H and  $\text{H}_2$ , for which the experimentally-derived formalism is taken from [Chaabouni et al. \(2012\)](#).

Regarding the diffusion of the species on the grains surface after their accretion, the model takes into account thermal diffusion. This mechanism depends on the diffusion energy of the species, which is the energy to bring to the species to hop from a grain site to another. These energies are computed as a fraction of the species respective binding energies, *ie* the energy needed by the species to desorb from the grains surface. For the surface the value of this ratio is of 0.4 as suggested by experiments and theoretical



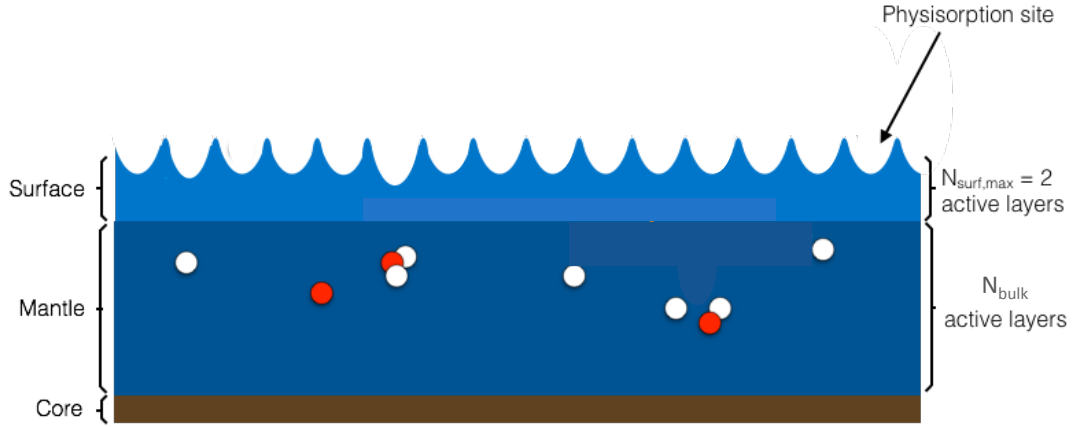


Figure 1.4: Representation of an interstellar grain as modeled by the NAUTILUS chemical model.

works made on H (see Ruaud et al., 2016, and the references therein), CO and CO<sub>2</sub> (see Karssemeijer and Cuppen, 2014). This value is then generalized to every species on the surface.

Once a species enter the grains bulk, the model considers that its diffusion is controlled by the diffusion of water ice as shown by the theoretical work of Ghesquière et al. (2015). Hence, for species which have a diffusion energy  $E_D < E_D^{\text{H}_2\text{O}}$ , their diffusion energy in the bulk is taken to be equal to  $E_D^{\text{H}_2\text{O}}$ . Moreover, the ratio between diffusion and binding energies is taken equal to 0.8 in the bulk (see also Ruaud et al., 2016).

#### 1.1.3.2.2 Grains surface reactions

The main mechanism considered in the model for grains surface reactions is the Langmuir-Hinshelwood mechanism, which considers that a reaction between two species happens through the following steps:

1. the adsorption of two reactants onto grains surface,
2. the diffusion of one (or both) reactant(s) on the surface,
3. the reaction between the two reactants upon encounter on the same grains site.

This mechanism depends mainly on the probability of the reaction between species  $i$  and  $j$ ,  $\kappa_{ij}$ . This coefficient is taken equal to 1 if the reaction between the two species is without barrier, ie in that case, the species will always react upon encounter. However, if the reaction has a barrier  $E_{A,ij} > 0$ , then the competition between the reaction and the diffusion (or desorption) of one of the reactants is considered, as suggested by Chang

et al. (2007) and Garrod and Pauly (2011). In that case the reaction happens if the activation energy of the reaction is lower than the diffusion energy of both reactants.

In the grains bulk, reactions happen via the same mechanism. However,  $\kappa_{ij}$  is there divided by the number of bulk layers, considering that the diffusion efficiency in the bulk decrease with increasing ices thickness.

The other reaction mechanism considered is the Eley-Rideal mechanism which can be decomposed as:

1. the adsorption of one of the reactants onto grains surface,
2. direct collision between a gas phase species (second reactant) and the adsorbed one,
3. possible reaction between both reactants one the grain site where the collision happened.

Note that this mechanism can only happen on grains surface (not in the bulk), where adsorbed species are in direct contact with the gas phase. Moreover, it is less frequent than the Langmuir-Hinshelwood one, but can still play an important role for the formation of specific species when the adsorbed reactant is very abundant (see Ruaud et al., 2015).

### 1.1.3.2.3 Dissociation

As for the gas phase, the grain chemistry takes into account the standard direct photodissociation by UV photons along with the photodissociation induced by secondary UV photons introduced by Prasad and Tarafdar (1983). These processes are effective on the surface as well as in the bulk of the grains. Indeed, the probability of absorption of each mono-layer of ice is low ( $P_{\text{abs}} \approx 0.007$  photons/mono-layer, Andersson and van Dishoeck, 2008). Hence, this hypothesis is reasonable considering that the average number of mono-layers of ice on the grains is of 100 mono-layers, and that consequently only 0.7% of the photons colliding with the surface would be absorbed before reaching the grains core.

### 1.1.3.2.4 Desorption

The desorption processes taken into account in the model are:

- the thermal desorption, *ie* evaporation, which depends on the temperature of the grain and the binding energy of the species considered,

- the CR desorption, which is due to the punctual heating of the grains by CR, which induces thermal desorption. It depends on the fraction of time the grain spend at the temperature due to the CR impact and the thermal desorption rate at this temperature,
- the chemical desorption, which considers for exothermic grains surface reactions, that part of the energy released can cause the desorption of their products. The formalism used in the model for this process is the one depicted in [Garrod et al. \(2007\)](#). They considered that the fraction of the products desorbed in the gas phase depends on their binding energies, the enthalpy of the reaction, and the fraction of the released energy that is lost to the surface. In the model used here, the parameters are selected to result in approximately a 1% efficiency evaporation for all species,
- the photodesorption, which is a non thermal process, and happens after the absorption of a UV photon by the surface. As recommended by [Bertin et al. \(2012\)](#) a unique photodesorption rate is taken for all surface species.

All the processes described above are summarized in figure 1.5.

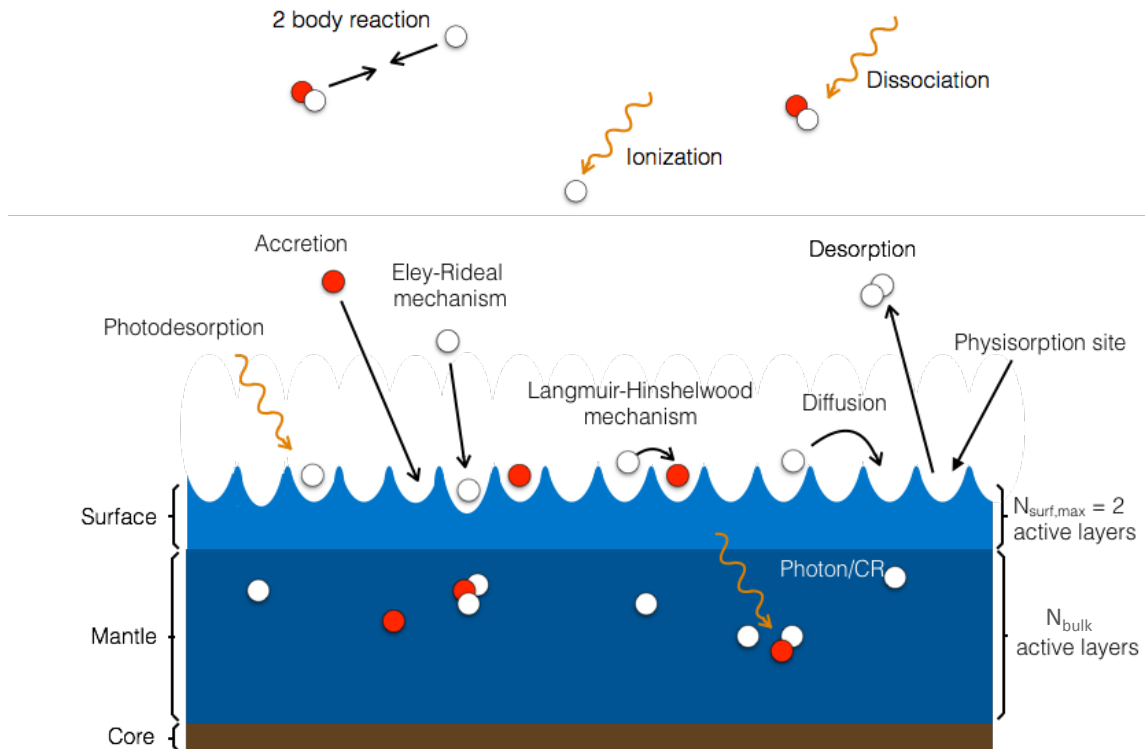


Figure 1.5: Summary of the chemical processes taken into account in the NAUTILUS 3-phases chemical model (from [Ruaud et al., 2016](#)).

## 1.2 ... OF STAR FORMATION

In addition to allow the formation of planets, liquid water, and Life, stars play a major role in the Universe. This role consists in the formation, destruction and redistribution of the interstellar matter through their lifecycle. Figure 1.6 illustrates this cycle of the interstellar matter through stars formation, life and decay. In the following, each step of this cycle is presented, with a special focus on star formation, which is the subject of interest of this thesis.

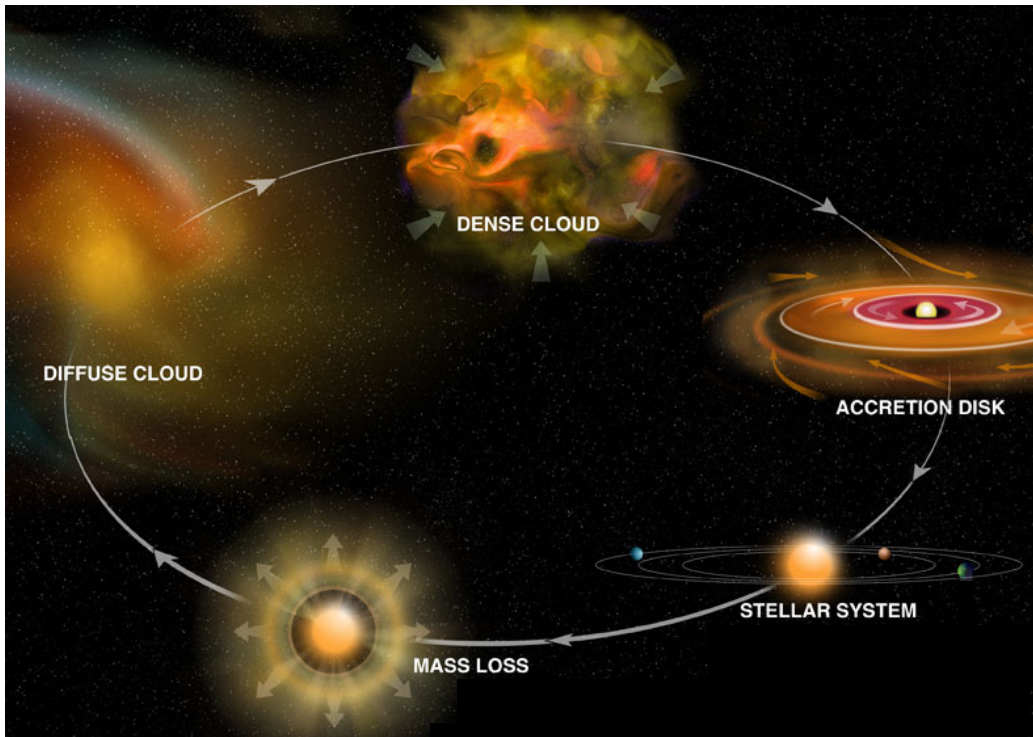


Figure 1.6: The cycle of interstellar matter. Credits: Bill Saxton, NRAO/AUI/NSF.

### 1.2.1 From diffuse clouds to dense clouds

Diffuse clouds are defined as part of the ISM where the density is of  $n_H \in [100 ; 500]$   $\text{part.cm}^{-3}$  and  $T_{\text{gas}} \in [30 ; 100]$  K (Snow and McCall, 2006). In these regions, the density is high enough to mitigate the interstellar radiation field ( $A_V > 0.2$ ) and  $\text{H}_2$  can accumulate without being instantaneously photodissociated. Under dynamical effect, such a diffuse cloud can condense into a dense cloud. These dense clouds are nearly opaque to the interstellar radiation field ( $A_V > 5$ ), which allows carbon to stay un-

der molecular form (preferentially CO). This opacity is due to their high dust grains density, as illustrated in 1.3. Dense clouds are therefore characterized by high proton densities ( $n_H > 10^4 \text{ part.cm}^{-3}$ ) which also implies low temperatures ( $T_{\text{gas}} \in [10 ; 50] \text{ K}$ , see [Snow and McCall, 2006](#)). Note that the opacity of such clouds to visual light is the reason they are also called dark clouds, as they will be named hereafter. As mentioned in section 1.1.2, dark clouds are regions where gas and grains chemistries are particularly efficient, allowing their chemical composition to evolve significantly during their lifetime of a few million years.

### 1.2.2 Cloud collapse and star formation

The details of the star formation process are still poorly constrained because it involves many different physical mechanisms over a huge range of spatial scales. However the main steps of its progress are known. In terms of mass, two type of stars exist: low-mass ( $\leq 10 M_{\odot}$ ) and high-mass ( $> 10 M_{\odot}$ ) stars. The formation process of high-mass stars is still a puzzling issue:

- they could form from the same process as low-mass stars, except that it would happen much faster because gravitational effects are much higher than for low-mass ones,
- they could form from the merging of low-mass star forming cores, since high-mass stars usually forms in dense clusters.

In the following and for the sake of clarity, only the formation process common to the two types of stars is described.

Figure 1.7 presents a detailed view of the different steps of star formation. When the prestellar cores that form within dark clouds become large enough to become gravitationally unstable, they start collapsing onto themselves. Typically, the density fluctuations that initiate the collapse can be caused by highly energetic events such as the collide of two dark clouds or even galaxies, or a nearby supernovae explosion that sends shocked matter into the cloud at very high velocity.

These increases in density are initially optically thin and the prestellar core collapses isothermally, with compressional heating evacuated through radiation. The efficiency of this radiative cooling drops as the density of the core increases at its center. When it can no longer equilibrate with the compressive calefaction, the evolution of the matter at the center of the core becomes adiabatic, and a hydrostatic core, known as the first hydrostatic core (FHSC), or first Larson's core ([Larson, 1969](#)), is formed at the center. The protostar is born. During a short period of time ( $< 1000$  years, see for example [Vaytet and Haugbolle, 2017](#)), the FHSC will continue to accrete surrounding material from its envelope, consequently increasing its mass, density and temperature.

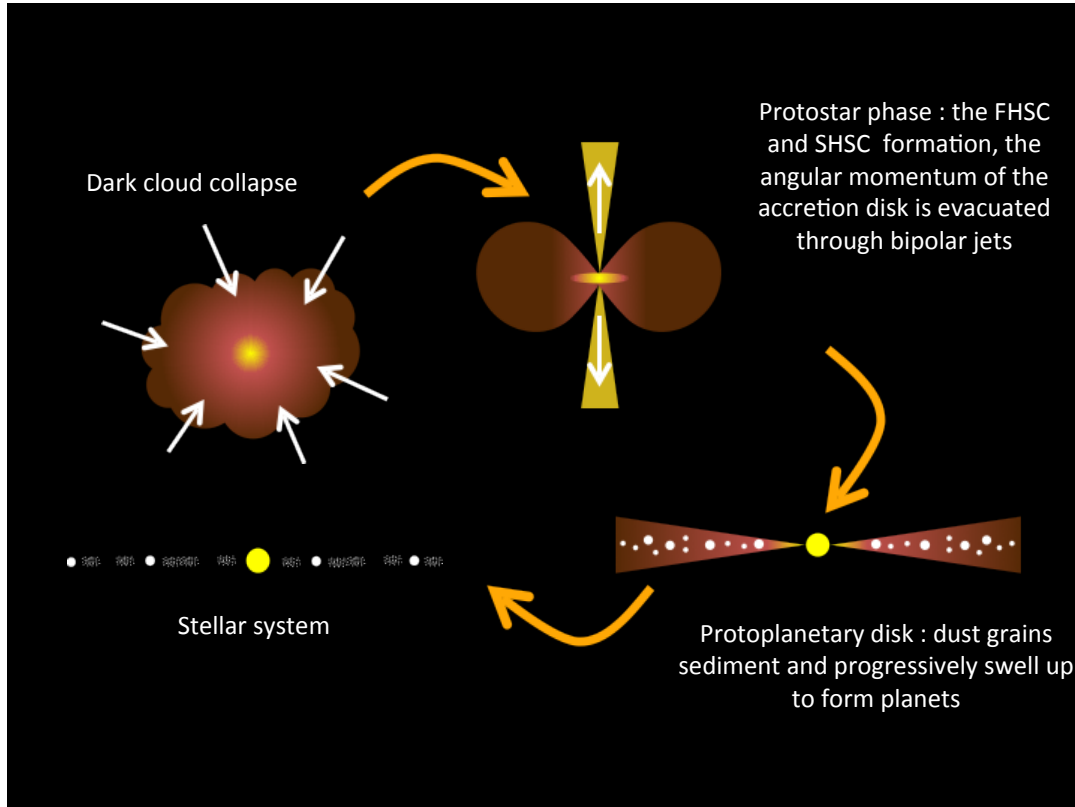


Figure 1.7: Steps of star formation. The figure can be seen as the detail of the right part of the cycle in figure 1.6, between the dark cloud and the solar system phases. The terms FHSC and SHSC mean respectively first and second hydrostatic core.

When its temperature exceeds  $\approx 2000$  K, the dissociation of  $H_2$  molecules inside the core is triggered. Because of the endothermic nature of this process, a second phase of collapse begins. When most of the  $H_2$  molecules have been split, the second collapse ceases and a much more dense and compact core forms, called the second Larson's core (SHSC, [Larson, 1969](#)). The core continues to slowly accrete material for a few hundred thousand years, until its temperature is high enough to trigger nuclear reactions and the protostar becomes a young star.

During all this process, the material surrounding the protostar also evolves. When the collapse begins, the material of the prestellar core progressively evolves into a rotating accretion disk around the protostar (see figure 1.6). When the FHSC is formed, the angular momentum of this disk is evacuated by the formation of bipolar jets that creates shocks in the surrounding envelope, triggering an efficient high temperature chemistry which products can fall back on the accretion disk. The latter loses most of its matter through both collapses, until the young star is formed. Afterwards, the disk is named protoplanetary disk, since it is within it that dust grains will sediment and progressively swell up to finally form planets. The stellar system is born.

### 1.2.3 The death of stars

Typically, stars die when they run out of fuel. When the core of a star runs out of hydrogen, it becomes unstable and contracts gravitationally. The radiative energy caused by this collapse pushes the outer shell of the star to expand until the star reaches the red giant phase. In the core of a red giant, helium fuses into carbon. Afterwards, the destiny of the star depends on its mass:

- for low-mass stars, once all the helium has transformed into carbon, the core collapses again and the outer layers of the stars are expelled via radiative effects. A planetary nebula is formed by the expelled layers, and the core remains as a white dwarf that will eventually cool to become a black dwarf.
- for high-mass stars, the red giant is still massive enough for the carbon in the core to fuse into heavier elements until it turns into iron and can no longer burn. At this stage, the star collapses again, causing the iron core to heat up and condense and protons and neutrons merge into neutrons. In less than a second, the (approximately) Earth-sized iron core turns into a neutron core of a few kilometers. The collapse makes the core heats up to billions of degrees and finally explode into a supernovae, redistributing the matter into the ISM. The supernovae remnant can then either be a neutron star or a black hole, depending on the star's initial mass.

The stars lifecycle is of particular interest for astrochemists because it regulates the chemistry of the ISM. Indeed, the several physical processes and parameters that can be found during this cycle are responsible for the creation, redistribution and destruction of all the molecules that compose the Universe. More specifically, the process of star formation has a paramount role in this cycle, since it allows the formation of the complex molecules such as COMs, which are believed to hold the keys to understand how Life appeared on Earth.

## 1.3 OBJECTIVES AND ORGANIZATION OF THE THESIS

The objective of this thesis is to give a new look at the chemistry of star formation using the recent enhancements of the NAUTILUS chemical model, such as the 3-phases model or the process of competition between reaction and diffusion/desorption. More particularly, I focus on the following points:

1. the problematic of sulphur depletion in dark clouds,
2. the revisit of sulphur chemistry in hot cores and corinos,
3. the development of a method to derive the initial parameters of collapsing prestellar cores from protostars observations based on physico-chemical models.



The 3 following chapters present respectively each of these studies and their results. Note that the first two studies presented hereafter have been published ([Vidal et al., 2017](#); [Vidal and Wakelam, 2018](#)). The last chapter concludes this thesis.





# 2 | RECONCILING SULPHUR CHEMISTRY WITH ITS ELEMENTAL ABUNDANCE IN DARK CLOUDS

## Contents

---

<b>2.1</b>	<b>INTRODUCTION . . . . .</b>	<b>47</b>
2.1.1	The sulphur depletion problem . . . . .	47
2.1.2	Current hypothesis on the reservoirs of sulphur in dark clouds	48
<b>2.2</b>	<b>PRESENTATION OF THE ENHANCED CHEMICAL NETWORK . . . . .</b>	<b>49</b>
2.2.1	Modification of the sulphur network . . . . .	49
2.2.2	Effects of the new network on the chemical model of dark clouds	51
2.2.2.1	The main sulphur bearing species . . . . .	51
2.2.2.2	The newly implemented sulphur bearing species . .	54
2.2.2.3	Comparison with the previous network . . . . .	58
<b>2.3</b>	<b>COMPARISON WITH OBSERVATIONS IN THE DARK CLOUD TMC-1 .</b>	<b>63</b>
2.3.1	Comparison with models A and B . . . . .	64
2.3.2	Variation of the elemental sulphur abundance . . . . .	65
2.3.2.1	Comparison with all observed gas phase species . .	66
2.3.2.2	Comparison with observed sulphur bearing gas phase species . . . . .	67
2.3.2.3	The new species HNCS and HSCN . . . . .	68
2.3.2.4	Sulphur bearing species on grains towards W33A .	69
2.3.3	Sulphur reservoirs in dark clouds . . . . .	70
<b>2.4</b>	<b>DISCUSSIONS AND SUMMARY . . . . .</b>	<b>73</b>
2.4.1	About the elemental abundance of sulphur . . . . .	73
2.4.2	About the reservoirs of sulphur in dark clouds . . . . .	73
2.4.3	About the observability of HCS . . . . .	74
2.4.4	Summary . . . . .	74

---



## 2.1 INTRODUCTION

Since the first detection of a S-bearing molecule in the interstellar medium (CS, [Penzias et al., 1971](#)), sulphur has become a subject of interest for many astrochemists. S-bearing molecules are indeed often used to probe the physical structure of star-forming regions ([Lada et al., 1991](#); [Plume et al., 1997](#); [Viti et al., 2001](#); [Sakai et al., 2014](#); [Podio et al., 2015](#)) and have been proposed as chemical clocks for hot cores ([Charnley, 1997](#); [Hatchell et al., 1998](#); [Wakelam et al., 2004a](#)). But sulphur chemistry in dense interstellar medium has also been at the centre of a puzzling issue for many years, namely the sulphur depletion problem ([Ruffle et al., 1999](#)).

### 2.1.1 The sulphur depletion problem

The sulphur depletion problem is a long lasting issue that originates from considerations from both observations and chemical modeling:

- From an observational point of view, unlike most of the other elements in the diffuse medium, the gas phase abundance of atomic sulphur is observed to be constant with cloud density, around its cosmic value of a few  $10^{-5}$  (see for instance [Jenkins, 2009](#)). However, in dark clouds the total abundance of detected S-bearing molecules (see 2.1 for a list of these species) only accounts for 0.1% of the cosmic abundance of atomic sulphur ([Tieftrunk et al., 1994](#); [Charnley, 1997](#)). Therefore, the main reservoirs of sulphur in dark clouds are still unknown.
- From a chemical modeling point of view, assuming an elemental abundance of sulphur in chemical models as high as its cosmic value produces predicted abundances of observable S-bearing molecules much higher than the observed one. Consequently, modelers usually assume that the elements (sulphur but other heavy elements as well) are initially depleted compared to their cosmic reference values and use the so-called "depleted" abundance of sulphur of a few  $10^{-8}$  ([Wakelam and Herbst, 2008](#)). The main issue of this assumption is that the considered "depleted" sulphur is in an unknown form and it is therefore not possible to conclude on the possible reservoirs of sulphur in dark clouds from these models. In this context, it seems that a review of the chemistry included in astrochemical models is necessary.

Hence, a more complete sulphur network as well as a better understanding of grain chemistry at low temperature are needed. They would indeed allow to run more realistic models of dark clouds and therefore suggest new hints to solve the sulphur depletion problem.

Table 2.1: List of the sulphur bearing species firmly detected in dark clouds, in the gas phase and in grain ices.

Species	References
Gas phase	
OCS	1
NS	1
H <sub>2</sub> S	1
CS	1
HCS <sup>+</sup>	1
H <sub>2</sub> CS	1
C <sub>2</sub> S	1
C <sub>3</sub> S	1
SO	1
SO <sub>2</sub>	1
HNCS	2
HSCN	2
Grain ices	
OCS	3
SO <sub>2</sub>	4

References: (1) Table 4 from [Agúndez and Wakelam \(2013\)](#), (2) [Adande et al. \(2010\)](#), (3) [Palumbo et al. \(1997\)](#), (4) [Boogert et al. \(1997\)](#)

### 2.1.2 Current hypothesis on the reservoirs of sulphur in dark clouds

The main hypothesis to explain the missing sulphur in dark clouds is that it is depleted onto interstellar grains. In cometary ices, which are thought to present chemical similarities with the ices formed in dark clouds ([Irvine et al., 2000](#)), H<sub>2</sub>S is the most abundant S-bearing molecule, at the level of 1.5% compared to water ([Bockelée-Morvan et al., 2000](#)). More recently, [Holdship et al. \(2016\)](#) derived the abundance and deuteration fraction of H<sub>2</sub>S in the low-mass protostar L1157-B1. By comparing the observations to chemical models with different branching ratios for the freeze out of S-bearing species into OCS and H<sub>2</sub>S, they found that a significant fraction of the sulphur is likely to be locked into the form of H<sub>2</sub>S on the grains. Chemical models also predict that, in the dense interstellar medium, atomic sulphur would stick on grains and be mostly hydrogenated to form H<sub>2</sub>S. To this day however only OCS ([Palumbo et al., 1997](#)) and SO<sub>2</sub> ([Boogert et al., 1997](#)) have been likely identified in icy grains bulk in dense molecular clouds surrounding high-mass protostars, and their estimated total abundance does not account for the missing sulphur. Upper limits of at most  $3 \times 10^{16} \text{ cm}^{-2}$  for the column density of H<sub>2</sub>S in icy grains bulk have been derived by [Smith \(1991\)](#), notably towards the line of sight of three late-type field stars lying behind the Taurus molecular cloud, but they are also too low for H<sub>2</sub>S to be the reservoir of sulphur

in dark clouds.

Laboratory experiments coupled with chemical models have recently brought new insight into the problem by studying the irradiation of H<sub>2</sub>S interstellar ice analogs by energetic protons and UV photons by [Garozzo et al. \(2010\)](#) and [Jiménez-Escobar and Muñoz Caro \(2011\)](#). Both studies found that solid H<sub>2</sub>S was easily destroyed to form other species such as OCS, SO<sub>2</sub>, CS<sub>2</sub> and H<sub>2</sub>S<sub>2</sub>.

In the study presented hereafter, I propose an enhancement of the sulphur chemical network for dark clouds models motivated by the recent observations of HNCS and HSCN in TMC-1 (CP) ([Adande et al., 2010](#)) and of CH<sub>3</sub>SH in IRAS 16293-2422 ([Majumdar et al., 2016](#)). My network also includes the network proposed by [Druard and Wakelam \(2012\)](#). I test the effect of the updated network on the outputs of the NAUTILUS chemical model for dark cloud conditions using different sulphur elemental abundances. More particularly, I focus my study on the main sulphur reservoirs as well as on the agreement between model predictions and the abundances observed in the dark cloud TMC-1 (CP). The state of the NAUTILUS chemical model used is the same as presented in section 1.1.3. In the following, I first detail the modifications of the chemical network and describe the new modeling results, including a comparison with the previous version of the network. Then I compare these results with observations towards the dark cloud TMC-1 (CP), to finally discuss and conclude on the results.

## 2.2 PRESENTATION OF THE ENHANCED CHEMICAL NETWORK

### 2.2.1 Modification of the sulphur network

The set of reactions added and revisited was constructed by Jean-Christophe Loison, a chemist from the Institute of Molecular Sciences (ISM) in Bordeaux. To update the sulphur chemical network, he first examined the existing KIDA network ([kida.uva.2014](#), [Wakelam et al., 2015a](#)) looking systematically at possible reactions between S and S<sup>+</sup> with the most abundant species in dense molecular clouds (CO, CH<sub>4</sub>, C<sub>2</sub>H<sub>2</sub>, c-C<sub>3</sub>H<sub>2</sub>) as well as the potential reactions between sulphur compounds and the most abundant reactive species in molecular clouds (C, C<sup>+</sup>, H, N, O, OH, CN). He found out that various neutral reactions were missing from KIDA (or other databases) such as C + H<sub>2</sub>S, C + H<sub>2</sub>CS and S + l,c-C<sub>3</sub>H. When previous experimental or theoretical studies exist, he used them to update the KIDA database when necessary. In order for the interested reader to learn about the methodology used to develop this database of S-bearing species chemical reactions, and especially because I did not conduct this part of the study, I invite him/her to read section 2 of [Vidal et al. \(2017\)](#), and its appendixes.

Table 2.2: Table of the 46 sulphur bearing species added to the network.

Neutrals	
CS <sub>2</sub>	HNCS
H <sub>2</sub> S <sub>3</sub> *	HSCN
S <sub>3</sub> *	H <sub>2</sub> C <sub>3</sub> S
S <sub>4</sub> *	HNCHS
S <sub>5</sub> *	HSCHN
S <sub>6</sub> *	HNCSH
S <sub>7</sub> *	NH <sub>2</sub> CHS
S <sub>8</sub> *	H <sub>2</sub> C <sub>2</sub> S
HC <sub>3</sub> S	NH <sub>2</sub> CS
HC <sub>2</sub> S	NH <sub>2</sub> CH <sub>2</sub> S
CH <sub>3</sub> S	NH <sub>2</sub> CH <sub>2</sub> SH
CH <sub>3</sub> SH	HSO
CH <sub>2</sub> SH	HNCHSH
HCNS	NH <sub>2</sub> CHSH
Ions	
CS <sub>2</sub> <sup>+</sup>	HSCN <sup>+</sup>
HCS <sub>2</sub> <sup>+</sup>	H <sub>2</sub> CNS <sup>+</sup>
H <sub>2</sub> C <sub>2</sub> S <sup>+</sup>	H <sub>2</sub> NCS <sup>+</sup>
H <sub>2</sub> C <sub>3</sub> S <sup>+</sup>	H <sub>2</sub> SCN <sup>+</sup>
CH <sub>3</sub> S <sup>+</sup>	HCNSH <sup>+</sup>
CH <sub>3</sub> SH <sup>+</sup>	HNCSH <sup>+</sup>
CH <sub>3</sub> SH <sub>2</sub> <sup>+</sup>	CH <sub>3</sub> CS <sup>+</sup>
HCNS <sup>+</sup>	NH <sub>2</sub> CHSH <sup>+</sup>
HNCS <sup>+</sup>	NH <sub>3</sub> CH <sub>2</sub> SH <sup>+</sup>

\* These species are not allowed to evaporate in the gas phase (see text).

Overall, I added (or reviewed in the case of reactions) 46 S-bearing species to the network along with 478 reactions in the gas phase, 305 reactions on the grains surface and 147 reactions in the grains bulk (see the table in appendix A). The newly introduced species are listed in Table 2.2. Note that, among these species, H<sub>2</sub>S<sub>3</sub> and S<sub>*n*</sub> (*n* = 3 to 8) are only present on the grains, *ie* they are formed on the surfaces and not allowed to evaporate (see also [Druard and Wakelam, 2012](#)). At 10 K, these species are not efficiently formed so they can be neglected. It should also be noted that the enhanced network includes the chemical schemes for carbon chains proposed in [Wakelam et al. \(2015b\)](#), [Loison et al. \(2016\)](#), [Hickson et al. \(2016\)](#), and [Loison et al. \(2017\)](#).

All the models presented hereafter are in 0D and run under dark cloud constant physical conditions, namely a gas and dust temperature of 10 K, a proton density of  $2 \times 10^4 \text{ cm}^{-3}$ , a cosmic ionization rate of  $1.3 \times 10^{-17} \text{ s}^{-1}$ , and a visual extinction of

Table 2.3: Initial abundances.  $*a(b)$  stands for  $a \times 10^b$ 

Element	$[X]_{\text{ini}}^*$	References
H <sub>2</sub>	0.5	
He	0.09	1
N	6.2(-5)	2
O	2.4(-4)	3
C <sup>+</sup>	1.7(-4)	2
S <sup>+</sup>	8.0(-8)	4
Si <sup>+</sup>	8.0(-9)	4
Fe <sup>+</sup>	3.0(-9)	4
Na <sup>+</sup>	2.0(-9)	4
Mg <sup>+</sup>	7.0(-9)	4
P <sup>+</sup>	2.0(-10)	4
Cl <sup>+</sup>	1.0(-9)	4
F	6.7(-9)	5

(1) Wakelam and Herbst (2008), (2) Jenkins (2009), (3) Hincelin et al. (2011), (4) Low-metal abundances from Graedel et al. (1982), (5) Depleted value from Neufeld et al. (2005)

15 mag. Plus, the time used for the models is  $10^7$  years, which is believed to be the maximal age a dark cloud can reach before undergoing gravitational collapse. Finally, the set of initial abundances is presented in in table 2.3.

## 2.2.2 Effects of the new network on the chemical model of dark clouds

In this section I highlight the impact of the enhanced sulphur network on the outputs of the Nautilus chemical model configured for dark clouds physical conditions. I first present the abundance evolution of the most abundant sulphur-bearing species as well as the newly implemented ones. Then I compare the outputs obtained with the new network with those obtained with the nominal network for the same model configuration.

### 2.2.2.1 The main sulphur bearing species

In the following, I study the abundance evolution of the main sulphur-bearing species during  $10^7$  years in dark clouds conditions as obtained with the enhanced network, both in the gas phase and on the grains. I selected these species since they contain more than 5 % of the elemental sulphur at one point of the model.



## 2.2.2.1.1 Gas-phase reservoirs: S, CS and SO

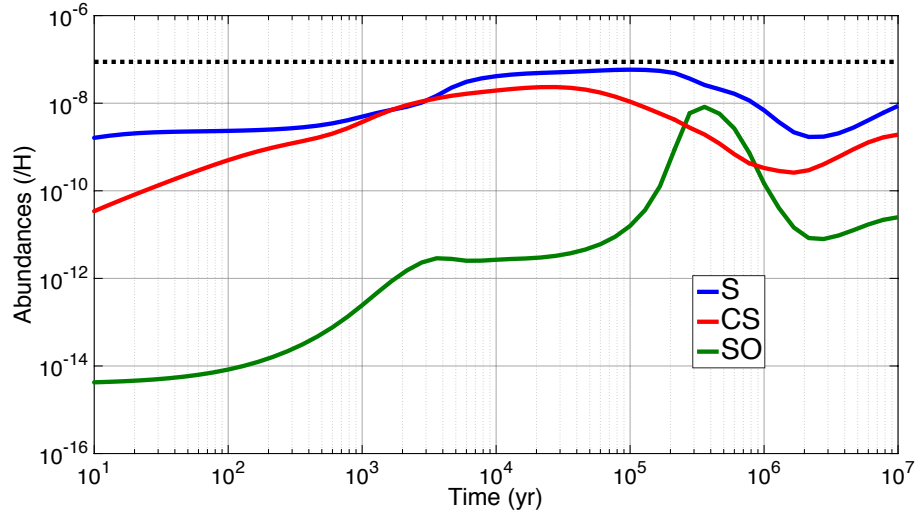


Figure 2.1: Abundances relative to H of the main gas phase S-bearing species S, CS and SO as a function of time for dark cloud physical conditions. The dotted line represents the elemental abundance of sulphur (here,  $[S]_{\text{ini}} = 8 \times 10^{-8}$ ).

Figure 2.1 shows the time evolution of the main sulphur-bearing species in the gas phase: atomic sulphur (S), carbon monosulfide (CS) and sulphur monoxide (SO). In the model, sulphur is initially in the form of  $S^+$  and between  $7.7 \times 10^3$  and  $4.6 \times 10^5$  years, S becomes the main sulphur reservoir (including species on grains). During this period, its abundance reaches a maximum at  $10^5$  years where it contains up to 73% of the elemental sulphur. The growth of the atomic S abundance up to this maximum seems to be mainly caused by the electronic recombination mechanisms of  $S^+$ , as well as of  $CS^+$  and  $HCS^+$ . The last two are related to  $S^+$  by the following reaction mechanism:



This mechanism is therefore very efficient because CH is rapidly formed by electronic recombination of  $CH_2^+$  which is itself formed by the ion-neutral reaction between elemental species  $C^+$  and  $H_2$ . Later, atomic sulphur is consumed by reactions with  $H_3^+$ ,  $CH_3$ , OH and  $O_2$ , which efficiently produce SO, causing the peak in its abundance at  $3.6 \times 10^5$  years. The CS abundance follows closely the atomic sulphur one, first growing from numerous reactions, including notably the electronic recombination of  $HCS^+$ ,  $C_2S^+$  and  $HC_3S^+$  and destruction of  $C_2S$  and by atomic carbon. It reaches a maximum between  $10^4$  and  $10^5$  years, becoming the second main reservoir of sulphur, containing up to 29% of the initial sulphur. However, CS does not accumulate in the gas phase because the hydrogenation of CS followed by dissociative recombination (DR) of  $HCS^+$

produce much more S and CH than H and CS (Montaigne et al., 2005).

### 2.2.2.1.2 Reservoirs on grains : HS and H<sub>2</sub>S

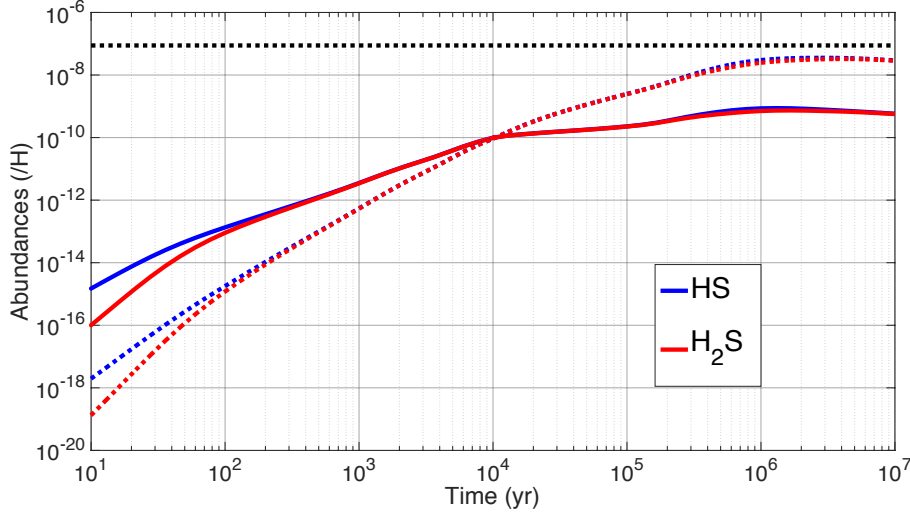


Figure 2.2: Abundances relative to H of the main S-bearing species on the grains HS and H<sub>2</sub>S as a function of time for dark cloud physical conditions, on the surfaces (solid line) and in the bulks (dashed line). The dotted line represents the elemental abundance of sulphur (here,  $[S]_{\text{ini}} = 8 \times 10^{-8}$ ).

On the grains, it appears that the most abundant species are the hydrosulfide radical (HS) and hydrogen sulfide (H<sub>2</sub>S). The abundances of these species, both on the surfaces (solid line) and in the bulks (dashed line), are depicted in Figure 2.2. At times prior to 100 years, both species are formed on the surfaces by the successive hydrogenation of atomic sulphur physisorbed on the grains. Once the species are formed, they begin to sink into the bulk. After a hundred years, both species continue to form on the surface and eventually enter into a loop created by the two following reactions:



Reaction (2.3) has a barrier and should not be efficient under dark cloud physical conditions. However, it becomes efficient in the model because of the reaction-diffusion competition (see section 1.1.3.2) which main effect is to increase the rates of reactions with activation barrier through tunneling (Ruaud et al., 2016). Hence, this cycle, supplied in HS by the hydrogenation of S on the grains, keeps increasing at equal rates the abundances of the two species during the remaining time of the model. As HS and H<sub>2</sub>S keep on sinking into the bulks, their abundances in the latter eventually

becomes higher than at the surfaces. At approximately  $6 \times 10^5$  years, HS and H<sub>2</sub>S (in the bulk) become the main reservoirs of sulphur, containing a total of more than 51% of the total amount of sulphur, that reaches more than 80% at times  $\geq 2.7 \times 10^6$  years, as described in table 2.4. The table also shows that this shared reservoir presents a slight preference for HS between 3 and 10% of the total amount of sulphur, depending on the age of the cloud.

Table 2.4: Description of the total amount of sulphur contained in HS and H<sub>2</sub>S in the grains bulk for times  $\geq 6 \times 10^5$  years. The prefix "b-" is for the bulk species.

Species	$6 \times 10^5$ yrs	$2.7 \times 10^6$ yrs	$10^7$ yrs
b-HS	29%	44%	43%
b-H <sub>2</sub> S	22%	36%	40%

This unexpected result relies on the competition between reaction and diffusion, which main parameter is the height of the reaction barrier. I have assumed for reaction (2.3) a barrier of  $E_A = 860$  K (Kurylo et al., 1971), which was measured at low temperature (in the 190-464 K range). However, the gas phase reaction  $H + H_2S$  has been measured in a wide range of temperature from 190 K up to 2237 K (Kurylo et al., 1971; Peng et al., 1999; Yoshimura et al., 1992). The rate constant shows strong non-Arrhenius behavior at low temperature which is likely due to the importance of tunneling. Peng et al. (1999) performed theoretical calculations of the barrier of the reaction equal to 1330 K at DFT level and 1930 K at QCISD(T) level. Considering these uncertainties, I also tested both these higher values of the barrier but it did not change significantly the results.

### 2.2.2.2 The newly implemented sulphur bearing species

Among the 45 new S-bearing species included in the network, I present below the results of the model for HNCS, the species around which most of the new network has been built, and CH<sub>3</sub>SH, which was recently detected in the envelope of the low-mass protostar IRAS 16293-2422 (Majumdar et al., 2016).

#### 2.2.2.2.1 HNCS and HSCN

Isothiocyanic acid HNCS is the most stable among possible CHNS isomers. It has been very well studied since its first detection in Sgr B2 (Frerking et al., 1979), and has been detected in the dark cloud TMC-1 (CP) (Adande et al., 2010). In contrast, thiocyanic acid HSCN is highly unstable and is about a factor of 3 less abundant in Sgr B2 than HNCS (Halfen et al., 2009). It has also been detected in TMC-1 (CP) with a similar

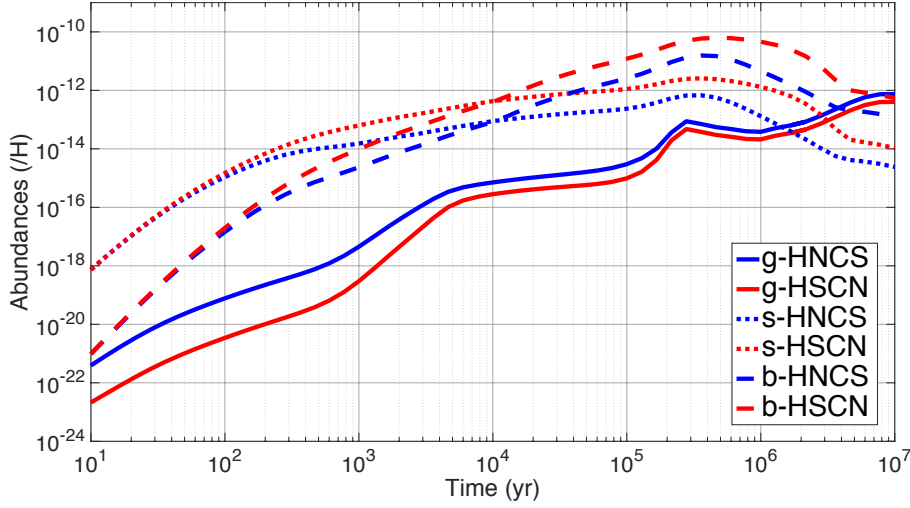


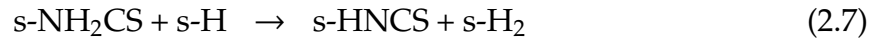
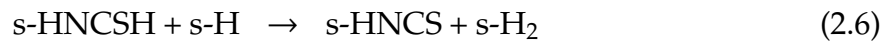
Figure 2.3: Abundances of HNCS (blue) and HSCN (red) relative to H as a function of time for dark cloud physical conditions in the gas phase (solid line), on the grains surface (dotted line) and in the grains bulk (dashed line).

abundance as compared to HNCS (Adande et al., 2010). It should be noted that the network for HNCS and HSCN is an improved version of the one proposed in Gronowski and Kolos (2014), which itself is a revised version of the network proposed in Adande et al. (2010).

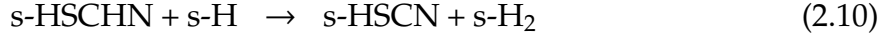
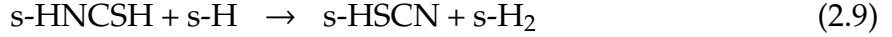
Figure 2.3 shows the time evolution of both species abundances in the three phases of the model. It appears that both species are essentially produced at the surface of the grains where their main formation reaction is:



HNCS and HSCN abundances on the grains surface are also regulated by hydrogenation loops similar to the one previously described for HS and H<sub>2</sub>S by reactions (2.2) and (2.3). The reactions involve are for HNCS:



and for HSCN:



At times  $> 2.8 \times 10^5$  years, as less and less atomic N is available, abundances of both species decrease on the surface. For HNCS, this decrease happens through the chemical desorption of the products of its hydrogenation, HNCSH and  $\text{NH}_2\text{CS}$ . For HSCN it happens through alternative hydrogenation pathways of HNCSH and HSCHN. Moreover, as the chemistry of both species is not efficient in the bulk, the increase in their abundances in this phase are primarily due to swapping with the surface.

In the gas phase, HNCS and HSCN abundances increase efficiently from chemical desorption from the grains following reaction (2.4), as well as from the following reaction mechanism:



Consequently, after  $2.8 \times 10^5$  years, as reaction (2.4) is less efficient because there is less N available, reaction (2.11) becomes the main formation pathway of HNCS and HSCN in the gas phase. Both species are also efficiently destroyed by atomic C via:



The depletion of atomic C on grains after  $10^5$  years then explains the increase in the gas phase abundance gradients for both species at this time.

#### 2.2.2.2.2 $\text{CH}_3\text{SH}$

Numerous previous detections of methyl mercaptan  $\text{CH}_3\text{SH}$  in hot cores such as Sgr B2 (Linke et al., 1979), G327.3-0.6 (Gibb et al., 2000) and Orion KL (Kolesníková et al., 2014) suggest that this species initially forms in the ices and then evaporates in hot cores. More recently, Majumdar et al. (2016) presented the detection of  $\text{CH}_3\text{SH}$  in IRAS 16293-2422 and proposed an associated chemical network to explain its observed abundance. This work is included in the enhanced sulphur network and has been completed, notably regarding grains chemistry. Figure 2.4 displays the time evolution of the  $\text{CH}_3\text{SH}$  abundance in the dark cloud model. As such, it appears from the results

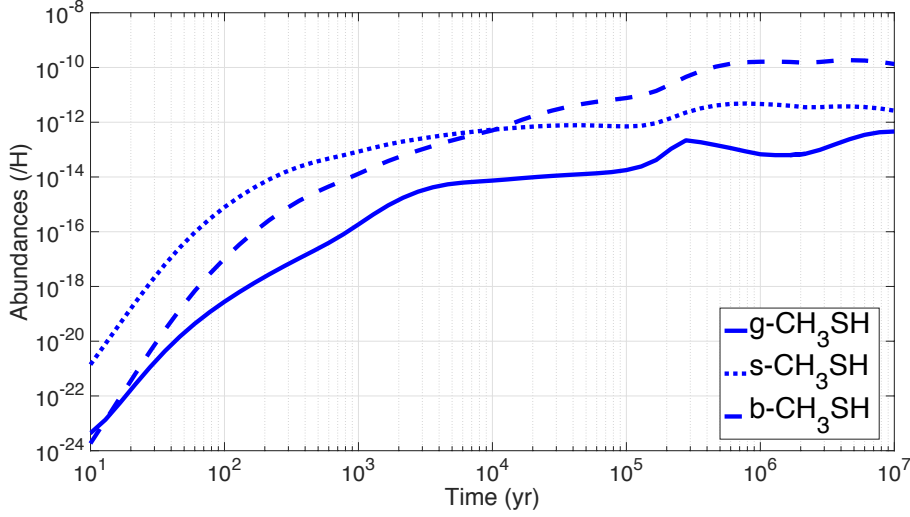


Figure 2.4: Abundances of  $\text{CH}_3\text{SH}$  relative to  $\text{H}$  as a function of time for dark cloud physical conditions in the gas phase (solid line), on the grains surface (dotted line) and in the grains bulk (dashed line).

that  $\text{CH}_3\text{SH}$  is mainly formed on the grains surface and is released into the gas phase by chemical desorption. The main formation processes on the grains are:



Moreover, similarly to  $\text{HNCS}$ , it seems that the chemistry of  $\text{CH}_3\text{SH}$  in the grains bulk is relatively inert and that its accumulation in this phase is mainly due to exchange with the grains surface.

As for  $\text{HNCS}$ ,  $\text{CH}_3\text{SH}$  is consumed by atomic  $\text{C}$  at times  $< 2.8 \times 10^5$  years following:



However after this time, in contrast to  $\text{HNCS}$ , gas phase  $\text{CH}_3\text{SH}$  is still produced from grains surface chemistry and chemical desorption, which can be explained by the fact that the  $\text{CS}$  abundance in the gas phase remains high, and gradually depletes to form  $\text{CH}_3\text{SH}$  through successive hydrogenations. Moreover, as the hydrogen atom abundance remains relatively constant on the grains surface because of cosmic-ray interactions with  $\text{H}_2$ , this formation pathway of  $\text{CH}_3\text{SH}$  keeps on being efficient throughout the model.

### 2.2.2.3 Comparison with the previous network

I now highlight the differences between the nominal model of dark cloud ran with the previous version of the network (hereafter model A), and the model ran with the enhanced sulphur network (hereafter model B). It should be noted that model A already includes the key parameter for sulphur chemistry studied in section 2.2.2.2, namely the hydrogenation loop between HS and H<sub>2</sub>S enabled by the reaction-diffusion competition mechanism. As the calculations show that numerous S-bearing species are impacted by the changes I made to the network, I present here only a selection of these species: C<sub>3</sub>S, H<sub>2</sub>CS, HCS, H<sub>2</sub>S, HS and SO. I selected these molecules because they present a difference between models A and B of more than one order of magnitude in the time period between 10<sup>5</sup> and 10<sup>6</sup> years and because their abundances rise above 10<sup>-12</sup> during this period. Indeed, the estimated ages of well-studied dark clouds such as TMC-1 or L134N are thought to correspond to this time period (see discussion in [Agúndez and Wakelam, 2013](#)). Moreover, an abundance of 10<sup>-12</sup> is considered as the common detection limit for species in the gas phase.

#### 2.2.2.3.1 C<sub>3</sub>S

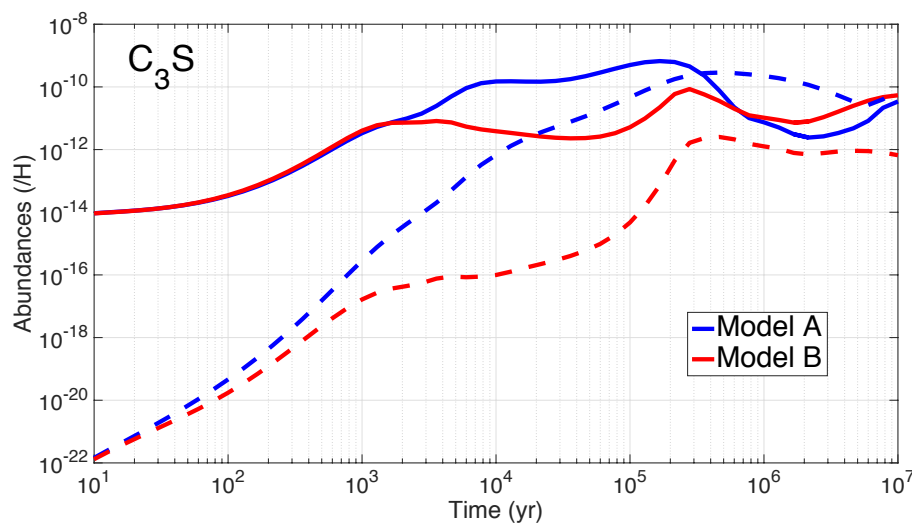


Figure 2.5: Comparison between models A (blue) and B (red) abundances of C<sub>3</sub>S relative to H as a function of time for dark cloud physical conditions in the gas phase (solid line) and in the grains bulk (long-dashed line).

Figure 2.5 displays the comparison of the abundances of C<sub>3</sub>S calculated for models A and B, both in the gas phase and in the grains bulk. It can be seen that the new network induces differences for this species that can reach up to two orders of magnitude in the gas phase and four orders of magnitude in the grains bulk at times around 10<sup>5</sup> years. In both models, C<sub>3</sub>S is mainly formed in the gas phase by the reaction:



$\text{HC}_3\text{S}^+$  being efficiently produced through reactions of atomic sulphur with  $\text{c,l-C}_3\text{H}_2^+$  and  $\text{c,l-C}_3\text{H}_3^+$ . The decrease of  $\text{C}_3\text{S}$  abundance in the grains bulk in model B (as compared to model A) is a direct result of its decrease in the gas phase, which is due to the following added reaction:



This reaction becomes efficient in model B at times  $> 10^3$  years when the abundance of atomic C in the gas phase reaches  $10^{-4}$ . Finally, after  $10^4$  years, while in model A the abundance of  $\text{C}_3\text{S}$  continues to increase because of reaction (2.17), in model B the small peak at  $2.8 \times 10^5$  years is due to the reaction:



Reaction (2.19) becomes more efficient than reaction (2.18) at this time because depletion is more efficient for atomic carbon ( $\sim 10^5$  years) than for atomic oxygen ( $\sim 8 \times 10^5$  years). It should be noted that branching ratios for the DR of  $\text{HC}_3\text{S}^+$  are unknown and the network may overestimate  $\text{C}_3\text{S}$  production and consequently its abundance.

### 2.2.2.3.2 $\text{H}_2\text{CS}$

The abundance of  $\text{H}_2\text{CS}$  in the gas phase presents a change similar to  $\text{C}_3\text{S}$  in its evolution between model A and B (see Figure 2.6). Its main reaction of formation in both models is the electronic recombination of  $\text{H}_3\text{CS}^+$ :



$\text{H}_3\text{CS}^+$  being efficiently produced through  $\text{S}^+ + \text{CH}_4$  reaction.  $\text{H}_2\text{CS}$  is less efficiently formed in model B after  $10^3$  years because, like  $\text{C}_3\text{S}$ , it is consumed by atomic C via the following reaction:



This reaction induces differences in the  $\text{H}_2\text{CS}$  abundance of more than two orders of magnitude between  $10^4$  and  $10^5$  years. As atomic carbon is depleted onto the grains,



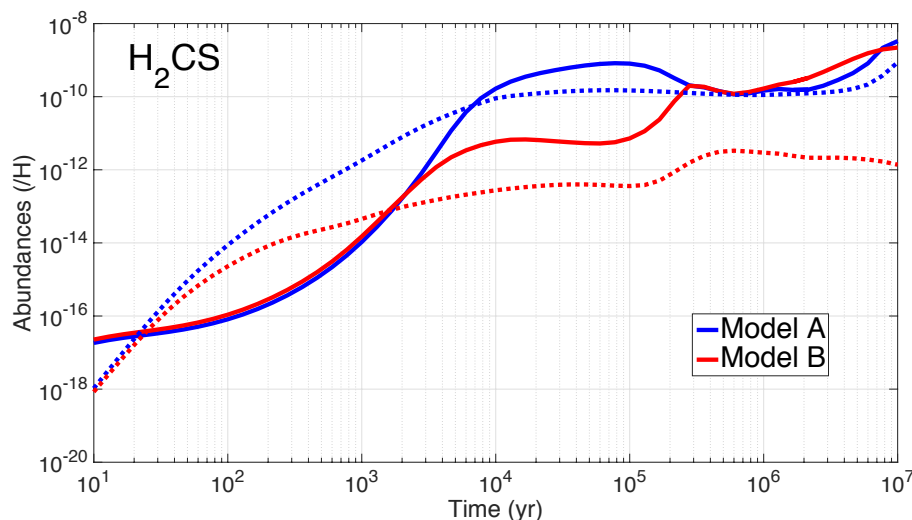


Figure 2.6: Comparison between models A (blue) and B (red) abundances of  $\text{H}_2\text{CS}$  relative to  $\text{H}$  as a function of time for dark cloud physical conditions in the gas phase (solid line) and on the grains surface (dotted line).

these reactions become less efficient after  $10^5$  years and the abundance of  $\text{H}_2\text{CS}$  increases again through reaction (2.20).

In contrast to  $\text{C}_3\text{S}$ ,  $\text{H}_2\text{CS}$  is also efficiently formed on the grains surface in both models by hydrogenation of  $\text{HCS}$ . However, in model B, two hydrogenation processes of  $\text{H}_2\text{CS}$  have been added, which cause its abundance on the grains surface to drop compared to model A by more than two orders of magnitude. Those processes are:



which ultimately lead to the formation of  $\text{CH}_3\text{SH}$  (see section 2.2.2.2). Moreover, as previously noted, the branching ratios for the DR of  $\text{H}_3\text{CS}^+$  are unknown and may in reality preferentially lead mainly to the breaking of the C-S bond, which would strongly decrease  $\text{H}_2\text{CS}$  abundance.

### 2.2.2.3.3 HCS

Figure 2.7 shows the time evolution of the  $\text{HCS}$  abundance in the gas phase in both models A and B. The figure displays that the overall effect of the enhanced network on this species is to increase its abundance in the gas phase above the detection level of  $10^{-12}$ . This potential observability of  $\text{HCS}$  in dark clouds will be discussed in section 2.4.3. In model A,  $\text{HCS}$  is mainly formed by the two following reactions:

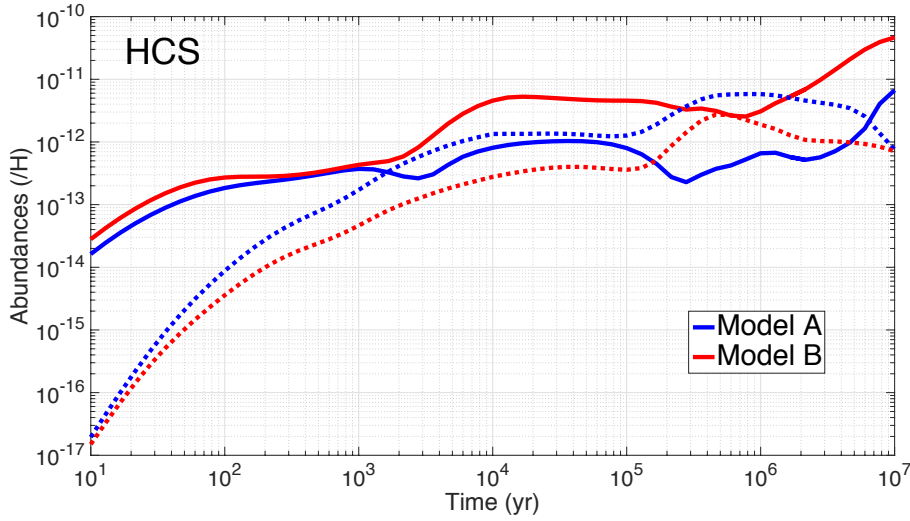


Figure 2.7: Comparison between models A (blue) and B (red) abundances of HCS relative to H as a function of time for dark cloud physical conditions in the gas phase (solid line) and on the grains surface (dotted line).



However, in model B two new reactions show a higher HCS production efficiency. Those reactions are:



It should be noted that HCS is also formed on the grains surface by the hydrogenation of CS, and that its abundance in this phase is decreased in model B because of numerous added reactions of HCS with atomic O and N, the latter forming the newly implemented species HNCS on the grains.

#### 2.2.2.3.4 HS, H<sub>2</sub>S and SO

I choose to describe the changes brought by the new model to HS, H<sub>2</sub>S and SO chemistries together because they are linked, notably on the grains surface.

On the one hand, in the gas phase, among those three species, the only one that presents a significant difference in model B (as compared to model A) is H<sub>2</sub>S (see figure

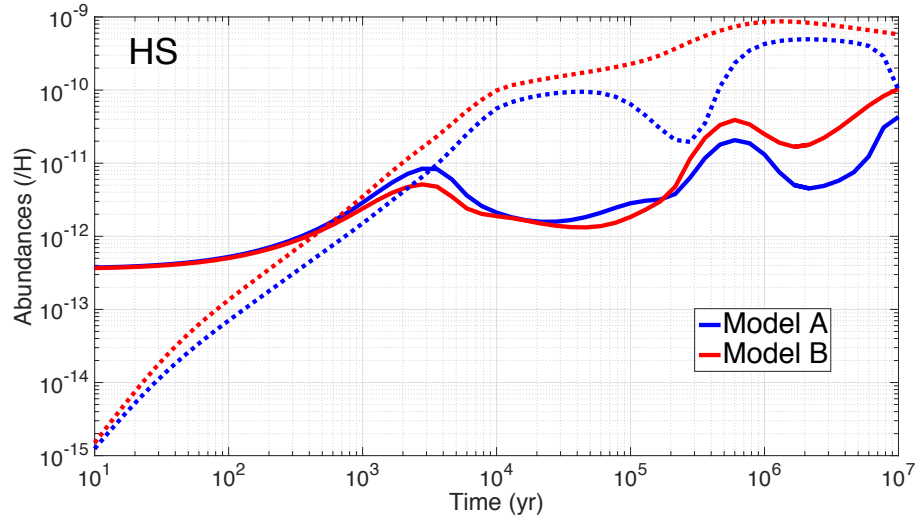


Figure 2.8: Comparison between models A (blue) and B (red) abundances of HS relative to H as a function of time for dark cloud physical conditions in the gas phase (solid line) and on the grains surface (dotted line).

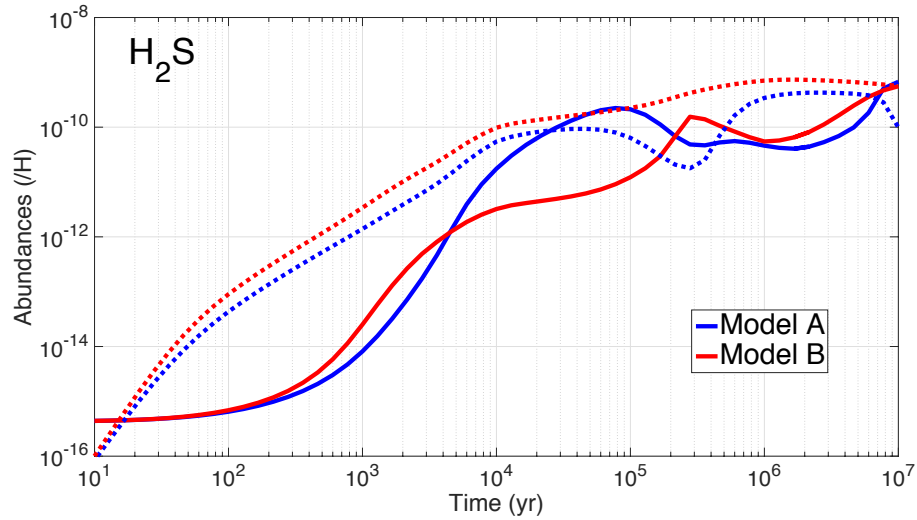


Figure 2.9: Comparison between models A (blue) and B (red) abundances of  $\text{H}_2\text{S}$  relative to H as a function of time for dark cloud physical conditions in the gas phase (solid line) and on the grains surface (dotted line).

2.9). This difference (that reaches more than one order of magnitude) appears between  $5 \times 10^3$  and  $3 \times 10^5$  years and is mainly due to the fact that reaction (2.26) slows down the increase of  $\text{H}_2\text{S}$  during this period of time. Besides this change, gas phase  $\text{H}_2\text{S}$  is efficiently formed in both models on the grains surface by the hydrogenation of HS (reaction (2.2)) enabled by the reaction-diffusion competition, followed by desorption.

On the other hand, the modifications of the network bring about a new reaction

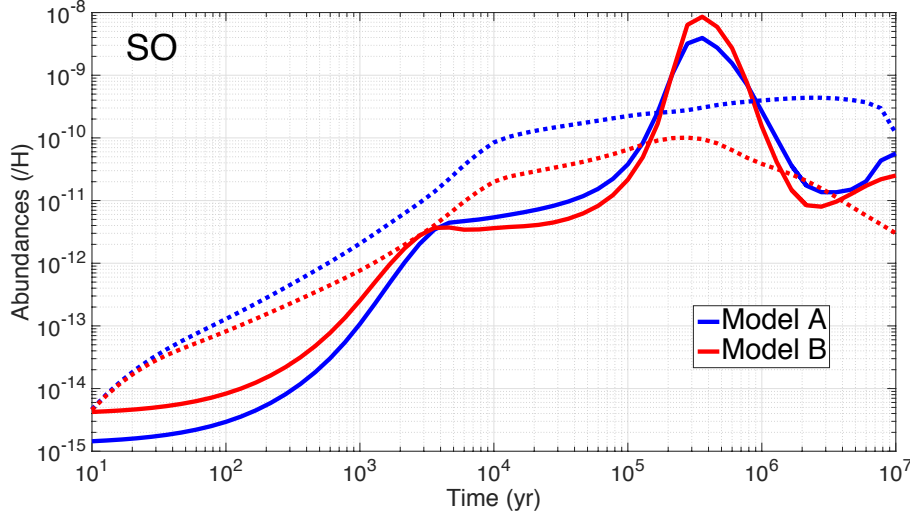
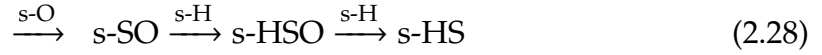


Figure 2.10: Comparison between models A (blue) and B (red) abundances of SO relative to H as a function of time for dark cloud physical conditions in the gas phase (solid line) and on the grains surface (dotted line).

mechanism on the grains surface which causes several changes to the abundances of HS, H<sub>2</sub>S and SO:



From model A to model B, the main effects of this reaction mechanism are:

- to globally increase the grains surface abundance of HS because of the added path (2.27),
- to globally increase the grains surface abundance of H<sub>2</sub>S because of the loop described in section 2.2.2.2, and therefore its abundance in the gas phase (except during the time period described above),
- to globally decrease the grains surface abundance of SO which is, in the enhanced network, successively hydrogenated to form HSO then HS (see reaction mechanism (2.28)).

## 2.3 COMPARISON WITH OBSERVATIONS IN THE DARK CLOUD TMC-1

I compare in this section the modeling results with observations of the well-studied dark cloud TMC-1 (CP) for which numerous observational constraints are available.

Indeed, more than 60 gas phase species have been detected in this source, and upper limits on the abundance of 7 more are available (see a review of these species in [Agúndez and Wakelam, 2013](#); [Adande et al., 2010](#)). For that purpose, I use the method of the so-called distance of disagreement described in [Wakelam et al. \(2006\)](#), and which is computed as follows:

$$D(t) = \frac{1}{N_{\text{obs}}} \sum_i | \log([X]_{\text{obs},i}) - \log([X]_i(t)) | \quad (2.29)$$

where  $n(X)_{\text{obs},i}$  and  $n(X)_i(t)$  are respectively the observed abundance (relative to H) of species  $i$  and its modeled one at time  $t$ .  $N_{\text{obs}}$  is the total number of observed species considered. The minimum of function  $D$  (hereafter noted  $D_{\text{min}}$ ) is then the minimum average difference (in magnitude) between modeled and observed abundances. I call the time for which this minimum is obtained the best fit time (hereafter noted  $t_{\text{BF}}$ ).

I detail the observed abundances I use for S-bearing species in table 2.5. For the other species, I use the abundances in [Gratier et al. \(2016\)](#) as well as Table 4 of [Agúndez and Wakelam \(2013\)](#) and the references therein.

Table 2.5: Observed abundances of sulphur bearing species in TMC-1 (CP) .  $*a(b)$  stands for  $a \times 10^b$

Species	$[X]_{\text{obs}}^*$	References
OCS	1.1(-9)	1
NS	4.0(-10)	2
CS	6.5(-9)	3
HCS <sup>+</sup>	2.5(-10)	3
H <sub>2</sub> CS	2.6(-9)	3
C <sub>2</sub> S	5.0(-9)	3
C <sub>3</sub> S	7.0(-10)	3
SO	1.0(-8)	4
SO <sub>2</sub>	1.5(-10)	5
HNCS	4.15(-12)	6
HSCN	6.3(-12)	6

References : (1) [Matthews et al. \(1987\)](#), (2) [McGonagle et al. \(1994\)](#), (3) [Gratier et al. \(2016\)](#), (4) [Lique et al. \(2006\)](#), (5) [Cernicharo et al. \(2011\)](#), (6) [Adande et al. \(2010\)](#)

### 2.3.1 Comparison with models A and B

I first compare the results of both models A and B with the observations of TMC-1 (CP) in order to assess the efficiency of the new network to reproduce observations in dark

clouds.

For the calculation of the corresponding distance of disagreement for both models, I take into account 58 of the 63 detected species because 5 of them are not implemented in one or either of the two networks (nominal and enhanced), namely HNCS, HSCN, HC<sub>3</sub>HO, CH<sub>2</sub>CCHCN and HC<sub>11</sub>N. Using equation (2.29), I find better agreement with observations for model B with  $D_{\min} = 0.766$  (against  $D_{\min} = 0.908$  for model A), giving a best fit time of  $2.8 \times 10^5$  years, same as model A. At this time, and assuming that the observed abundances are reproduced by the model when the difference between the two is smaller than one order of magnitude, the fractions of reproduced molecules are 64% and 67% respectively for model A and model B. This difference between the two models can be explained by the fact that model A reproduces 3 species that model B does not, namely CH<sub>3</sub>CCH, CH<sub>3</sub>C<sub>4</sub>H and C<sub>6</sub>H. However, model B reproduces 5 other species than model A fails to reproduce, namely C<sub>2</sub>O, CH<sub>3</sub>CHO, l-C<sub>3</sub>H<sub>2</sub>, CH<sub>2</sub>CHCN and HNC<sub>3</sub>. A summary of these results is shown in Table 2.6.

Table 2.6: Results of the comparison of models A and B with observations in the dark cloud TMC-1 (CP)

Model	$D_{\min}$	$t_{\text{BF}}$ (yr)	Fraction of reproduced molecules
A	0.908	$2.8 \times 10^5$	64%
B	0.766	$2.8 \times 10^5$	67%

For both models, 5 of the 9 S-bearing species taken into account in the comparison are reproduced : OCS, CS, C<sub>3</sub>S, SO and SO<sub>2</sub>, and model B gives a slightly better agreement than model A for these species. Moreover, model B reproduces only two more species than model A among the 58 species considered, and these species are both carbon chains. The similarity of the results comes from the fact that model A also includes the reaction-diffusion competition rendering the hydrogenation loop described in section 2.2.2.2 efficient, which is a key parameter for sulphur chemistry. However, the goal of this study is to evaluate the efficiency of the enhanced network (model B) to reproduce S-bearing species abundances, which should be done by considering all the species it takes into account. Therefore I hereafter choose to exclude model A from the study and focus only on model B.

### 2.3.2 Variation of the elemental sulphur abundance

In order to assess the issue of sulphur depletion in chemical models of dark clouds with the enhanced network, I run the model for 4 different values of the elemental sulphur abundance and compare the results with observations to determine which one leads to a better agreement with the observed species abundances. These values vary from

the so-called depleted one ( $8 \times 10^{-8}$ ), which is commonly used by chemical models to reproduce observations and which I used previously in this study, to the cosmic one ( $1.5 \times 10^{-5}$ ). The different values of the sulphur elemental abundances used and the labels of their associated models are summarized in Table 2.7. Apart from sulphur, the other species elemental abundances I use are those reported in table 2.3.

Table 2.7: Set of elemental sulphur abundances.  $*a(b)$  stands for  $a \times 10^b$

Model	$[S]_{\text{ini}}^*$
1	8(-8)
2	5(-7)
3	5(-6)
4	1.5(-5)

In the following, I first compare for each model the calculated abundances of gas phase species with those determined from observations of TMC-1 (CP). The only sulphur-bearing species observed on the grains being OCS and  $\text{SO}_2$  in the molecular cloud surrounding the deeply embedded protostar W33A, I then compare the modeled abundances of these species on the grains with the observed ones.

### 2.3.2.1 Comparison with all observed gas phase species

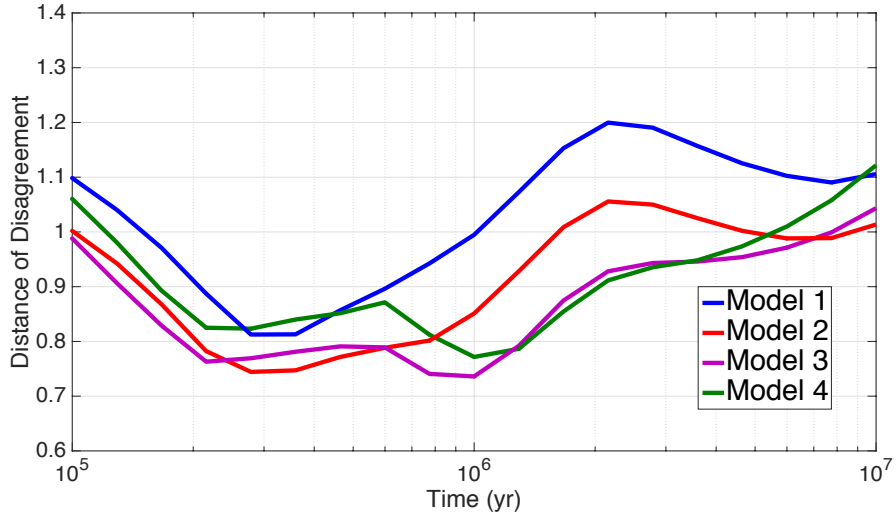


Figure 2.11: Distances of disagreement for models 1, 2, 3 and 4 considering 62 detected species in TMC-1 (CP).

To assess the overall agreement of the enhanced network with observations, I compute the distance of disagreement for models 1, 2, 3 and 4. For these calculations I take



into account three more species than previously, because HNCS, HSCN and HC<sub>3</sub>HO are taken into account in the new network, for a total of 61 species considered. Figure 2.11 displays these distances of disagreement between 10<sup>5</sup> and 10<sup>7</sup> years, the time period when the minimum values are reached.

On the one hand, it first directly appears that model 1 is rejected since its minimum of distance of disagreement does not go below 0.8 contrary to the other models. This result hints that large depletion of the elemental sulphur is no longer needed to reproduce the observations in dark clouds. Second, model 3 is the best model in that it presents the distance of disagreement with the lowest minimum of  $D_3(t_{\text{BF}}) = 0.736$  with  $t_{\text{BF}} = 10^6$  years which is still a reasonable estimated age for TMC-1 (CP). Moreover at that time, 44 of the 61 species considered (72%) are reproduced by the model within a factor of 10. This result means that the elemental sulphur abundance which the new model theoretically needs to best reproduce the observations is around  $[S]_{\text{ini}} = 5 \times 10^{-6}$ . Model 2 is the second best model in terms of minimum of distance of disagreement, with  $D_2(t_{\text{BF}}) = 0.744$  with  $t_{\text{BF}} = 2.8 \times 10^5$  years, where it reproduces 42 of the 61 species. However, in terms of number of species reproduced, model 4 is better than model 2 since it reproduces 44 of the 61 species at its best fit time, but its minimum of distance of disagreement is slightly higher than model 2 and 3 (0.772).

On the other hand, Figure 2.11 shows that the maximum difference between the distances of disagreement of the four models is lower than 0.3. Hence, for a given time, the average of the differences of abundances between two models (for a same species) is lower than a factor of 2. The distance of disagreement is thus not very sensitive to the elemental sulphur abundance. This result can be explained by the fact that among the 61 observed species I consider for the calculations, only 11 of them are S-bearing species.

### 2.3.2.2 Comparison with observed sulphur bearing gas phase species

Considering the low sensitivity of the distance of disagreement (with 61 observed species) to the elemental sulphur abundance and because the improvement of the network concerns mainly sulphur chemistry, I also assess the efficiency of the model by checking its agreement with only the observations of the S-bearing species detected in TMC-1 (CP). Figure 2.12 is the same as Figure 2.11 but considering only the 11 detected S-bearing gas phase species in TMC-1 (CP). These species are OCS, NS, HCS<sup>+</sup>, CS, H<sub>2</sub>CS, CCS, C<sub>3</sub>S, SO, SO<sub>2</sub> (see Agúndez and Wakelam, 2013, for a review), HNCS, and HSCN (Adande et al., 2010). First and as expected, the distances of disagreement are much more sensitive to the elemental sulphur abundance than in the previous case, with a maximum of differences between them of 1.6.

Second, the figure shows that the distance of disagreement for models 1 and 2 never goes down below 0.7 whereas the other two present their minima under 0.4.



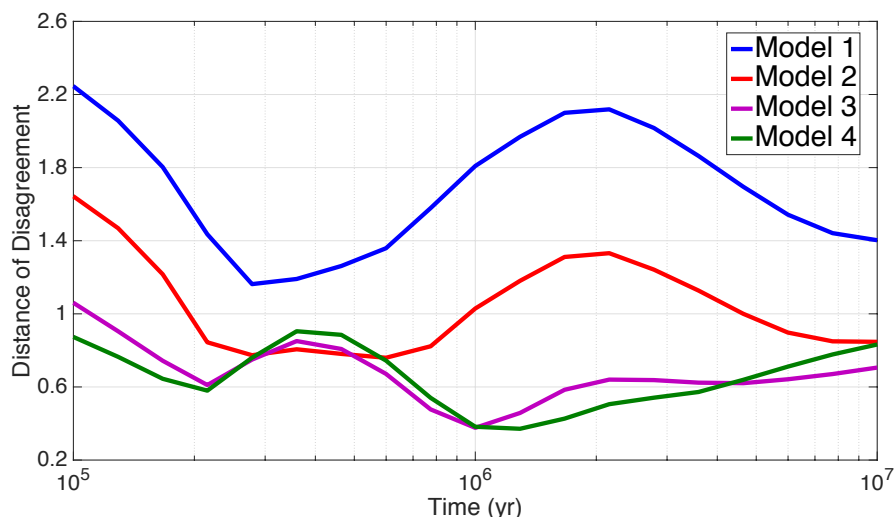


Figure 2.12: Distances of disagreement for models 1, 2, 3 and 4 considering only the 11 detected S-bearing species in TMC-1 (CP).

Hence, this result confirms the one obtained in section 2.3.2.1, namely that model 1 is the worst model. Especially, this means that the depleted elemental sulphur abundances of  $8 \times 10^{-8}$  and  $5 \times 10^{-7}$  do not allow the model to reproduce the observations of S-bearing species with the enhanced network.

Finally, at the times of their respective minima, models 3 and 4 reproduce all the S-bearing molecules considered. Model 4 is the one that presents the distance of disagreement with the lowest minimum of  $D_4(t_{\text{BF}}) = 0.371$  with  $t_{\text{BF}} = 1.3 \times 10^6$  years. Furthermore, model 3 allows to obtain a minimum of the distance of disagreement that is nearly equal to the one found for Model 4, namely  $D_3(t_{\text{BF}}) = 0.376$  with  $t_{\text{BF}} = 10^6$  years. In both cases, the best fit time is in the acceptable range for the age of TMC-1 (CP). These results suggest that the model is able to reproduce the observations of S-bearing species in TMC-1 (CP) using the cosmic elemental abundance of sulphur  $[S]_{\text{ini}} = 1.5 \times 10^{-5}$  or an abundance only 3 times lower.

### 2.3.2.3 The new species HNCS and HSCN

As the enhanced network was mainly built around HNCS and its isomers, it is important to check that the modeling results correctly fit the observations of these species. Adande et al. (2010) identified the  $7_{0,7} \rightarrow 6_{0,6}$  and  $8_{0,8} \rightarrow 7_{0,7}$  transitions of HNCS and HSCN towards TMC-1 (CP) and were able to derive a corresponding ratio  $\frac{[\text{HNCS}]}{[\text{HSCN}]} = 1.4 \pm 0.7$  and abundances for HNCS and HSCN of respectively  $4.15 \times 10^{-12}$  and  $3 \times 10^{-12}$ . Figure 2.13 shows the simulated abundances of HNCS and HSCN in the case of the cosmic elemental abundance for sulphur (model 4) as well as their observed abundances in TMC-1 (CP) (horizontal dashed lines). At the best fit time of model 4 ( $t_{\text{BF}} = 1.3 \times 10^6$  years), I obtain a ratio of 1.68 which matches the observed value. Moreover, the figure

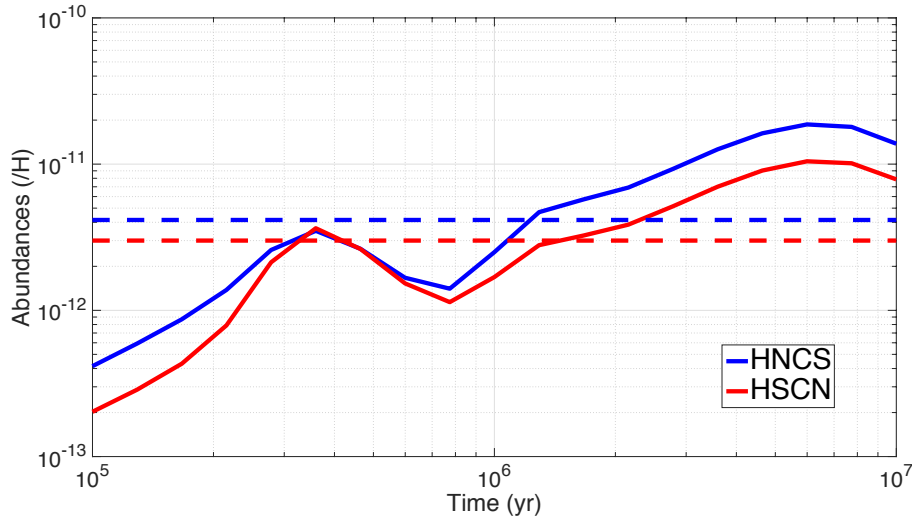


Figure 2.13: Comparison of the simulated gas phase abundances of HNCS and HSCN with the observed ones in TMC-1 (CP) (horizontal dashed lines).

shows that at this time, the differences between the observed and calculated abundances of HNCS and HSCN are less than a factor 1.2 and 1.1, respectively. This result confirms the efficiency of the network to model the chemistry of HNCS, especially using the cosmic elemental abundance of sulphur. It should be noted that model 3 also allows to reproduce well the observed abundance of HNCS and HSCN at  $t_{\text{BF}} = 10^6$  years, with a corresponding ratio also equal to 1.68.

#### 2.3.2.4 Sulphur bearing species on grains towards W33A

Only two solid S-bearing species have been detected in icy grains bulk : OCS (Palumbo et al., 1997) and  $\text{SO}_2$  (Boogert et al., 1997). Both species have been detected towards the deeply embedded protostar W33A and I can therefore use the results of the models in the dark cloud configuration to compare with these observations. In order to do so, I have to compare for a given species its observed abundance ( $7 \times 10^{-8}$  and  $6.2 \times 10^{-7}$  for OCS and  $\text{SO}_2$ , respectively) with the sum of its simulated abundances on the grains surface and in the grains bulk. For both species, Figure 2.14 displays the comparison between their total computed abundances in icy grains bulk for the four models and their observed ones between  $10^5$  and  $10^7$  years. The age of the giant molecular cloud W33 is indeed supposed to lie in that time frame (Messineo et al., 2015).

Figure 2.14 (a) shows that both models 3 and 4 reproduce the observed abundance of OCS in icy grains bulk, at  $7.74 \times 10^5$  and  $2.15 \times 10^6$  years respectively. Moreover, considering the fact that most of the young stellar objects detected in W33 have an estimated age of a few million years (see for example Messineo et al., 2015), the most favored model is Model 4. Regarding  $\text{SO}_2$ , Figure 2.1 (b) shows that the model for which its modeled abundance comes the closest to its observed one is model 4. Both

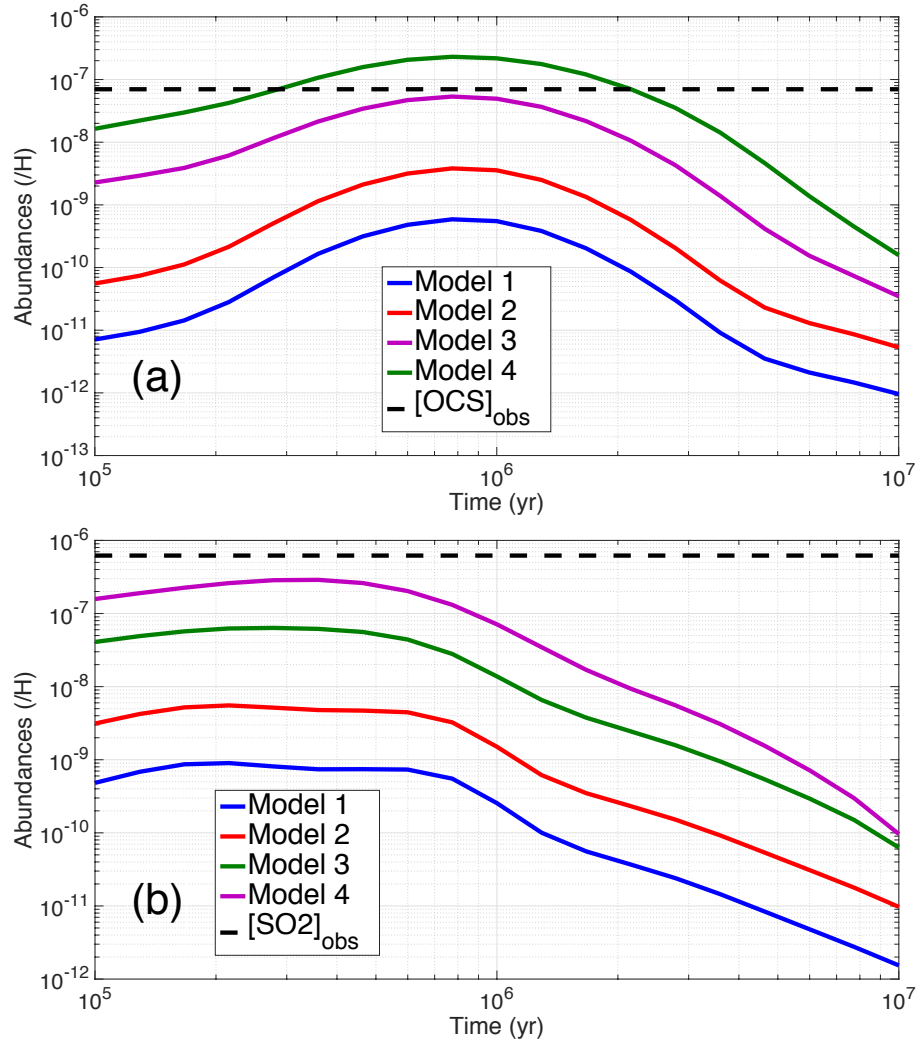


Figure 2.14: Comparison of the computed abundances of solid OCS (a) and  $SO_2$  (b) for models 1, 2, 3 and 4 (solid lines) with the observed one towards W33A (black dashed lines).

comparisons suggest once again that the enhanced network needs an elemental sulphur abundance close to the cosmic one in order to best reproduce the observations. Note that I assume here that the detections of OCS and  $SO_2$  ices are real although the two species are not in the list of "firmly detected" species of [Boogert et al. \(2015\)](#).

### 2.3.3 Sulphur reservoirs in dark clouds

In section 2.2.2.1, I studied the chemistry of the main S-bearing species using the elemental abundances listed in table 2.3, more particularly the depleted abundance of sulphur of  $[S]_{ini} = 8 \times 10^{-8}$ . Now that I determined that in order to reproduce S-bearing species observations in dark clouds the model needs an elemental abundance of sulphur close to the cosmic one, I need to assess the impact of the use of such an

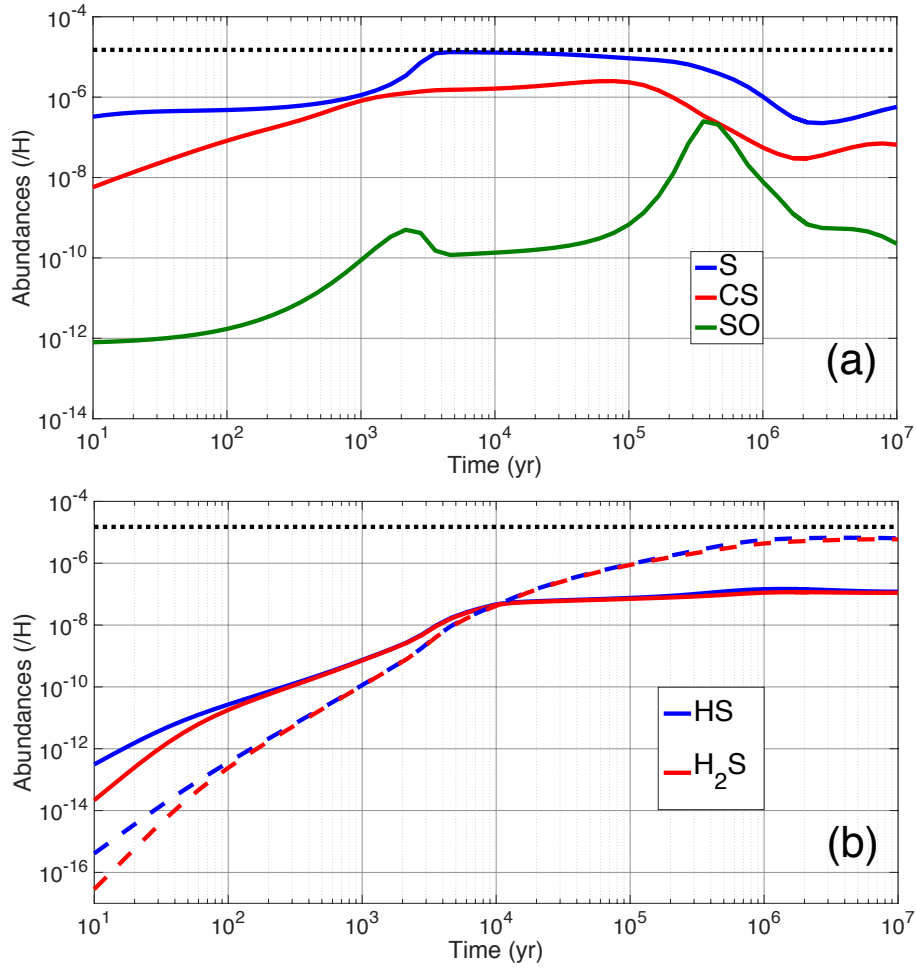


Figure 2.15: Abundances of the sulphur reservoirs relative to H as a function of time for dark cloud physical conditions : (a) in the gas phase, (b) on the grains surface (solid line) and bulk (dashed line). The dotted line represents the elemental abundance of sulphur (here,  $[S]_{\text{ini}} = 1.5 \times 10^{-5}$ ).

abundance on the reservoirs and their respective chemistries.

Figure 2.15 (a) and (b) are respectively the same as Figure 2.1 and 2.2, but for the model ran with the cosmic elemental abundance of sulphur of  $[S]_{\text{ini}} = 1.5 \times 10^{-5}$ . What appears is that the reservoirs are unchanged. Moreover, the differences are mainly quantitative and their respective chemistries stay the same as described in section 2.2.2.1, with the exception of the two following points:

- Adsorption of atomic S on the grains is much more efficient when using the cosmic elemental abundance of sulphur, which causes its abundance to drop near  $3 \times 10^3$  years, much sooner than when using the depleted one  $[S]_{\text{ini}} = 8 \times 10^{-8}$ . However, atomic S still stays the main reservoir of sulphur between  $2.8 \times 10^3$  and  $4.6 \times 10^5$  years, containing at its maximum 88% of the initial sulphur.

- With  $[S]_{\text{ini}} = 1.5 \times 10^{-5}$ , SO is no longer a main sulphur-bearing species as defined in section 2.2.2.1. Indeed, at  $3.6 \times 10^5$  years, time when its abundance peaks, it now only contains less than 2% of the initial sulphur.

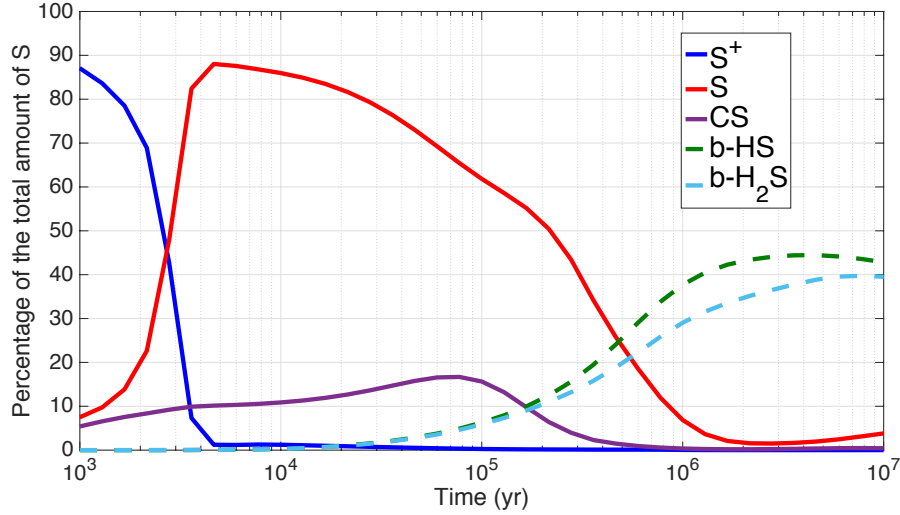


Figure 2.16: Percentage of the total amount of sulphur contained in the reservoirs as a function of time for dark cloud physical condition using a cosmic elemental abundance of sulphur  $[S]_{\text{ini}} = 1.5 \times 10^{-5}$ .

Figure 2.16 displays the percentage of the total amount of sulphur contained in the reservoirs between  $10^3$  and  $10^7$  years using a cosmic elemental abundance of sulphur. According to the figure and depending on the age of the cloud, the reservoirs are:

- $S^+$  in the gas phase from the beginning of the model and until  $2.8 \times 10^3$  years, which is obvious since it is the initial form of sulphur,
- Neutral atomic sulphur in the gas phase between  $2.8 \times 10^3$  and  $4.6 \times 10^5$  years, containing between 25 and 88% of the total amount of sulphur, depending on the age of the cloud. During this period of time, CS also contains a significant amount of sulphur, namely between 9 and 16%. It should be noted that these repartition of the sulphur is a bit different from the one studied in section 2.2.2.1, which is due to the change of the sulphur elemental abundance,
- HS and  $H_2S$  in the grains bulk for older clouds, containing a total of more than 51% of the total amount of sulphur, that reaches more than 80% at times  $\geq 2.7 \times 10^6$  years, as described in table 2.4. This shared reservoir shows a slight preference for HS between 3 and 10% of the total amount of sulphur, depending on the age of the cloud.

The aforementioned results are also true when using an elemental abundance of sulphur of  $[S]_{\text{ini}} = 5 \times 10^{-6}$  (3 times depleted), which also allows to reproduce obser-

variations of S-bearing species in dark clouds. Indeed the percentages presented above only differ from less than 2% of the total amount of sulphur.

## 2.4 DISCUSSIONS AND SUMMARY

### 2.4.1 About the elemental abundance of sulphur

The comparison of the enhanced model with the gas phase observations in TMC-1 (CP) (see section 2.3) favors the use of an elemental abundance of sulphur between  $[S]_{\text{ini}} = 5 \times 10^{-6}$  and  $[S]_{\text{ini}} = 1.5 \times 10^{-5}$ . As most of the estimations of the cosmic abundance of sulphur lie between these two values (Federman et al., 1993; Sofia et al., 1994; Tieftrunk et al., 1994; Ruffle et al., 1999; Shalabiea, 2001), the model does not require additional depletion of sulphur. Moreover, the results on the comparison with the observations of OCS and SO<sub>2</sub> in icy grains bulk towards W33A confirm that a cosmic elemental abundance of sulphur is required from the model in order to reproduce the observed abundances.

### 2.4.2 About the reservoirs of sulphur in dark clouds

Two main hypotheses exist to explain the observed depletion of sulphur in dark clouds: either the sulphur is in a yet undiscovered form in the gas phase, which could be atomic sulphur, or it could be locked in icy grains bulk. The latter hypothesis is supported by the observation of H<sub>2</sub>S as the most important S-bearing species in cometary ices (Bockelée-Morvan et al., 2000), which are thought to present chemical similarities with the ices processed during hot cores formation (Irvine et al., 2000). Moreover, as hydrogenation is the most effective process in grains chemistry, models predict that when sulphur atoms stick on the grains, they will consequently form H<sub>2</sub>S (Garrod et al., 2007). However, H<sub>2</sub>S has never been detected in dark cloud ices. Additionally, upper limits to its column density towards three high-mass protostars and three late type stars lying behind TMC-1 (CP) have been derived from observations by Smith (1991). These limits, despite large uncertainties, are believed to be too small to account for the missing sulphur in dark clouds and alternative hypotheses have recently been proposed (Jiménez-Escobar and Muñoz Caro, 2011; Druard and Wakelam, 2012; Martín-Doménech et al., 2016).

As seen in section 2.3.3, the results of the models with the enhanced sulphur network seem to support both of the main hypotheses about the reservoirs of sulphur, depending on the age of the observed dark cloud. Indeed, according to the results, if the age of the cloud is less than  $4.6 \times 10^5$  years then atomic sulphur in the gas phase is the main reservoir of sulphur. However if the cloud is older, then the results show that because of a hydrogenation cycle between HS and H<sub>2</sub>S, enabled by the reaction-



diffusion competition and the accumulation of these species in the bulk, the reservoirs of sulphur are nearly equally HS and H<sub>2</sub>S in the grains bulk. The upper limit on the abundance of H<sub>2</sub>S in ices provided by the observations is between  $3 \times 10^{-7}$  and  $3 \times 10^{-6}$  (assuming an abundance of H<sub>2</sub>O in ices of  $10^{-4}$  and based on [Smith, 1991](#)). It should be noted that these upper limits are derived using the infrared transition strengths obtained by [Ferraro et al. \(1980\)](#), which has been obtained in pure H<sub>2</sub>S ice. The intensity strengths can be notably different in interstellar ice analogues. As the total abundances of H<sub>2</sub>S on the grains in model 3 and 4 at the best fit time ( $10^6$  years) are respectively  $1.5 \times 10^{-6}$  and  $4.4 \times 10^{-6}$ , it appears that the enhanced network results are in agreement with the upper limits of [Smith \(1991\)](#) and therefore in favor of a joint HS and H<sub>2</sub>S sulphur reservoir in icy grains bulk in dark clouds. This result is in agreement with the results depicted in appendix E of [Furuya et al. \(2015\)](#). Indeed, they also find that HS and H<sub>2</sub>S are likely to be the main reservoirs of sulphur, notably due to the same hydrogenation loop described by equations (2.2) and (2.3). Observational constraints on the icy grains bulk abundance of HS would be useful to validate this hypothesis. However, The  $v = 0 \rightarrow v = 1$  transition of HS lies around  $2599 \text{ cm}^{-1}$  in the gas phase ([Bernath et al., 1983](#)) and has never been observed in ice. The calculated IR strength (at DFT or MP2 level using Gaussian) is 3 orders of magnitude less efficient than water and 4 order of magnitude less efficient than OCS. Subsequently, even if solid HS is the reservoir of sulphur in dark clouds, the lack of sensibility of IR detection may prevent its observation.

### 2.4.3 About the observability of HCS

In order to assess the observability of HCS in the gas phase of TMC-1 (CP) (see section 2.2.2.3), we proceed using a local thermodynamic equilibrium calculation of the HCS emission spectrum in the 3 and 2 mm atmospheric windows with  $T_{ex} = 10 \text{ K}$ , a column density of HCS of  $1 \times 10^{12} \text{ cm}^{-2}$  (corresponding to a gas phase abundance of HCS of approximately  $10^{-10}$  as obtained with model 4 in the time frame between  $10^5$  and  $10^7$  years), assuming a wide source (no beam dilution) and a linewidth of  $1 \text{ km/s}$ . We estimate that the brightest line would be the one at  $80553.516 \text{ MHz}$  with a main beam temperature of  $2 \text{ mK}$ . This result infers that for a  $5\sigma$  detection of HCS in the gas phase, it would take more than a thousand hours of observations with the IRAM 30m. We therefore conclude that HCS is unlikely to be detected in the gas phase in dark clouds even if its abundance grows notably above  $10^{-12}$  in the models.

### 2.4.4 Summary

In this chapter I have presented a study of sulphur chemistry in dark clouds based on the enhancement of the sulphur chemical network and the recent advancements in the NAUTILUS chemical model regarding grain ices processes ([Ruaud et al., 2016](#)). In order to study the effects of the new network on the modeling of sulphur chemistry in dark clouds, I ran several 0D models with typical dark cloud physical conditions, namely

a gas and dust temperature of 10 K, an atomic proton total density of  $2 \times 10^4 \text{ cm}^{-3}$ , a cosmic ionization rate of  $1.3 \times 10^{-17} \text{ s}^{-1}$ , and a visual extinction of 15 mag. The time I used for all models was  $10^7$  years, which is believed to be the maximal age a dark cloud can reach before undergoing gravitational collapse.

As the main goal was to study the impact of the modifications of the sulphur network on its chemistry in dark clouds, I first detailed the chemistry of the reservoirs of sulphur and of the newly implemented species of interest: HNCS, HSCN and  $\text{CH}_3\text{SH}$ . Second, I have studied the S-bearing species the most affected by the network modifications, namely  $\text{C}_3\text{S}$ ,  $\text{H}_2\text{CS}$ , HCS,  $\text{H}_2\text{S}$ , HS and SO, and how their chemistries are consequently modified.

The second part of my study was dedicated to evaluate the efficiency of the new network to reproduce observations of dark clouds, and especially to assess if the new model could infer new hints on the missing sulphur in these objects. For that purpose, I compared the outputs of the model to observations in the dark clouds TMC-1 (CP) and towards the protostar W33A using four different elemental abundances of sulphur, ranging from the commonly used "depleted" one ( $[\text{S}]_{\text{ini}} = 8 \times 10^{-8}$ ) to the cosmic one ( $[\text{S}]_{\text{ini}} = 1.5 \times 10^{-5}$ ). It appears from the results that the NAUTILUS chemical model does not need a depleted elemental abundance of sulphur anymore in order to reproduce dark clouds observations of S-bearing species. In fact the observations are best reproduced using as elemental abundance of sulphur its cosmic one or a value three times lower ( $[\text{S}]_{\text{ini}} = 5 \times 10^{-6}$ ). As most of the estimations of the cosmic abundance of sulphur lie between these two values, the model does not require additional depletion of sulphur.

This result then allows to give new hints on the sulphur reservoirs in dark clouds. According to the model run with the cosmic elemental abundance of sulphur, the reservoirs of sulphur in dark clouds are:

- $\text{S}^+$  in the gas phase from the beginning of the model and until  $2.8 \times 10^3$  years (initial form of sulphur),
- Atomic sulphur in the gas phase between  $2.8 \times 10^3$  and  $4.6 \times 10^5$  years, containing between 25 and 88% of the total amount of sulphur, depending on the age of the cloud. During this period of time, CS also contains a significant amount of sulphur, namely between 9 and 16%.
- HS and  $\text{H}_2\text{S}$  in the grains bulk for older clouds, containing a total of more than 51% of the total amount of sulphur, that reaches more than 80% at times  $\geq 2.7 \times 10^6$  years. This shared reservoir shows a slight preference for HS between 3 and 10% of the total amount of sulphur, depending on the age of the cloud.



It should be noted that the joint HS/H<sub>2</sub>S reservoirs is mainly due to a hydrogenation cycle between HS and H<sub>2</sub>S, which is enabled by the recently implemented competition between reaction and diffusion on grains surface. These results are also true when using an elemental abundance of sulphur of  $[S]_{\text{ini}} = 5 \times 10^{-6}$  (3 times depleted), which also allows to reproduce observations of S-bearing species in dark clouds. Moreover, this repartition of the sulphur agrees with the common idea that the reservoirs of sulphur in dark clouds are either in an unobservable gas phase form (such as atomic S) or trapped in grain ices under H<sub>2</sub>S form due to successive hydrogenations of atomic S adsorbed on grains surface. Finally, these results are also in agreement with the observational upper limit on H<sub>2</sub>S in grain ices obtained by [Smith \(1991\)](#) as well as recent studies (see [Furuya et al., 2015](#); [Holdship et al., 2016](#)). Unfortunately, the reservoirs I found are yet unobservable, especially because current instruments lack the IR sensitivity needed to observe HS and H<sub>2</sub>S in grain ices.

Overall, this study proves the importance of keeping on improving astrochemical models, especially regarding the processes they take into account and their chemical network. Moreover, being able to efficiently reproduce dark clouds sulphur chemistry using as elemental abundance of sulphur the cosmic one paves the way for new studies on sulphur chemistry during the following steps of star formation.

# 3 | A NEW LOOK AT SULPHUR CHEMISTRY IN HOT CORES AND CORINOS

## Contents

---

<b>3.1</b>	<b>INTRODUCTION</b>	<b>79</b>
<b>3.2</b>	<b>MODELS PARAMETERS</b>	<b>80</b>
3.2.1	H <sub>2</sub> <i>ad hoc</i> formation mechanism	81
3.2.2	Parent dark cloud parameters	81
3.2.3	Hot core models parameters	83
3.2.3.1	The 0D static model parameters	83
3.2.3.2	The 1D static model parameters	83
3.2.3.3	The 0D dynamic model parameters	84
<b>3.3</b>	<b>HOT CORE CHEMISTRY</b>	<b>85</b>
3.3.1	0D models	85
3.3.1.1	Oxygen chemistry	85
3.3.1.2	Sulphur chemistry	89
3.3.1.3	Comparisons to observations	98
3.3.2	1D static models	99
3.3.3	0D dynamic models	101
<b>3.4</b>	<b>DISCUSSIONS AND SUMMARY</b>	<b>102</b>
3.4.1	About the modification of the density profile of the dynamic model	102
3.4.2	About H <sub>2</sub> S and the initial abundance of sulphur	103
3.4.3	About the sensitivity to the type of model	104
3.4.4	About the importance of the pre-collapse chemical composition	104
3.4.5	Summary	105

---



## 3.1 INTRODUCTION

As the process of star formation begins with the gravitational collapse of a dark cloud, density and temperature increase at its center (see section 1.2.2). In this context, hot cores are defined as the small ( $< 0.1$  pc), dense ( $n_H > 2 \times 10^7 \text{ cm}^{-3}$ ), and warm ( $T > 100$  K) region that consequently forms around the forming star. Because of their high temperatures, these regions are characterized by the sublimation of icy mantles of dust grains originated from the depletion of gas phase species in their parent dark cloud. Therefore, because hydrogenation is the most effective chemical reaction in ices, they present high abundances of hydrogenated molecules such as water ( $\text{H}_2\text{O}$ ), hydrogen sulfide ( $\text{H}_2\text{S}$ ), or complex organic molecules such as methanol ( $\text{CH}_3\text{OH}$ , see Schöier et al., 2002, and the references therein). Once evaporated in the hot core, these species undergo further gas phase chemical reactions (Wakelam et al., 2004a; Garrod and Herbst, 2006; Herbst and van Dishoeck, 2009). Hot cores were originally defined for high-mass stars (see for example Kurtz et al., 2000; van der Tak, 2004), but it is now generally admitted that low-mass protostars present the same kind of physico-chemical structure called "hot corinos" (Ceccarelli et al., 1996; Ivezic and Elitzur, 1997). They differ from their high-mass counterparts mainly in size and consequently in infall timescale, which could maybe impact the chemical composition. Our Sun being a low-mass star, the chemistry that takes place in these "small" hot cores is important to understand the history of the material from which planetary systems such as ours are formed. In this chapter, I use the expression "hot core" as a generic term to designate the hot and dense regions surrounding both high-mass and low-mass protostars.

To model the chemistry of hot cores, several types of models exist throughout the literature (see for instance Charnley, 1997; Hatchell et al., 1998; Garrod and Herbst, 2006; Wakelam et al., 2011; Hincelin et al., 2016). Ranging from simple 0D static gas phase models to complex 3D gas-grains ones, different assumptions are made for each type of model, regarding for instance the age of the parent cloud or its free-fall time. These numerous approaches to hot cores chemistry and the different hypotheses they imply raise the question of the uniformity of the results obtained by these models.

In the previous chapter, I have showed the first chemical model able to reproduce sulphur observations in dark clouds using as elemental abundance of sulphur the cosmic one. Thanks to this result, I was able to give new results on the sulphur chemistry in dark clouds. Then, as hot cores form within dark clouds, and therefore from their chemical compositions, it makes sense to study the modeling of sulphur chemistry in the hot cores. Indeed, sulphur bearing species are often used to probe the evolution of hot cores because their abundance is particularly sensitive to physical and chemical variations. For example, the ratios  $\text{SO}_2/\text{SO}$ ,  $\text{SO}_2/\text{H}_2\text{S}$  and  $\text{OCS}/\text{H}_2\text{S}$  have been proposed as chemical clocks in these regions (Charnley, 1997; Hatchell et al., 1998; Wakelam et al., 2011), SO is often used to trace small scale heating processes such as shocked

regions (Viti et al., 2001; Podio et al., 2015), or the centrifugal barrier (Sakai et al., 2014), and OCS can efficiently trace the infalling-rotating envelope (Oya et al., 2016). However, observations of S-bearing species in hot cores is a puzzling issue, since a large variety of sulphur compositions have been observed towards different hot cores and therefore no global trend has yet been found (see figure 5 of Woods et al., 2015, and the references therein). In parallel with this result, it appears that a given set of hot cores can present similar sulphur composition (see for example Minh, 2016), which would suggest similar evolutionary stages. The correct modeling of sulphur chemistry in such hot and dense regions is therefore crucial for a better understanding of the star formation process.

Taking into account the aforementioned issues, the goal of the following chapter is to present a comprehensive study of the modeling of S-bearing species in hot cores in the light of the results of the previous chapter. More particularly, since the sulphur reservoirs are found to be highly dependent on the age of dark clouds (see section 2.3.3), I try to determine how the chemical composition of a dark cloud before its collapse, *ie* the chemical history of the to-be-formed hot core (or pre-collapse chemical composition), impacts the sulphur chemistry. In order to do so, I study the evolution of the abundances of the main S-bearing species observed in hot cores as given by different types of models using several physico-chemical parameters. A secondary goal of this chapter is to seize the opportunity of using different types of models to highlight the differences that can appear between their respective results, and begin to tackle the issue of the uniformity of the results obtained with different types of hot core chemical models. The different types of models and their respective parameters I use are presented in the first section. Then I present the results of these hot core models for sulphur chemistry, to finally discuss these results in the light of the issues I want to address in the last section.

## 3.2 MODELS PARAMETERS

For all the models presented hereafter, I use the same version of the time dependent gas-grain NAUTILUS chemical model as in the previous chapter (see section 1.1.3 for a complete description of the model), as well as the same chemical network. In the following I first present the *ad hoc* formation mechanism of  $\text{H}_2$  I had to add to the NAUTILUS chemical model as well as the issue of  $\text{H}_2$  formation at high temperatures that it tackles. Then I describe the parameters of the parent dark cloud models I use to get the same pre-collapse chemical compositions for all hot cores models, as well as the parameters of the latter.

### 3.2.1 H<sub>2</sub> *ad hoc* formation mechanism

Despite the fact that H<sub>2</sub> is the most abundant molecule in the universe, the modeling of its formation remains one of the most important issue in astrochemistry (see [Wakelam et al., 2017](#), for a review), especially in the hot and dense regions of the ISM such as hot cores. Indeed, H<sub>2</sub> cannot be formed efficiently enough in the gas phase to explain its abundance, and it is now well established that it forms mainly on the grain icy surfaces ([Hollenbach and Salpeter, 1971](#)). However, in hot cores, where the temperature is high enough for the grain ices to be evaporated, the grain are left bare, undermining the usual formalism for H<sub>2</sub> formation in ices. Nonetheless, [Cazaux et al. \(2005\)](#) shown that H<sub>2</sub> formation on bare grains could be efficient up to 1000 K, which implies the necessity for chemical model to take into account an *ad hoc* formalism for the formation of H<sub>2</sub> at high temperatures. Hence, given the high temperature regimes encountered in this study, I implemented into the NAUTILUS model the *ad hoc* formation mechanism for H<sub>2</sub> described in [Harada et al. \(2010\)](#). They consider that the formation rate of H<sub>2</sub> can be written as:

$$\frac{dn(\text{H}_2)}{dt} = \frac{1}{2} n_H v_H n_g \sigma_g S(T) \epsilon \quad (3.1)$$

where  $n_H$  is the total number density of protons and  $v_H$  the thermal velocity of hydrogen atoms, respectively in  $\text{part.cm}^{-3}$  and  $\text{cm.s}^{-1}$ ,  $n_g$  the number density of grains in  $\text{part.cm}^{-3}$ ,  $\sigma_g$  the cross section of a grain in  $\text{cm}^2$ ,  $S$  the sticking coefficient for hydrogen atom as a function of temperature, and  $\epsilon$  the recombination efficiency. I use for the recombination efficiency the results from [Cazaux et al. \(2005\)](#), and for the sticking coefficient the expression derived by [Chaabouni et al. \(2012\)](#).

### 3.2.2 Parent dark cloud parameters

In order to model the chemistry of a given hot core, one must consider as initial condition the chemical composition of its parent dark cloud before it collapses. Moreover, if I want to be able to compare the outputs of the different types of models of hot cores I run, it makes sense to use the same initial chemical composition. Hence, I begin by running a model with the commonly used dark clouds physical parameters, namely a gas and dust temperature of 10 K, a proton total density of  $2 \times 10^4 \text{ cm}^{-3}$ , a cosmic ionization rate of  $1.3 \times 10^{-17} \text{ s}^{-1}$ , and a visual extinction of 15 mag. The set of initial abundances is summarized in table 3.1. It is different from table 2.3 only in its sulphur elemental abundance. Indeed, as previously showed, the model does not require additional depletion of sulphur from its cosmic value to reproduce dark clouds observations and I then choose to use it as initial abundance of sulphur.

Table 3.1: Initial abundances.  $*a(b)$  stands for  $a \times 10^b$ .

Element	$[X]_{\text{ini}}^*$	References
H <sub>2</sub>	0.5	
He	0.09	1
N	6.2(-5)	2
O	2.4(-4)	3
C <sup>+</sup>	1.7(-4)	2
S <sup>+</sup>	1.5(-5)	2
Si <sup>+</sup>	8.0(-9)	4
Fe <sup>+</sup>	3.0(-9)	4
Na <sup>+</sup>	2.0(-9)	4
Mg <sup>+</sup>	7.0(-9)	4
P <sup>+</sup>	2.0(-10)	4
Cl <sup>+</sup>	1.0(-9)	4
F	6.7(-9)	5

(1) Wakelam and Herbst (2008), (2) Jenkins (2009), (3) Hincelin et al. (2011), (4) Low-metal abundances from Graedel et al. (1982), (5) Depleted value from Neufeld et al. (2005)

Table 3.2: Oxygen and sulphur reservoirs in both LEDC and EDC cases. The prefix "b-" is for the bulk species.

LEDC	
Oxygen	Sulphur
O (42%)	S (61%)
CO (26%)	CS (15%)
EDC	
Oxygen	Sulphur
b-H <sub>2</sub> O (53%)	b-HS (35%)
b-H <sub>2</sub> CO (9%)	b-H <sub>2</sub> S (26%)

I showed in section 2.3.3 that the evolution time of the parent cloud is critical for the sulphur reservoirs and I observe the same kind of results for oxygen in the parent cloud model. Hence, in order to study the importance of its chemical history on the hot cores composition, I extract the outputs of the parent cloud model at two different final times for all models:  $10^5$  and  $10^6$  years. Both these ages are acceptable for dark clouds and allow to get two very different chemical compositions of the cloud before it collapses (see table 3.2):

- In the case of the less evolved dark cloud (hereafter noted LEDC), most of the oxygen and sulphur are still in the gas phase in atomic form (respectively 42 and

61% of their total amount), or in the form of CO (26%) and CS (15%), respectively. The remainder is, for both species, locked in icy grains bulk, mainly in the form of H<sub>2</sub>O, HS and H<sub>2</sub>S.

- In the case of the evolved dark cloud (hereafter noted EDC), more than 95% of the oxygen is locked in the ices mainly in the form of H<sub>2</sub>O (53%) and H<sub>2</sub>CO (9%). As for sulphur, more than 90% is locked in the ices, mostly in the form of HS (35%) and H<sub>2</sub>S (26%).

I then use both LEDC and EDC chemical compositions as initial abundances for the different hot core models.

### 3.2.3 Hot core models parameters

In order to conduct a comprehensive study of the sulphur chemistry in hot cores, as well as to highlight the discrepancies between the different models commonly used in the literature, I use three types of hot cores models:

1. 0D static models for which I consider constant physical parameters throughout the model time,
2. 1D static models for which each cell of the spatial grid evolves with constant physical parameter as a 0D model,
3. 0D dynamic models for which each cell of the spatial grid evolves with time dependant physical parameters.

In the following I present the densities and temperatures of these three types of hot core models.

#### 3.2.3.1 The 0D static model parameters

I begin to run 0D models with the main purpose of getting a comprehensive look at sulphur chemistry in hot core. As [Charnley \(1997\)](#) showed the important role of temperature on sulphur chemistry in such environments, I present calculations for a typical hot core density of  $2 \times 10^7 \text{ cm}^{-3}$ , and two temperature regimes of 100 and 300 K. Hence I obtain four 0D models with different pre-evaporative compositions (EDC and LEDC) and temperatures (100 and 300 K).

#### 3.2.3.2 The 1D static model parameters

The 1D model follows the physical structure for the envelope of the low-mass protostar IRAS 16293-2422 from [Crimier et al. \(2010\)](#), which was constrained through multi-wavelength dust and molecular observations. Indeed this protostar is believed to have a hot core within the  $\sim 150 \text{ AU}$  around its centre (see [Schöier et al., 2002](#)). The density and temperature radial evolutions are shown in figure 3.1 (a) and (b), respectively



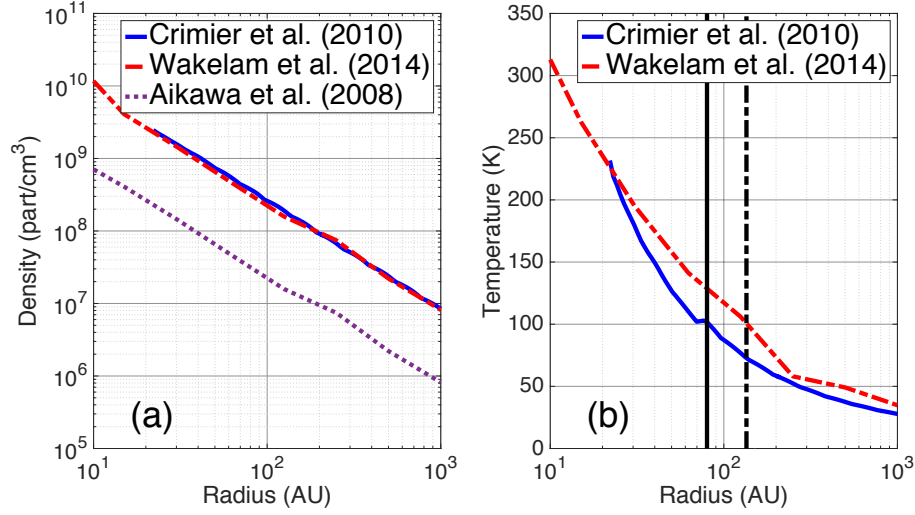


Figure 3.1: Radial structure of the 1D static and 0D dynamic models at final time for: (a) density, for which I plot the initial structure from Aikawa et al. (2008) as reference, (b) temperature, for which I plot the limit of the hot core ( $T > 100$  K) for the 1D static ( $R_{\text{HC}}^{\text{1D}} = 80$  AU, solid black vertical line) and 0D dynamic ( $R_{\text{HC}}^{\text{0D}} = 135$  AU, dashed black vertical line).

(solid blue lines). For this model, the spatial limit of the hot core ( $T > 100$  K) is located at  $R_{\text{HC}}^{\text{1D}} = 80$  AU (solid vertical black line on figure 3.1 (b)).

### 3.2.3.3 The 0D dynamic model parameters

The structure I use for the dynamic model is the modified structure of Aikawa et al. (2008) used in Wakelam et al. (2014) and Majumdar et al. (2016), and was computed from the radiation hydrodynamic (RHD) model from Masunaga and Inutsuka (2000). It initially starts from a parent cloud with a central density of  $\sim 6 \times 10^4 \text{ cm}^{-3}$ , a radius of  $4 \times 10^4$  AU and a total mass of  $3.852 M_{\odot}$ . Then the model follows the collapse of the prestellar core, which eventually forms a protostellar core after  $2.5 \times 10^5$  yr. Finally, the protostar grows by mass accretion from the envelope for  $9.3 \times 10^4$  yr. As in Wakelam et al. (2014), I have multiplied by 10 all the densities of the models in order for the final physical structure of the dynamic model to be similar to the 1D structure of Crimier et al. (2010). The consequence of this modification will be discussed in section 3.4.1 (see also section 4.5 of Wakelam et al., 2014). Figure 3.1 (a) shows the resulting final density radial evolution (dashed red line) as well as the previous one (dotted purple line), and figure 3.1 (b) the final temperature radial evolution (dashed red line). For this model, the spatial limit of the hot core ( $T > 100$  K) is located at  $R_{\text{HC}}^{\text{0D}} = 135$  AU (dashed black line on figure 3.1 (b)).

The designations and physical parameters of all the models presented in this paper are summarized in table 3.3.

Table 3.3: Summary of the models designations and physical parameters.

Simulations	Physical parameters	Pre-collapse evolution time
0D Static models		
0DS100LEDC	$T = 100 \text{ K}, n_H = 2 \times 10^7 \text{ cm}^{-3}$	$10^5 \text{ yrs}$
0DS300LEDC	$T = 300 \text{ K}, n_H = 2 \times 10^7 \text{ cm}^{-3}$	$10^5 \text{ yrs}$
0DS100EDC	$T = 100 \text{ K}, n_H = 2 \times 10^7 \text{ cm}^{-3}$	$10^6 \text{ yrs}$
0DS300EDC	$T = 300 \text{ K}, n_H = 2 \times 10^7 \text{ cm}^{-3}$	$10^6 \text{ yrs}$
1D Static models		
1DSLEDC	Structure from <a href="#">Crimier et al. (2010)</a>	$10^5 \text{ yrs}$
1DSEDC	Structure from <a href="#">Crimier et al. (2010)</a>	$10^6 \text{ yrs}$
0D Dynamic models		
0DDLDC	Modified structure from <a href="#">Aikawa et al. (2008)</a>	$10^5 \text{ yrs}$
0DDEDC	Modified structure from <a href="#">Aikawa et al. (2008)</a>	$10^6 \text{ yrs}$

### 3.3 HOT CORE CHEMISTRY

#### 3.3.1 0D models

In this section, I aim to do a comprehensive study of sulphur chemistry in hot cores environments. In particular, I study the importance of the temperature as well as the pre-collapse chemical composition using the four 0D models defined in section 3.2.3.1. Sulphur chemistry in the hot gas phase is known to be intertwined with the distribution of reactive oxygen: O, O<sub>2</sub>, and OH ([Charnley, 1997](#); [Wakelam et al., 2004a](#); [Esplugues et al., 2014](#)). Hence I begin with a description of the chemistry of these species, then study the chemistry of the main S-bearing species observed towards hot and dense objects: SO, SO<sub>2</sub>, H<sub>2</sub>S, OCS, CS, and H<sub>2</sub>CS.

##### 3.3.1.1 Oxygen chemistry

The left, middle and right panels of figure 3.2 show the abundances of respectively O, O<sub>2</sub>, and OH, for the LEDC (top) and EDC (bottom) pre-collapse compositions. I first describe the chemistry of atomic oxygen, and then that of O<sub>2</sub> and OH together because they are strongly linked in the LEDC cases.

###### 3.3.1.1.1 Atomic oxygen

For atomic oxygen in the 0DS100LEDC case (cf figure 3.2 (a)), the temperature is not high enough for all the mantle of grains to evaporate and O reacts mainly with the S-bearing species available in the gas phase. It initially reacts with CS which is the second most abundant S-bearing species in the gas phase (see table 3.2), to form S

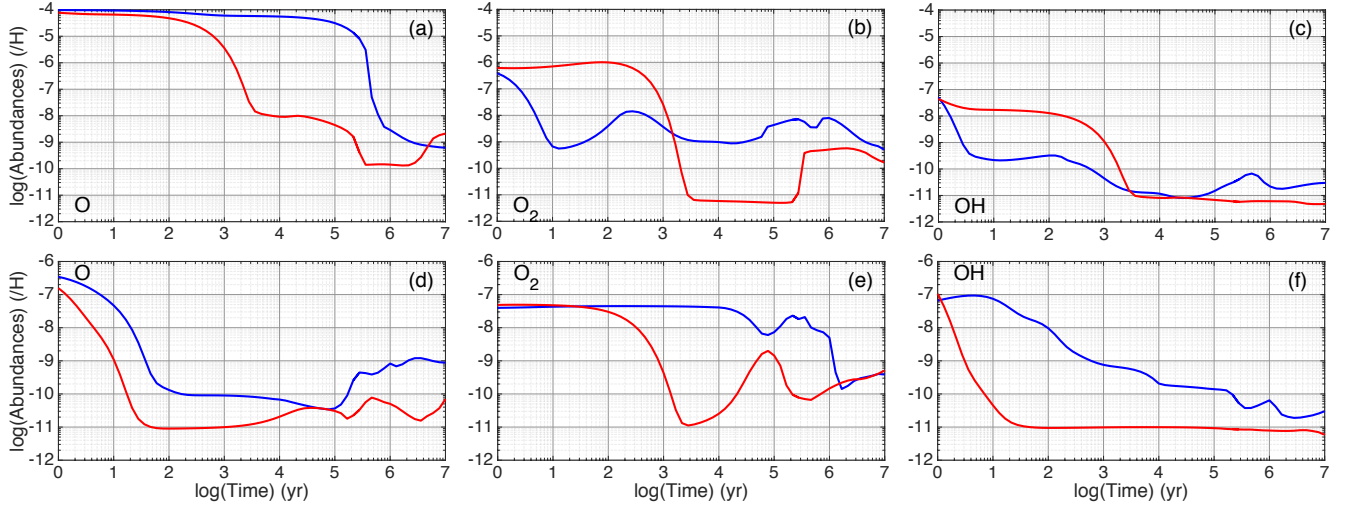


Figure 3.2: Abundances of O, O<sub>2</sub>, and OH relative to H as a function of time for hot core conditions:  $n_H = 2 \times 10^7 \text{ cm}^{-3}$  and  $T = 100 \text{ K}$  (blue line) or  $300 \text{ K}$  (red line), and for LEDC (top panel) and EDC (bottom panel) pre-collapse compositions.

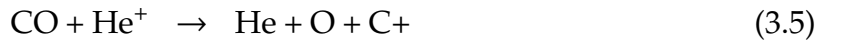
and CO. As the abundance of CS consequently decreases, O is then mainly destroyed through formation of SO and SO<sub>2</sub>:



In the 0D300LEDC case (cf figure 3.2 (a)), the temperature of the core is high enough for hydrocarbons (species of the form H<sub>x</sub>C<sub>n</sub>), formed and trapped on the grains during the dark cloud phase, to evaporate. They participate in the consumption of O by forming mainly CO, causing its abundance to decrease much faster than in the 0D100LEDC case. However, the most efficient reaction at this temperature is:



Towards the end ( $t > 10^6 \text{ yrs}$ ), the abundance of atomic oxygen increases again from the reaction:



as well as photodissociation by secondary UV photons of SO and SO<sub>2</sub>.

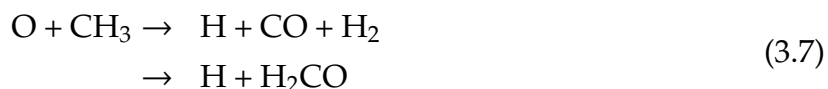
With the pre-collapse composition of the EDC, contrary to the LEDC, most of the

oxygen is trapped in grains bulk, mainly under the form of  $\text{H}_2\text{O}$ ,  $\text{H}_2\text{CO}$ , and  $\text{CO}$  (see table 3.2). Hence, few atomic oxygen is available in the gas phase even after sublimation of the grains bulk, which explains that its initial abundance in both EDC cases is lower by two orders of magnitude compared to LEDC ones. In the 0DS100EDC case (cf figure 3.2 (d)), the temperature of the core is hot enough to sublimate light species, especially HS and NS, which are two of the sulphur reservoirs in the pre-collapse composition. These species react rapidly with O to form SO and NO for  $10^4$  years. After this time, it is HCNS which reacts mainly with atomic oxygen through the following reactions:



The global increase of abundance of O at the end of the model is due to reaction (3.5).

In the 0D300EDC case (cf figure 3.2 (d)), most of the sublimated hydrocarbons efficiently form  $\text{CH}_3$ , which consumes O in the first hundred years following:



Afterwards, O abundance increases slowly, mainly from the reaction:



#### 3.3.1.1.2 $\text{O}_2$ and OH

In both 0DS100LEDC and 0DS300LEDC models, dioxygen chemistry is strongly linked to S and OH chemistry via:



At 100 K (cf figure 3.2 (b)), atomic carbon initially destroys  $\text{O}_2$  faster than it is created by reaction (3.10) through:



Then, atomic sulphur consumes both  $\text{O}_2$  and  $\text{OH}$  (cf figure 3.2 (c)) within a timescale of a thousand years, respectively via reaction (3.9) and:



Afterwards, both species chemistries are linked by reaction (3.10). The short increase of both abundances near  $10^6$  years is mainly due to the formation of  $\text{OH}$  via electronic recombination of  $\text{HOCS}^+$  and  $\text{HSO}_2^+$ .

At 300 K however (cf figure 3.2 (b)), atomic carbon is initially rapidly consumed by the two evaporated hydrocarbons  $\text{C}_4\text{H}_2$  and  $\text{C}_2\text{H}_2$ , and does not destroy  $\text{O}_2$  as efficiently as at 100 K. Instead,  $\text{OH}$  is formed rapidly via reaction (3.4) (cf figure 3.2 (c)), which causes the  $\text{O}_2$  abundance to increase through reaction (3.10) in the first hundred years. Then  $\text{O}_2$  and  $\text{OH}$  are consumed in a few thousands years respectively by reaction (3.9) and:



It should be noted that the increase in  $\text{O}_2$  abundance near  $10^5$  years is due to the following ion-neutral reactions:



In the EDC cases, atomic oxygen is not abundant enough in the gas phase for reaction (3.10) to be efficient. Hence, there is no evident link between  $\text{O}_2$  and  $\text{OH}$  chemistries as in the LEDC cases. For the 0D100EDC model (cf figure 3.2 (e)), the abundance of dioxygen first slowly grow for a few hundred years from the reaction:



$\text{O}_2\text{H}$  is also destroyed by  $\text{H}$  to form  $\text{OH}$ , and when there is not enough  $\text{O}_2\text{H}$  left in the gas phase,  $\text{HCO}$  then reacts with  $\text{O}_2$  causing its abundance to decrease after a few thousands years. Moreover, reaction (3.9) also becomes efficient after  $10^4$  years and

O<sub>2</sub> abundance starts to drop at this time. The increase near 10<sup>5</sup> years is mainly due to reaction (3.15).

In the 0D300EDC (cf figure 3.2 (e)), the CH<sub>3</sub> formed from the evaporated hydrocarbon destroys efficiently O<sub>2</sub> for a few thousands years via:



Afterwards, the abundance of O<sub>2</sub> globally increases from the following reactions:



OH abundance generally decreases in both EDC models. For the 0D100EDC case (cf figure 3.2 (f)), this decrease is mainly due to:



As for the 0D300EDC (cf figure 3.2 (f)), it is mainly due to reaction (3.13) and (3.21).

#### 3.3.1.2 Sulphur chemistry

In the following, I take a comprehensive look at the chemistry of the main neutral S-bearing species detected in hot cores namely SO, SO<sub>2</sub>, OCS, H<sub>2</sub>S, H<sub>2</sub>CS and CS.

##### 3.3.1.2.1 SO, SO<sub>2</sub>, and OCS in the LEDC case

Figure 3.3 displays the abundances of SO, SO<sub>2</sub>, and OCS in both LEDC (top panel) and EDC (bottom panel) cases. In the 0DS100LEDC case, these three species are initially destroyed by atomic carbon explaining their respective drops in the first 10 years of the model:



SO abundance then grows first mainly from reaction (3.12), then reactions (3.2) and

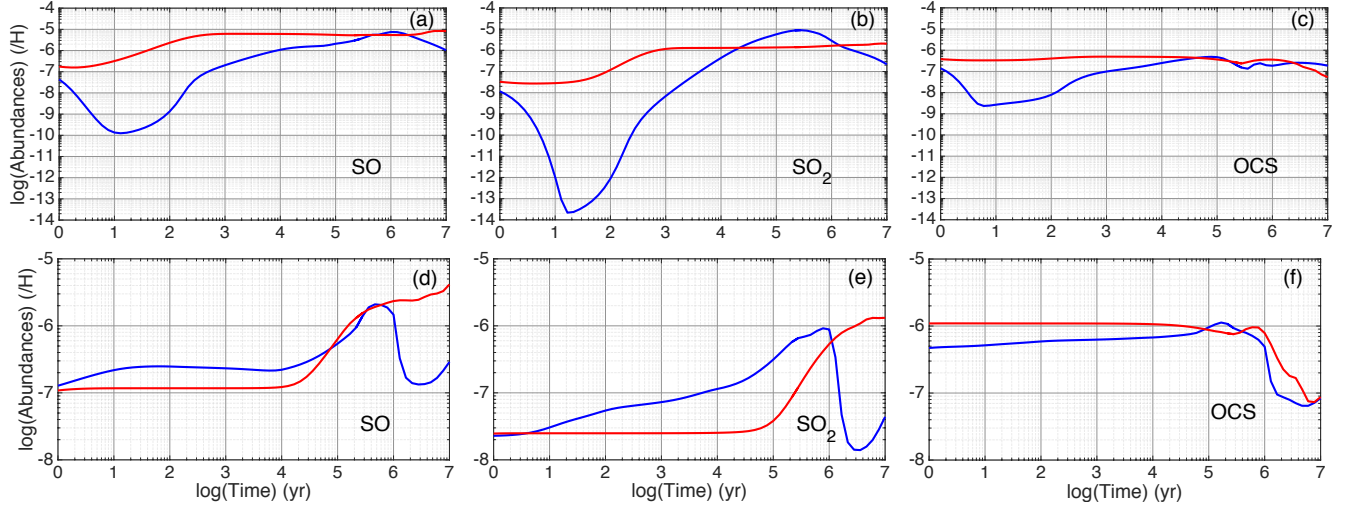


Figure 3.3: Abundances of SO, SO<sub>2</sub>, and OCS relative to H as a function of time for hot core conditions:  $n_H = 2 \times 10^7 \text{ cm}^{-3}$  and  $T = 100 \text{ K}$  (blue line) or  $300 \text{ K}$  (red line), and for LDC (top panel) and EDC (bottom panel) pre-collapse compositions.

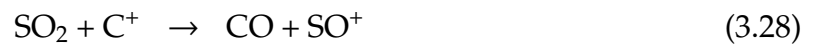
(3.9) (cf figure 3.3 (a)). After  $10^6$  years, as only a small amount of reactive oxygen remains in the gas phase, SO is no longer efficiently produced. It is instead mainly destroyed by CH through:



SO<sub>2</sub> is linked with SO mainly by reaction (3.3), as well as:

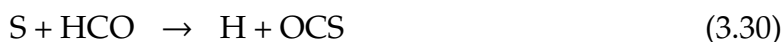


which is only efficient when OH is abundant enough in the gas phase (i.e. at the early beginning of the model, cf figure 3.2 (c)). Hence, SO<sub>2</sub> abundance grows from  $10^{-10}$  to a few  $10^{-5}$  years from these reactions (cf figure 3.3 (b)). Afterwards, SO<sub>2</sub> is destroyed by H<sub>3</sub><sup>+</sup> and C<sup>+</sup> following:



After its consumption by atomic carbon, OCS is also efficiently formed until  $10^5$  years from HCO and HCS (cf figure 3.3 (c)):





For the remainder of the model,  $\text{HCO}^+$  is formed efficiently from the reaction of  $\text{H}_3^+$  with CO, and reacts with OCS:



OCS abundance remains however stable at this time because of reaction (3.25).

In the 0DS300LEDC case, as seen in the previous oxygen study,  $\text{C}_4\text{H}_2$  and  $\text{C}_2\text{H}_2$  thermally desorb from grains bulk. Both these species react initially with atomic carbon with reaction rates higher by more than two orders of magnitude than those of reactions (3.22), (3.23) and (3.24) preventing SO,  $\text{SO}_2$  and OCS from abrupt initial consumptions. Therefore SO and  $\text{SO}_2$  form rapidly from reactions (3.9), (3.12) and (3.26) (cf figure 3.3 (a) and (b)). When the abundance of reactive oxygen drops around  $10^3$  years, their abundances will undergo only small variations. Indeed as the main reactions ruling SO chemistry are no longer efficient because of the lack of reactive oxygen in the gas phase, reactions that recycle SO via  $\text{HSO}^+$  allow its abundances to reach a quasi-static regime until the end of the model. For instance, due to the high temperature, high abundance of evaporated  $\text{H}_2\text{O}$  and CO render efficient the two following reactions:



The SO thus formed is then put back in  $\text{HSO}^+$ :



As a result,  $\text{SO}_2$  abundances shows only a small increase during the final part of the model, mainly due to reaction (3.26).

OCS abundance does not vary much in the 0DS300LEDC case (cf figure 3.3 (c)). When atomic oxygen is still abundant in the gas phase, OCS is mainly formed through reaction (3.29). Afterwards it is destroyed by secondary UV photons to form S and CO, and by  $\text{H}_3^+$  through:





HOCS<sup>+</sup> then recombines electronically to form either CS and OCS, which explains why the latter abundance decreases slowly.

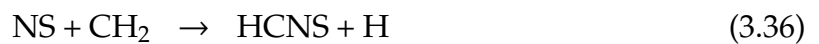
#### 3.3.1.2.2 SO, SO<sub>2</sub>, and OCS in the EDC case

The bottom panel of figure 3.3 displays the abundances of SO, SO<sub>2</sub>, and OCS in both EDC cases. On the one hand, it appears that the chemistry of these species does not depend as much on the temperature as in the LEDC cases. This can be explained by the poor abundance of reactive oxygen, especially atomic oxygen, in the gas phase in the EDC cases as compared with the LEDC cases. Table 3.4 displays the amount of reactive oxygen (relative to that of total oxygen) in the gas phase at the first time step of each hot core model. It shows that in the LEDC cases at least 33% of the total amount of oxygen is under reactive form in the gas phase, against at most 0.1% in the EDC cases.

Table 3.4: Description of the reactive oxygen composition in the gas phase at the first time step of the hot core models (post-collapse composition). The values display the percentage relative to the total abundance of oxygen.

LEDC	
100 K	300 K
41%	33%
EDC	
100 K	300 K
0.1%	< 0.09%

On the other hand the chemistry of SO, SO<sub>2</sub>, and OCS looks relatively inert, except for the last part of the model ( $t > 10^5$  years). Indeed, in the 0DS100EDC case, SO and SO<sub>2</sub> (cf figure 3.3 (d) and (e)) are at first slowly formed through reactions (3.12) and (3.26), respectively. As the abundance of HCNS grows from the evaporated NS through:

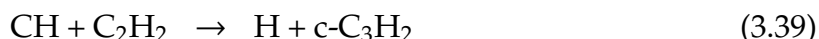


the abundance of SO grows steeper from  $10^4$  years thanks to reaction (3.6). Finally, after  $10^6$  years, SO is consumed by CH through reactions (3.25). The strong link of SO<sub>2</sub> with SO via reaction (3.26), coupled with reaction (3.27), makes its abundance drops

at the same time. Regarding OCS (cf figure 3.3 (f)), its abundance increases at first in the 0DS100EDC case from reaction (3.20), then from reaction (3.30) after  $10^4$  years. Towards the end of the model, as for SO and SO<sub>2</sub>, OCS is destroyed by CH via:



In the 0DS300EDC case, the chemistry of SO, SO<sub>2</sub> and OCS differs from the 0DS100EDC case from two main points: first, the abundance of OH decreases much faster in the 0DS300EDC case (cf figure 3.2 (f)), diminishing even more the quantity of reactive oxygen in the gas phase, causing the abundances of SO, SO<sub>2</sub>, and OCS to stay relatively constant during at least the first  $10^5$  years of the model. Secondly, CH is much less abundant at 300 K (by two to three orders of magnitude) because it is effectively destroyed by evaporated H<sub>2</sub>O and C<sub>2</sub>H<sub>2</sub>:



Hence, SO and SO<sub>2</sub> abundances keep on increasing at the end of the model (cf figure 3.3 (d) and (e)) and do not decrease as in the 0DS100EDC case. However, the lack of CH do not prevent the late-time decrease of OCS (cf figure 3.3 (f)), which is ruled by the same reactions as in the 0DS300LEDC case, namely its photodissociation by secondary UV photon and reaction (3.31).

#### 3.3.1.2.3 H<sub>2</sub>S, H<sub>2</sub>CS, and CS in the LEDC case

Figure 3.4 is the same as figure 3.3 but for H<sub>2</sub>S, H<sub>2</sub>CS, and CS. In the 0DS100LEDC case, as for SO, SO<sub>2</sub>, and OCS, H<sub>2</sub>S and H<sub>2</sub>CS (cf figure 3.4 (a) and (b)) are both initially destroyed by atomic carbon via the following reactions:



The following increase in H<sub>2</sub>S abundance is mainly due to two coupled reactions:

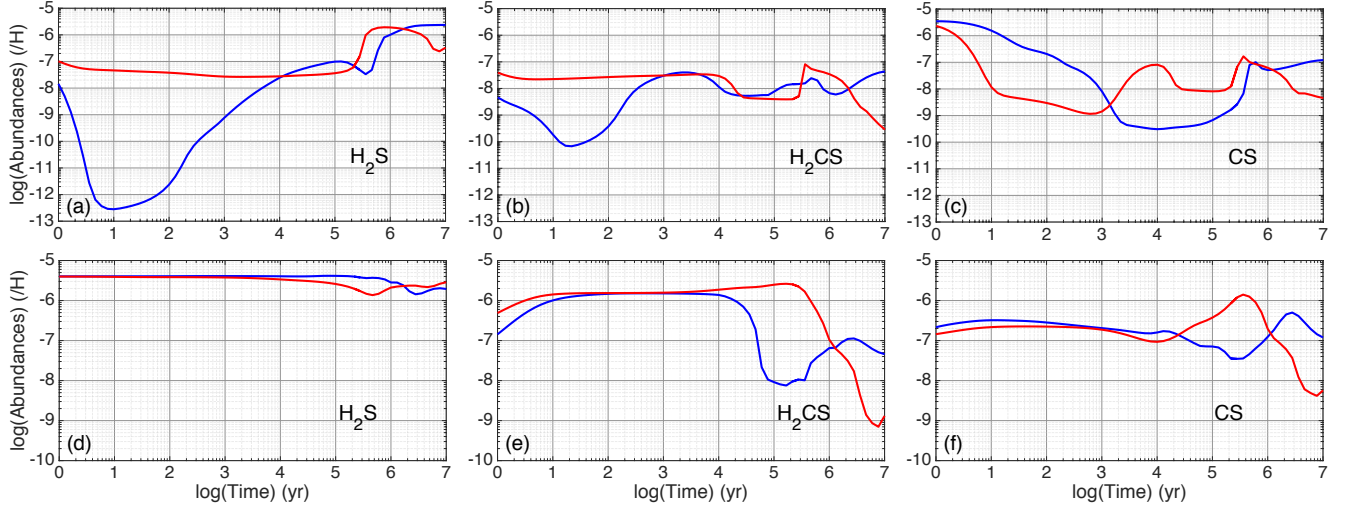


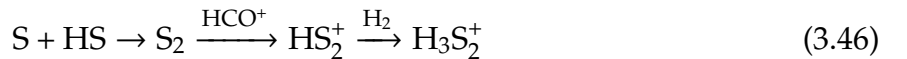
Figure 3.4: Abundances of  $\text{H}_2\text{S}$ ,  $\text{H}_2\text{CS}$ , and  $\text{CS}$  relative to  $\text{H}$  as a function of time for hot core conditions:  $n_{\text{H}} = 2 \times 10^7 \text{ cm}^{-3}$  and  $T = 100 \text{ K}$  (blue line) or  $300 \text{ K}$  (red line), and for LEDC (top panel) and EDC (bottom panel) pre-collapse compositions.



Indeed,  $\text{CH}_2\text{SH}$  evaporates slowly from grains surface in the physical conditions of the model. Reacting with atomic nitrogen via reaction (3.42), it forms both  $\text{H}_2\text{S}$  and  $\text{HCN}$ . The latter then also forms  $\text{H}_2\text{S}$ . The combination of these two reactions explains the steep increase in  $\text{H}_2\text{S}$  abundance between  $10$  and  $10^5$  years. Afterwards, it decreases from the following ion-neutral reactions:



Towards the end of the model,  $\text{H}_2\text{S}$  is efficiently produced by the electronic recombination of  $\text{H}_3\text{S}_2^+$ , provided by the following reaction mechanism:



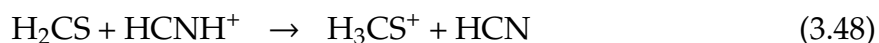
This mechanism is made efficient by the increase of the abundance of  $\text{HS}$  during this period of time.

$\text{H}_2\text{CS}$  gas phase chemistry at  $100 \text{ K}$  (in both LEDC and EDC cases, cf figure 3.4 (b)

and (e), respectively) is intertwined with its grain chemistry because the temperature is not high enough for its complete thermal desorption from grain ices. Hence, after its destruction by atomic carbon, H<sub>2</sub>CS grows from:



Then its abundance decreases because of its destruction by HCNH<sup>+</sup> in the gas phase, as well as by hydrogenation in the grains bulk. Indeed the latter contributes to the depletion of H<sub>2</sub>CS from the gas phase at this time because the chemistry has reached adsorption/desorption equilibrium. The reactions in question are respectively:



where the prefix "b-" is for the bulk species. Afterwards, H<sub>2</sub>CS abundance increases again, mainly from the electronic recombination of H<sub>3</sub>CS<sup>+</sup> and reaction (3.47).

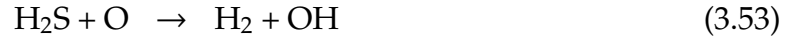
Contrary to the other S-bearing species studied in this paper, CS is not destroyed by atomic carbon during the early phase of the model (cf figure 3.4 (c)). It is instead destroyed during a longer period of time (approximately 10<sup>4</sup> years) by atomic oxygen, contributing efficiently to lock gas phase oxygen into CO via:



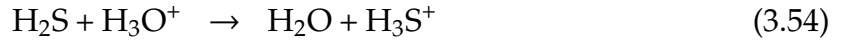
CS abundance then grows mainly from reaction (3.22) as well as from the following reaction mechanism:



As previously observed, atomic carbon is preferentially consumed by evaporated hydrocarbon in the 0DS300LEDC case and therefore has a limited impact on sulphur chemistry compared to the 0DS100LEDC case. Hence, H<sub>2</sub>S (cf figure 3.4 (a)) is first destroyed by atomic hydrogen and oxygen for 10<sup>3</sup> years via:



$\text{H}_2\text{S}$  is after formed by the electronic recombination of  $\text{H}_3\text{S}_2^+$  provided by a similar reaction mechanism than (3.46), except that instead of  $\text{HCO}^+$ , it is the  $\text{H}_3\text{O}^+$  ion which mainly reacts with  $\text{S}_2$  to form  $\text{HS}_2^+$ . Indeed  $\text{H}_3\text{O}^+$  is much more abundant in the gas phase at 300 K than at 100 K because it comes mainly from  $\text{H}_2\text{O}$  which is totally evaporated from grain at this temperature. Furthermore, it is  $\text{H}_3\text{O}^+$  which destroys  $\text{H}_2\text{S}$  at the end of the model:



At 300 K,  $\text{H}_2\text{CS}$  is fully depleted from grains surface and bulk and is affected only by gas phase chemistry (cf figure 3.4 (b)). Partially consumed by atomic carbon during the first 10 years, it is then formed mainly through reaction (3.47) and destroyed by reaction (3.48).

In the 0DS300LEDC case, CS is also initially destroyed by atomic oxygen via reaction (3.50) (cf figure 3.4 (c)), but for a shorter time than in the 0DS100LEDC case. The increase in its abundance at  $10^3$  years is mostly due to a reaction mechanism starting from the evaporated  $\text{C}_4\text{H}_2$ :



Then CS is mainly destroyed by  $\text{HCNH}^+$  via:



Finally, the last increase in its abundance is due to the reaction mechanism (3.51).

#### 3.3.1.2.4 $\text{H}_2\text{S}$ , $\text{H}_2\text{CS}$ , and CS in the EDC case

In the EDC cases and prior to collapse,  $\text{H}_2\text{S}$  in icy grains bulk is the second reservoir of sulphur, containing 26% of the total amount of sulphur (see table 3.2). Hence its abundance in both EDC cases is generally higher than in the LEDC ones. Moreover, in the 0DS100EDC case (cf figure 3.4 (d)),  $\text{H}_2\text{S}$  initially forms efficiently from its abundant reservoirs counterpart HS via:

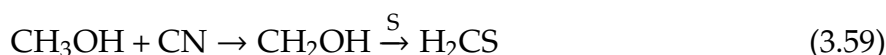


It is also produced during most of the model from the slow evaporation of methanol, which is the fourth reservoir of oxygen in the EDC case, and through the following reaction mechanism:



Towards the end,  $\text{H}_2\text{S}$  is destroyed via reaction (3.44).

In the 0DS100EDC case (cf figure 3.4 (e)),  $\text{H}_2\text{CS}$  is first formed via reaction (3.47) as well as from methanol slow depletion with the following reaction mechanism, similar to (3.58):



As in the 0DS100LEDC case,  $\text{H}_2\text{CS}$  chemistry is afterwards linked with its grain chemistry via reactions (3.48) and (3.49), making its abundance drop at  $10^5$  years. At the end of the model  $\text{H}_2\text{CS}$  abundance increases again from reaction (3.47) and electronic recombination of  $\text{H}_3\text{CS}^+$ .

Due to the small amount of reactive oxygen in the EDC cases compared to the LEDC cases (see table 3.4), CS is not destroyed by atomic oxygen at the beginning of the model (cf figure 3.4 (e)). At 100 K, it is instead formed rapidly via:



with HCS coming from the small fraction of  $\text{H}_2\text{S}$  destroyed by reaction (3.40). Afterward, CS is destroyed for a few  $10^5$  years by OH and HS via reaction 3.20 and:



When  $\text{CS}_2$  abundance is high enough, it is hydrogenated back into CS, causing the abundance of the latter to grow again at the end of the model.

In the 0DS300EDC case, all the methanol is directly depleted in the gas phase and rapidly forms  $\text{CH}_3$  through many different reactions. Hence, as  $\text{CH}_3$  abundance is rapidly much higher than in the 0DS100EDC case,  $\text{H}_2\text{S}$  is mainly destroyed at 300 K

via (cf figure 3.4 (d)):



This high abundance of  $\text{CH}_3$  in the gas phase also causes  $\text{H}_2\text{CS}$  to be efficiently formed for a few  $10^5$  years by reaction (3.47) (cf figure 3.4 (e)). Afterwards, as in the 0DS300LEDC case, the steep decrease of its abundance is mainly due to reaction (3.48).

Finally, CS chemistry in the 0DS300EDC case is similar to the 0DS100EDC case, except for the fact that OH abundance at 300 K is much lower than at 100 K (cf figure 3.4 (f)). Hence, CS is mainly destroyed by reaction (3.61). Moreover, as  $\text{CS}_2$  abundance grows faster at 300 K than at 100 K, the peak in CS abundance happens sooner in the 0DS300LEDC case. At the end, CS is destroyed like  $\text{H}_2\text{CS}$ , by  $\text{HCNH}^+$  via reaction (3.56).

### 3.3.1.3 Comparisons to observations

The species studied in this section have been detected in many hot cores and corinos, and their respective observed abundances present differences among sources that can go as high as three orders of magnitude (see for example table 5 of Wakelam et al., 2004b, and reference therein). These variations are often explained by differences among the ages of the sources, or among the temperatures of their respective hot cores or corinos (see discussion in Herpin et al., 2009). Therefore, it would be complex, as well as out of the scope of the present study, to quantitatively compare my results to observations. Qualitatively however, I can raise the two following points:

1. The total amount of sulfur observed in massive hot cores generally accounts only for a small part of its cosmic abundance (around 0.1%, see Hatchell et al., 1998; van der Tak, 2004; Wakelam et al., 2004b; Herpin et al., 2009), which contrasts with my modeling results where most of the sulphur appears to be under the form of gas phase SO,  $\text{SO}_2$ ,  $\text{H}_2\text{S}$ , and OCS at the ages that are expected for such objects. Uncertainties on massive hot cores observations due to the fact they are mostly very distant sources, therefore not spatially resolved, as well as uncertainties on the high temperature network could explain these discrepancies. However, among this type of sources, the hot core of Orion KL presents a high abundance of  $\text{H}_2\text{S}$  of  $2.5 \times 10^{-6}$ , accounting for more than 15% of the total amount of sulphur (Minh et al., 1990), as well as higher abundances of SO and  $\text{SO}_2$  than in other massive hot cores (Sutton et al., 1995). It appears that, even if the models fail to reproduce the observed abundances of these molecules for most massive hot cores observations, both the EDC case models can reproduce the Orion KL abundances of  $\text{H}_2\text{S}$ , SO, and  $\text{SO}_2$  within one order of magnitude in a range of



time acceptable for this structure, between  $10^4$  and  $10^6$  years. However in this range of time, the models tend to overestimate the abundances of OCS, CS and  $\text{H}_2\text{CS}$ , which suggests that work still has to be done regarding the modeling of the chemistry of these species, or their observations.

2. The only hot corinos towards which all the S-bearing species studied in this paper have been observed is IRAS 16293-2422. The abundances derived from observations of SO,  $\text{SO}_2$ , OCS,  $\text{H}_2\text{CS}$  and  $\text{H}_2\text{S}$  in the dense inner part of its envelope ( $\leq 150$  AU, see table 7 of [Schöier et al., 2002](#)) can be reproduced within one order of magnitude only by the 0DS100LEDC case model in a range of time compatible with one derive by [Schöier et al. \(2002\)](#), between a few  $10^3$  and a few  $10^4$  years. This result would imply that IRAS 16293-2422 has formed in a parent cloud that would have collapsed at an age of approximately  $10^5$  years.

These results suggest that, following the results of the previous chapter, the NAUTILUS chemical model can reproduce observations of S-bearing molecules in  $\text{H}_2\text{S}$ -rich hot cores and in hot corinos using as initial abundance of sulphur its cosmic one. However it appears that work still has to be conducted regarding the high temperature network, especially for OCS,  $\text{H}_2\text{CS}$ , and CS.

### 3.3.2 1D static models

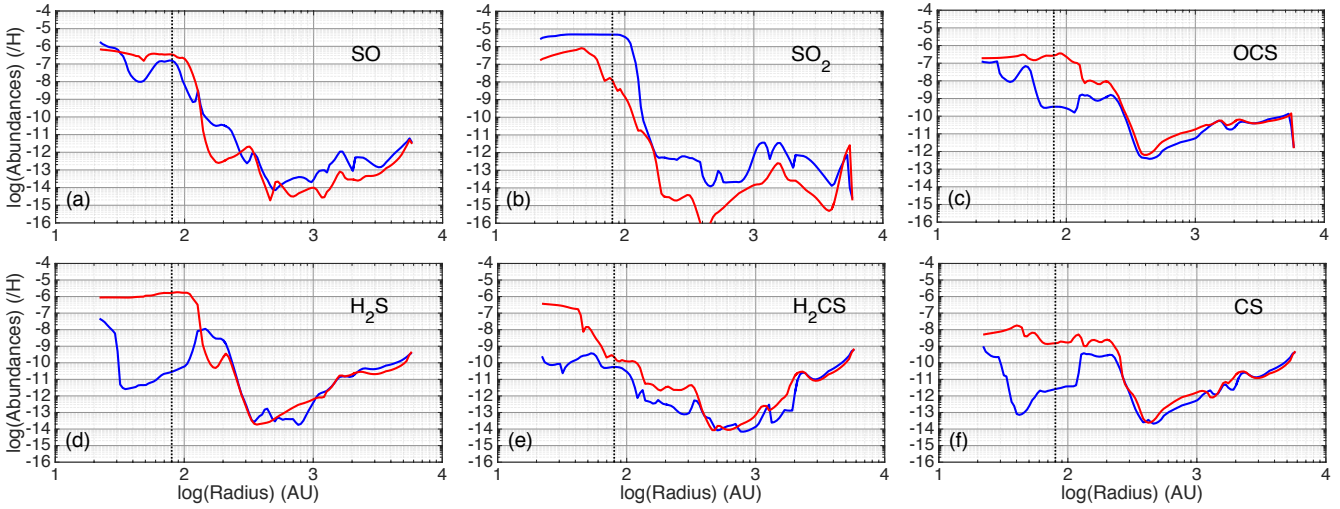


Figure 3.5: Abundances of SO,  $\text{SO}_2$ , and OCS (top panel) and  $\text{H}_2\text{S}$ ,  $\text{H}_2\text{CS}$ , and CS (bottom panel), relative to H as a function of the radius to the star IRAS 16293-2422 according to the 1D structure of [Crimier et al. \(2010\)](#), for the LDC (blue line) and EDC (red line) pre-collapse compositions. Both models were run for a period of  $3.5 \times 10^5$  years so the results would be comparable to those of the 0D dynamic models. The black dotted line represent the hot core spatial limit  $R_{\text{HCHC}} = 80$  AU,  $T > 100$  K.



In this section I study the results of the two 1D static models whose parameters are described in section 3.2.3.2 and table 3.3. The goal is to evaluate the impact of the pre-collapse chemical composition of the parent cloud on the computed abundances of the main S-bearing species SO, SO<sub>2</sub>, OCS, H<sub>2</sub>S, H<sub>2</sub>CS, and CS. Both LEDC and EDC models were run for a period of  $3.5 \times 10^5$  years so as to make the results comparable to those of the 0D dynamic models presented in section 3.3.3.

Figure 3.5 displays the abundances of each of these species for both 1DSLEDC (blue lines) and 1DSEDC (red lines) pre-collapse compositions. On the one hand, for a radius greater than 300 AU, which corresponds to the outermost and coldest ( $T < 50$  K) part of the envelope of the protostar, most considered species present only small local differences in their abundances between the LEDC and EDC cases, lower than one order of magnitude. Only SO and SO<sub>2</sub> presents significant differences that can go to more than two orders of magnitude (cf figure 3.5 (b)). This makes sense since, even at these cold temperatures, their gas phase chemistries are highly dependent on the abundance of reactive oxygen available in the gas phase, especially compared to the other species considered (see section 3.3.1).

On the other hand, in the inner part of the envelope ( $R < 300$  AU) where the temperature goes from 50 to 200 K (see right panel of figure 3.1), all species abundances show significative differences between the LEDC and EDC pre-collapse compositions. These differences can go from two to more than six orders of magnitude. Within the hot core limits (delimited by a black dotted line in figure 3.5 at  $R_{\text{HC}}^{\text{1D}} < 80$  AU,  $T > 100$  K), the species which are the most sensitive to the pre-collapse composition appear to be H<sub>2</sub>S, H<sub>2</sub>CS, and CS with differences of more than three orders of magnitude (cf figure 3.5 (d), (e) and (f), respectively). For H<sub>2</sub>S, these differences are explained by its dependance on the parent cloud evolution time. Indeed, in the EDC case, H<sub>2</sub>S in icy grains bulk is the second reservoirs of sulphur in the pre-collapse composition, containing 26% of the total amount of sulphur, whereas in the LEDC case, it only contains 5% (see table 3.2). Hence, in the inner part of the envelope and the hot core, where the temperature is high enough for H<sub>2</sub>S thermal desorption, its abundance is much higher in the EDC case. Moreover, figure 3.4 shows that in that case, H<sub>2</sub>S is not efficiently destroyed in the gas phase. Regarding H<sub>2</sub>CS, it efficiently forms at high temperature in the gas phase from CH<sub>3</sub> (via reaction (3.47)), which is much more abundant in the EDC case because of evaporated methanol and hydrocarbons accumulated on grain during the parent cloud evolution. Finally, in the EDC case, CS is not as efficiently destroyed in the gas phase as in the LEDC case (see figure 3.4) because of the low abundance of reactive oxygen (see table 3.4).

I can finally highlight that the 1D static models show that the pre-collapse composition of the parent cloud appears to be critical for the sulphur bearing species in hot core physical conditions. Indeed, we can see from figure 3.5 that a hot core that formed

from a young parent cloud will be poor in  $\text{H}_2\text{S}$  and rich in  $\text{SO}_2$ , whereas a hot core formed from a more evolved parent cloud would be rich in  $\text{H}_2\text{S}$  and  $\text{H}_2\text{CS}$ .

### 3.3.3 0D dynamic models

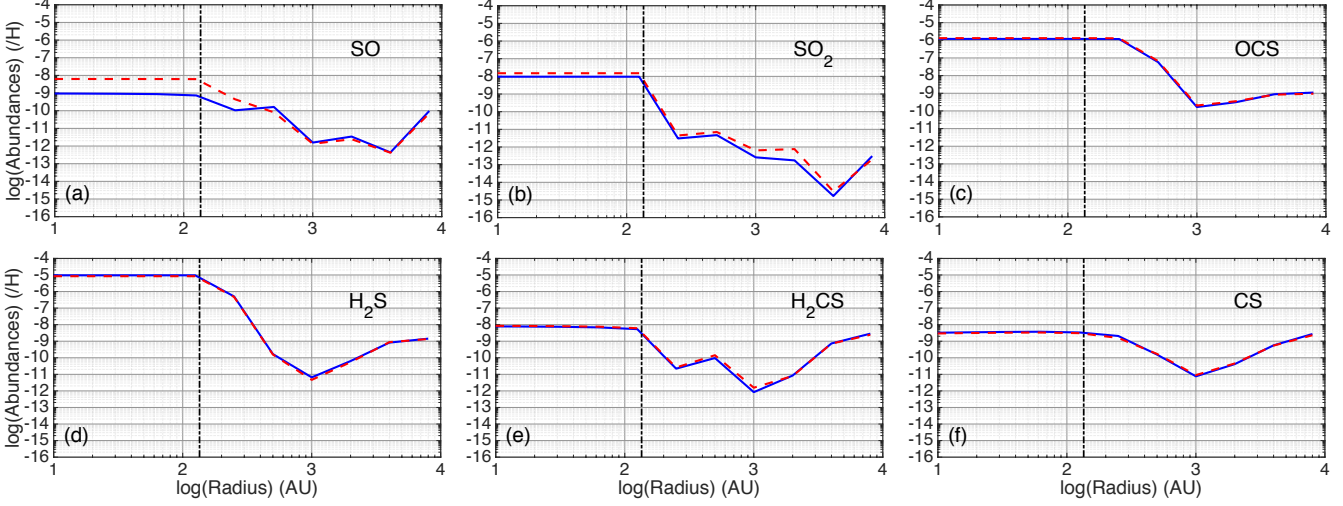


Figure 3.6: Abundances of SO,  $\text{SO}_2$ , and OCS (top panel) and  $\text{H}_2\text{S}$ ,  $\text{H}_2\text{CS}$ , and CS (bottom panel), relative to H as a function of the radius to the star IRAS 16293-2422 according to the modified structure of Aikawa et al. (2008), for the LDC (blue line) and EDC (red dashed line) pre-collapse compositions. The vertical black dashed line represents the hot core spatial limit  $R_{\text{HC}} = 135$  AU,  $T > 100$  K.

In this section, I carry out the same study as in the previous section but for the 0D dynamic models 0DDLDC and 0DDEDC described in section 3.2.3.3 and table 3.3.

Figure 3.6 is the same as figure 3.5 but for the 0D dynamic models. What strikes directly on this figure is that the pre-collapse chemical composition of the parent cloud appears to have little or no effect on the abundances of the considered S-bearing species. Only SO presents significant difference in the hot core (delimited by a vertical black dashed line in figure 3.6 at  $R_{\text{HC}} < 135$  AU,  $T > 100$  K), and even this difference is not of more than a factor seven (cf figure 3.6 (a)). A possible explanation of this lack of differences would be that the free-fall time considered in these models is long enough for both models to evolve towards the same chemical composition. Indeed, if the initial pre-collapse chemical composition has enough time to evolve in an environment cold enough for species not to evaporate, it will tend towards a state similar to the EDC case, *ie* with an evolved grains surface and bulk chemistry, notably with most of the sulphur transformed into HS,  $\text{H}_2\text{S}$ , and OCS on the grains. Hence, the hot core chemical composition of both 0DDLDC and 0DDEDC would be very similar.

Moreover, the global increase I made on the density profile of the model would tend to accelerate the chemistry and adsorption of species on the grains and therefore reduce the chemical timescale. I expect that by using the original model of [Aikawa et al. \(2008\)](#) I would get more differences and thus a more important impact of the pre-collapse chemical composition on the hot core chemistry.

### 3.4 DISCUSSIONS AND SUMMARY

#### 3.4.1 About the modification of the density profile of the dynamic model

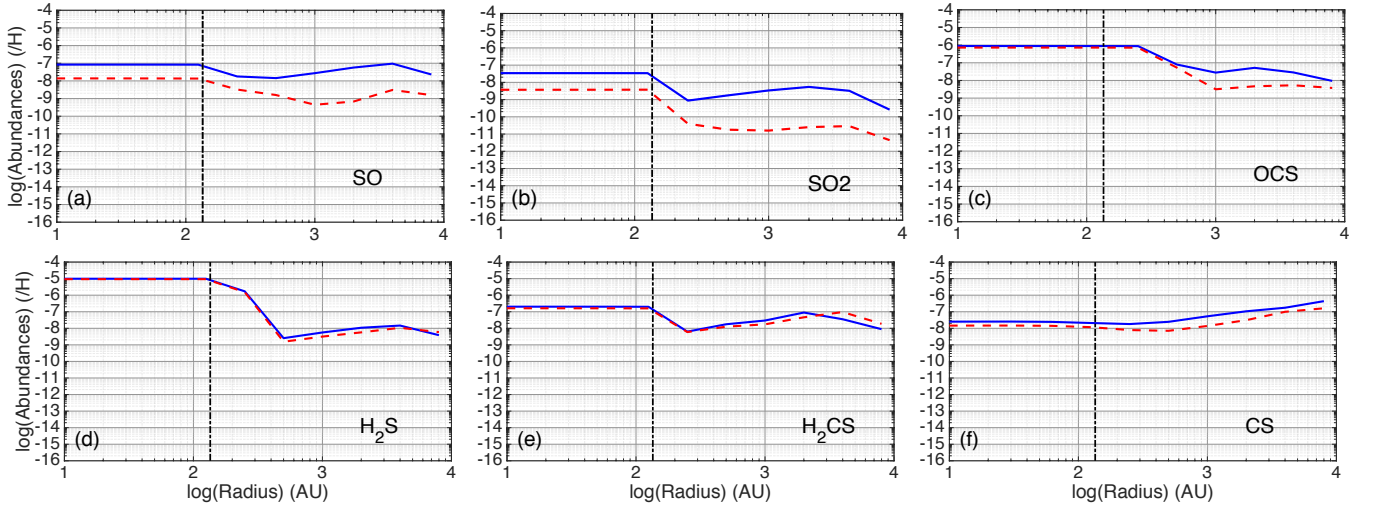


Figure 3.7: Abundances of SO, SO<sub>2</sub>, and OCS (top panel) and H<sub>2</sub>S, H<sub>2</sub>CS, and CS (bottom panel), relative to H as a function of the radius to the star IRAS 16293-2422 according to the original structure of [Aikawa et al. \(2008\)](#), for the LEDC (blue line) and EDC (red dashed line) pre-collapse compositions. The vertical black dashed line represents the hot core spatial limit  $R_{\text{HC}} = 135 \text{ AU}$ ,  $T > 100 \text{ K}$ .

In order to evaluate the impact of the modification of the density radial profile for the 0D dynamic model on sulphur chemistry, I ran 0DDLEDC and 0DDEDC cases, but using this time the original physical structure of [Aikawa et al. \(2008\)](#). Figure 3.7 is therefore the same as figure 3.6, but for the models ran with the original density profile of [Aikawa et al. \(2008\)](#). As expected, the results display larger differences between the LEDC and EDC pre-collapse compositions cases which can be explained by a slower chemistry due to lower densities. Moreover, as discussed in [Wakelam et al. \(2014\)](#), lower densities tend to decrease adsorption of species on grains (and consequently depletion), and therefore stimulates gas phase chemistry at low temperature, which explains why the abundances of the studied species are higher in the envelope in the original structure case. However the resulting abundances in the hot core do not

change drastically (at most a bit more than one order of magnitude) and are even the same for OCS and H<sub>2</sub>S (cf figure 3.7 (c) and (d), respectively). As discussed in section 3.3.3, this could be explained by a long free-fall time which would let the chemistry enough time for H<sub>2</sub>S and OCS to accumulate on the grains before thermal depletion in the hot core. More complete studies of the effect of density and free-fall time on the chemistry of a collapsing envelopes and hot cores appears to be needed in order to fully understand such comparisons.

### 3.4.2 About H<sub>2</sub>S and the initial abundance of sulphur

The present study was conducted under the light of the results of the previous chapter regarding sulphur reservoirs in dark clouds, namely that depending on the age of the cloud, the reservoirs of sulphur could either be atomic sulphur in the gas phase (LEDC case) or H<sub>2</sub>S and HS in icy grains bulk nearly equally sharing more than 51% of the total amount of sulphur (EDC case). Another result was that the NAUTILUS model could reproduce the S-bearing observations in the dark cloud TMC-1 using as initial abundance of sulphur its cosmic one, or three times depleted. Hence, throughout all this chapter I present results obtained using the cosmic abundance of sulphur of  $1.5 \times 10^{-5}$  (Jenkins, 2009). With this initial abundance of sulphur, the H<sub>2</sub>S abundances obtained in the hot core in the dynamic model with the modified as well as the original structure from Aikawa et al. (2008) is as high as  $10^{-5}$ . Such a high abundance of H<sub>2</sub>S is not consistent with the abundance derived from the observation of IRAS 16293-2422 ( $2.7 \times 10^{-7}$ , see Wakelam et al., 2004b).

On the one hand, to understand why the model overestimates the H<sub>2</sub>S abundance, I ran all the models presented in this paper with an initial abundance of  $5 \times 10^{-6}$ . It first should be noted that it only changes the presented results quantitatively, linearly diminishing the abundances of the studied species by approximately a factor three. Regarding H<sub>2</sub>S in the dynamical case, this initial depletion of sulphur allows an estimation of its abundance in the hot core slightly overestimated around  $3 \times 10^{-6}$ , but which could be considered in accordance with the observations (within a one order of magnitude margin).

On the other hand, the overestimation of H<sub>2</sub>S I find could be due to the efficient formation paths due to slowly evaporating CH<sub>2</sub>SH and CH<sub>3</sub>OH at 100 K studied in section 3.3.1 (reactions (3.42) and (3.43)). This is in contradiction with previous theoretical and laboratory studies that predict that in high temperature gas phase, the H<sub>2</sub>S evaporated from grain ices is preferentially destroyed to form SO and SO<sub>2</sub>, or molecules with two S atoms such as H<sub>2</sub>S<sub>2</sub> or HS<sub>2</sub> (Charnley, 1997; Wakelam et al., 2004a; Druard and Wakelam, 2012; Esplugues et al., 2014; Martín-Doménech et al., 2016). Hence, this result could be a hint to missing efficient destruction gas phase reactions in the H<sub>2</sub>S chemistry in the current network.

### 3.4.3 About the sensitivity to the type of model

Table 3.5: Comparison of the abundances obtained in the LEDC case for the 1D static and 0D dynamic models.  $a(b)$  stands for  $a \times 10^b$

Species	$[X]_{1DSLEDC}$	$[X]_{0DDLEDC}$
R = 50 AU (Hot core)		
SO	5.7(-8)	9.0(-10)
SO <sub>2</sub>	1.4(-5)	9.5(-9)
OCS	3.0(-7)	1.2(-6)
H <sub>2</sub> S	1.2(-11)	9.5(-6)
H <sub>2</sub> CS	7.4(-10)	7.6(-9)
CS	1.2(-12)	3.3(-9)
R = 500 AU (Envelope)		
SO	2.3(-14)	1.6(-10)
SO <sub>2</sub>	1.2(-13)	4.7(-12)
OCS	2.2(-12)	5.8(-8)
H <sub>2</sub> S	1.1(-13)	1.7(-10)
H <sub>2</sub> CS	2.7(-14)	1.4(-10)
CS	1.2(-13)	1.7(-10)

One goal of this study was to highlight the differences between static and dynamic model of hot core. In order to do so I used a 1D static model and a 0D dynamic model of IRAS 16293-2422. The results show that the 1D model favors a hot core sulphur chemistry dominated by SO<sub>2</sub> and SO in the LEDC case and H<sub>2</sub>S in the EDC case while the 0D dynamic model displays in both cases high abundances of H<sub>2</sub>S and OCS and low abundances of SO<sub>2</sub> and SO. Table 3.5 displays the abundances obtained for both types of models in the LEDC case, at 50 AU (in the hot core) and 500 AU (in the envelope). In the light of the difference in abundance that exists for a given species between the two type of models, one can easily conclude on the sensitivity to the type of model to use to compute the chemistry of a hot core and its collapsing envelope. Especially in the hot core, these differences can reach as much as six orders of magnitude, rendering critical the choice of the model used to compare results with possible observations or related works.

### 3.4.4 About the importance of the pre-collapse chemical composition

The observations of S-bearing species in hot cores are still a puzzling issue, since a large variety of sulphur compositions have been observed towards different hot cores and therefore no global trend has been found yet (see figure 5 of Woods et al., 2015, and the references therein). However, a given set of hot cores can present similar sulphur compositions (see for example Minh, 2016), which would suggest similar evolutionary stages. In this chapter, I investigated the importance of the pre-collapse chemical



composition on the hot core chemistry of S-bearing species. My results on 0D and 1D models (section 3.3.1 and 3.3.2) support that, given the fast evolution of sulphur chemistry in the parent cold clouds, the pre-collapse chemical composition is a critical parameter for hot core models. This could partially explain the absence of a global trend for sulphur compositions in observed hot cores from different parent clouds, as well as supports the fact that for parent clouds collapsing at similar ages and physical environments, hot cores can have similar sulphur compositions. However, the study of the dynamic model (section 3.3.3) raises the question of the role of the free-fall time on sulphur evolution, which would also explains similar composition for different hot cores, especially those where  $\text{H}_2\text{S}$  and  $\text{OCS}$  are found more abundant than the other species (see for example [Herpin et al., 2009](#)).

#### 3.4.5 Summary

In this chapter, I aimed to take a comprehensive look at the chemistry of sulphur in hot cores. In order to do so, I first conducted an extensive study with simple 0D models of the chemistry of the main S-bearing species observed towards hot cores, namely  $\text{SO}$ ,  $\text{SO}_2$ ,  $\text{OCS}$ ,  $\text{H}_2\text{S}$ ,  $\text{H}_2\text{CS}$ , and  $\text{CS}$ . Then I presented and compared the results from two types of models (1D static and 0D dynamic), in order to highlight the sensitivity of chemistry to the choice of model used in astrochemical studies, especially for hot cores.

First, my 0D extensive study highlighted five main results:

1. The total amount of reactive oxygen in the gas phase is critically depending on the pre-collapse composition of the hot core (cf table 3.4) as well as the hot core temperature;
2. Sulphur chemistry in hot and dense gas depends also highly on the pre-collapse composition, mainly because of its impact on reactive atomic oxygen, carbon and hydrogen, which all participate actively in most of the sulphur chemistry in such environment;
3. Sulphur chemistry in hot and dense gas depends highly on the temperature, partly because it is directly and indirectly linked with hydrocarbon evaporated from grain ices, and their main destruction products  $\text{CH}_2$  and  $\text{CH}_3$ ;
4. I found efficient paths of formation of gas phase  $\text{H}_2\text{S}$  that could be responsible for its overestimation in most of the hot core results. Studies of the gas phase chemistry of this species need to be continued to ensure the relevance of the network.
5. I found agreement between at least one of the models and observations in the hot core of Orion KL as well as the hot corino of IRAS 16293-2422. These results suggests that using as elemental abundance of sulphur the cosmic one, the NAUTILUS chemical model can not only reproduce dark clouds observations but can also reproduce hot cores and corinos observations.

Second, my study of the 1D static and 0D dynamic models led to the following conclusions:

1. The pre-collapse chemical composition of the parent cloud is a key parameter for 1D static models of sulphur chemistry in hot cores. Indeed, the computed abundances showed that it can imply differences up to six orders of magnitude for a given species in the hot core. However, the pre-collapse composition appears to only have a small impact on the chemical composition of the envelope. Finally the 1D model shows that a hot core that was formed from a young parent cloud will be poor in  $\text{H}_2\text{S}$  and rich in  $\text{SO}_2$ , while a hot core formed from a more evolved parent cloud would be rich in  $\text{H}_2\text{S}$  and  $\text{H}_2\text{CS}$ .
2. The 0D dynamic models conducted in this work revealed only small differences between the results of the less evolved and the evolved pre-collapse chemical composition, showing only a weak dependence of the hot core sulphur chemistry on the pre-collapse composition. Indeed, for both cases the model predicts high abundances of  $\text{H}_2\text{S}$  and  $\text{OCS}$  and low abundances of  $\text{SO}_2$  and  $\text{SO}$ . However, this result is thought to be due to the rather long free-fall time used in the model, which would let enough time for sulphur to be adsorbed on grains and to form mainly  $\text{H}_2\text{S}$  and  $\text{OCS}$  in the envelope before thermal depletion. It is expected that for a shorter free-fall time the differences between the two pre-collapse composition cases would be larger. Future work should focus on this importance of the free-fall time, since it could, along with the pre-collapse chemical composition, explain the large variety of abundances of S-bearing species observed in hot cores.

Finally, the comparison between the 1D static and 0D dynamic models displayed large differences on the computed abundances that can go as high as six orders of magnitude in the hot core. This result highlights the sensitivity to the choice of models in astrochemical study, especially when comparing results with observations, or with results from other papers.

Overall, the study presented in this chapter has raised the importance of investigating different physico-chemical conditions of formation of protostars using chemical modeling. Indeed, it appears that parameters such as hot core temperatures and pre-collapse chemical composition could be key elements to explain the variety of observed S-bearing species abundances values in hot core and corinos.

# 4 | CONSTRAINING THE INITIAL PHYSICAL PARAMETERS OF COLLAPSING PRESTELLAR CORES

## Contents

---

4.1	INTRODUCTION . . . . .	109
4.2	RHD CHEMICAL COLLAPSE MODELS OF LOW-MASS STAR FORMATION . . . . .	109
4.2.1	The database . . . . .	109
4.2.1.1	Bonnor-Ebert spheres . . . . .	110
4.2.1.2	The Lagrangian grid . . . . .	111
4.2.1.3	Initial setup of the collapse models . . . . .	113
4.2.2	Chemical modeling . . . . .	114
4.2.2.1	Selection of the reference dataset for chemical modeling . . . . .	114
4.2.2.2	Parameters of the chemical modeling . . . . .	115
4.3	POST-TREATMENT OF THE CHEMICAL OUTPUTS AND RESULTS . . . . .	116
4.3.1	Search for tracers of initial physical parameters of collapse . . . . .	116
4.3.1.1	Definition of the regions of study . . . . .	116
4.3.1.2	Correlations in the Hot Corinos Region . . . . .	119
4.3.2	Constraints on the envelope of Class 0 protostars . . . . .	126
4.3.2.1	Presentation of the method . . . . .	127
4.3.2.2	Results on the envelope of IRAS 16293-2422 . . . . .	129
4.3.2.3	Summary of the results on the source sample . . . . .	132
4.4	DISCUSSIONS AND SUMMARY . . . . .	139
4.4.1	About the modeling bias . . . . .	140
4.4.2	About the applicability of the method on the HCR dataset . . . . .	141
4.4.3	Summary . . . . .	142

---





## 4.1 INTRODUCTION

The work presented in this chapter was initially motivated by the recent release of a database of 143 radiation hydrodynamical (RHD) low-mass star formation models by [Vaytet and Haugbolle \(2017\)](#). Each model simulates the 1D collapse of a spherical prestellar core described by a given set of initial physical parameters, and stops shortly after the formation of the second Larson’s core (see section 1.2.2), when the collapse is believed to cease. Therefore, the outputs of a given model give for each cell of the initial grid and for each time step the corresponding 1D physical structure of the collapsing core. Hence, the application of a chemical model on these outputs would result in a large set of chemical data from which information can be retrieve thanks to statistical methods.

Therefore, the study presented hereafter is based on the idea of using statistical methods to derive useful information on the chemistry of low-mass star formation using the dataset of [Vaytet and Haugbolle \(2017\)](#) coupled with the NAUTILUS chemical model. More particularly, it aims to challenge the possibility of putting constraints on the initial parameters of collapse of low-mass star using chemical modeling. In the first section, I detail the dataset of [Vaytet and Haugbolle \(2017\)](#) and how I selected the data to be compatible with NAUTILUS, as well as the resulting chemical models. From this newly-formed chemical dataset, I highlight species that could be possible tracers of initial physical parameters of collapse (hereafter IPPC). Additionally, I developed a simple method to find constraints on the IPPC of observed low-mass Class 0 proto-stars. These results are presented in the second section. I will then discuss these results to finally conclude.

It should be noted that this part of my work is somewhat independent of the previous chapters, as it does not focus only on sulphur chemistry in star formation.

## 4.2 RHD CHEMICAL COLLAPSE MODELS OF LOW-MASS STAR FORMATION

### 4.2.1 The database

For this study I used the dataset of 1D low-mass star formation models from [Vaytet and Haugbolle \(2017\)](#). This database was developed in order to be used for astrochemical studies, and especially designed for statistical studies. It is composed of 143 models that follows the formation of a protostar (see section 1.2.2), from the initial isothermal collapse to the first hydrostatic core (FHSC, or first Larson’s core), and then to the second collapse and the formation of the second Larson’s core. Each of the models consider the initial parent core as a Bonnor-Ebert (BE) sphere ([Bonnor, 1956](#); [Ebert,](#)

1955), which is a common representation of an prestellar core. To solve the equation of RHD for each model, Vaytet and Haugbolle (2017) used a 1D fully implicit Godunov Lagrangian code. In the following, I will focus on the description of the initial setup of the BE sphere physical parameters as well as the Lagrangian grid used in the models and its interest for the chemical modeling. For more details on the RHD model I invite the reader to study its description in Vaytet et al. (2012) and Vaytet et al. (2013).

#### 4.2.1.1 Bonnor-Ebert spheres

A BE sphere is defined as a solution of the Emden equation of equilibrium between pressure and gravitational force within an isothermal prestellar core. Considering that the equation of state of the gas contained in the sphere is that of an ideal gas, the Emden equation can be written as:

$$\frac{1}{r^2} \frac{d}{dr} \left( \frac{r^2 d\rho}{\rho dr} \right) = -\frac{4\pi G}{c_s^2} \rho \quad (4.1)$$

where  $r$  is the radius and  $\rho$  the density of the sphere,  $G$  the gravitational constant, and  $c_s$  the isothermal sound speed. The BE solution of this differential equation consists in fixing the boundary conditions such as:

$$\rho(0) = \rho_c, \quad (4.2)$$

$$\left. \frac{d\rho}{dr} \right|_0 = 0, \quad (4.3)$$

$$P_0 = c_s^2 \rho(R_0) \quad (4.4)$$

where  $\rho_c$  is the density at the center of the sphere,  $P_0$  the external pressure of the core and  $R_0$  the outer radius of the sphere. The two first equations (4.2) and (4.3) can be interpreted as imposing a finite density  $\rho_c$ , as well as a continuous density gradient at the center of the sphere. The last equation (4.4) states that the core is bound by an external pressure  $P_0$  equal to the internal pressure of the core. This is equivalent to state that the outer radius of the sphere is the radius for which the internal density is equal to the outer density of the ambient gas.

By working on the BE sphere problem, one commonly defines the density contrast  $\gamma_D = \frac{\rho}{\rho_c}$  and the dimensionless radius  $\xi = \frac{r}{r_c}$ , where  $r_c$  is the characteristic radius defined as:

$$r_c = \frac{c_s}{\sqrt{4\pi G \rho_c}} \quad (4.5)$$

These variables allow the simplification of the Emden equation so that by setting the variable change  $u = \ln(\gamma_D)$  we get:

$$\frac{1}{\xi^2} \frac{d}{d\xi} \left( \xi^2 \frac{du}{d\xi} \right) = -e^u \quad (4.6)$$

Consequently, the boundary conditions (4.2) and (4.3) become:

$$u(0) = 0, \quad (4.7)$$

$$\left. \frac{du}{d\xi} \right|_0 = 0 \quad (4.8)$$

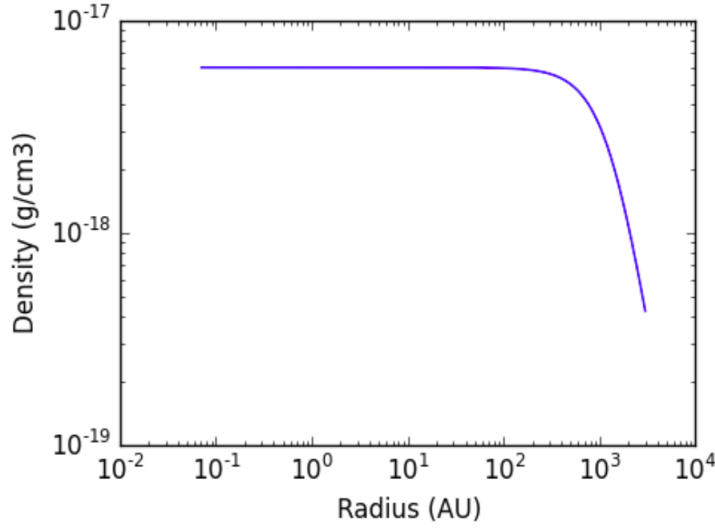


Figure 4.1: Example of a typical density profile of Bonnor-Ebert sphere.

Figure 4.1 displays an example of a typical initial density profile obtained with the BE solution. Regarding the temperature, since the Emden equation concerns only isothermal cores, the BE spheres are therefore isothermal. For each prestellar core of the dataset, once the physical parameters of the core fixed, the resulting density profile is used as inputs for the RHD model.

#### 4.2.1.2 The Lagrangian grid

In order to follow the evolution of the material within a given prestellar core during its collapse, the RHD model considers a one-dimensional Lagrangian mesh of 4096 cells, representing successive parcels of the core along its radius. Figure 4.2 displays for a given core a representation of the mesh used in the model and its evolution throughout the collapse. In the initial state ( $t = 0$ , top panel), the mesh is superimposed on the radius of the core. Hence the outer radius of the outermost cell is equal to the radius  $R_0$

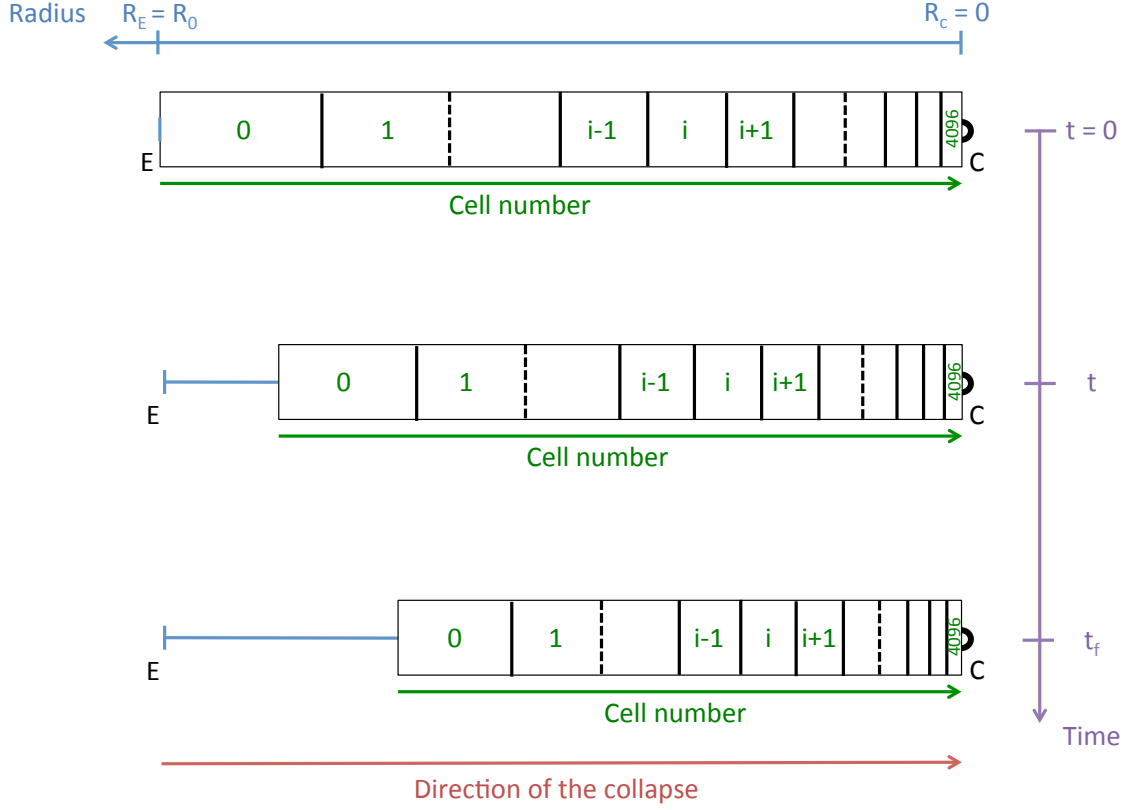


Figure 4.2: Representation of the one-dimensional Lagrangian grid used in the RHD models.

of the initial BE sphere, and the inner radius of the innermost cell is  $R_c = 0$ . Moreover, in order to obtain a higher resolution towards the center of collapse C (black cercle), the cell sizes are decreased progressively with decreasing radius such as:

$$\Delta R_i = (1 + \alpha) \Delta R_{i+1} \quad (4.9)$$

where  $\Delta R_i$  is the width of cell  $i$  and  $\alpha = 8 \times 10^{-4}$ . During the collapse ( $t$ , middle panel), the mesh moves toward the center of the core, each of the cells enclosing the mass of the parcel of material it was initially matched with, notably by decreasing in size. Indeed, since the mass of each cell stays constant during the collapse, their respective densities can increase only if their sizes decrease. In the following, I will therefore use the term "cell" to refer to its corresponding parcel of material.

The particular interest of using a Lagrangian mesh is that there are no mass exchanges between the cells. Regarding the chemical modeling, it means that the final chemical composition of each cell depends only on its initial chemical composition and

the evolution of its physical parameters. Therefore, 0D dynamic chemical models can be run independently for each of the cells. Hence, as the radius of a given cell is known at each time, the chemical modeling allows to trace the global evolution of the chemical composition of the prestellar core during its collapse.

In the following, I describe how the initial setups of the collapse models were chosen.

#### 4.2.1.3 Initial setup of the collapse models

For all models, the common used value for the density contrast is  $\gamma_D = 14.1$ , which is the maximal value to obtain an unstable sphere, and which corresponds to a dimensionless radius  $\xi = 6.45$ . In order to fully define the gas density of each initial BE sphere, fixed values for its temperature  $T_0$  and radius  $R_0$  were chosen. For these parameters, the central density and mass of the corresponding critical BE sphere, *ie* which defines a stable prestellar core, can be found via:

$$\rho_c = \left(\frac{\xi}{R_0}\right)^2 \frac{k_B T_0}{4\pi\mu m_H G} \quad (4.10)$$

$$M_{BE} = 2.4 \frac{c_s^2}{G} R_0 \quad (4.11)$$

where  $k_B$  is the Boltzmann's constant,  $\mu$  the mean atomic weight ( $=2.31$ ) and  $m_H$  the hydrogen atom mass. The initial core mass  $M_0$  is then chosen for the ratio  $\epsilon_M = \frac{M_{BE}}{M_0}$  to have values below 1, corresponding to a core that would undergo gravitational collapse. The central density of the core can now be expressed as:

$$\rho_c = 5.78 M_0 \left(\frac{4\pi}{3} R_0^3\right)^{-1} \quad (4.12)$$

And its corresponding free-fall time as:

$$t_{ff} = \sqrt{\frac{3\pi}{32G\rho_c}} \quad (4.13)$$

The initial parameter space (cf Fig. 1 of [Vaytet and Haugbolle \(2017\)](#)) was chosen for  $\epsilon_M$  to cover a wide range of values between 0 and 1 while using a set of different initial core masses, temperatures and radii, respectively ranging from 0.2 to 8  $M_\odot$ , 5 to 30 K and 3000 to 30000 AU. Such a wide parameter space allows to work with models covering a large diversity of prestellar cores in which low-mass protostars can form. The second column of table 4.1 (labelled "Original dataset") summarizes the range of values for each IPPC of interest in the present study. For the sake of clarity, it should

be noted that I include the free-fall time in the term "IPPC", even if it is not a physical parameters.

Table 4.1: Initial physical parameters ranges for the original dataset and the reference dataset for chemical modeling

IPPC	Original dataset	Reference dataset
$M_0$ ( $M_\odot$ )	[0.2 , 8]	[0.5 , 8]
$T_0$ (K)	[5 , 30]	[10 , 30]
$R_0$ (AU)	[3000 , 30000]	[3000 , 30000]
$\rho_0$ (part.cm <sup>-3</sup> )	[2.98×10 <sup>4</sup> , 1.20×10 <sup>8</sup> ]	[5.98×10 <sup>4</sup> , 1.20×10 <sup>8</sup> ]
$t_{\text{ff}}$ (kyrs)	[4.31 , 272.83]	[4.31 , 192.92]

The initial RHD parameters are set such as:

- The radiation temperature is initially in equilibrium with the gas temperature;
- The radiative flux is set to zero everywhere;
- At the center of the grid, the boundary conditions are reflexive;
- At the edge of the sphere, the hydrodynamical variables have a null gradient boundary condition, and the radiative variables are set to their initial values inside the ghost cell, which is a virtual cell outside the core representing its direct vicinity.

These values have been chosen so that the numerical RHD computations could converge, and that the vicinity of the core does not affect its evolution during the collapse.

## 4.2.2 Chemical modeling

### 4.2.2.1 Selection of the reference dataset for chemical modeling

The outputs dataset gives the physical parameters of the 4096 cells of the Lagrangian grid at every time step of the RHD models. Given the NAUTILUS temperature validity domain ([10 K - 800 K]), I first had to rule out the models with an initial temperature  $T_0 < 10$  K. With this first selection, 110 models out of 143 are useable for the chemical model application. For each remaining model, and in order to respect the maximal temperature limit, I then ruled out all the cells which temperatures rise above 800 K during the collapse. Finally, for the computing time of NAUTILUS to be acceptable, I selected a number of 16 cells per RHD model that I chose to be equally spaced between the outermost cell of the grid and the last inner cell which temperatures stay below 800 K. As such the reference dataset for chemical modeling includes 110 RHD models,

each of them comprising 16 cells.

In the third column of table 4.1 (labeled "Reference dataset") are displayed the resulting ranges for the studied IPPC. By comparing them with those of the original dataset, we can see that the selection process has only a small impact on the ranges of the IPPC. Indeed, with the exception of the obvious difference of ranges for  $T_0$  between the two datasets, the differences of range for  $\rho_0$  and  $t_{\text{ff}}$  are due to only two models (#113 and #132) that are ruled out because of their initial temperatures. Hence, the reference dataset still accounts for a significant range of possible IPPC. A table summarizing the models of the reference dataset and their IPPC of interest can be found in appendix B.

#### 4.2.2.2 Parameters of the chemical modeling

After the selection of a reference dataset suitable for the application of the NAUTILUS chemical model, the idea is now to run for each cell of the selected prestellar cores a 0D dynamic chemical model while separately saving its radius at each time step.

As dark clouds are believed to evolve during a period of time which is not negligible for the chemistry before they can become gravitationally unstable (see section 1.2.1), I first had to consider the chemical evolution of each prestellar core before its collapse to obtain chemical inputs data for the corresponding chemical model. To that effect, a standard 0D model of a dark cloud was run for each of the 110 selected prestellar cores, using as temperature their respective initial temperatures  $T_0$  and as proton total density the initial external density of the collapsing core ( $n_H = \rho_0$ ). The choice to use the initial external density and not the central density can be justified by the fact that, given the selection of cells explained in the previous section, most of the selected cells have a initial density closer to the external density of their respective prestellar cores. Moreover, all the initial BE sphere density profiles used show a difference between central and external density of at most one order of magnitude (cf figure 4.1), which also justifies to suppose an uniform density for the dark cloud runs.

Other parameters of interest for the chemical modeling such as visual extinction and cosmic ionization rate were set to their commonly used values for dark cloud models, respectively 15 mag and  $1.3 \times 10^{-17}$ . The same set of initial abundances (see table 3.1) and network as the previous chapter were used for all dark cloud models. The resulting models were run for  $10^6$  years, and their computed chemical compositions used as inputs for the 0D dynamic chemical modeling of the corresponding cells of collapsing prestellar cores. It should be noted that I use the same formalism of  $\text{H}_2$  *ad hoc* formation than introduced in section 3.2.1 for the collapsing core runs, since some of the selected cells obviously evolve in high temperature regimes.



### 4.3 POST-TREATMENT OF THE CHEMICAL OUTPUTS AND RESULTS

In the following, I treat all the selected cells independently from each other. Hence, the outputs of the chemical modeling of the collapsing prestellar cores describe for each of the  $110 \times 16 = 1760$  cells and each time step the abundances of the species included in the chemical network. Moreover, because most of the youngest low-mass stellar objects studied in the literature are Class 0 protostars, and because I want my results to be applicable to real case studies, I focus my study of these outputs on the final time step of the chemical models, when both Larson's cores are formed, and the object is therefore a Class 0 protostar.

#### 4.3.1 Search for tracers of initial physical parameters of collapse

The initial idea of this study is to search for possible species that could trace the IPPC. In order to do so, I first wanted to study the correlation between the abundance distribution of each species at final time (when the protostar is formed) and the IPPC  $M_0$ ,  $T_0$ ,  $R_0$ ,  $\rho_0$  and  $t_{\text{ff}}$ .

Figure 4.3 displays as an example the distribution of the abundances of gaseous water ( $\text{H}_2\text{O}$ ) as a function of the initial densities. As such, a quick look at the figure shows that the expected correlations would be very low. However, I can expect to find interesting correlations by studying separately the two groups of cells (yellow and blue) that seem to appear. In order to do so, a better understanding of this clear separation of the cells is needed.

##### 4.3.1.1 Definition of the regions of study

When the abundances of  $\text{H}_2\text{O}$  are plotted with respect to their corresponding final temperatures (cf figure 4.3), it appears that the jump in abundances between  $10^{-8}$  and  $10^{-4}$  is linked to the temperature of the cells, and three temperature intervals that can be chemically explained appear:

1. The first interval between 10 and approximately 100 K (blue dots in figure 4.3) corresponds to cells within a temperature regime where water molecules are scarce in the gas phase because most of them are adsorbed on grains surface, and the temperature is not high enough for them to thermally desorb,
2. The second interval between 100 and 145 K (green dots in figure 4.3) corresponds to cells where water molecules on the grains surface have begun to desorb in the gas phase, but the physical conditions are such that it prevents complete water desorption,

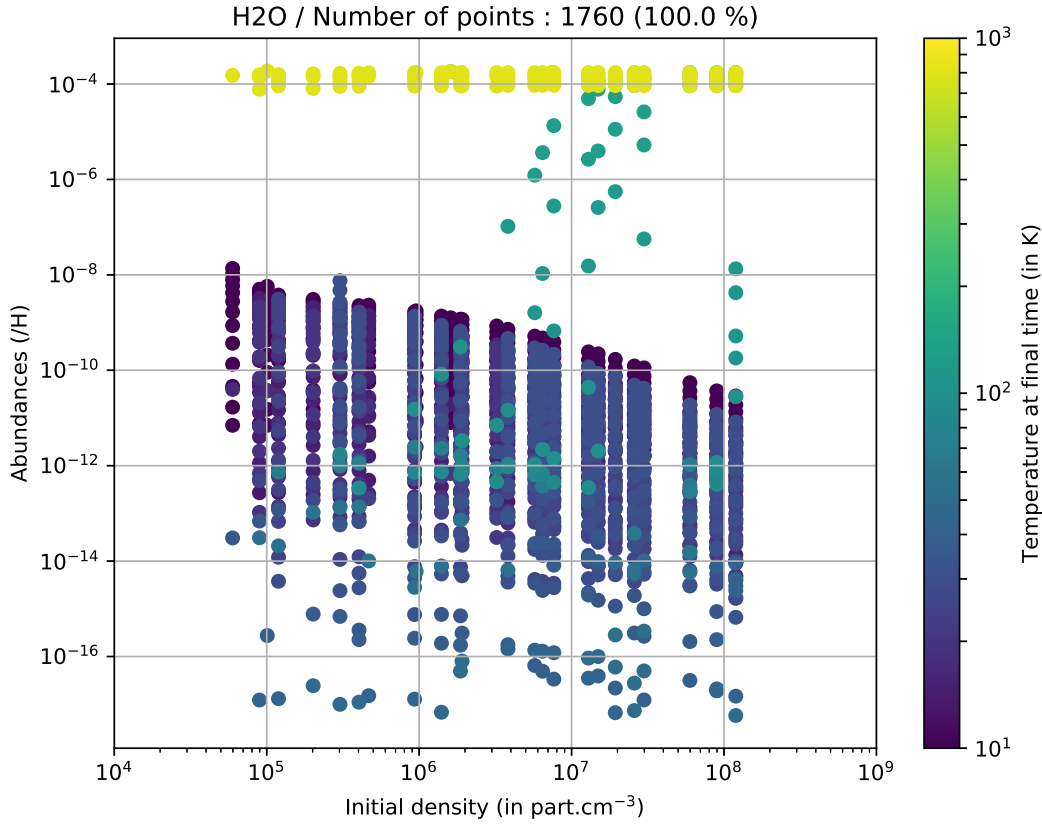


Figure 4.3: Distribution of the abundances of  $\text{H}_2\text{O}$  relative to  $\text{H}$  at the final time of the collapse as a function of the initial densities of the collapsing prestellar cores. The color coding represents the final temperatures of the cells.

3. The third interval for temperatures above 145 K (yellow dots in figure 4.3) corresponds to cells which have stayed in a high temperature regime ( $> 100$  K) long enough for all the water to desorb in the gas phase and reach its hot corino common abundance of approximately  $10^{-4}$ .

In order to better visualize these temperature intervals, I plot in figure 4.4 the abundance of water for all cells as a function of their final temperatures and radii. Here the temperature intervals appear clearly as expected. Furthermore, supplementary information brought by the radii allow to confirm that cells within the first temperature interval are located in the outer part of the cores (further than a few tenths of AU), *ie* their envelopes, while cells within the two remaining intervals are located in the inner part of the cores, *ie* their hot corinos. I can thus define regions corresponding to each temperature range:

1. An Envelopes Region (ER), which corresponds to the temperature interval of 10 to 100 K and contains 1590 cells,

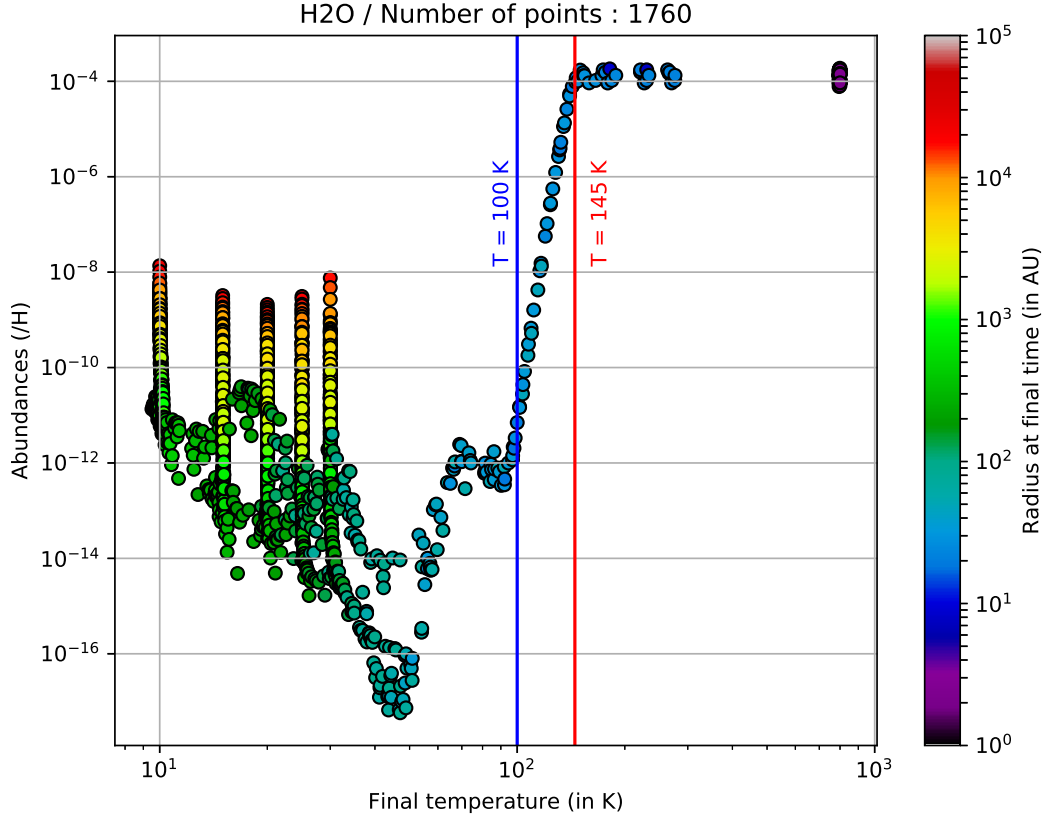


Figure 4.4: Distribution of the abundances of  $\text{H}_2\text{O}$  relative to  $\text{H}$  at the final time of the collapse as a function of the final temperatures. The color coding represents the final radii of the cells. The blue and red vertical bars delimit the three temperature intervals defined above.

2. A Transitional Region (TR), which corresponds to the temperature interval of 100 to 145 K and contains 33 cells,
3. A Hot Corinos Region (HCR), which corresponds to the temperature interval above 145 K and contains 137 cells.

It should be noted that the separation of the cells regarding final temperatures studied here for water is common to most of the species of the chemical network. However, for the remaining species, the defined temperature intervals will not necessarily fit their abundance distributions. Indeed, TPD experiments on more volatile species ( $E_D < E_D^{\text{H}_2\text{O}}$ ) show that they begin to desorb in the gas phase before water, but have their main desorption peak at the water desorption temperature (see [Fayolle et al., 2011](#); [Ruaud et al., 2016](#)). Plus, more refractory species ( $E_D > E_D^{\text{H}_2\text{O}}$ ) partly co-desorb with water, but are expected to desorb mainly at temperature higher than water (see for example [Chaabouni et al., 2018](#)). However, as the defined intervals would be consistent in first approximation with more volatile species, and because more refractory species only account for less than 15% of the total number of species in the chemical

network, I choose to apply the region differentiation as defined above to all species regardless of their desorption energies. For the following correlation study, I decide to ignore the 33 points from the TR because they represent less than 2% of the total number of cells. Hence, the resulting loss of information is negligible.

I then study the correlations between species abundances and IPPC using the Spearman's correlation coefficient ( $\rho_S$ ). It assesses how well the relationship between two variables can be described using a monotonic function. Hence, it is more suitable to this study than the commonly used Pearson's coefficient, which evaluates the linear relationship between two variables. Indeed, at the sight of the corresponding figures (see for example figure 4.3), I do not expect to often find linear relationship between the abundance of a given species and the IPPC. Finally I restrain my study to observed or observable species, since the aim of my study is to find possible tracers of IPPC.

In the ER, the results of correlations are inconclusive since the majority of the resulting correlation coefficients are too low ( $< 0.2$  in absolute value) or concern unobservable species. Hence I only present here my correlation results for the HCR.

#### 4.3.1.2 Correlations in the Hot Corinos Region

Table 4.2: Summary of the calculated Spearman's coefficients between the abundances at final time of the 482 gaseous species of the chemical network and the IPPC.

Initial physical parameters	$ \rho_S _{max}$	Number of species with $ \rho_S  > 0.6$
$M_0$	0.389	0
$T_0$	0.978	137
$R_0$	0.909	88
$\rho_0$	0.983	117
$t_{ff}$	0.983	117

Table 4.2 summarizes the calculated Spearman's coefficient (for a extensive description, see appendix C). In the HCR, it appears that numerous correlations can be found between species abundances and IPPC, except for  $M_0$  for which I find only low Spearman coefficients ( $< 0.4$  in absolute value).

Among the species linked with one of the IPPC ( $|\rho_S| > 0.6$ ), 11 are detected toward the well studied Class 0 protostar IRAS 16293-2422. Here I present the results of the correlation for 4 of these species, for which the abundances of the HCR cells spread over more than 3 orders of magnitude:  $\text{CH}_3\text{CN}$ ,  $\text{H}_2\text{CS}$ , NS and OCS. For the other species for which the abundances spread over a smaller range of values, the results would be difficult to compare with observations. In that case, the variation of abun-

dances would indeed not be significant enough for the corresponding species to be clear tracers, especially given the common uncertainties on observed abundances.

Figures 4.5, 4.6, 4.7 and 4.8 display the respective abundances of the 4 selected species as a function of their respective best correlated IPPC. Note that  $\text{H}_2\text{CS}$  is best correlated with the free-fall time and the density of the collapsing cores, when  $\text{CH}_3\text{CN}$ , NS and OCS are best correlated with the initial temperature. Here I try to understand how these correlations can be explained with chemistry.

#### 4.3.1.2.1 $\text{CH}_3\text{CN}$

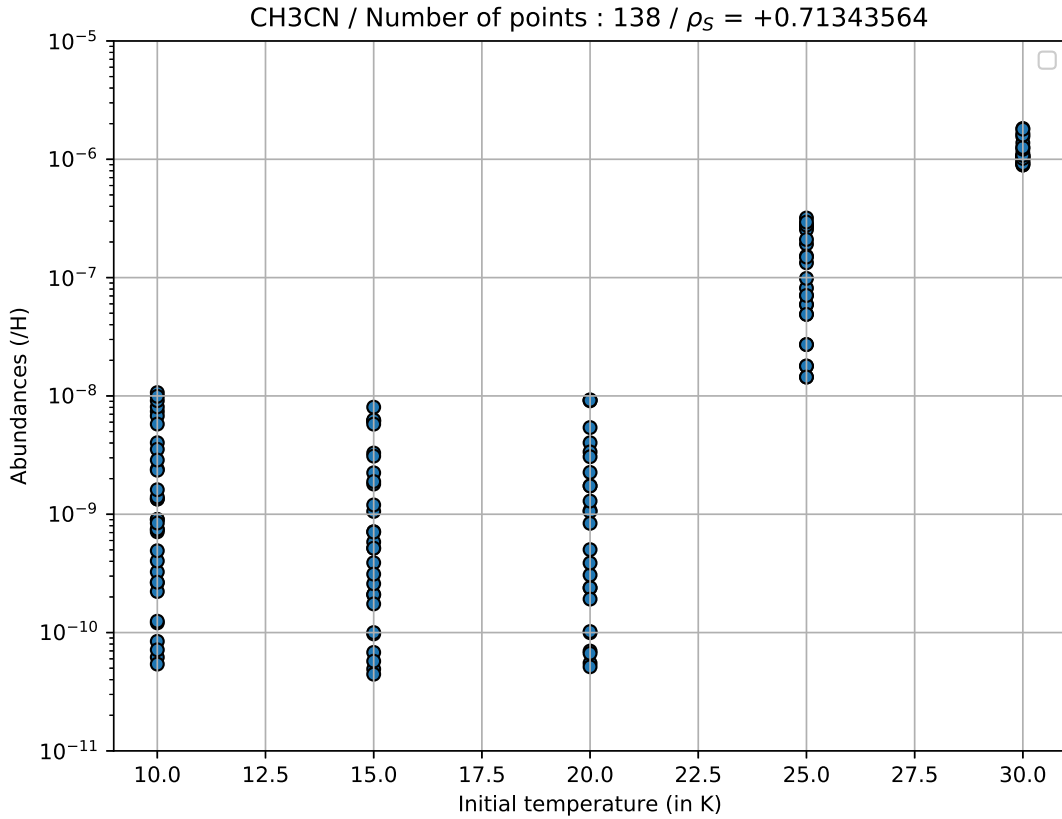


Figure 4.5: Distribution of the abundances of  $\text{CH}_3\text{CN}$  relative to H at the final time of the collapse as a function of the initial temperature.

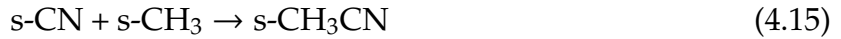
Figure 4.5 shows that the abundance of acetonitrile ( $\text{CH}_3\text{CN}$ ) in the HCR is positively correlated with the initial temperature of the collapsing prestellar cores with a Spearman's coefficient of 0.713. This means that the more  $\text{CH}_3\text{CN}$  is abundant in a hot corino, the higher the initial temperature of its parent core is. More precisely, an observer that would detect  $\text{CH}_3\text{CN}$  in a hot corino with an observed abundance  $[\text{CH}_3\text{CN}]_{\text{obs}}$  could interpret this correlation such as:

- If  $[CH_3CN]_{\text{obs}} \leq 10^{-8}$ , then the initial temperature of the parent core of the hot corino would be  $T_0 \leq 20$  K,
- If  $10^{-8} \leq [CH_3CN]_{\text{obs}} < 10^{-6}$ , then the initial temperature would be around 25 K,
- If  $[CH_3CN]_{\text{obs}} \geq 10^{-6}$ , then the initial temperature would be  $T_0 \geq 30$  K.

Indeed, in the chemical model,  $CH_3CN$  is known to efficiently form on the grains surface during the dark cloud lifetime (see Andron et al., submitted to MNRAS) through the hydrogenation of adsorbed  $H_2CCN$ , the latter being preferentially formed in the gas phase following:



At the end of the initial cloud runs,  $CH_3CN$  abundance reaches higher values when the temperature of the cloud is higher. This increase can go up to 2 orders of magnitude in the interval of initial temperatures considered, which would explain the shape of the abundances distribution of  $CH_3CN$  seen on figure 4.4, and the resulting correlation. This appears to be due to photodissociation by CR induced UV photons of HCN and  $CH_3OH$  the grains surface, which is efficient for all initial temperatures and forms respectively CN and  $CH_3$ . Since the diffusivity of the molecules in grain ices increases with temperature, the CN and  $CH_3$  thus produced can efficiently diffuse on the grains surface at higher temperature, resulting in the increase in  $CH_3CN$  abundance via the grains surface reaction:



Afterwards during the collapse,  $CH_3CN$  thermally desorbs in the gas phase where its abundance remains stable because its main destruction reaction is:



and its product  $CH_3CNH^+$  forms  $CH_3CN$  again via electronic recombination.

#### 4.3.1.2.2 $H_2CS$

Figure 4.6 shows that the abundance of thioformaldehyde ( $H_2CS$ ) in the HCR is positively correlated with the free-fall time with a Spearman's coefficient of 0.633 (left panel), as well as anti-correlated with the initial density with a Spearman's coefficient of -0.630 (right panel). In order to understand these correlations and their corresponding abundance distributions, one must first realize that free-fall time and initial density

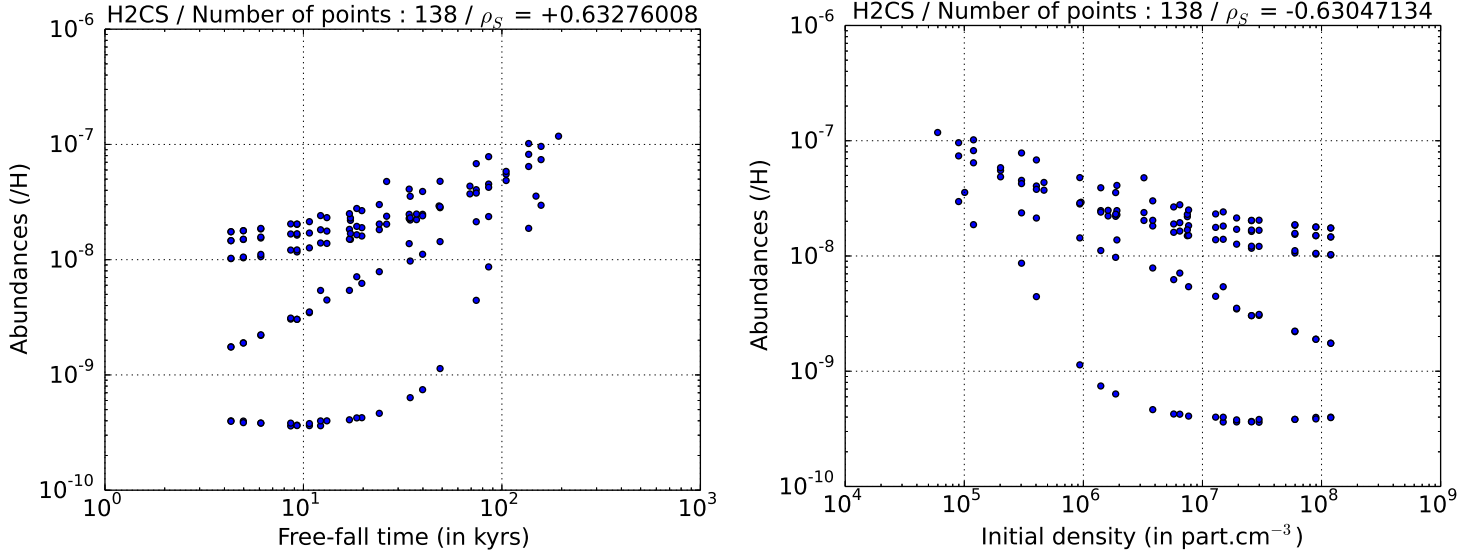


Figure 4.6: Distribution of the abundances of  $\text{H}_2\text{CS}$  relative to  $\text{H}$  at the final time of the collapse as a function of the free-fall time (left panel) and the initial density (right panel).

are perfectly anti-correlated because of equation (4.13). Hence, parent prestellar cores with a low initial density have long free-fall time and conversely, those with a high initial density have short free-fall time. This explains why the distributions in figure 4.6 appears as the mirror of each other, as well as why the Spearman's coefficient are nearly equal in absolute value. Hence, given an observed abundance  $[\text{H}_2\text{CS}]_{\text{obs}}$  in a hot corino, an observer could interpret this correlation such as:

- If  $[\text{H}_2\text{CS}]_{\text{obs}}$  is close to  $10^{-7}$ , then the free-fall time of the parent core of the hot corino would be rather long, around  $10^2$  kyrs. Respectively, the initial density would be around  $10^5 \text{ part.cm}^{-3}$ ,
- If  $[\text{H}_2\text{CS}]_{\text{obs}} < 10^{-9}$ , then the free-fall time would be rather short, below 50 kyrs. Respectively, the initial density would be above  $10^6 \text{ part.cm}^{-3}$

I find that in parent dark clouds with high density,  $\text{H}_2\text{CS}$  forms rapidly on the grains surface through hydrogenation of  $\text{HCS}$ , but is ultimately hydrogenated in either  $\text{CH}_2\text{SH}$  or  $\text{CH}_3\text{S}$  (see section 3.3.1.2). In low density clouds however,  $\text{H}_2\text{CS}$  is formed much slower on grains surface, which prevents its efficient hydrogenation. Hence at the end of the initial cloud runs, the differences in  $\text{H}_2\text{CS}$  abundances between a slow and a fast collapsing parent core can reach up to 2 orders of magnitude. These differences can afterwards variate during the collapse, since fast collapsing cells will reach high temperatures faster than slow collapsing cells. Indeed, once thermally desorbed in the gas phase at high temperatures,  $\text{H}_2\text{CS}$  abundance can endure significant variations (see section 3.3.1.2), which could explain the range of abundances that

corresponds to fast collapsing cells ( $t_{\text{ff}} < 50$  kyrs) in figure 4.6. For slow collapsing cells,  $\text{H}_2\text{CS}$  can continue to form on grains surface at low density before its thermal desorption. At that time however, the reactants of its main formation and destruction reactions at high temperature regime, such as atomic sulphur and  $\text{CH}_3$ , are scarce in the gas phase, which could explain the smaller range of abundances for slow collapsing cells ( $t_{\text{ff}} > 50$  kyrs).

#### 4.3.1.2.3 NS

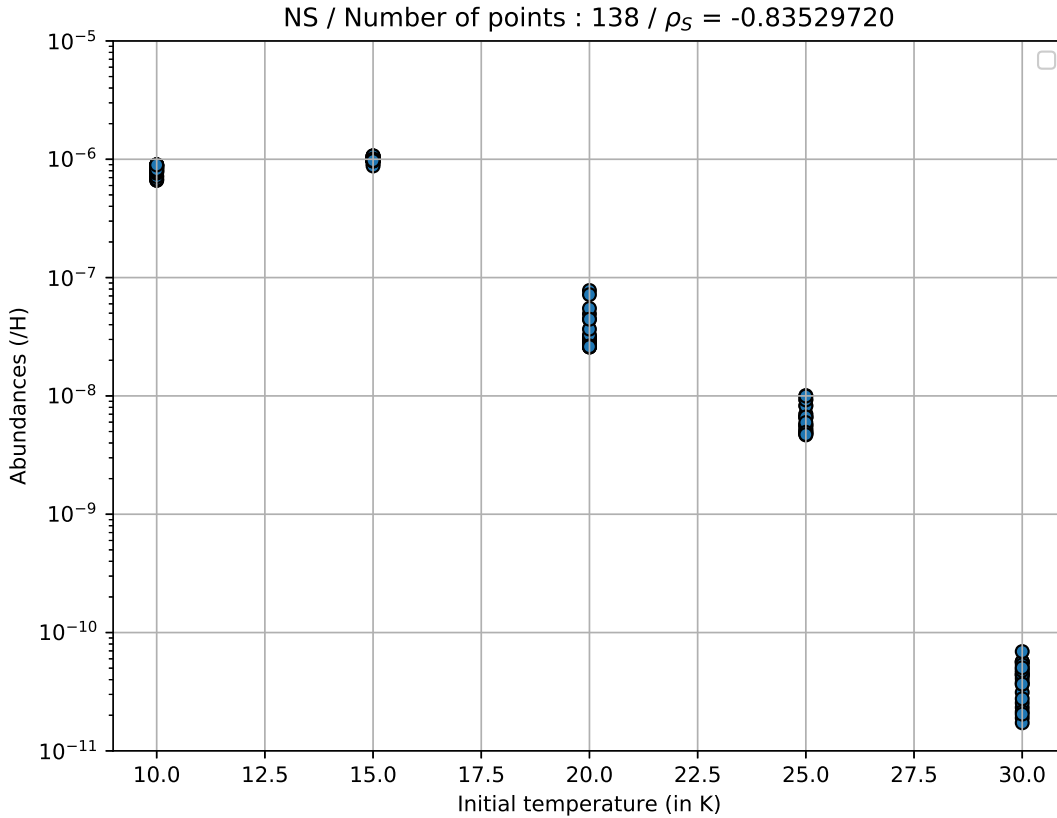


Figure 4.7: Distribution of the abundances of NS relative to H at the final time of the collapse as a function of the initial temperature.

Figure 4.7 displays the abundance distribution in the HCR of mononitrogen monosulfide (NS) and its good anti-correlation with the initial temperature of the collapsing prestellar cores with a Spearman's coefficient of -0.835. The corresponding Pearson's correlation coefficient is even lower (-0.843), which implies a nearly linear relationship between this two set of parameters. As such, this relationship defines NS as a precise tracer of the initial temperature of parent cores. Hence, for an observed value of NS in a hot corino  $[\text{NS}]_{\text{obs}}$ , one could deduce the following:

- If  $[\text{NS}]_{\text{obs}}$  is close to  $10^{-6}$ , then the initial temperature of the parent core of the hot



corino would be  $T_0 \leq 15$  K,

- If  $10^{-8} < [NS]_{\text{obs}} \leq 10^{-7}$ , then the initial temperature would be around 20 K,
- If  $10^{-9} < [NS]_{\text{obs}} \leq 10^{-8}$ , then the initial temperature would be around 25 K,
- If  $[NS]_{\text{obs}} < 10^{-10}$ , then the initial temperature would be  $T_0 \geq 30$  K.

Indeed, in the chemical model, NS is at first efficiently formed in the initial cloud runs on the grains surface from the main reservoir of sulphur HS (see section 2.3.3) via:



This reaction is efficient in all the initial runs, regardless of the initial temperature, and the NS formed on the surfaces tends to sink in the grains bulk. However, it appears that the higher the temperature of the cloud, the more atomic oxygen can diffuse in the grains bulk. This has for main effect to destroy NS in the bulk via:



This destruction of NS is therefore more efficient at high temperatures, which results in a difference between its abundance in initial clouds at 10 K and 30 K that can go up to four orders of magnitude. Moreover, once NS thermally desorbs in the hot gas, it is consumed by the following reaction:



Where the  $\text{CH}_2$  comes from gas phase photodissociation by secondary UV photons of  $\text{CH}_4$ , which itself forms from the  $\text{CH}_3$  produced by the destruction of thermally desorbed methanol ( $\text{CH}_3\text{OH}$ ) and methyl formate ( $\text{HCOOCH}_3$ ). This reaction is believed to be more efficient for cells that spend more time in a high temperature regime, which explains why those coming from parent cores with  $T_0 = 30$  K have such a low NS abundances compared to those coming from parents cores with  $T_0 = 10$  K.

However, this result should be taken with caution since work still has to be done to complete the NS chemical network, as discussed in Vidal et al. (2017).

#### 4.3.1.2.4 OCS

Figure 4.8 displays the abundances distribution in the HCR of carbonyl sulfide (OCS), which is similar to the NS one. Indeed, as for NS, OCS abundances in the HCR are well anti-correlated with the initial temperature of the collapsing prestellar cores, with a Spearman's coefficient of -0.869. Hence, OCS appears to be a very good tracer

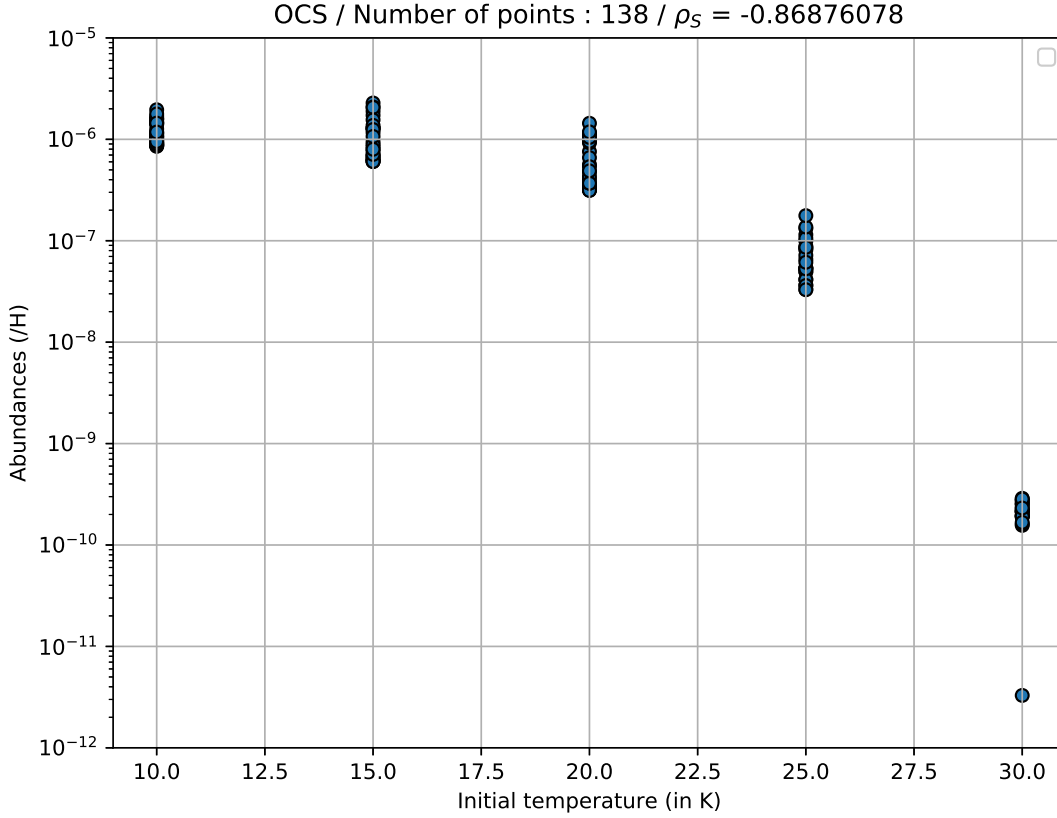


Figure 4.8: Distribution of the abundances of OCS relative to H at the final time of the collapse as a function of the initial temperatures.

of the initial temperature. For an observed value of OCS in a hot corino  $[OCS]_{\text{obs}}$ , one could deduce the following:

- If  $[OCS]_{\text{obs}}$  is close to  $10^{-6}$ , then the initial temperature of the parent core of the hot corino would be  $T_0 \leq 20$  K,
- If  $[OCS]_{\text{obs}}$  is close to  $10^{-7}$ , then the initial temperature would be around 25 K,
- If  $[OCS]_{\text{obs}} < 10^{-9}$ , then the initial temperature would be  $T_0 \geq 30$  K.

It should be noted that this characterization is less precise than the one deduced from NS correlation, however I am much more confident in the completeness of the OCS chemical network than in the NS one, and therefore more confident about OCS correlation results.

From a chemical point of view, as for the previous species, the difference in OCS abundance as a function of the initial temperature can be explained with the chemistry of the initial cloud runs. Indeed, in all of them OCS is at first mainly produced in the gas phase via:



It is also produced on the grains surface via:



However, the higher the temperature of the initial cloud is, the less OCS is formed on the grains surface. Indeed, at low temperature, reaction (4.21) stays efficient until the end of the parent cloud model because CO remains abundant on the grains surface. When the temperature rises however, the surface OH originated from the photodissociation by CR induced UV photons of water and methanol, which are both abundant on the grains surface, seems to efficiently consume the remaining CO through:



This reaction is believed to become efficient at high temperatures because of the increase diffusivity of OH on grains surface. Indeed, this mechanism causes differences between OCS abundances in initial clouds at 10 K and 30 K that can go up to five orders of magnitude, which would explain the corresponding correlation plot in figure 4.8. After thermal depletion during the collapse, as seen in section 3.3.1.2, OCS abundance in the gas phase should not vary more than one order of magnitude.

In the following section, I present the main part of my work, which focuses on the ER dataset. Indeed, because the correlations between species abundances and IPPC in this region are not conclusive, I decided to exploit this part of the dataset in another way. Hence, I developed a simple method to efficiently constrain the IPPC from observations of Class 0 protostar envelopes.

### 4.3.2 Constraints on the envelope of Class 0 protostars

As aforementioned, this section presents the main part of my work on the collapsing prestellar cores dataset. After concluded that no interesting correlations would be found with the ER data, I decided to try and simply compare them to sets of abundances observed in various Class 0 protostars envelopes, with the aim to find possible constraints on their respective IPPC. In the following, I first describe the method and the observational dataset, then continue on the presentation of a comprehensive example of the application of the method to the envelope of IRAS 16293-2422. Finally, I present the summary of the method applied to a sample of 12 sources.

## 4.3.2.1 Presentation of the method

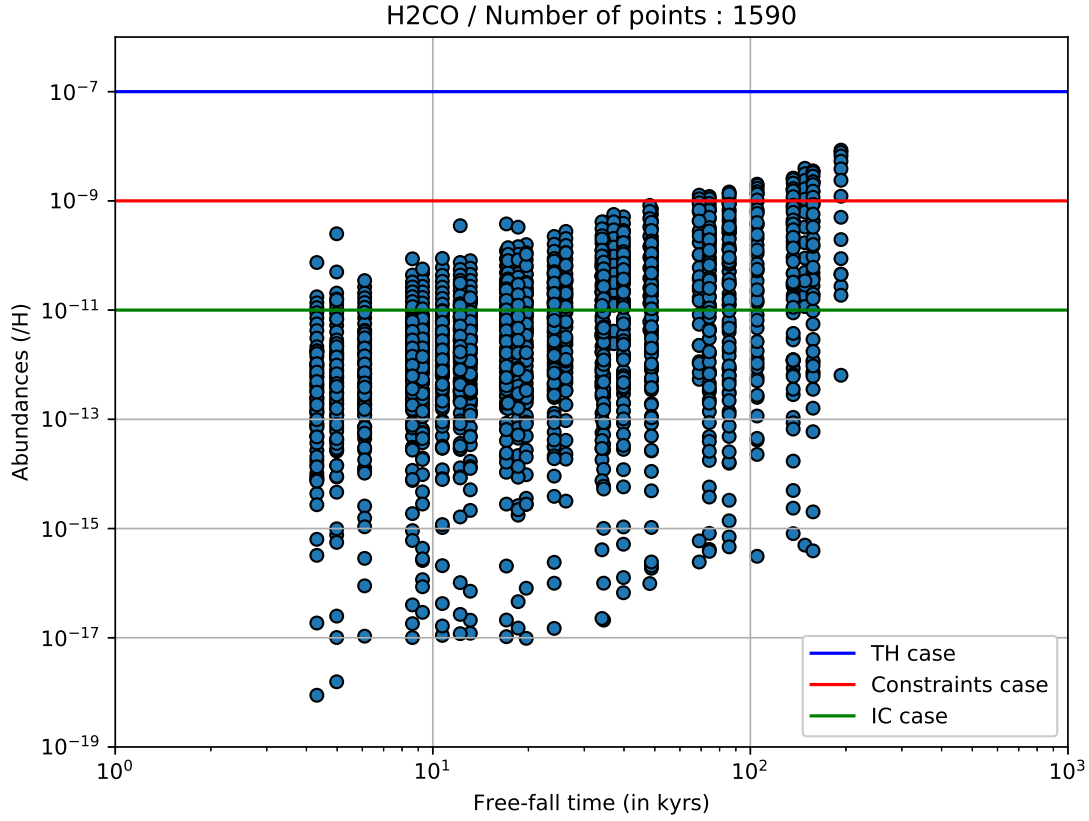


Figure 4.9: Example of the 3 possible cases of constraints that can be derived from the method with the distribution of the abundances of  $\text{H}_2\text{CO}$  relative to  $\text{H}$  at the final time of the collapse as a function of the free-fall time. The blue line represents the TH case, the red one the case when constraints can be derived, and the green one the inconclusive case.

Given a dataset of observed species and their respective abundances in a Class 0 protostellar envelope, the principle of the method is to compare for each species its observed abundance to its corresponding abundance distributions in the ER for each of the IPPC considered in this study:  $M_0$ ,  $T_0$ ,  $R_0$ ,  $\rho_0$  and  $t_{\text{ff}}$ . As showed in figure 4.9, the results of such comparison can then either be one of the following:

- The observed abundance is higher than all the abundances in the ER distribution, and no constraints can be found. I note this case TH (Too High),
- The observed abundance intersects its respective ER distributions such as only a part of the studied IPPC range is compatible with the observations. Hence, the resulting constraint on the IPPC values will either be a single value, an interval, an upper limit or a lower limit. It should be noted that the latter are in fact also intervals since they are only defined within the studied IPPC range of values (see Reference Dataset column in table 4.1).

- The observed abundance intersects its respective ER distributions such as all the studied IPPC values are compatible, which means that no constraints on the IPPC can be found within its considered range of values. I note this case IC (InConclusive) in the following.

I do not characterize the case when the observed abundance is lower than all the abundances in the ER distribution. Indeed, for a species to be observable in the gas phase of the envelope, its abundance should be at least higher than  $10^{-12}$ , and most of species ER distribution covers a range of abundances that nearly always goes well below this limit. Hence, for each species not in the TH case, the method returns an interval of possible values for each IPPC. The final possible intervals for the source are then obtained for each IPPC as the intersection of all the corresponding intervals obtained with each species.

Table 4.3: Summary of the observational dataset used for the method.  $N_{\text{obs}}$  is the number of observed species used.

Sources	$N_{\text{obs}}$	Observed species used	References
IRAS 16293-2422	19	CO, HCO <sup>+</sup> , CN, HCN, HNC, HC <sub>3</sub> N, CH <sub>3</sub> CN, CCH, c-C <sub>3</sub> H <sub>2</sub> , CH <sub>3</sub> CCH, H <sub>2</sub> CO, CH <sub>3</sub> OH, CS, SO, SO <sub>2</sub> , OCS, HCS <sup>+</sup> , H <sub>2</sub> CS, N <sub>2</sub> H <sup>+</sup>	<a href="#">Schöier et al. (2002)</a>
N1333-I2	12	CO, CS, SO, HCO <sup>+</sup> , N <sub>2</sub> H <sup>+</sup> , HCN, HNC, CN, HC <sub>3</sub> N, H <sub>2</sub> CO, CH <sub>3</sub> OH, CH <sub>3</sub> CN	<a href="#">Jørgensen et al. (2004, 2005)</a>
N1333-I4A, N1333-I4B, L1448-C, VLA1623	11	CO, CS, SO, HCO <sup>+</sup> , N <sub>2</sub> H <sup>+</sup> , HCN, HNC, CN, HC <sub>3</sub> N, H <sub>2</sub> CO, CH <sub>3</sub> OH	<a href="#">Jørgensen et al. (2004, 2005)</a>
L1527, L483, L723, L1157	10	CO, CS, SO, HCO <sup>+</sup> , N <sub>2</sub> H <sup>+</sup> , HCN, HNC, CN, HC <sub>3</sub> N, H <sub>2</sub> CO	<a href="#">Jørgensen et al. (2004, 2005)</a>
L1448-I2	9	CO, CS, SO, HCO <sup>+</sup> , N <sub>2</sub> H <sup>+</sup> , HCN, HNC, CN, HC <sub>3</sub> N	<a href="#">Jørgensen et al. (2004)</a>
L1551-I5	7	CO, CS, SO, HCO <sup>+</sup> , N <sub>2</sub> H <sup>+</sup> , HNC, HC <sub>3</sub> N	<a href="#">Jørgensen et al. (2004)</a>

The set of observational data used for the application of the method includes 12 Class 0 protostar envelopes toward which had been observed between 7 and 19 species included in the chemical network. This set is summarized in table 4.3. To quantify

the uncertainty on the observed abundance of a given species, one usually use the  $\chi^2$  statistics:

$$\chi^2 = \sum_{i=1}^{N_L} \left[ \frac{F_{\text{mod},i} - F_{\text{obs},i}}{\sigma_i} \right]^2 \quad (4.23)$$

where  $F_{\text{mod},i}$  and  $F_{\text{obs},i}$  are respectively the modeled and observed integrated line intensities and  $\sigma_i$  the uncertainty in observation  $i$  (in K.km.s<sup>-1</sup>), and  $N_L$  is the number of lines. Hence, In order to ensure consistency while taking into account uncertainties on observed abundances, I define a systematic procedure to cope with the fact that  $\chi^2$  data on calculated abundances are not available for all observations and species. Hence, for each species I proceed as follows:

- If the corresponding  $\chi^2$  value is available, I use an error margin of a factor of 3 on the observed abundance if  $\chi^2 < 10$ , and of a factor of 10 if  $\chi^2 \geq 10$ ,
- If the corresponding  $\chi^2$  value is unavailable, I use the number of lines  $N_L$  as a criteria for the error margin definition, and use an error margin of a factor of 3 if  $N_L > 1$ , and of a factor of 10 otherwise.

In figure 4.10, I display a comprehensive example of the application of the method to one species. I consider here SO<sub>2</sub> in IRAS 16293-2422, which has an observed abundance of  $2.25 \times 10^{-10}$ , and search for constraints on the initial density of the parent prestellar core. An error margin of a factor 3 is used because the  $\chi^2$  value is 0.5 (calculated with  $N_L = 10$ ). The figure shows that the observed abundance can only be compatible with an initial density of the parent core between  $1.20 \times 10^5$  and  $8.96 \times 10^7$  part.cm<sup>-3</sup>.

#### 4.3.2.2 Results on the envelope of IRAS 16293-2422

Table 4.4 shows the results of the application of the method to Schöier et al. (2002)'s observations of IRAS 16293-2422. This source is an ideal example because the high number of species considered allows to display all the interesting features that can be found when applying the method to the other sources. Indeed, all the possible types of constraint defined in section 4.3.2.1 are found. For example, the constraint on  $T_0$  given by CO is a single value (15 K) compatible with the upper limits given by HCO<sup>+</sup>, SO and OCS, when the  $\rho_0$  and  $t_{\text{ff}}$  constraints given by CH<sub>3</sub>CCH and SO<sub>2</sub> are intervals. However, as for the other sources, it appears that the main type of constraints stays lower or upper limits.

The result which is by far the most interesting, is that only one species gives contradictory results. In the present case it is HCO<sup>+</sup> that shows contradictory constraints on  $R_0$ ,  $\rho_0$  and  $t_{\text{ff}}$ . However its high corresponding  $\chi^2$  value indicates that the HCO<sup>+</sup>

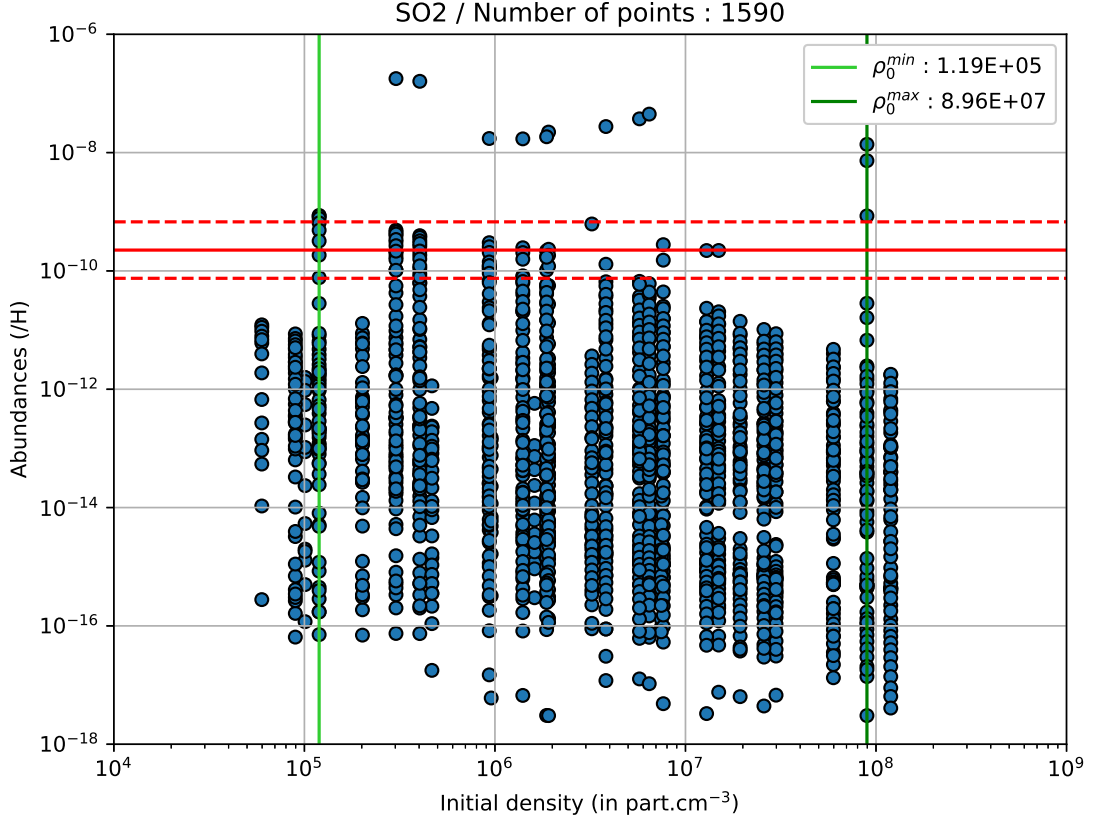


Figure 4.10: Comprehensive example of the application of the method on observed  $\text{SO}_2$  in IRAS 16293-2422. The horizontal red line represents the observed abundance relative to H of  $2.25 \times 10^{-10}$  and the dashed ones its uncertainty factor of 3. The light and dark green horizontal lines respectively represent the minimal and maximal values of the initial density  $\rho_0$  that are constrained by the observed abundance.

abundance derived from the observations is not trustworthy. Furthermore, [Quénard et al. \(2018a\)](#) used 3D modeling of  $\text{HCO}^+$  and its isotopologues emission in IRAS 16293-2422 to show that the contribution of the envelope of to the  $\text{HCO}^+$  emission is negligible compared to the contribution of the outflows. Consequently, the observed abundance of  $\text{HCO}^+$  is not suitable to trace the physico-chemical parameters of the envelope. Moreover, if I slightly increase the uncertainty factor used for this species, the resulting constraints agrees with the others. Table 4.5 displays the constraints obtained with  $\text{HCO}^+$  with an uncertainty factors of 12, 13 and 15. It shows that if I use an uncertainty factor of 12 or 13, the constraints on  $\rho_0$  and  $t_{\text{ff}}$  would agree with those given by the other species, but will considerably reduce the constrained intervals for the three IPPC considered. However, for an uncertainty factor of 15, which would still be acceptable given the  $\text{HCO}^+$   $\chi^2$  value, the results do not change the final constraints obtained with the other species. As it would be contradictory to increase the constraints on the IPPC using a species for which the abundance is the least constrained, I choose to use a uncertainty factor of 15 for  $\text{HCO}^+$ .



### 4.3. POST-TREATMENT OF THE CHEMICAL OUTPUTS AND RESULTS

Table 4.4: Summary of the application of the method to Schöier et al. (2002)’s observations of IRAS 16293-2422. IC stands for InConclusive and ND means that no data were available. Upper and lower limits are only defined within their corresponding IPPC range of values (see table 4.1). In red are contradictory results, and in blue the final constraints on the IPPC of the source.  $e$  is the uncertainty factor.

Species	$M_0$ ( $M_\odot$ )	$T_0$ (K)	$R_0$ (AU)	$\rho_0$ (part.cm $^{-3}$ )	$t_{\text{ff}}$ (kyrs)	$\chi^2$	$N_L$	$e$
CO	IC	15	IC	$\geq 8.96E+04$	$\leq 157.52$	0.2	3	3
HCO $^+$	$\geq 2$	$\leq 20$	$\geq 20000$	$\leq 2.02E+05$	$\geq 105.01$	10.9	3	10
CN	IC	IC	IC	IC	IC	1.2	4	3
HCN	IC	IC	IC	$\leq 8.96E+07$	$\geq 4.98$	2.3	3	3
HNC	IC	IC	IC	$\leq 8.96E+07$	$\geq 4.98$	0.2	3	3
HC $_3$ N	IC	IC	IC	$\leq 2.99E+07$	$\geq 8.63$	0.1	3	3
CH $_3$ CN	$\geq 2$	IC	IC	$\leq 8.96E+07$	$\geq 4.98$	0.9	7	3
CCH	IC	IC	IC	IC	IC	0.3	4	3
c-C $_3$ H $_2$	IC	IC	IC	IC	IC	5.7	6	3
CH $_3$ CCH	$\geq 1$	IC	IC	[1.20E+05 ; 8.96E+07]	[4.98 ; 136.41]	1.7	6	3
H $_2$ CO	IC	IC	IC	$\leq 8.96E+07$	$\geq 4.98$	1.9	7	3
CH $_3$ OH	IC	IC	IC	IC	IC	1.2	23	3
CS	IC	IC	$\geq 5000$	$\leq 3.82E+06$	$\geq 24.11$	0.5	3	3
SO	$\geq 1$	$\leq 25$	IC	$\leq 8.96E+07$	$\geq 4.98$	1.8	9	3
SO $_2$	$\geq 1$	IC	IC	[1.20E+05 ; 8.96E+07]	[4.98 ; 136.41]	0.5	10	3
OCS	IC	$\leq 25$	IC	IC	IC	1.5	7	3
HCS $^+$	IC	IC	$\geq 5000$	$\leq 3.23E+06$	$\geq 26.25$	7.0	2	3
H $_2$ CS	IC	IC	IC	$\leq 5.97E+07$	$\geq 6.10$	1.4	6,4	3
N $_2$ H $^+$	$\geq 1$	IC	IC	IC	IC	ND	1	10
Constraints	[2 ; 8]	15	[5000 ; 30000]	[1.20E+05 ; 3.23E+06]	[26.25 ; 136.41]			

Table 4.5: Constraints given by HCO $^+$  with slightly increased uncertainty factors (compared to the one used in table 4.4).

$e$	$M_0$ ( $M_\odot$ )	$T_0$ (K)	$R_0$ (AU)	$\rho_0$ (part.cm $^{-3}$ )	$t_{\text{ff}}$ (kyrs)
12	$\geq 2$	$\leq 25$	$\geq 20000$	$\leq 3.02E+05$	$\geq 85.74$
13	$\geq 2$	$\leq 25$	$\geq 12000$	$\leq 4.67E+05$	$\geq 69.02$
15	IC	$\leq 25$	IC	$\leq 7.46E+06$	$\geq 17.26$

It appears that the method allows to successfully give constraints on the IPPC of the prestellar core in which IRAS 16293-2422 has formed (in blue in table 4.4). Moreover, the fact that 94% (18/19) of the species-specific constraints agree with each other gives confidence in this result. From an astrochemical point of view, these results, and in particular those regarding initial density and temperature, force to reconsider the value commonly used in chemical models to simulate the initial core in which IRAS 16293-2422 had formed. Indeed, to this time, the common set of values used were usually  $\leq 10$  K for the initial temperature and a few  $10^4$  part.cm $^{-3}$  for the initial density (see for example Majumdar et al., 2017; Quénard et al., 2018b; Vidal and Wakelam, 2018). My study reveals however that the values astrochemist should use are slightly higher,



namely an initial density within the interval  $[1.20 \times 10^5 ; 3.23 \times 10^6]$   $\text{part.cm}^{-3}$  and an initial temperature of 15 K.

#### 4.3.2.3 Summary of the results on the source sample

##### 4.3.2.3.1 Summary per source

Table 4.6: Summary of the constraints on the IPPC obtained with the method on the 12 studied sources. The percentage of agreement (noted PA) displayed in the last column represents the number of species agreeing with the final constraints.

Sources	$M_0$ ( $M_\odot$ )	$T_0$ (K)	$R_0$ (AU)	$\rho_0$ ( $\text{part.cm}^{-3}$ )	$t_{\text{ff}}$ (kyrs)	PA
IRAS 16293	[2 ; 8]	15	[5000 ; 30000]	[1.20E+05 ; 3.23E+06]	[26.25 ; 136.41]	94.0%
L1448-I2	[1 ; 8]	[10 ; 20]	[3000 ; 30000]	[8.96E+04 ; 2.58E+07]	[9.28 ; 157.52]	88.9%
L1448-C	[1 ; 8]	15	[5000 ; 30000]	[8.96E+04 ; 5.74E+06]	[19.69 ; 157.52]	90.9%
N1333-I2	4	10	30000	5.98E+04	192.92	91.7%
N1333-I4A	[2 ; 8]	10	[20000 ; 30000]	[5.98E+04 ; 2.01E+05]	[105.01 ; 192.92]	90.9%
N1333-I4B	2	10	20000	1.01E+05	148.51	90.9%
L1527	[2 ; 8]	[10 ; 15]	[20000 ; 30000]	[8.96E+04 ; 1.20E+05]	[136.41 ; 157.52]	100%
VLA1623	[1 ; 8]	15	[5000 ; 20000]	[3.02E+05 ; 7.65E+06]	[17.05 ; 85.74]	90.9%
L483	[2 ; 4]	10	[20000 ; 30000]	[5.98E+04 ; 1.01E+05]	[148.51 ; 192.92]	90.0%
L723	4	10	30000	5.98E+04	192.92	90.0%
L1157	[2 ; 8]	[10 ; 20]	[20000 ; 30000]	[8.96E+04 ; 1.20E+05]	[136.41 ; 157.52]	90.0%
L1551-I5	[2 ; 4]	10	[20000 ; 30000]	[8.96E+04 ; 1.01E+05]	[148.51 ; 157.52]	85.7%

Table 4.6 presents a summary of the IPPC constraints I find for each source listed in table 4.3 using my method (for a more comprehensive description of the results, see appendix D). As the table shows, the main result of this study is that the method allows to derive constraints on all the IPPC for all sources, except for  $R_0$  in the case of L1448-I2. The latter is due to the fact that for 7 of the 9 species considered for this source I applied an uncertainty factor of 10 because of the low quality of the corresponding observations (see table D.1 in appendix D), making it the least constrained source of the study.

The most unexpected result however, is that at most one species per source gives contradictory constraints except for L1527 for which the percentage of agreement, *ie* the percentage of species giving results that agree with the final constraint, is of a 100%. Hence, the percentage of agreement for the sources considered is always higher than 85%, which confirms the effectiveness of the method to derive constraints on IPPC from the ER. Furthermore, except in the case of IRAS 16293-2422 (see the previous section), the species that gives contradictory constraints for the concerned sources is always  $\text{N}_2\text{H}^+$ . Indeed, as can be seen in figure 4.11,  $\text{N}_2\text{H}^+$  abundances distribution in the ER as a function of  $T_0$  is such that either its observed abundance is too high and corresponds to  $T_0 \geq 20$  K, either it is too low, which is the case for L1527, and the re-

sult is inconclusive. In the first case, the resulting constraint on  $T_0$  is for all concerned sources contradictory with at least one other species constraint. This issue appears in 10 of the 11 sources from [Jørgensen et al. \(2004\)](#), and is believed to be mainly due to an overestimation of  $\text{N}_2\text{H}^+$  abundances because only one of its line had been observed in all of these sources. Additionally, most protostars are believed to form in cold prestellar cores which temperatures are rarely higher than 20 K (see for example [Agúndez and Wakelam, 2013](#), and the references therein). Therefore, I decided to ignore the constraint of  $\text{N}_2\text{H}^+$  on  $T_0$  in my study.

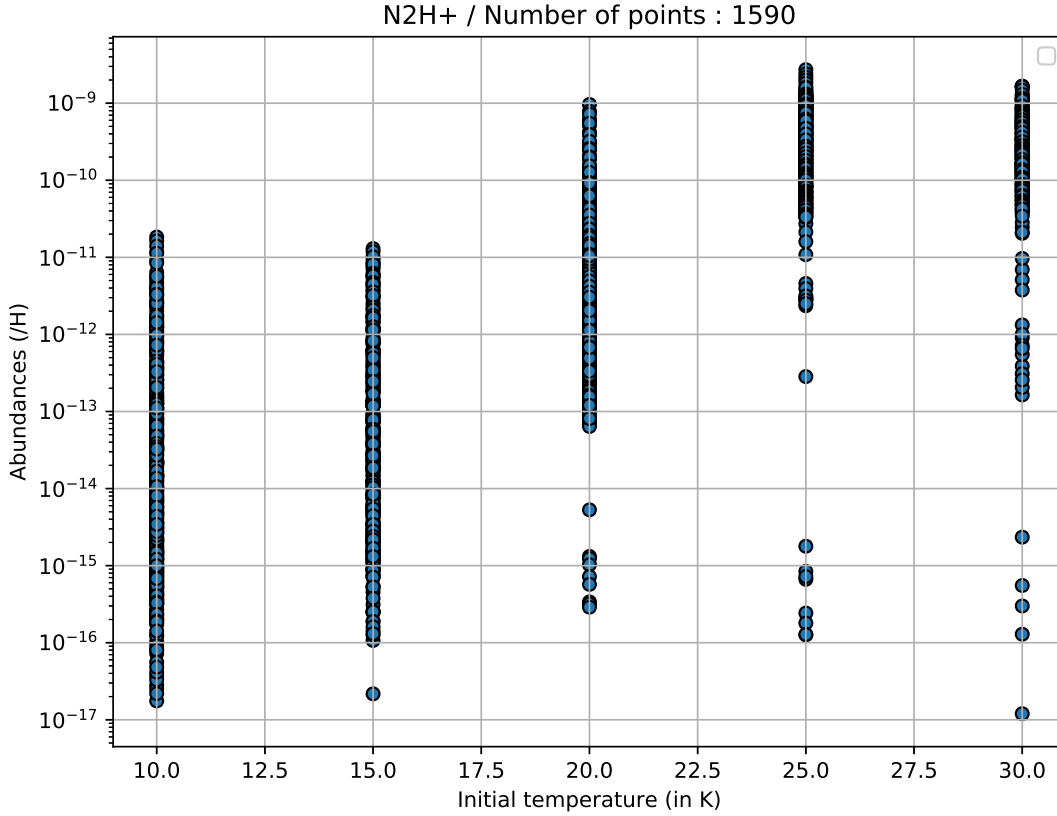


Figure 4.11: Abundances distribution of  $\text{N}_2\text{H}^+$  relative to H in the ER as a function of  $T_0$ .

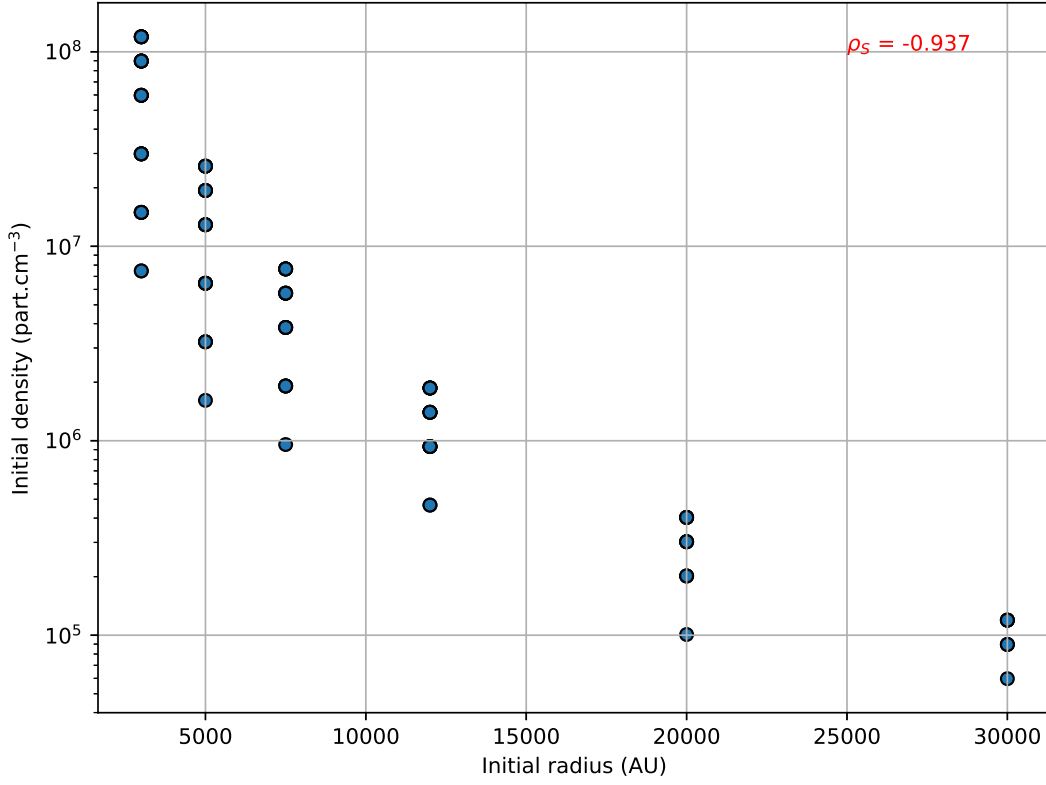
Table 4.6 also displays that for N1333-I2, N1333-I4B and L723, all IPPC are constrained to single values. These results are the direct consequence of constraints due to one species for each source. For N1333-I4B (see table D.5 in appendix D), the concerned species is  $\text{CH}_3\text{OH}$ , which corresponding  $\chi^2$  value is high ( $\chi^2 = 11.4$ ), and the results could therefore be discussed. However, the constraints of the 9 other species agree with these values. Plus, because the source constraints obtained without  $\text{CH}_3\text{OH}$  would only be slightly larger, this result remains acceptable. For L723 and N1333-I2, the species that gives the single value constraints is  $\text{HCO}^+$ , which in both sources has a well constrained observed abundance (respectively  $\chi^2 = 0.61$  and  $\chi^2 = 0.59$  with 4 and

3 lines observed, see tables D.9 and D.3 in appendix D). Moreover, in the case of L723, these constraints agree with those given by the 9 other species considered. In the case of N1333-I2, the  $\rho_0$  and  $t_{\text{ff}}$  strict constraints given by  $\text{HCO}^+$  only conflict with those of  $\text{N}_2\text{H}^+$ . However, as discussed above, the observed abundance of  $\text{N}_2\text{H}^+$  is not well constrained compare to the  $\text{HCO}^+$ . Furthermore because the constraints given by  $\text{HCO}^+$  agree with those of the 10 remaining species considered, I decided to solve the conflict by ignoring the  $\text{N}_2\text{H}^+$  constraints on  $\rho_0$  and  $t_{\text{ff}}$ . Overall, these single values constraints should however be taken with caution, since this kind of results is model-dependent, *ie* the direct consequences of the discretization of the parameters space in the collapse models database.

Another interesting feature of table 4.6 is that  $M_0$  is the least constrained IPPC. Coupled with the results found on correlation in the HCR in section 4.3.1 (see table 4.2), this result hints the complexity of obtaining constraints on the initial mass of the parent core of forming star using chemistry. On the contrary,  $T_0$  and  $\rho_0$  (and consequently  $t_{\text{ff}}$ ) appear to be easily constrainable with chemistry, which makes sense since temperature and density variation throughout star formation are two of the main parameters affecting the chemistry. Finally, regarding  $R_0$ , it appears that I am able to derive relatively precise constraints on its values which could seem puzzling at first since the link between the chemistry of a source and the initial radius of its parent core is not easy to apprehend. However, when studying the correlation figure between  $R_0$  and  $\rho_0$  (see figure 4.12), the anti-correlation between the two parameters is striking. Indeed, the corresponding Spearman coefficient is very close to -1. The link between the two IPPC is due to equation (4.10) which links the  $R_0$  to the central density  $\rho_c$ . This explains the efficiency of the method on deriving constraints on  $R_0$ .

Finally it seems interesting to figure out whether these constraints obtained with the 1590 cells of the ER allow to find collapse models in the reference dataset that correspond to each of the sources. Table 4.7 references all the collapse models corresponding to their respective sources, as well as the sources respective parent molecular clouds. Note that L483, L723 and L1157 are isolated sources, *ie* they do not lie in a giant molecular clouds.

At the first sight it looks evident that L1448-I2 is the least constrained source since the constraints obtained on its IPPC can correspond to half of the models of the reference dataset (55/110). For the other sources however, the corresponding number of collapse models is much lower. Indeed, for L1448-C and VLA1623, which constrained intervals for  $M_0$ ,  $\rho_0$  and  $t_{\text{ff}}$  are slightly larger than other sources, I find respectively 13 and 11 corresponding collapse models, 9 of them being common between the two sources. Among these 9 are the 8 models corresponding to IRAS 16293-2422, which hints that these 3 sources could have formed in similar physical environments. This similarity of the results for IRAS 16293-2422 and VLA1623 is supported by the fact that

Figure 4.12: Correlation figure between  $R_0$  and  $\rho_0$ .

both these sources originate from the  $\rho$ -Ophiuchi molecular cloud, and are therefore likely to have formed in similar environment. I also find similar results for N1333-I4A, L1527 and L1157 which also have at least 3 corresponding models in common among their respective 5, 5 and 7 ones, despite the fact they do not originate from the same parent cloud. Finally, the five remaining sources only correspond respectively to one of the collapse models of the reference dataset, and these models are either number 115 or 134. For L483 and L1551-I5, this result is rather surprising since their respective IPPC constraints are not single values as found for N1333-I2, N1333-I4B and L723, and shows the effectiveness of the method on constraining initial physical condition of collapse. Moreover, models 115 and 134 only differ in their initial masses and radii, which keeps hinting the fact that low-mass protostars are formed in prestellar cores with similar physical parameters, regardless of their respective parent clouds. Overall, the results displayed in table 4.7 could be of great interest for future chemical modeling of the considered sources, since it gives a catalog of possible physical models of collapse corresponding to these sources.

#### 4.3.2.3.2 Summary per IPPC

In order to study the repartition of the source constraints for each IPPC, I plot for

Table 4.7: Summary of the corresponding collapse models for each source within the reference dataset, as well as their respective parent molecular clouds (noted PMC, when relevant).

Sources	PMC	RHD model number	Total number
IRAS 16293-2422	$\rho$ -Ophiuchi	70,75,94,97,103,109,122,128	8
L1448-I2	Perseus	6-8,38-40,42-44,48-50,54-56,60-62,67,69-71,74-76,80-82,86-88,93-94,96-98,102-104,108-110,115,117-119,121-123,127-129,136-138,140-142	55
L1448-C	Perseus	39,70,75,81,94,97,103,109,118,122,128,137,141	13
N1333-I2	Perseus	134	1
N1333-I4A	Perseus	115,117,134,136,140	5
N1333-I4B	Perseus	115	1
L1527	Taurus	115,136,137,140,141	5
VLA1623	$\rho$ -Ophiuchi	39,43,70,75,81,87,94,103,109,122,128	11
L483	-	134	1
L723	-	134	1
L1157	-	115,136-138,140-142	7
L1551-I5	Taurus	115	1

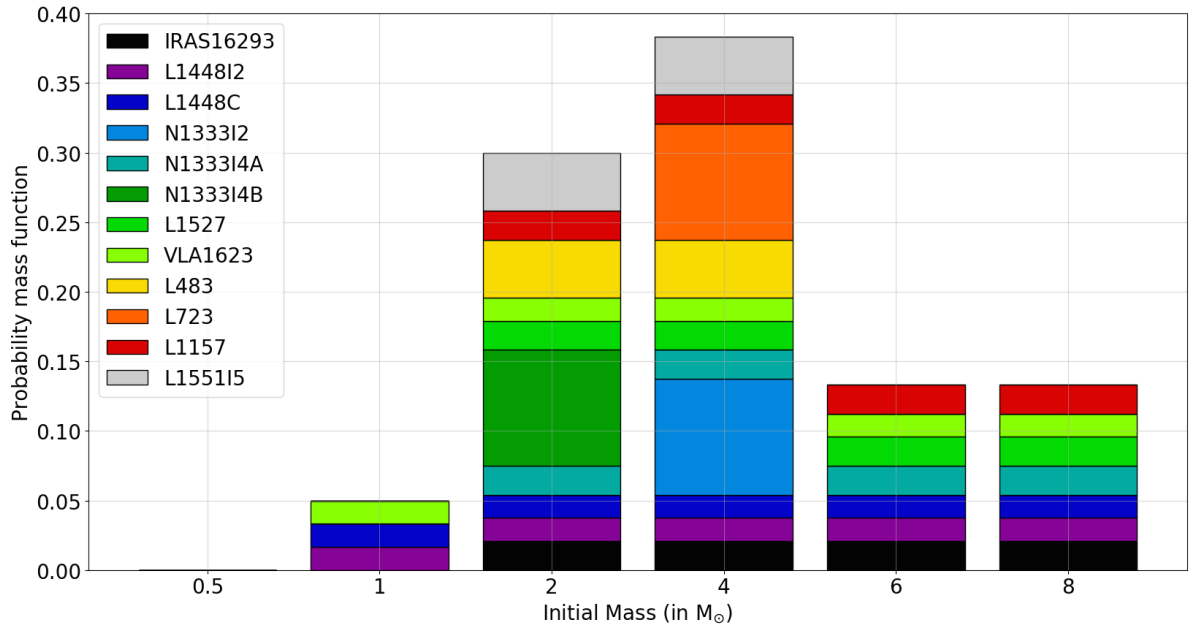


Figure 4.13: Probability mass function on the sample of 12 sources obtained for  $M_0$ .

each of them their respective probability mass functions on the sample of sources. Hence the probability of finding a low-mass protostar with a particular value of the IPPC is calculated via:

$$P(y_i) = \frac{1}{N_s} \sum_{s=1}^{N_s} \delta_{is} \frac{1}{N_y(s)} \quad (4.24)$$

where  $Y = \{y_i\}_{i \in [1, N_y^{tot}]}$  is the distribution of possible values of the IPPC considered,  $N_s = 12$  is the total number of sources considered,  $\delta_{is}$  is the Dirac function assessing the match between the source  $s$  and the IPPC value  $y_i$ , and  $N_y(s)$  is the number of IPPC values constrained for the source  $s$ . The corresponding plots also display in color the contribution of each of the sources to the mass function. Consequently, in the following, I express the results in terms of probabilities for the sake of clarity. However, it should be noted that these probabilities are defined for a relatively small sample of sources (12). Therefore, the probabilities presented hereafter are likely to change for a larger sample.

Figure 4.13 displays the results for  $M_0$  which is, as stated previously, the least constrained of the IPPC considered. Nevertheless, it appears that tendencies can still be inferred from these constraints. First, the probability of finding sources with  $M_0 < 1 M_\odot$  is null, and of only of 5% for a parent prestellar core of mass  $M_0 = 1 M_\odot$ . Second, parent cores of mass  $M_0 = 2 M_\odot$  and  $M_0 = 4 M_\odot$  corresponds to a total probability of respectively 68%. Finally, higher mass parent cores also agree with a significant fraction of the sources, but with a much lower probability than for the previous values, namely 26%. This repartition of the source constraints hints that low-mass stars are born mostly from prestellar cores of masses higher than  $1 M_\odot$ . Furthermore, it highlights that a large fraction of low-mass stars should form from prestellar cores of masses within the interval  $[2 ; 4] M_\odot$ .

Figure 4.14 shows the results obtained for  $R_0$ . As discussed previously,  $R_0$  appears relatively well constrained by the method, since only two of its possible values agree with more than 4 of the sources with probabilities higher than 35%. These values correspond to the largest parent prestellar cores considered ( $R_0 \geq 20000$  AU), which suggests that low-mass stars have a total 77% probability to be born from such large cores. The probability for low-mass stars to form from cores with radii within the interval  $[5000 ; 20000]$  AU is rather low ( $0.07 \times 3 = 21\%$ ) compared to the previous values. However, IRAS 16293-2422 and VLA 1623 are constrained within this interval, which hints that these sources represents particular cases of low-mass star formation. It should finally be noted that the probability to find sources corresponding to the smallest parent prestellar core ( $R_0 = 3000$  AU) is close to 0.

The results regarding  $\rho_0$  and  $t_{ff}$  are displayed in figure 4.15. As both these parameters are perfectly anti-correlated, the top figure appears as the mirror of the bottom one. One of the most interesting results regarding these IPPC is that prestellar cores

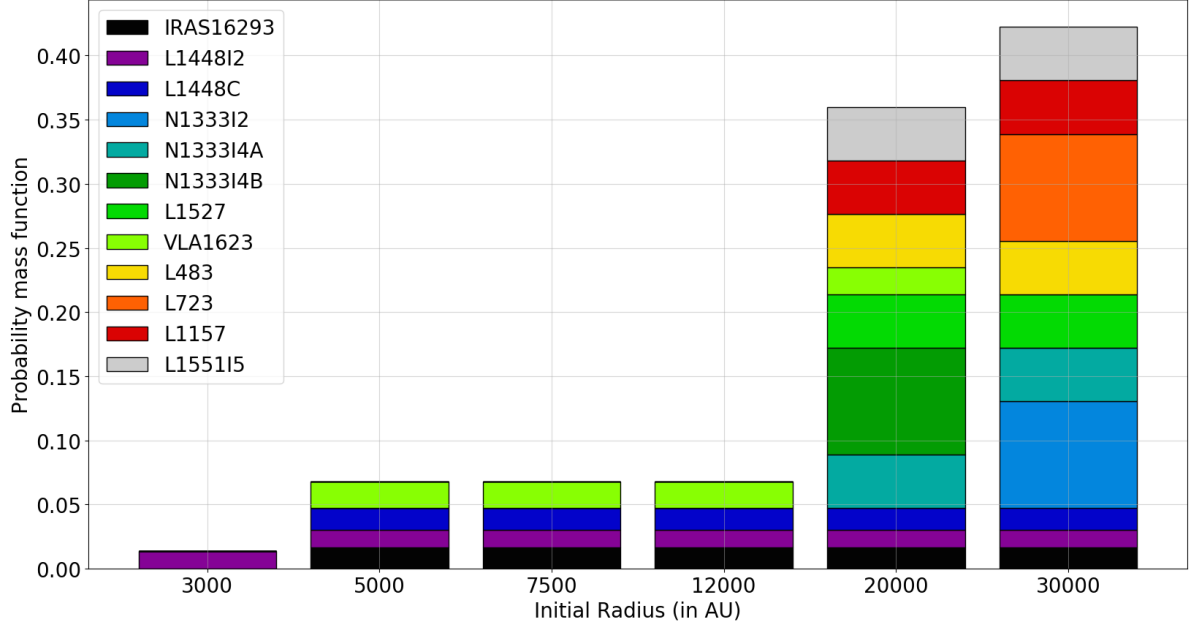


Figure 4.14: Probability mass function on the sample of 12 sources obtained for  $R_0$ .

of density  $> 10^7 \text{ part.cm}^{-3}$  (respectively of  $t_{\text{ff}} < 17 \text{ kyrs}$ ) appear to be ruled out of the possible parent cores of low-mass stars. Indeed, the probability of finding such sources is only of 0.8%. Moreover, as the initial density increases (respectively  $t_{\text{ff}}$  decreases), the probabilities decrease. Another interesting result is that 8 of the 12 sources are constrained within the interval  $[5.97 \times 10^4 ; 2.02 \times 10^5] \text{ part.cm}^{-3}$  (respectively  $t_{\text{ff}} \in [105.01 ; 192.92] \text{ kyrs}$ ) indicating that approximately 70% of low-mass stars are born in prestellar cores with relatively low densities and high free-fall times. However, as found for  $R_0$ , VLA 1623 and IRAS 16293-2422 appear to represent a particular type of low-mass protostars since they are incompatible with these small values and would preferentially have formed in core with higher density between  $3.02 \times 10^5$  and  $3.23 \times 10^6 \text{ part.cm}^{-3}$  (respectively  $t_{\text{ff}} \in [26.25; 85.74] \text{ kyrs}$ ), interval which corresponds to a rather low probability compared to the previous one, namely 21%. This result hints that low-mass stars can form from prestellar cores with densities (respectively free-fall times) within a rather large range of values.

Finally, figure 4.16 displays the results for  $T_0$ . This IPPC is the best constrained one, which results in a clearer repartition of the mass function. First, temperatures above 20 K appear to be ruled out of the possible values since none of the sources agreed with them. Second, all sources match with an initial temperature of either 10 or 15 K, corresponding to a total probability of 94%. This shows a common trend among low-mass stars to form from a low temperature parent prestellar core, and particularly cores with  $T_0 = 10 \text{ K}$ . Finally, the two sources corresponding to  $T_0 = 20 \text{ K}$  (L1448-I2 and L1157) are both the least constrained sources regarding initial temperature. Since the resulting

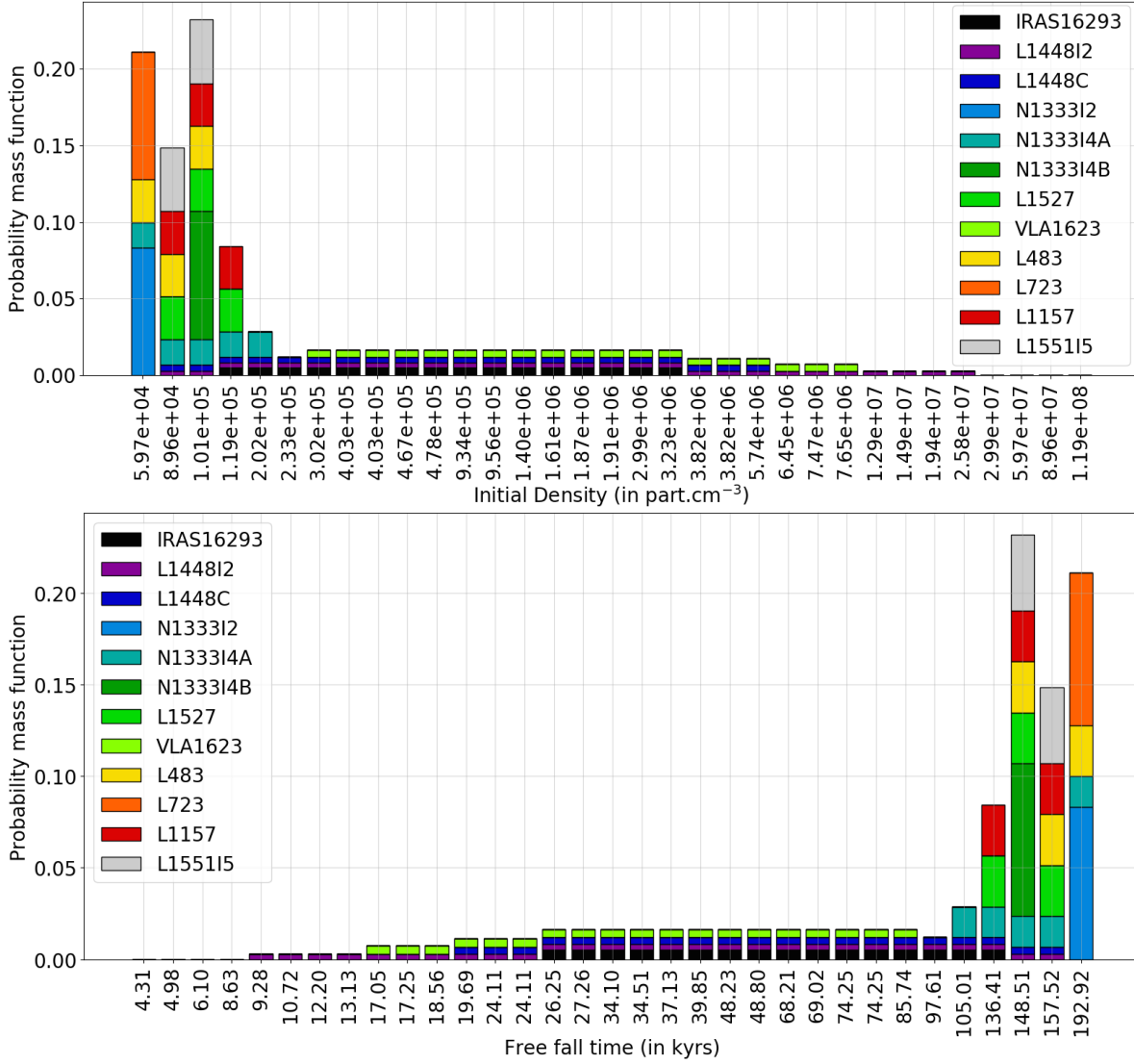


Figure 4.15: Probability mass function on the sample of 12 sources obtained for  $\rho_0$  and  $t_{ff}$ .

probability is only of 6%, it appears low-mass stars have a really small probability to form in cores with temperatures as high as 20 K.

## 4.4 DISCUSSIONS AND SUMMARY

In the following, I discuss the dependence of my results on the models used. Another aspect that I discuss below is the applicability of the method used in the ER to the HCR dataset.



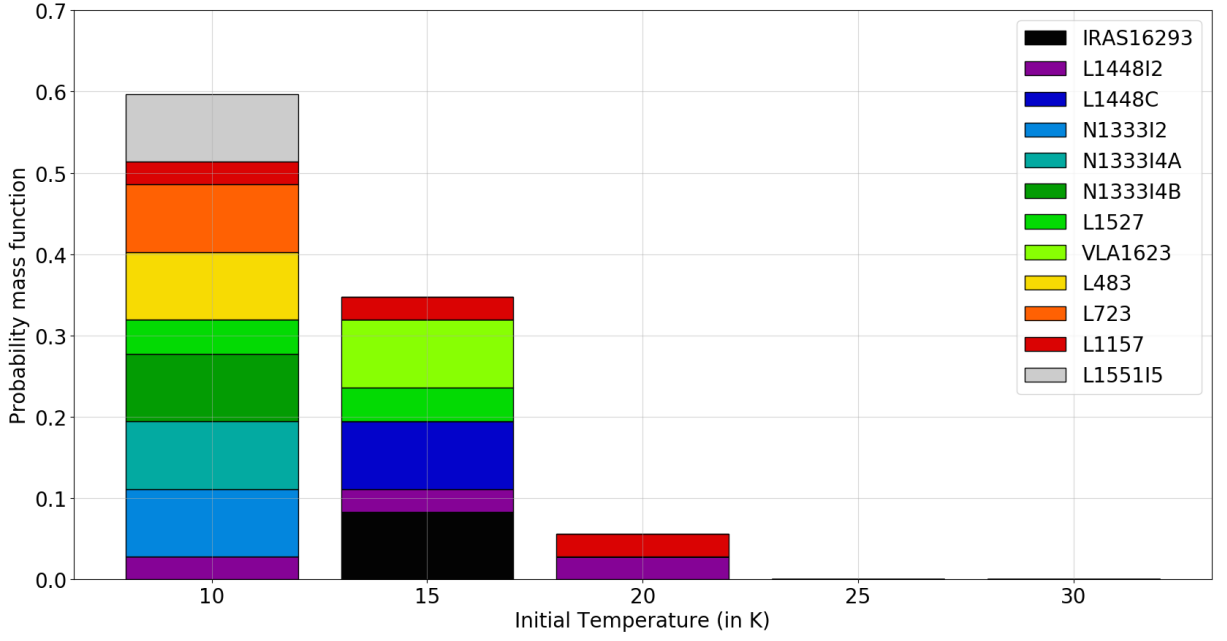


Figure 4.16: Probability mass function on the sample of 12 sources obtained for  $T_0$ .

#### 4.4.1 About the modeling bias

Since I used the combination of two (physical and chemical) models, all the aforementioned results are model dependent. On the one hand, regarding the physical model, the completeness of the chemical abundances distribution over the range of the IPPC is limited by the discretization of the parameter space, especially for  $M_0$  and  $R_0$ . A more complete representation of these parameters could affect the results by modifying the abundance distribution of the species considered. Future similar study would therefore benefit of such a completion of the parameter space. However, the fact that I can find possible scenarii for each of the 12 sources considered in the ER study imply confidence on the fact that the limits of the parameters space are large enough to represent a significant majority of existing low-mass protostars.

On the other hand, the temperature validity domain of the NAUTILUS chemical model, especially its lower limit of 10 K forces limitations on my study. Indeed, as colder prestellar cores can also theoretically form low-mass protostars, the chemical evolution of these cores (available in the original dataset of [Vaytet and Haugbolle \(2017\)](#)) could also fit the sources considered in my ER study and therefore enlarge the range of possible  $T_0$  I found. To solve this issue, complementary studies on the modeling of the chemistry in such low-temperature regimes are still needed. Furthermore, as work remains to be conducted on the chemical network, especially for NS, the results on the NS correlation with  $T_0$  are susceptible to change in the future. However the chemical network for  $\text{CH}_3\text{CN}$ ,  $\text{H}_2\text{CS}$  and  $\text{OCS}$  have been completed recently

(Vidal et al., 2017, Andron et al., submitted to MNRAS), which gives confidence in the correlation results presented for these species.

Finally, the most important modeling bias is due to the fact that I used 1D models. Indeed, compared to more comprehensive 2D or 3D collapse models, 1D models do not allow to access as much detailed information, especially regarding physical structure that form towards the center during collapse such as outflows or the centrifugal barrier (Sakai et al., 2014). However 2D and 3D models require long computation times and imply large amount of output data, which would not have been compatible with the number of models and sources used in this chapter.

#### 4.4.2 About the applicability of the method on the HCR dataset

For the sake of completeness, I also tried to apply the method developed for the ER data on the joined TR and HCR data. Both sets were taken into account in order to ensure an optimal fit with the observed data. Indeed, the cells of the TR are located at radii smaller or of the same order of magnitude (tens of AU, see figure 4.4) as the spatial resolution of the observations of hot corinos I used. These observations are the data from Schöier et al. (2002) on the hot corinos of the binary IRAS 16293-2422 obtained with their jump model, PILS data on the hot corino within IRAS 16293-2422B (Jørgensen et al., 2016; Coutens et al., 2016; Lykke et al., 2017; Drozdovskaya et al., 2018) and Taquet et al. (2015) COMs observations of the hot corinos N1333-I2 and I4B. The number of species considered for each source was respectively 11, 9, 7 and 7.

Unfortunately for all sources, at least two species gave contradictory constraints on at least two IPPC, and I was unable to derive satisfactory constraints. This failure of the method on the TR+HCR dataset could be mostly explained by the following factors:

- An incompleteness of the gas phase high temperature network for some of the species considered, especially COMs. Moreover, a lack of understanding of high temperature chemical mechanism such as the formation of  $H_2$  (see Wakelam et al., 2017, for a review on the subject) could also put uncertainties on the obtained chemical abundances in this region.
- Uncertainties on the observed abundances, notably regarding beam dilution, since the sizes of the lobe obtained with the observations are bigger or of the same order of magnitude than the scale considered in the HCR. Moreover, at the considered scale, the envelopes and outflows could also alter the quality of the observations.
- The use of 1D models, since they do not allow to represent the complex physical structures that appear during the collapse at its center, such as outflows and the centrifugal barrier. Hence a lack of precision is expected regarding the modeling of the inner part of the collapsing core, and consequently the HCR.

Nevertheless, the fact that the application of the method to the TR+HCR dataset was inconclusive does not contradict the results obtained for the ER one. In fact, I am confident in the completeness of the NAUTILUS chemical network for the species considered in the temperatures and densities regimes of the ER. Furthermore, the spatial scales considered in this region limit the uncertainties due to beam dilution. Finally, the one study I found that tried to constrained IPPC was that of [Jaber Al-Edhari et al. \(2017\)](#), who inferred from cyanopolyynes observations and chemical modeling that IRAS 16293-2422 underwent a collapse with a  $t_{\text{ff}} \leq 100$  kyrs. By agreeing with my own, this result is a first confirmation of the ability of constraining IPPC from chemical study based on a large set of physical model of collapsing prestellar cores.

#### 4.4.3 Summary

In this chapter I have presented a large scale chemical study of Class 0 protostars formation, focusing on the constraint of five initial physical parameters of collapse (IPPC) of interest:  $M_0$ ,  $T_0$ ,  $R_0$ ,  $\rho_0$  and  $t_{\text{ff}}$ . The study was based on a dataset of 110 1D physical models of collapsing prestellar cores through the formation of the first and second Larson's core. From this dataset I extracted the outputs of 16 parcel of material per model, accordingly to the validity domain of the NAUTILUS chemical model, that I treated independently from each other for statistical purposes. I then ran 0D dynamic chemical models on each of the 1760 resulting cells.

As the initial idea of my study was to use such a large dataset to infer statistical results, I first tried to find possible tracers of the IPPC by studying their respective correlations with each of the abundance distribution of the species present in the chemical network. In order to do so, I defined two physical regions in the protostellar envelope from the water abundance distribution: the Envelope Region (ER) corresponding to the 1590 cells within the outer part of the protostellar envelope ( $T < 100$  K) and the Hot Corino Region (HCR) corresponding to 138 cells within the hot corino ( $T > 145$  K). As the correlation obtained for the ER were mostly inconclusive, I focused my study on the correlation within the HCR. Despite the fact that I found no satisfactory correlations with  $M_0$ , my study shows for the four remaining IPPC  $T_0$ ,  $R_0$ ,  $\rho_0$  and  $t_{\text{ff}}$  that numerous possible tracers were good candidates, with maximal Spearman coefficient up to more than 0.9 in absolute value for all four. I presented the results on four of the tracer candidates observed in IRAS 16293-2422 in the light of their respective chemistries:  $\text{CH}_3\text{CN}$ ,  $\text{H}_2\text{CS}$ , NS and OCS.  $\text{H}_2\text{CS}$  was found to be a possible tracer for the free-fall time and the initial density, while the three remaining species are found to be possible tracers of the initial temperature of the parent prestellar core.

In order to work on the ER dataset, I also developed a simple method of comparison of the abundance distributions with the observations. From this method I was

able to derive the IPPC for 12 Class 0 protostars from observations of 7 to 19 species towards their envelopes. Moreover, all the constraints are obtained with the percentage of agreement between species of more than 85%, which implies confidence in the method and its results. The specific result obtained for each source could be of great interest for the future modeling of their chemistry (see table 4.7). Looking at the results for each IPPC, I was also able to derive the following probabilities for low-mass protostars. It should be noted that these probabilities are defined within the sample of 12 sources I used, and could therefore evolve using a larger sample of sources:

- The probability for them to form from parent cores with masses  $\leq 1 M_{\odot}$  appears to be of only 5%, while the favored interval  $[2 ; 4] M_{\odot}$  reaches a probability of 68%. The outermost interval  $[6 ; 8] M_{\odot}$  corresponds to a total probability of 26% and could therefore correspond to a non-negligible number of low-mass protostars,
- The initial temperatures, which are the most constrained IPPC, are efficiently constrained between 10 and 15 K, with all sources agreeing with either or both values. Hence, the total probability for low-mass sources to form in prestellar cores with such temperatures reaches 94%. This result hints that, even if it is theoretically possible, low-mass star would tend not to form from hotter parent cores ( $T_0 \geq 20$  K),
- The initial radii are also well constrained with the method because of their correlation with initial densities. The result shows that low-mass stars form preferentially in vast parent prestellar cores of  $R_0 \geq 20000$  AU, with a probability of 77%. This limit is however very model dependent since the chosen value for  $R_0$  in the original dataset are highly spaced when higher than 7500 AU,
- Finally, the most interesting result regarding the initial densities and the free-fall times is that low-mass stars appear to have a ridiculously low probability (0.8%) to form in parent prestellar cores of density higher than  $10^7 \text{ part.cm}^{-3}$  ( $t_{\text{ff}} < 17$  kyrs). Moreover, 70% of low-mass stars appear to be born in cores with densities within the interval  $[5.97 \times 10^4 ; 2.02 \times 10^5] \text{ part.cm}^{-3}$  (respectively  $t_{\text{ff}} \in [105.01 ; 192.92]$  kyrs). Finally the fact that the possible values obtained for all sources span between a few  $10^4$  and  $10^6 \text{ part.cm}^{-3}$  (20 to 192 kyrs for the free-fall time) hints that low-mass stars can form in parent cores with various possible densities (or free-fall times).

Another interesting results of this study is that two sources (IRAS 16293-2422 and VLA1623) have constraints on  $R_0$ ,  $\rho_0$  and  $t_{\text{ff}}$  within intervals which are not the favored ones, hinting that they could be representatives of a specific type of protostars which forms from medium-sized prestellar cores with higher densities (respectively smaller free-fall time) than the majority of low-mass protostars. In order to confirm this dual trend, a similar study with a higher number of sources should be conducted.

Overall, the presented study gives hints on the potential of such large scale chemical modeling study, notably the ability to put new constraints on the modeling of the formation of low-mass stars, as well as finding chemical tracers of physical parameters. Moreover, I only used here the data at the final time of the physico-chemical model, and other results could be found using data at different timesteps. For example, one could search chemical tracers of the elusive FHSC stage, which would help to confirm the various observations of possible candidates for FHSC (see for example [Gerin et al., 2015](#); [Maureira et al., 2017](#)), and therefore suggest new hints on their physico-chemical parameters. Finally, the constant improve of chemical models and observations should allow to build larger datasets and precise the presented results.

# 5 | CONCLUSIONS AND PERSPECTIVES

Astrochemical studies of star formation are of particular interest because they provide a better understanding of how the chemical composition of the Universe has evolved, from the diffuse interstellar medium to the formation of stellar systems and the life they can shelter. Recent advances in chemical modeling, and particularly a better understanding of grains chemistry, now allow to bring new hints on the chemistry of the star formation process, as well as the structures it involves.

The objective of this thesis was to give a new look at the chemistry of star formation using the recent enhancements of the NAUTILUS chemical model, such as the 3-phases model or the process of competition between reaction and diffusion/desorption. To that aim, I first focused on the sulphur chemistry throughout star formation, from its evolution in dark clouds to hot cores and corinos. Afterwards, I decided to develop a method for the derivation of the initial parameters of collapse of dark clouds via the use of a physico-chemical database of collapse models, and comparison to observations of Class 0 protostars.

## RECONCILING SULPHUR CHEMISTRY WITH ITS ELEMENTAL ABUNDANCE IN DARK CLOUDS

The first study of my thesis consisted in a review of the sulphur chemical network and the assessment of its effect on sulphur modeling in dark clouds. In order to do so, I added (or reviewed in the case of reactions) 46 S-bearing species to the network along with 478 reactions in the gas phase, 305 reactions on the grains surface and 147 reactions in the grains bulk. I then ran several 0D models with typical dark cloud physical conditions. Then, I first detailed the chemistry of the reservoirs of sulphur and of the newly implemented species of interest. Second, I studied the S-bearing species that are the most affected by the network modifications and how their chemistries are consequently modified.

In a second part, I evaluated the efficiency of the new network to reproduce ob-

servations of dark clouds, and especially to assess if the new model could infer new hints on the sulphur depletion problem in such objects. For that purpose, I compared the outputs of the model to observations in the dark clouds TMC-1 (CP) and in grains ices towards the protostar W33A using four different elemental abundances of sulphur, ranging from the commonly used "depleted" one ( $[S]_{\text{ini}} = 8 \times 10^{-8}$ ) to the cosmic one ( $[S]_{\text{ini}} = 1.5 \times 10^{-5}$ ). It appeared from the results that the NAUTILUS chemical model does not need a depleted elemental abundance of sulphur anymore in order to reproduce dark clouds observations of S-bearing species. In fact the observations are best reproduced using as elemental abundance of sulphur its cosmic one or a value three times lower ( $[S]_{\text{ini}} = 5 \times 10^{-6}$ ). As most of the estimations of the cosmic abundance of sulphur lie between these two values, the NAUTILUS chemical model becomes the first one that does not require additional depletion of sulphur. This result then allowed me to derive new hints on the sulphur reservoirs in dark clouds. According to the model ran with the cosmic elemental abundance of sulphur, the reservoirs of sulphur in dark clouds are:

- $S^+$  in the gas phase from the beginning of the model and until  $2.8 \times 10^3$  years (initial form of sulphur),
- Atomic sulphur in the gas phase between  $2.8 \times 10^3$  and  $4.6 \times 10^5$  years, containing between 25 and 88% of the total amount of sulphur, depending on the age of the cloud. During this period of time, CS also contains a significant amount of sulphur, namely between 9 and 16%,
- HS and  $H_2S$  in the grains bulk for older clouds, containing a total of more than 51% of the total amount of sulphur, that reaches more than 80% at times  $\geq 2.7 \times 10^6$  years. This shared reservoir shows a slight preference for HS between 3 and 10% of the total amount of sulphur, depending on the age of the cloud. This result is in accordance with the upper limit on the abundance of  $H_2S$  derived from observations in grains ices.

The above results are also true when using an elemental abundance of sulphur of  $[S]_{\text{ini}} = 5 \times 10^{-6}$  (3 times depleted), which also allows to reproduce observations of S-bearing species in dark clouds. Moreover, this repartition of the sulphur aligns with the common idea that the reservoirs of sulphur in dark clouds are either in a unobservable gas phase form (such as atomic S) or trapped in grain ices under  $H_2S$  form due to successive hydrogenations of atomic S adsorbed on grains surface. Unfortunately, the reservoirs I found are yet unobservable, especially because current instruments lack the InfraRed sensibility needed to observe HS and  $H_2S$  in grain ices.

**Perspectives:** The ability to reproduce observations of sulphur bearing species in dark clouds using as elemental abundance its cosmic one paves the way to numerous possible sulphur studies in star forming regions. However, to confirm my results,



---

better observational constraints on  $\text{H}_2\text{S}$  in grains ices is necessary. As an example, regarding the possible reservoirs, as the solid  $\text{H}_2\text{S}$  should be released in the gas phase during star formation, observations could be conducted in regions such as shocks or protoplanetary disks to confirm  $\text{H}_2\text{S}$ 's role of sulphur reservoir. The future launch of the James Webb Space Telescope (JWST) should allow such a better characterization of the sulphur reservoirs in dark clouds. More importantly, the effects of the enhancement of the model as well as its sulphur network proves the importance of keeping on updating chemical models and networks to ensure correct astrochemical modeling.

## A NEW LOOK AT SULPHUR CHEMISTRY IN HOT CORES AND CORINOS

During the second part of my thesis, I aimed to take a comprehensive look at the chemistry of sulphur in hot cores in the light of the results obtained in dark clouds. A secondary objective was to assess the consequences of the geometrical and dynamical simplification commonly used to model such complex objects. In order to do so, I first conducted an extensive study with simple 0D models of the chemistry of the main S-bearing species observed towards hot cores, using two pre-collapse compositions: an evolved and a less evolved dark clouds. Then I presented and compared the results from two types of models (1D static and 0D dynamic), in order to highlight the sensitivity of chemistry to the choice of model used in astrochemical studies, especially for hot cores.

First, my 0D extensive study highlighted five main results:

1. The total amount of reactive oxygen in the gas phase is critically depending on the pre-collapse composition of the hot core (cf table 3.4) as well as the hot core temperature;
2. Sulphur chemistry in hot and dense gas depends also highly on the pre-collapse composition, mainly because of its impact on reactive atomic oxygen, carbon and hydrogen, which all participate actively in most of the sulphur chemistry in such environment;
3. Sulphur chemistry in hot and dense gas depends highly on the temperature, partly because it is directly and indirectly linked with hydrocarbon evaporated from grain ices, and their main destruction products  $\text{CH}_2$  and  $\text{CH}_3$ ;
4. I found efficient paths of formation of gas phase  $\text{H}_2\text{S}$  that could be responsible for its overestimation in most of the hot core results. Studies of the gas phase chemistry of this species need to be continued to ensure the relevance of the network.
5. I found agreement between the models ran with an evolved pre-collapse composition and the observations in Orion KL, as well as with one of the model ran with



the less evolved pre-collapse composition and observations in the hot corino of IRAS 16293-2422. These results suggest that using as elemental abundance of sulphur the cosmic one, the NAUTILUS chemical model can not only reproduce dark clouds observations but can also reproduce hot cores and corinos observations.

Second, my study of the 1D static and 0D dynamic models led to the following conclusions:

1. The pre-collapse chemical composition of the parent cloud is a key parameter for 1D static models of sulphur chemistry in hot cores. Indeed, the computed abundances showed that it can imply differences up to six orders of magnitude for a given species in the hot core. However, the pre-collapse composition appears to only have a small impact on the chemical composition of the envelope. Finally the 1D model shows that a hot core that was formed from a young parent cloud will be poor in  $\text{H}_2\text{S}$  and rich in  $\text{SO}_2$ , while a hot core formed from a more evolved parent cloud would be rich in  $\text{H}_2\text{S}$  and  $\text{H}_2\text{CS}$ .
2. The 0D dynamic models conducted in this work revealed only small differences between the results of the less evolved and the evolved pre-collapse chemical composition, showing only a weak dependence of the hot core sulphur chemistry on the pre-collapse compositions. Indeed, for both cases the model predicts high abundances of  $\text{H}_2\text{S}$  and  $\text{OCS}$  and low abundances of  $\text{SO}_2$  and  $\text{SO}$ . However, this result is thought to be due to the rather long free-fall time used in the model, which would let enough time for sulphur to be adsorbed on grains and to form mainly  $\text{H}_2\text{S}$  and  $\text{OCS}$  in the envelope before thermal depletion. It is expected that for a shorter free-fall time the differences between the two pre-collapse composition cases would be larger.

Finally, the comparison between the 1D static and 0D dynamic models displayed large differences on the computed abundances that can go as high as six orders of magnitude in the hot core. This result highlights the sensitivity to the choice of models in astrochemical studies, especially when comparing results with observations, or with results from other papers.

**Perspectives:** The extensive study of the main sulphur bearing species in hot cores and corinos can be used as a reference for the future modeling of sulphur chemistry in these regions. The variations of the chemical compositions with the pre-collapse composition and the physical parameters give hints on the reasons for the differences found in hot cores and corinos observations, and should be investigated further. Moreover, future work should focus on the importance of the free-fall time, since it could also explain the large variety of abundances of S-bearing species observed in hot cores.

---

## CONSTRAINING THE INITIAL PHYSICAL PARAMETERS OF COLLAPSING PRESTELLAR CORES

For the final part of my thesis, I have worked on chemical study of Class 0 protostars formation, with the aim of developing a method to constraint their initial physical parameters of collapse (IPPC). The study was based on a dataset of 110 radiation hydrodynamical 1D physical models of collapsing prestellar cores through the formation of the first and second Larson's core. From this dataset I extracted the outputs of 16 parcels of material per model, accordingly to the validity domain of the NAUTILUS chemical model, that I treated independently from each other for statistical purposes. I then ran 0D dynamical chemical models on each of the 1760 resulting cells.

As the initial idea of my study was to use such a large dataset to infer statistical results, I first tried to find possible tracers of the IPPC by studying their respective correlations with each of the abundance distribution of the species present in the chemical network. In order to do so, I defined two physical regions in the protostellar envelope from the water abundance distribution: the Envelope Region (ER) and the Hot Corino Region (HCR). As the correlation obtained for the ER were mostly inconclusive, I focused my study on the correlation within the HCR. Despite the fact that I found no satisfactory correlations with  $M_0$ , my study shows for the four remaining IPPC  $T_0$ ,  $R_0$ ,  $\rho_0$  and  $t_{\text{ff}}$  that numerous possible tracers were good candidates. I presented the results on four of the tracer candidates observed in IRAS 16293-2422 at the light of their respective chemistries:  $\text{CH}_3\text{CN}$ ,  $\text{H}_2\text{CS}$ ,  $\text{NS}$ , and  $\text{OCS}$ .  $\text{H}_2\text{CS}$  was found to be a possible tracer for the free-fall time and the initial density, while the three remaining species are found to be possible tracers of the initial temperature of the parent prestellar core.

In order to work on the ER dataset, I also developed a simple method of comparison of the abundance distributions with the observations. From this method I was able to derive the IPPC for 12 Class 0 protostars from observations of 7 to 19 species towards their envelopes. Moreover, all the constraints were obtained with the percentage of agreement between species of more than 85%, which implies confidence in the method and its results. The specific result obtained for each source could be of great interest for the future modeling of their chemistry. Looking at the results for each IPPC, I was also able to derive the following probabilities for low-mass protostars. It should be noted that these probabilities are defined within the sample of 12 sources I used, and could therefore evolve using a larger sample of sources:

- The probability for them to form from parent prestellar cores with masses  $\leq 1 M_{\odot}$  appears to be of only 5%, while the favored interval  $[2 ; 4] M_{\odot}$  reaches a probability of 68%. The outermost interval  $[6 ; 8] M_{\odot}$  corresponds to a total probability of 26% and could therefore correspond to a non-negligible number of low-mass protostars,

- The initial temperatures, which are the most constrained IPPC, are efficiently constrained between 10 and 15 K, with all sources agreeing with either or both values. Hence, the total probability for low-mass sources to form in prestellar cores with such temperatures reaches 94%. This result hints that, even if it is theoretically possible, low-mass star would tend not to form from hotter parent cores ( $T_0 \geq 20$  K),
- The initial radii are also well constrained with the method because of their correlation with initial densities. The result shows that low-mass stars form preferentially in vast parent prestellar cores of  $R_0 \geq 20000$  AU, with a probability of 77%. This limit is however very model dependent since the chosen value for  $R_0$  in the original dataset are highly spaced when higher than 7500 AU,
- Finally, the most interesting result regarding the initial densities and the free-fall times is that low-mass stars appear to have a ridiculously low probability (0.8%) to form in parent prestellar cores of density higher than  $10^7 \text{ part.cm}^{-3}$  ( $t_{\text{ff}} < 17$  kyrs). Moreover, 70% of low-mass stars appear to be born in cores with densities within the interval  $[5.97 \times 10^4 ; 2.02 \times 10^5] \text{ part.cm}^{-3}$  (respectively  $t_{\text{ff}} \in [105.01 ; 192.92]$  kyrs). Finally the fact that the possible values obtained for all sources span between a few  $10^4$  and  $10^6 \text{ part.cm}^{-3}$  (20 to 192 kyrs for the free-fall time) hints that low-mass stars can form in parent cores with various possible densities.

Another interesting results of this study is that two sources (IRAS 16293-2422 and VLA1623) have constraints on  $R_0$ ,  $\rho_0$  and  $t_{\text{ff}}$  within intervals which are not the favored ones, hinting that they could be representatives of a specific type of protostars which forms from medium-sized prestellar cores with higher densities (respectively smaller free-fall time) than the majority of low-mass protostars considered in my sample.

**Perspectives:** This last study proves the potential of such large scale chemical modeling study, notably the ability to put new constraints on the modeling of the formation of low-mass stars, as well as finding chemical tracers of physical parameters. Regarding the tracers of IPPC I found, simultaneous observations of  $\text{CH}_3\text{CN}$ , NS and OCS in protostellar envelopes at high angular resolution could allow to derive their respective initial temperatures of collapse  $T_0$ . Moreover, I only used here the data at the final time of the physico-chemical model, and other results could be found using data at different timesteps. For example, one could search chemical tracers of the elusive FHSC stage, which would help to confirm the various observations of possible candidates for FHSC, and therefore suggest new hints on their physico-chemical parameters. To that purpose, I submitted a proposal of observations with the Plateau de Bure Interferometer which is currently observed. Plus, as more and more observations of protostars are conducted, studies should be conducted to enlarge the sample of sources I used and therefore refine the probabilities. Finally, the constant improve of chemical models and observations should allow to build larger datasets and precise the presented results.



# SUMMARY OF SULPHUR COMPOUNDS REACTIONS REVIEW

In the following I present the table of reactions added or reviewed in the enhanced network which results are presented in chapter 2.  $\alpha$ ,  $\beta$ , and  $\gamma$  are the coefficient used to compute the Arrhenius-Kooij reaction rate  $k(T) = \alpha(T/300)^\beta \times \exp(-\gamma/T)$ . Note that in that case  $\gamma = E_A$ . In some specific cases described below, they are used in another formulation of the reaction rate.

For reactions between ions and neutral species with a dipole moment (indicated by the mention "Ionpol1-2" in the comments section of the table), the reaction rate coefficients are computed using the Su-Chesnavich capture approach (see discussions in [Woon and Herbst, 2009](#); [Wakelam et al., 2010](#)). In that case the reaction rate is expressed using two formulas, one for lower and one for higher temperatures. The temperature at which we change formula is computed by the relation:

$$T_m = \frac{\mu_D^2}{(8\alpha_p k_B)} \quad (\text{A.1})$$

where  $\mu_D$  is the dipole moment (in statC.cm) ,  $\alpha_p$  the dipole polarizability (in cm<sup>3</sup>) and  $k_B$  the Boltzmann constant (in erg.K<sup>-1</sup>). Hence the reaction rate (in cm<sup>3</sup>.molecule<sup>-1</sup>.s<sup>-1</sup>) is computed following:

$$k_{T \leq T_m} = \alpha\beta(0.62 + 0.4767\gamma(300/T)^{0.5}) \quad (\text{A.2})$$

$$k_{T > T_m} = \alpha\beta(1 + 0.0967\gamma(300/T)^{0.5} + (\gamma^2/10.526)(300/T)) \quad (\text{A.3})$$

All of these formalisms are described in [Wakelam et al. \(2012\)](#).

# A. SUMMARY OF SULPHUR COMPOUNDS REACTIONS REVIEW

Table A.1: Table of the sulphur compounds reactions added or reviewed in the network studied in chapter 2

N°	Reaction		$\alpha$	$\beta$	$\gamma$	References / Comments
GAS PHASE REACTIONS						
1.	He <sup>+</sup> + HNCS	→ HNCS <sup>+</sup> + He	0.1	3.0E-9	2.92	KIDA, Ionpol1-2 ( $T_m = 638$ K), (Gronowski and Kolos, 2014)
		→ HNC + S <sup>+</sup> + He	0.30	3.0E-9	2.92	
		→ HCN + S <sup>+</sup> + He	0.20	3.0E-9	2.92	
		→ H + CN + S <sup>+</sup> + He	0.30	3.0E-9	2.92	
		→ NH <sup>+</sup> + CS + He	0.10	3.0E-9	2.92	
2.	He <sup>+</sup> + HSCN	→ HSCN <sup>+</sup> + He	0.20	2.8E-9	5.17	KIDA, Ionpol1-2 ( $T_m = 2005$ K), (Gronowski and Kolos, 2014)
		→ SH <sup>+</sup> + CN + He	0.40	2.8E-9	5.17	
		→ H + NCS <sup>+</sup> + He	0.40	2.8E-9	5.17	
3.	He <sup>+</sup> + HCNS	→ HCNS <sup>+</sup> + He	0.10	2.7E-9	5.45	Capture rate theory, Ionpol1-2 ( $T_m = 2075$ K)
		→ HCN + S <sup>+</sup> + He	0.30	2.7E-9	5.45	
		→ HNC + S <sup>+</sup> + He	0.20	2.7E-9	5.45	
		→ H + CN + S <sup>+</sup> + He	0.20	2.7E-9	5.45	
		→ CH <sup>+</sup> + NS + He	0.20	2.7E-9	5.45	
4.	H <sup>+</sup> + H <sub>2</sub> S	→ H <sub>2</sub> S <sup>+</sup> + H	0.85	4.51E-9	1.77	KIDA, Ionpol1-2 ( $T_m = 233$ K), (Smith et al., 1992)
		→ HS <sup>+</sup> + H <sub>2</sub>	0.15	4.51E-9	1.77	
5.	H <sup>+</sup> + CS	→ CS <sup>+</sup> + H	1.0	4.89E-9	3.28	KIDA, Ionpol1-2 ( $T_m = 800$ K)
6.	H <sup>+</sup> + C <sub>2</sub> S	→ C <sub>2</sub> S <sup>+</sup> + H	1.0	6.2E-9	4.12	KIDA, Ionpol1-2 ( $T_m = 800$ K)
7.	H <sup>+</sup> + C <sub>3</sub> S	→ C <sub>3</sub> S <sup>+</sup> + H	1.0	7.33E-9	4.39	KIDA, Ionpol1-2 ( $T_m = 800$ K)
8.	H <sup>+</sup> + SO	→ SO <sup>+</sup> + H	1.0	4.38E-9	2.93	KIDA, Ionpol1-2 ( $T_m = 800$ K)
9.	H <sup>+</sup> + SO <sub>2</sub>	→ SO <sub>2</sub> <sup>+</sup> + H	0.5	4.2E-9	3.1	Capture rate theory, Ionpol1-2 ( $T_m = 654$ K)
		→ SO <sup>+</sup> + OH	0.5	4.2E-9	3.1	
10.	H <sup>+</sup> + H <sub>2</sub> CS	→ H <sub>2</sub> CS <sup>+</sup> + H	0.25	5.3E-9	2.61	(Sen et al., 1992)
		→ HCS <sup>+</sup> + H <sub>2</sub>	0.50	5.3E-9	2.61	
		→ CS <sup>+</sup> + H + H <sub>2</sub>	0.25	5.3E-9	2.61	
11.	H <sup>+</sup> + CH <sub>3</sub> SH	→ CH <sub>3</sub> S <sup>+</sup> + H <sub>2</sub>	0.50	5.5E-9	2.3	(Anicich, 2003)
		→ CH <sub>3</sub> <sup>+</sup> + H <sub>2</sub> S	0.25	5.5E-9	2.3	
		→ HCS <sup>+</sup> + H <sub>2</sub> + H <sub>2</sub>	0.25	5.5E-9	2.3	
12.	H <sup>+</sup> + HNCS	→ HNCS <sup>+</sup> + H	0.40	5.9E-9	2.92	Ionpol1-2 ( $T_m = 638$ K), (Gronowski and Kolos, 2014)
		→ HNC + SH <sup>+</sup>	0.30	5.9E-9	2.92	
		→ NH + HCS <sup>+</sup>	0.20	5.9E-9	2.92	
		→ H <sub>2</sub> + NCS <sup>+</sup>	0.10	5.9E-9	2.92	
13.	H <sup>+</sup> + HSCN	→ HSCN <sup>+</sup> + H	0.40	5.46E-9	5.17	Capture rate theory, Ionpol1-2 ( $T_m = 2005$ K)
		→ HCN + SH <sup>+</sup>	0.30	5.46E-9	5.17	
		→ HNC + SH <sup>+</sup>	0.20	5.46E-9	5.17	
		→ H <sub>2</sub> + NCS <sup>+</sup>	0.10	5.46E-9	5.17	
14.	H <sup>+</sup> + HCNS	→ HCNS <sup>+</sup> + H	0.20	5.3E9	5.45	Capture rate theory, Ionpol1-2 ( $T_m = 2075$ K)
		→ CH <sub>2</sub> <sup>+</sup> + NS	0.30	5.3E-9	5.45	
		→ SH <sup>+</sup> + HCN	0.50	5.3E-9	5.45	
15.	H <sup>+</sup> + NH <sub>2</sub> CHS	→ NH <sub>3</sub> + HCS <sup>+</sup>	5.0E-9	0	0	(Anicich, 2003)
		→ NH <sub>2</sub> CHS <sup>+</sup> + H	0			
16.	H <sup>+</sup> + NH <sub>2</sub> CH <sub>2</sub> SH	→ NH <sub>3</sub> + H <sub>3</sub> CS <sup>+</sup>	5.0E-9	0	0	(Anicich, 2003)
		→ NH <sub>2</sub> CH <sub>2</sub> SH <sup>+</sup> + H	0			

Table A.1 – continued from previous page

N°	Reaction	$\alpha$	$\beta$	$\gamma$	Comments
17.	H + SH $\rightarrow$ H <sub>2</sub> + S	2.5E-11	0	0	(Cupitt and Glass, 1975; Peng et al., 1999; Maiti et al., 2004; Nicholas et al., 1979; Tiee et al., 1981; Bradley et al., 1973).
18.	H + H <sub>2</sub> S $\rightarrow$ H <sub>2</sub> + HS	1.50E-11	0	860	(Kurylo et al., 1971; Peng et al., 1999)
19.	H + HS <sup>+</sup> $\rightarrow$ H <sub>2</sub> + S <sup>+</sup>	1.1E-10	0	0	(Millar et al., 1986)
20.	H + H <sub>2</sub> S <sup>+</sup> $\rightarrow$ H <sub>2</sub> + HS <sup>+</sup>	2.2E-10	0	0	(Millar et al., 1986)
21.	H + H <sub>3</sub> S <sup>+</sup> $\rightarrow$ H <sub>2</sub> + H <sub>2</sub> S <sup>+</sup>	6.0E-11	0	0	(Millar et al., 1986)
22.	H + H <sub>2</sub> C <sub>2</sub> S <sup>+</sup> $\rightarrow$ HC <sub>2</sub> S <sup>+</sup> + H <sub>2</sub>	1.0E-10	0	0	Capture rate theory
23.	H + C <sub>2</sub> S $\rightarrow$ CH + CS $\rightarrow$ S + C <sub>2</sub> H	0 0			No exothermic bimolecular exit channel leading to negligible rate constant at low temperature.
24.	H + HCS $\rightarrow$ H <sub>2</sub> + CS $\rightarrow$ H <sub>2</sub> CS	1.5E-10 0	0	0	Capture rate theory
25.	H + CH <sub>3</sub> S $\rightarrow$ H <sub>2</sub> + H <sub>2</sub> CS $\rightarrow$ CH <sub>3</sub> + SH	3.0E-11 3.0E-12	0 0	0	Capture rate theory
26.	H + CH <sub>2</sub> SH $\rightarrow$ H <sub>2</sub> + H <sub>2</sub> CS $\rightarrow$ CH <sub>3</sub> + SH	1.0E-11 1.6E-10	0 0	0	Capture rate theory
27.	H + HC <sub>3</sub> S $\rightarrow$ H <sub>2</sub> + C <sub>3</sub> S $\rightarrow$ C <sub>2</sub> H <sub>2</sub> + CS	1.0E-11 3.0E-11	0 0	0	Capture rate theory.
28.	H + HSO <sup>+</sup> $\rightarrow$ SO <sup>+</sup> + H <sub>2</sub> $\rightarrow$ O + H <sub>2</sub> S <sup>+</sup> $\rightarrow$ HS <sup>+</sup> + OH $\rightarrow$ S + H <sub>2</sub> O <sup>+</sup> $\rightarrow$ S <sup>+</sup> + H <sub>2</sub> O	2.0E-10 0 0 0 0	0	0	By comparison with H + H <sub>2</sub> S <sup>+</sup>
29.	H <sub>2</sub> + S <sup>+</sup> $\rightarrow$ H + HS <sup>+</sup> $\rightarrow$ H <sub>2</sub> S <sup>+</sup> + h $\nu$	8.0E-11 1.0E-17	0 -0.2	9860 0	(Millar et al., 1986), The H <sub>2</sub> S <sup>+</sup> + h $\nu$ rate constant is from KIDA.
30.	H <sub>2</sub> + HS <sup>+</sup> $\rightarrow$ H + H <sub>2</sub> S <sup>+</sup> $\rightarrow$ H <sub>3</sub> S <sup>+</sup> + h $\nu$	7.0E-11 1.4E-16	0 -0.6	6380 0	(Millar et al., 1986), The H <sub>3</sub> S <sup>+</sup> + $\nu$ rate constant is from KIDA.
31.	H <sub>2</sub> + H <sub>2</sub> S <sup>+</sup> $\rightarrow$ H + H <sub>3</sub> S <sup>+</sup>	5.0E-12	0	2900	(Millar et al., 1986)
32.	H <sub>2</sub> + CS <sup>+</sup> $\rightarrow$ H + HCS <sup>+</sup>	4.3E-10	0	0	(Anicich, 2003)
33.	H <sub>2</sub> + C <sub>2</sub> S <sup>+</sup> $\rightarrow$ H + HC <sub>2</sub> S <sup>+</sup>	4.3E-10	0	0	Same as CS <sup>+</sup> + H <sub>2</sub>
34.	H <sub>2</sub> + C <sub>3</sub> S <sup>+</sup> $\rightarrow$ H + HC <sub>3</sub> S <sup>+</sup>	4.3E-10	0	0	Same as CS <sup>+</sup> + H <sub>2</sub>
35.	C <sup>+</sup> + S $\rightarrow$ S <sup>+</sup> + C	1.3E-9	0	0	KIDA
36.	C <sup>+</sup> + H <sub>2</sub> S $\rightarrow$ H <sub>2</sub> S <sup>+</sup> + C $\rightarrow$ HCS <sup>+</sup> + H	0.252 0.748	1.49E-9 1.49E-9	1.77 1.77	KIDA, Ionpol1-2 ( $T_m$ = 253 K), (Anicich, 2003)
37.	C <sup>+</sup> + SO $\rightarrow$ CO + S <sup>+</sup> $\rightarrow$ CO <sup>+</sup> + S $\rightarrow$ CS <sup>+</sup> + O $\rightarrow$ C + SO <sup>+</sup>	0.25 0.25 0.25 0.25	1.4E-9 1.4E-9 1.4E-9 1.4E-9	2.93 2.93 2.93 2.93	KIDA, Ionpol1-2 ( $T_m$ = 643 K).
38.	C <sup>+</sup> + SO <sub>2</sub> $\rightarrow$ SO <sup>+</sup> + CO	1	1.44E-9	2.96	KIDA, Ionpol1-2 ( $T_m$ = 654 K),(Anicich, 2003)
39.	C <sup>+</sup> + CH <sub>3</sub> SH $\rightarrow$ CH <sub>3</sub> <sup>+</sup> + HCS	0.80	1.75E-9	2.33	Capture rate theory,

# A. SUMMARY OF SULPHUR COMPOUNDS REACTIONS REVIEW

Table A.1 – continued from previous page

N°	Reaction		$\alpha$	$\beta$	$\gamma$	Comments
		$\rightarrow \text{CH}_3\text{S}^+ + \text{CH}$	0.20	1.75E-9	2.33	Ionpol1-2 ( $T_m = 407$ K) (Ani-cich, 2003)
40.	$\text{C}^+ + \text{HNCS}$	$\rightarrow \text{HNCS}^+ + \text{C}$ $\rightarrow \text{HNC}^+ + \text{CS}$ $\rightarrow \text{CH}^+ + \text{NCS}$	0.20 0.80 0	1.85E-9 1.85E-9	2.92 2.92	Ionpol1-2 ( $T_m = 638$ K), (Gronowski and Kolos, 2014)
41.	$\text{C}^+ + \text{HSCN}$	$\rightarrow \text{HSCN}^+ + \text{C}$ $\rightarrow \text{HCS}^+ + \text{CN}$	0.20 0.80	1.71E-9 1.71E-9	5.17 5.17	Ionpol1-2 ( $T_m = 2005$ K) (Gronowski and Kolos, 2014)
42.	$\text{C}^+ + \text{HCNS}$	$\rightarrow \text{HCNS}^+ + \text{C}$ $\rightarrow \text{HCN}^+ + \text{CS}$ $\rightarrow \text{HCN} + \text{CS}^+$	0.20 0.20 0.60	1.6E-9 1.6E-9 1.6E-9	5.45 5.45 5.45	Capture rate theory, Ionpol1-2 ( $T_m = 2075$ K)
43.	$\text{C}^+ + \text{NH}_2\text{CHS}$	$\rightarrow \text{H} + \text{HCN} + \text{HCS}^+$	1.0	2.0E-9	5.6	Capture rate theory, Ionpol1-2 ( $T_m = 2000$ K).
44.	$\text{C}^+ + \text{NH}_2\text{CH}_2\text{SH}$	$\rightarrow \text{CH}_2\text{NH}_2 + \text{HCS}^+$	1.0	2.0E-9	1.3	Capture rate theory, Ionpol1-2 ( $T_m = 142$ K).
45.	$\text{C}^+ + \text{C}_2\text{S}$	$\rightarrow \text{C}_2\text{S}^+ + \text{C}$ $\rightarrow \text{C}_3 + \text{S}^+$ $\rightarrow \text{C}_3^+ + \text{S}$ $\rightarrow \text{CS} + \text{C}_2^+$	0.2 0.7 0 0.1	1.95E-9 1.95E-9	4.12 4.12	KIDA, Ionpol1-2 ( $T_m = 800$ K).
46.	$\text{C}^+ + \text{C}_3\text{S}$	$\rightarrow \text{C}_3\text{S}^+ + \text{C}$ $\rightarrow \text{C}_4^+ + \text{S}$ $\rightarrow \text{C}_3^+ + \text{CS}$ $\rightarrow \text{C}_3 + \text{CS}^+$ $\rightarrow \text{C}_2^+ + \text{C}_2\text{S}$	0.25 0.25 0.25 0.25 0	2.28E-9 2.28E-9 2.28E-9 2.28E-9	4.39 4.39 4.39 4.39	KIDA, Ionpol1-2 ( $T_m = 800$ K) (Gingerich et al., 1994) (Belau et al., 2007) (Hochlaf et al., 2007) (Nicolas et al., 2006)
47.	$\text{C} + \text{HS}^+$	$\rightarrow \text{H} + \text{CS}^+$ $\rightarrow \text{S} + \text{CH}^+$ $\rightarrow \text{CH} + \text{S}^+$ $\rightarrow \text{HS} + \text{C}^+$	9.9E-10	0	0	KIDA
48.	$\text{C} + \text{HS}$	$\rightarrow \text{H} + \text{CS}$	2.0E-10	0	0	Capture rate theory
49.	$\text{C} + \text{H}_2\text{S}^+$	$\rightarrow \text{H} + \text{HCS}^+$	1.0E-9	0	0	KIDA
50.	$\text{C} + \text{H}_2\text{S}$	$\rightarrow \text{HCS} + \text{H}$	2.5E-10	0	0	(Deeyamulla and Husain, 2006; Galland et al., 2001)
51.	$\text{C} + \text{SO}$	$\rightarrow \text{CO} + \text{S}$ $\rightarrow \text{CS} + \text{O}$	1.0E-10 1.0E-10	0 0	0 0	Capture rate theory
52.	$\text{C} + \text{NS}$	$\rightarrow \text{CN} + \text{S}$	2.0E-10	0	0	Capture rate theory
53.	$\text{C} + \text{NS}^+$	$\rightarrow \text{CN} + \text{S}^+$ $\rightarrow \text{N} + \text{CS}^+$	6.0E-10 0	0	0	Capture rate theory
54.	$\text{C} + \text{SO}^+$	$\rightarrow \text{CO} + \text{S}^+$ $\rightarrow \text{CS} + \text{O}^+$ $\rightarrow \text{C}^+ + \text{SO}$	6.0E-10 0 0	0	0	Capture rate theory
55.	$\text{C} + \text{HCO}$	$\rightarrow \text{C}_2\text{O} + \text{H}$ $\rightarrow \text{CO} + \text{CH}$	2.0E-11 1.8E-10	0 0	0 0	Capture rate theory
56.	$\text{C} + \text{HCS}$	$\rightarrow \text{H} + \text{C}_2\text{S}$ $\rightarrow \text{S} + \text{C}_2\text{H}$ $\rightarrow \text{CS} + \text{CH}$	2.0E-10 1.0E-10 0	0 0	0 0	Capture rate theory
57.	$\text{C} + \text{H}_2\text{CS}$	$\rightarrow \text{CH}_2 + \text{CS}$ $\rightarrow \text{H} + \text{HCCS}$	1.0E-10 2.0E-10	0 0	0 0	(Husain and Ioannou, 1999)
58.	$\text{C} + \text{CH}_3\text{S}$	$\rightarrow \text{CH}_3 + \text{CS}$	3.0E-10	0	0	Capture rate theory



Table A.1 – continued from previous page

N°	Reaction	$\alpha$	$\beta$	$\gamma$	Comments
59.	C + CH <sub>2</sub> SH → CH <sub>3</sub> + CS	3.0E-10	0	0	Capture rate theory
60.	C + CH <sub>3</sub> SH → CH <sub>3</sub> + HCS	3.0E-10	0	0	(Shannon et al., 2014)
61.	C + SO <sub>2</sub> → CO + SO	8.0E-11	0	0	(Dorthe et al., 1991; Deeyamulla and Husain, 2006)
62.	C + OCS → CS + CO	1.0E-10	0	0	(Dorthe et al., 1991; Deeyamulla and Husain, 2006)
63.	C + HNCS → HNC + CS	1.0E-10	0	0	Capture rate theory
	→ HCN + CS	1.0E-10	0	0	
64.	C + HSCN → HCN + CS	2.0E-10	0	0	Capture rate theory
65.	C + HCNS → HCN + CS	2.0E-10	0	0	Capture rate theory
66.	C + C <sub>2</sub> O → C <sub>2</sub> + CO	2.0E-10	0	0	Capture rate theory
	→ C <sub>3</sub> + O	0			
67.	C + C <sub>2</sub> S → C <sub>2</sub> + CS	2.0E-10	0	0	Capture rate theory
68.	C + HCCS → H + C <sub>3</sub> S	1.0E-10	0	0	Capture rate theory
	→ C <sub>2</sub> H + CS	1.0E-10	0	0	
69.	C + H <sub>2</sub> CCS → C <sub>2</sub> H <sub>2</sub> + CS	3.0E-10	0	0	Capture rate theory
70.	C + NH <sub>2</sub> CHS → CH <sub>2</sub> NH + CS	3.0E-10	0	0	Capture rate theory
71.	C + NH <sub>2</sub> CHO → CH <sub>2</sub> NH + CO	3.0E-10	0	0	Capture rate theory
72.	C + NH <sub>2</sub> CH <sub>2</sub> SH → CH <sub>3</sub> NH <sub>2</sub> + CS	3.0E-10	0	0	Capture rate theory
73.	C + C <sub>3</sub> S → C <sub>3</sub> + CS	3.0E-10	0	0	Capture rate theory
74.	C + HC <sub>3</sub> S → C <sub>2</sub> H + C <sub>2</sub> S	0	0	0	Capture rate theory
	→ H + C <sub>4</sub> S	5.0E-11	0	0	
	→ l-C <sub>3</sub> H + CS	5.0E-11	0	0	
	→ c-C <sub>3</sub> H + CS	5.0E-11	0	0	
75.	C + C <sub>4</sub> S → C <sub>4</sub> + CS	2.0E-10	0	0	Capture rate theory
76.	CH + CS → C <sub>2</sub> S + H	1.5E-10	0	0	(Le Picard and Canosa, 1998)
	→ C <sub>2</sub> H + S	5.0E-11	0	0	
77.	CH + C <sub>3</sub> S → H + C <sub>4</sub> S	1.0E-10	0	0	By comparison with
	→ CS + l-C <sub>3</sub> H	1.0E-10	0	0	CH + alkenes, alkynes
78.	CH <sub>2</sub> + NS → HCNS + H	4.0E-11	0	0	(Fikri et al., 2002; Eshchenko et al., 2002)
79.	CH <sub>3</sub> <sup>+</sup> + CS → CH <sub>3</sub> CS <sup>+</sup> + hν	1.0E-13	-1.0	0	By comparison with CH <sub>3</sub> <sup>+</sup> + CO
80.	CH <sub>3</sub> <sup>+</sup> + H <sub>2</sub> S → CH <sub>3</sub> S <sup>+</sup> (CH <sub>2</sub> SH <sup>+</sup> ) + H <sub>2</sub>	1.00	2.48E-10	1.77	Ionpol1-2 ( <i>T<sub>m</sub></i> = 253 K) (Anichich, 2003)
81.	C <sub>2</sub> H + CS → C <sub>3</sub> S + H	2.0E-10	0	0	(Lander et al., 1990; Petrie, 1996)
82.	C <sub>2</sub> H + C <sub>3</sub> S → H + C <sub>5</sub> S	1.0E-10	0	0	By comparison with
	→ CS + C <sub>4</sub> H	1.0E-10	0	0	CH + alkenes, alkynes
83.	C <sub>2</sub> H + CH <sub>3</sub> SH → C <sub>2</sub> H <sub>2</sub> + CH <sub>3</sub> S	1.0E-10	0	0	By comparison with CN +
	→ C <sub>2</sub> H <sub>2</sub> + CH <sub>2</sub> SH	3.0E-11	0	0	CH <sub>3</sub> SH and C <sub>2</sub> H + CH <sub>3</sub> OH
84.	C <sub>2</sub> H <sub>3</sub> + CS → H + H <sub>2</sub> C <sub>3</sub> S	3.0E-12	0	300	See appendix A of Vidal et al. (2017)
85.	CN + CH <sub>3</sub> SH → HCN + CH <sub>3</sub> S	2.0E-10	0	0	(Decker and Macdonald, 2001)
	→ HCN + CH <sub>2</sub> SH	7.0E-11	0	0	
86.	N + HS <sup>+</sup> → H + NS <sup>+</sup>	7.4E-10	0	0	KIDA
	→ S + NH <sup>+</sup>	0			
	→ S <sup>+</sup> + NH	0			



# A. SUMMARY OF SULPHUR COMPOUNDS REACTIONS REVIEW

Table A.1 – continued from previous page

N°	Reaction	$\alpha$	$\beta$	$\gamma$	Comments
87.	N + HS $\rightarrow$ H + NS	1.0E-10	0	0	KIDA
88.	N + H <sub>2</sub> S <sup>+</sup> $\rightarrow$ H <sub>2</sub> + NS <sup>+</sup>	7.90E-10	0	0	KIDA
	$\rightarrow$ NH + HS <sup>+</sup>	0			
	$\rightarrow$ NH <sup>+</sup> + HS	0			
89.	N + NS $\rightarrow$ N <sub>2</sub> + S	4.0E-11	-0.2	20	Equal to N + NO rate constant
90.	N + NS <sup>+</sup> $\rightarrow$ N <sub>2</sub> + S <sup>+</sup>	6.0E-10	0	0	Capture rate theory
91.	N + SO <sup>+</sup> $\rightarrow$ NO <sup>+</sup> + S	0			
	$\rightarrow$ NO + S <sup>+</sup>	0			
	$\rightarrow$ O + NS <sup>+</sup>	5.0E-11	0	0	(Fehsenfeld and Ferguson, 1973)
92.	N + HCS $\rightarrow$ HCN + S	1.0E-10	0.17	0	Capture rate theory
93.	N + CH <sub>3</sub> S $\rightarrow$ CH <sub>3</sub> + NS	6.00E-11	0	0	Capture rate theory
94.	N + CH <sub>2</sub> SH $\rightarrow$ HCN + H <sub>2</sub> S	6.00E-11	0	0	Capture rate theory
95.	N + HCCS $\rightarrow$ HCN + CS	8.0E-11	0	0	Capture rate theory
96.	N + C <sub>2</sub> S $\rightarrow$ CN + CS	3.0-11	0.17	0	Capture rate theory
97.	N + HC <sub>3</sub> S $\rightarrow$ HCN + C <sub>2</sub> S	1.0E-10	0	0	Capture rate theory
98.	N + C <sub>4</sub> S $\rightarrow$ CN + C <sub>3</sub> S	1.5E-11	0.17	0	Capture rate theory
	$\rightarrow$ C <sub>3</sub> N + CS	1.5E-11	0.17	0	
99.	NH + CS $\rightarrow$ HNC + S	1.0E-11	0	1200	See appendix A of Vidal et al. (2017)
100.	NH + HCS $\rightarrow$ HNCS + H	5.0E-11	0	0	Capture rate theory
101.	NH + HCS <sup>+</sup> $\rightarrow$ HNCS <sup>+</sup> + H	1.0	7.2E-10	5.1	Capture rate theory, Ionpol1-2 ( $T_m = 1729$ K).
102.	NH + CCS $\rightarrow$ HCN + CS	2.0E-11	0	0	Capture rate theory
	$\rightarrow$ HNC + CS	2.0E-11	0	0	
103.	NH <sub>2</sub> <sup>+</sup> + CS $\rightarrow$ H <sub>2</sub> NCS <sup>+</sup> + h $\nu$	2.4E-11	-1.0	0	(Adams et al., 1980)
104.	NH <sub>2</sub> + CS $\rightarrow$ HNCS + H	1.0E-12	0	600	See appendix A of Vidal et al. (2017)
105.	NH <sub>2</sub> + HCS <sup>+</sup> $\rightarrow$ H <sub>2</sub> NCS <sup>+</sup> + H	0.998	9.0E-10	4.7	KIDA, Ionpol1-2 ( $T_m = 1648$ K)
	$\rightarrow$ HNCSH <sup>+</sup> + H	0.002	9.0E-10	4.7	(Gronowski and Kolos, 2014)
106.	NH <sub>3</sub> <sup>+</sup> + CS $\rightarrow$ H <sub>2</sub> NCS <sup>+</sup> + H	1.0E-9	-0.4	0	Capture rate theory
107.	NH <sub>3</sub> + HCS <sup>+</sup> $\rightarrow$ CS + NH <sub>4</sub> <sup>+</sup>	1.0	9.5E-10	3.8	KIDA, Ionpol1-2 ( $T_m = 1068$ K) (Gronowski and Kolos, 2014)
108.	O + HS <sup>+</sup> $\rightarrow$ OH + S <sup>+</sup>	2.9E-10	0	0	KIDA
	$\rightarrow$ H + SO <sup>+</sup>	2.9E-10	0	0	
109.	O + HS $\rightarrow$ H + SO	1.60E-10	0.17	0	KIDA (Cupitt and Glass, 1975).
110.	O + H <sub>2</sub> S <sup>+</sup> $\rightarrow$ OH + HS <sup>+</sup>	3.1E-10	0	0	KIDA
	$\rightarrow$ H <sub>2</sub> + SO <sup>+</sup>	3.1E-10	0	0	
111.	O + NS $\rightarrow$ NO + S	3.0E-11	0	0	Equal to high pressure rate constant from the O + NO $\rightarrow$ NO <sub>2</sub> reaction
	$\rightarrow$ SO + N	0.0			
112.	O + NS <sup>+</sup> $\rightarrow$ NO <sup>+</sup> + S	6.1E-10	0	0	KIDA
	$\rightarrow$ NO + S <sup>+</sup>	0			
113.	O + CH <sub>3</sub> <sup>+</sup> $\rightarrow$ H <sub>2</sub> + HCO <sup>+</sup>	2.05E-10	0	0	(Anicich, 2003)
	$\rightarrow$ H <sub>2</sub> + HOC <sup>+</sup>	2.05E-10	0	0	(Scott et al., 2000)
	$\rightarrow$ H <sub>2</sub> CO <sup>+</sup> + H	1.0E-15	0	0	

Table A.1 – continued from previous page

N°	Reaction	$\alpha$	$\beta$	$\gamma$	Comments
114.	O + CS $\rightarrow$ CO + S	2.61E-10	0	758	(Lilenfeld and Richardson, 1977)
115.	O + CS <sup>+</sup> $\rightarrow$ CO + S <sup>+</sup> $\rightarrow$ CO <sup>+</sup> + S	0 6.0E-11	0	0	KIDA
116.	O + HCS $\rightarrow$ H + OCS $\rightarrow$ HS + CO $\rightarrow$ OH + CS $\rightarrow$ S + HCO	1.0E-10 0 0 0	0 0	0	(Rice et al., 1993) (Rice and Chabalowski, 1994)
117.	O + CH <sub>3</sub> S $\rightarrow$ CH <sub>3</sub> + SO	4.0E-11	0	0	(Ewig et al., 1987)
118.	O + CH <sub>2</sub> SH $\rightarrow$ H <sub>2</sub> CO + HS $\rightarrow$ H <sub>2</sub> CS + OH	4.0E-11 4.0E-11	0 0	0	(Grotheer et al., 1989)
119.	O + C <sub>2</sub> H <sub>3</sub> <sup>+</sup> $\rightarrow$ H <sub>2</sub> + HC <sub>2</sub> O <sup>+</sup> $\rightarrow$ H + H <sub>2</sub> C <sub>2</sub> O <sup>+</sup> $\rightarrow$ CH <sub>3</sub> <sup>+</sup> + CO	0 8.5E-11 5.0E-12	0 0 0	0	(Scott et al., 2000)
120.	O + HCNS $\rightarrow$ HCO + NS $\rightarrow$ HCN + SO	5.0E-10 5.0E-10	0 0	0	See appendix A of Vidal et al. (2017)
121.	O + HCCS $\rightarrow$ HCO + CS	1.6E-10	0	0	Capture rate theory
122.	O + C <sub>2</sub> S $\rightarrow$ CS + CO	9.0E-11	0	0	(Shackleford et al., 1972; Bauer et al., 1985)
123.	O + C <sub>3</sub> S $\rightarrow$ CO + C <sub>2</sub> S	1.94E-11	0	231	KIDA.
124.	O + HC <sub>3</sub> S $\rightarrow$ OH + C <sub>3</sub> S $\rightarrow$ HCO + C <sub>2</sub> S	5.0E-11 5.0E-11	0 0	0	Capture rate theory
125.	O + C <sub>4</sub> S $\rightarrow$ C <sub>3</sub> S + CO $\rightarrow$ CS + C <sub>3</sub> O	9.0E-11 1.0E-11	0 0	0	Capture rate theory
126.	OH + CS $\rightarrow$ OCS + H $\rightarrow$ SH + CO	1.7E-10 3.0E-11	0 0	0	(Adriaens et al., 2010) (Rice et al., 1993)
127.	OH + SO $\rightarrow$ SO <sub>2</sub> + H	8.2E-11	0	0	(Blitz et al., 2000; Jourdain et al., 1979)
128.	OH + H <sub>2</sub> S $\rightarrow$ H <sub>2</sub> O + HS	4.0E-12	-0.2	0	(Lin et al., 1985; Mousavipour et al., 2003; Ellingson and Truhlar, 2007)
129.	OH + CH <sub>3</sub> SH $\rightarrow$ H <sub>2</sub> O + CH <sub>3</sub> S $\rightarrow$ H <sub>2</sub> O + CH <sub>2</sub> SH	8.0E-12 2.5E-11	-0.4 -0.4	0	(Hynes and Wine, 1987) (Butkovskaya and Setser, 1999)
130.	OH + C <sub>3</sub> S $\rightarrow$ CO + HCCS $\rightarrow$ H + SC <sub>3</sub> O	2.0E-10 0	0	0	Capture rate theory
131.	S <sup>+</sup> + CH $\rightarrow$ H + CS <sup>+</sup>	1.0	1.12E-9	3.33	KIDA, Ionpol1-2 ( $T_m = 800$ K)
132.	S <sup>+</sup> + CH <sub>2</sub> $\rightarrow$ H + HCS <sup>+</sup>	1.0	1.09E-9	1.41	KIDA, Ionpol1-2 ( $T_m = 149$ K)
133.	S <sup>+</sup> + CH <sub>3</sub> $\rightarrow$ H + H <sub>2</sub> CS <sup>+</sup>	3.0E-10	0	0	Similar to S <sup>+</sup> + CH <sub>4</sub>
134.	S <sup>+</sup> + CH <sub>4</sub> $\rightarrow$ H + H <sub>3</sub> CS <sup>+</sup> $\rightarrow$ HCS <sup>+</sup> + H <sub>2</sub> + H	3.0E-10 2.0E-11	0 0	0	(Anicich, 2003)
135.	S <sup>+</sup> + C <sub>2</sub> $\rightarrow$ C + CS <sup>+</sup>	8.1E-10	0	0	KIDA
136.	S <sup>+</sup> + C <sub>2</sub> H $\rightarrow$ H + C <sub>2</sub> S <sup>+</sup>	1.0	1.34E-9	1.34	KIDA, Ionpol1-2 ( $T_m = 133$ K)
137.	S <sup>+</sup> + C <sub>2</sub> H <sub>2</sub> $\rightarrow$ H + HC <sub>2</sub> S <sup>+</sup>	9.7E-10	0	0	(Anicich, 2003)
138.	S <sup>+</sup> + C <sub>2</sub> H <sub>4</sub> $\rightarrow$ HCS <sup>+</sup> + CH <sub>3</sub> $\rightarrow$ CH <sub>3</sub> CS <sup>+</sup> + H	7.0E-10 3.0E-10	0 0	0	(Anicich, 2003)
139.	S <sup>+</sup> + c-C <sub>3</sub> H <sub>2</sub> $\rightarrow$ H + HC <sub>3</sub> S <sup>+</sup>	1.0	1.2E-9	5.54	Capture rate theory, Ionpol1-2 ( $T_m = 800$ K)

# A. SUMMARY OF SULPHUR COMPOUNDS REACTIONS REVIEW

Table A.1 – continued from previous page

N°	Reaction	$\alpha$	$\beta$	$\gamma$	Comments
140.	$S^+ + \text{l-C}_3\text{H}_2 \rightarrow \text{H} + \text{HC}_3\text{S}^+$	1.0	1.33E-9	6.11	Capture rate theory, Ionpol1-2 ( $T_m = 800$ K)
141.	$S^+ + \text{C}_4\text{H} \rightarrow \text{H} + \text{C}_4\text{S}^+$ $\rightarrow \text{C}_3\text{H}^+ + \text{CS}$	0.5 0.5	1.42E-9 1.42E-9	1.13 1.13	KIDA, Ionpol1-2 ( $T_m = 94$ K).
142.	$S^+ + \text{C}_4\text{H}_2 \rightarrow \text{c-C}_3\text{H}_2^+ + \text{CS}$ $\rightarrow \text{l-C}_3\text{H}_2^+ + \text{CS}$ $\rightarrow \text{C}_4\text{H}^+ + \text{HS}$ $\rightarrow \text{H} + \text{HC}_4\text{S}^+$ $\rightarrow \text{S} + \text{C}_4\text{H}_2^+$	1.2E-10 0 0 4.8E-10 7.2E-10	0 0 0 0 0	0 0 0 0 0	KIDA
143.	$S^+ + \text{NH}_3 \rightarrow \text{S} + \text{NH}_3^+$	1.0	6.4E-10	3.65	Ionpol1-2 ( $T_m = 800$ K) (Anicich, 2003)
144.	$S^+ + \text{O}_2 \rightarrow \text{SO}^+ + \text{O}$	1.8E-11	0	0	(Anicich, 2003)
145.	$S^+ + \text{NO} \rightarrow \text{S} + \text{NO}^+$	1.0	4.0E-10	0.411	Ionpol1-2 ( $T_m = 12$ K) (Anicich, 2003)
146.	$S^+ + \text{H}_2\text{S} \rightarrow \text{S}_2^+ + \text{H}_2$ $\rightarrow \text{S}_2\text{H}^+ + \text{H}$ $\rightarrow \text{H}_2\text{S}^+ + \text{S}$	0.75 0.25 0	8.2E-10 8.2E-10	1.77 1.77	Ionpol1-2 ( $T_m = 233$ K) (Anicich, 2003)
147.	$\text{S} + \text{H}_3^+ \rightarrow \text{HS}^+ + \text{H}_2$ $\rightarrow \text{H} + \text{H}_2\text{S}^+$	2.0E-9 0.4E-9	0 0	0 0	(Milligan and McEwan, 2000)
148.	$\text{S} + \text{HCO}^+ \rightarrow \text{HS}^+ + \text{CO}$	3.30E-10	0	0	KIDA
149.	$\text{S} + \text{N}_2\text{H}^+ \rightarrow \text{HS}^+ + \text{N}_2$	1.1E-9	0	0	KIDA
150.	$\text{S} + \text{CH}^+ \rightarrow \text{H} + \text{CS}^+$ $\rightarrow \text{C} + \text{HS}^+$ $\rightarrow \text{CH} + \text{S}^+$	4.7E-10 4.7E-10 4.7E-10	0 0 0	0 0 0	KIDA
151.	$\text{S} + \text{CH}_3^+ \rightarrow \text{H}_2 + \text{HCS}^+$ $\rightarrow \text{H}_2\text{CS}^+ + \text{H}$	1.40E-9 0	0	0	KIDA
152.	$\text{S} + \text{CH}_5^+ \rightarrow \text{HS}^+ + \text{CH}_4$	1.30E-9	0	0	KIDA
153.	$\text{S} + \text{C}_2\text{H}_2^+ \rightarrow \text{S}^+ + \text{C}_2\text{H}_2$ $\rightarrow \text{H} + \text{HC}_2\text{S}^+$	5.0E-10 5.0E-10	0 0	0 0	Capture rate theory
154.	$\text{S} + \text{C}_2\text{H}_3^+ \rightarrow \text{H}_2 + \text{HC}_2\text{S}^+$ $\rightarrow \text{H} + \text{H}_2\text{C}_2\text{S}^+$ $\rightarrow \text{CH}_3^+ + \text{CS}$	0 1.0E-9 0	0 0	0	Capture rate theory
155.	$\text{S} + \text{C}_2\text{H}_4^+ \rightarrow \text{H} + \text{H}_2 + \text{HC}_2\text{S}^+$ $\rightarrow \text{CH}_3 + \text{HCS}^+$ $\rightarrow \text{CH}_3^+ + \text{HCS}$ $\rightarrow \text{C}_2\text{H}_3^+ + \text{HS}$ $\rightarrow \text{H} + \text{CH}_3\text{CS}^+$ $\rightarrow \text{H}_2 + \text{H}_2\text{C}_2\text{S}^+$	0 1.0E-10 0 0 1.0E-10 1.0E-10	0 0	0 0 0 0	(Anicich, 2003)
156.	$\text{S} + \text{c-C}_3\text{H}_2^+ \rightarrow \text{H} + \text{HC}_3\text{S}^+$ $\rightarrow \text{C}_2\text{H} + \text{HCS}^+$	1.0E-9 0	0	0	KIDA
157.	$\text{S} + \text{l-C}_3\text{H}_2^+ \rightarrow \text{H} + \text{HC}_3\text{S}^+$ $\rightarrow \text{C}_2\text{H} + \text{HCS}^+$	1.0E-9 0	0	0	KIDA
158.	$\text{S} + \text{t-C}_3\text{H}_2^+ \rightarrow \text{H} + \text{HC}_3\text{S}^+$ $\rightarrow \text{C}_2\text{H} + \text{HCS}^+$	1.0E-9 0	0	0	KIDA
159.	$\text{S} + \text{c-C}_3\text{H}_3^+ \rightarrow \text{H}_2 + \text{HC}_3\text{S}^+$ $\rightarrow \text{H} + \text{H}_2\text{C}_3\text{S}^+$ $\rightarrow \text{CS} + \text{C}_2\text{H}_3^+$	1.0E-10 0 0	0	0	See appendix A of Vidal et al. (2017)

Table A.1 – continued from previous page

N°		Reaction	$\alpha$	$\beta$	$\gamma$	Comments
		$\rightarrow \text{HCS}^+ + \text{C}_2\text{H}_2$	4.0E-10	0	0	
160.	$\text{S} + \text{l-C}_3\text{H}_3^+$	$\rightarrow \text{H}_2 + \text{HC}_3\text{S}^+$	1.0E-10	0	0	See appendix A of <a href="#">Vidal et al. (2017)</a>
		$\rightarrow \text{H} + \text{H}_2\text{C}_3\text{S}^+$	2.0E-10	0	0	
		$\rightarrow \text{CS} + \text{C}_2\text{H}_3^+$	0			
		$\rightarrow \text{HCS}^+ + \text{C}_2\text{H}_2$	2.0E-10	0	0	
161.	$\text{S} + \text{CH}$	$\rightarrow \text{CS} + \text{H}$	1.4E-10	0	0	Capture rate theory
162.	$\text{S} + \text{CH}_2$	$\rightarrow \text{HCS} + \text{H}$	1.4E-10	0	0	<a href="#">(Zhang et al., 2004)</a>
		$\rightarrow \text{CS} + \text{H}_2$	0			
163.	$\text{S} + \text{CH}_3$	$\rightarrow \text{H}_2\text{CS} + \text{H}$	1.4E-10	0	0	KIDA
164.	$\text{S} + \text{C}_2$	$\rightarrow \text{CS} + \text{C}$	2.0E-10	0	0	Capture rate theory
165.	$\text{S} + \text{C}_2\text{H}$	$\rightarrow \text{C}_2\text{S} + \text{H}$	1.0E-10	0	0	Capture rate theory
		$\rightarrow \text{CS} + \text{CH}$				
166.	$\text{S} + \text{C}_2\text{H}_3$	$\rightarrow \text{H} + \text{H}_2\text{CCS}$	6.0E-11	0	0	Capture rate theory
		$\rightarrow \text{CH}_3 + \text{CS}$	4.0E-11	0	0	
		$\rightarrow \text{SH} + \text{C}_2\text{H}_2$	1.0E-11	0	0	
167.	$\text{S} + \text{l-C}_3\text{H}$	$\rightarrow \text{CS} + \text{C}_2\text{H}$	7.0E-11	0	0	<a href="#">(Flores et al., 2001, 2002)</a>
		$\rightarrow \text{C}_3\text{S} + \text{H}$	3.0E-11	0	0	
168.	$\text{S} + \text{c-C}_3\text{H}$	$\rightarrow \text{CS} + \text{C}_2\text{H}$	5.0E-11	0	0	<a href="#">(Flores et al., 2002)</a>
		$\rightarrow \text{C}_3\text{S} + \text{H}$	5.0E-11	0	0	
169.	$\text{S} + \text{l,t-C}_3\text{H}_2$	$\rightarrow \text{C}_2\text{H}_2 + \text{CS}$	1.0E-10	0	0	Capture rate theory
		$\rightarrow \text{C}_2\text{H}_2 + \text{CS}$	0	0	0	
		$\rightarrow \text{HC}_3\text{S} + \text{H}$	1.0E-10	0	0	
170.	$\text{S} + \text{c-C}_3\text{H}_2$	$\rightarrow \text{C}_2\text{H}_2 + \text{CS}$	1.0E-10	0	0	See appendix A of <a href="#">Vidal et al. (2017)</a>
		$\rightarrow \text{C}_2\text{H}_2 + \text{CS}$	0			
		$\rightarrow \text{HC}_3\text{S} + \text{H}$	1.0E-10	0	0	
171.	$\text{S} + \text{C}_4$	$\rightarrow \text{C}_3 + \text{CS}$	1.0E-10	0	0	Capture rate theory
172.	$\text{S} + \text{C}_4\text{H}$	$\rightarrow \text{CS} + \text{l-C}_3\text{H}$	5.0E-11	0	0	Capture rate theory
		$\rightarrow \text{C}_4\text{S} + \text{H}$	5.0E-11	0	0	
173.	$\text{S} + \text{C}_6$	$\rightarrow \text{C}_5 + \text{CS}$	1.0E-10	0	0	Capture rate theory
174.	$\text{S} + \text{C}_2\text{N}$	$\rightarrow \text{CS} + \text{CN}$	7.0E-11	0.17	0	Capture rate theory
175.	$\text{S} + \text{H}_2\text{CN}$	$\rightarrow \text{SH} + \text{HCN}$	3.0E-11	0	0	Radical-radical reaction leading to direct H atom abstraction and H + HCNS through H <sub>2</sub> CNS formation
		$\rightarrow \text{SH} + \text{HNC}$	0	0	0	
		$\rightarrow \text{H} + \text{HCNS}$	3.0E-11	0	0	
176.	$\text{S} + \text{C}_3\text{N}$	$\rightarrow \text{CS} + \text{C}_2\text{N}$	1.0E-10	0	0	Capture rate theory
		$\rightarrow \text{C}_2\text{S} + \text{CN}$	0			
177.	$\text{S} + \text{C}_4\text{N}$	$\rightarrow \text{CS} + \text{C}_3\text{N}$	7.0E-11	0.17	0	Capture rate theory
178.	$\text{S} + \text{C}_2\text{S}$	$\rightarrow \text{CS} + \text{CS}$	1.0E-10	0	0	Capture rate theory
179.	$\text{S} + \text{NH}$	$\rightarrow \text{NS} + \text{H}$	1.0E-10	0	0	Capture rate theory
180.	$\text{S} + \text{NH}_2$	$\rightarrow \text{NS} + \text{H}_2$	0			HNS + H exit channel may be endothermic and NS + H <sub>2</sub> may involve high exit transi- tion state. Back dissociation of the H <sub>2</sub> NS complex, first step of the reaction, is then likely fa- vored and we neglect this reac- tion
		$\rightarrow \text{HNS} + \text{H}$				

# A. SUMMARY OF SULPHUR COMPOUNDS REACTIONS REVIEW

Table A.1 – continued from previous page

N°	Reaction	$\alpha$	$\beta$	$\gamma$	Comments
181.	$S + OH \rightarrow SO + H$	6.6E-11	0	0	(Jourdain et al., 1979)
182.	$S + H_2O^+ \rightarrow SO^+ + H_2$	4.0E-10	0	0	Capture rate theory
	$\rightarrow O + H_2S^+$	0	0	0	
	$\rightarrow HS^+ + OH$	4.0E-10	0	0	
	$\rightarrow H + HSO^+$	0	0	0	
	$\rightarrow S^+ + H_2O$	2.0E-10	0	0	
183.	$S + O_2 \rightarrow SO + O$	2.0E-12	-0.6	0	(Lu et al., 2004).
184.	$S + CO^+ \rightarrow CO + S^+$	1.1E-9	0	0	KIDA
185.	$S + HCO \rightarrow H + OCS$	8.0E-11	0	0	(Loison et al., 2012)
	$\rightarrow SH + CO$	4.0E-11	0	0	
186.	$S + CCO \rightarrow CO + CS$	1.0E-10	0	0	(Loison et al., 2012)
	$\rightarrow C + OCS$	0			
187.	$S + C_4S \rightarrow C_3S + CS$	1.0E-10	0	0	Capture rate theory
188.	$S + CH_3O \rightarrow CH_3 + SO$	4.0E-11	0	0	(Ewig et al., 1987)
189.	$S + CH_2OH \rightarrow H_2CO + HS$	4.0E-11	0	0	(Grotheer et al., 1989)
	$\rightarrow H_2CS + OH$	4.0E-11	0	0	
190.	$HS^+ + H_2O \rightarrow S + H_3O^+$	1	8.5E-10	5.41	KIDA
191.	$HS^+ + HNC \rightarrow HNCs^+ + H$	0.1	1.04E-9	6.41	Capture rate theory,
	$\rightarrow HSCN^+ + H$	0	1.04E-9	6.41	Ionpol1-2 ( $T_m = 800$ K)
	$\rightarrow HCNH^+ + S$	0.9	1.04E-9	6.41	
192.	$HS^+ + HCN \rightarrow HNCs^+ + H$	0			Capture rate theory,
	$\rightarrow HCNH^+ + S$	1.0	9.53E-10	6.62	Ionpol1-2 ( $T_m = 800$ K)
193.	$H_2S^+ + HNC \rightarrow HNCsH^+ + H$	0.1	9.97E-10	6.41	Capture rate theory,
	$\rightarrow HCNH^+ + SH$	0.9	9.97E-10	6.41	Ionpol1-2 ( $T_m = 800$ K)
	$\rightarrow H_3S^+ + CN$	0			
194.	$H_2S^+ + HCN \rightarrow HCNH^+ + SH$	1.0	9.46E-10	6.62	Capture rate theory, Ionpol1-2 ( $T_m = 800$ K).
195.	$H_2S + H_3^+ \rightarrow H_2 + H_3S^+$	1	2.67E-9	1.77	KIDA
196.	$H_2S + H_3O^+ \rightarrow H_2O + H_3S^+$	1	1.27E-9	1.77	KIDA
197.	$H_2S + HCO^+ \rightarrow CO + H_3S^+$	1	1.12E-9	1.77	KIDA
198.	$CO + HSO^+ \rightarrow SO + HCO^+$	1.0E-9	0	0	(Hunter and Lias, 1998; Cheng et al., 1997)
199.	$H_2O + HSO^+ \rightarrow SO + H_3O^+$	2.0E-9	0	0	Capture rate theory
200.	$SO + H_3^+ \rightarrow H_2 + HSO^+$	1.0	2.58E-9	2.93	KIDA
201.	$SO + HCO^+ \rightarrow CO + HSO^+$	1.0E-9	0	1500	(Hunter and Lias, 1998; Cheng et al., 1997)
202.	$C_3S + H_3^+ \rightarrow HC_3S^+ + H_2$	1.0	4.29E-9	4.39	Capture rate theory, Ionpol1-2 ( $T_m = 800$ K).
203.	$C_3S + H_3O^+ \rightarrow HC_3S^+ + H_2O$	1.0	1.88E-9	4.39	Capture rate theory, Ionpol1-2 ( $T_m = 800$ K).
204.	$C_3S + HCO^+ \rightarrow HC_3S^+ + CO$	1.0	1.61E-9	4.39	Capture rate theory, Ionpol1-2 ( $T_m = 800$ K).
205.	$CH_3SH + H_3^+ \rightarrow H_2 + CH_3SH_2^+$	1	3.2E-9	2.3	Capture rate theory, Ionpol1-2 ( $T_m = 407$ K).
206.	$CH_3SH + H_3O^+ \rightarrow H_2O + CH_3SH_2^+$	1	1.5E-9	2.3	Capture rate theory, Ionpol1-2 ( $T_m = 407$ K).

Table A.1 – continued from previous page

N°	Reaction	$\alpha$	$\beta$	$\gamma$	Comments
207.	$\text{CH}_3\text{SH} + \text{HCO}^+ \rightarrow \text{CO} + \text{CH}_3\text{SH}_2^+$	1	1.3E-9	2.3	Capture rate theory, Ionpol1-2 ( $T_m = 407$ K).
208.	$\text{HNCS} + \text{H}_3^+ \rightarrow \text{H}_2\text{NCS}^+ + \text{H}_2$ $\rightarrow \text{HNCSH}^+ + \text{H}_2$	0.50 0.50	3.47E-9 3.47E-9	2.92 2.92	KIDA, Ionpol1-2 ( $T_m = 638$ K), (Gronowski and Kolos, 2014)
209.	$\text{HSCN} + \text{H}_3^+ \rightarrow \text{H}_2\text{SCN}^+ + \text{H}_2$ $\rightarrow \text{HNCSH}^+ + \text{H}_2$	0.50 0.50	3.20E-9 3.20E-9	5.17 5.17	KIDA, Ionpol1-2 ( $T_m = 2005$ K), (Gronowski and Kolos, 2014)
210.	$\text{HCNS} + \text{H}_3^+ \rightarrow \text{H}_2\text{CNS}^+ + \text{H}_2$ $\rightarrow \text{HCNSH}^+ + \text{H}_2$	0.50 0.50	3.10E-9 3.10E-9	5.45 5.45	Capture rate theory, Ionpol1-2 ( $T_m = 2075$ K)
211.	$\text{HNCS} + \text{HCO}^+ \rightarrow \text{H}_2\text{NCS}^+ + \text{CO}$ $\rightarrow \text{HNCSH}^+ + \text{CO}$	0.50 0.50	1.32E-9 1.32E-9	2.92 2.92	KIDA, Ionpol1-2 ( $T_m = 638$ K), (Gronowski and Kolos, 2014)
212.	$\text{HSCN} + \text{HCO}^+ \rightarrow \text{H}_2\text{SCN}^+ + \text{CO}$ $\rightarrow \text{HNCSH}^+ + \text{CO}$	0 1.00	1.18E-9 1.18E-9	5.17 5.17	KIDA, Ionpol1-2 ( $T_m = 2005$ K), (Gronowski and Kolos, 2014)
213.	$\text{HCNS} + \text{HCO}^+ \rightarrow \text{H}_2\text{CNS}^+ + \text{CO}$ $\rightarrow \text{HCNSH}^+ + \text{CO}$	0.50 0.50	1.22E-9 1.22E-9	5.45 5.45	Capture rate theory, Ionpol1-2 ( $T_m = 2075$ K)
214.	$\text{H}_2\text{CCS} + \text{H}_3^+ \rightarrow \text{CH}_3\text{CS}^+ + \text{H}_2$	1.0	2.90E-9	2.39	Capture rate theory, Ionpol1-2 ( $T_m = 145$ K).
215.	$\text{H}_2\text{CCS} + \text{HCO}^+ \rightarrow \text{CH}_3\text{CS}^+ + \text{CO}$	1.0	1.17E-9	2.39	Capture rate theory, Ionpol1-2 ( $T_m = 145$ K).
216.	$\text{NH}_2\text{CHS} + \text{H}_3^+ \rightarrow \text{NH}_2\text{CHSH}^+ + \text{H}_2$ $\rightarrow \text{NH}_3\text{CHS}^+ + \text{H}_2$ $\rightarrow \text{NH}_3^+ \text{HCS}^+ + \text{H}_2$	1.0 0 0	3.68E-9	5.6	Capture rate theory, Ionpol1-2 ( $T_m = 2075$ K)
217.	$\text{NH}_2\text{CHS} + \text{HCO}^+ \rightarrow \text{NH}_2\text{CHSH}^+ + \text{CO}$	1.0	1.40E-9	5.6	Capture rate theory, Ionpol1-2 ( $T_m = 2075$ K).
218.	$\text{NH}_2\text{CH}_2\text{SH} + \text{H}_3^+ \rightarrow \text{NH}_3\text{CH}_2\text{SH}^+ + \text{H}_2$	1.0	3.66E-9	1.4	Capture rate theory, Ionpol1-2 ( $T_m = 142$ K).
219.	$\text{NH}_2\text{CH}_2\text{SH} + \text{HCO}^+ \rightarrow \text{NH}_3\text{CH}_2\text{SH}^+ + \text{CO}$	1.0	1.39E-9	1.4	Capture rate theory, Ionpol1-2 ( $T_m = 142$ K).
220.	$\text{S}^+ + \text{e}^- \rightarrow \text{S} + \text{h}\nu$	3.9E-12	-0.63	0	KIDA
221.	$\text{HS}^+ + \text{e}^- \rightarrow \text{H} + \text{S}$	2.0E-7	-0.5	0	KIDA
222.	$\text{H}_2\text{S}^+ + \text{e}^- \rightarrow \text{H} + \text{HS}$ $\rightarrow \text{H} + \text{H} + \text{S}$ $\rightarrow \text{H}_2\text{S} + \text{h}\nu$	1.5E-7 1.5E-7 1.1E-10	-0.5 -0.5 -0.7	0 0 0	KIDA
223.	$\text{H}_3\text{S}^+ + \text{e}^- \rightarrow \text{H} + \text{H}_2\text{S}$ $\rightarrow \text{H}_2 + \text{HS}$ $\rightarrow \text{H} + \text{H} + \text{HS}$ $\rightarrow \text{H} + \text{H}_2 + \text{S}$	4.8E-8 4.2E-8 1.6E-7 2.8E-8	-0.86 -0.86 -0.86 -0.86	0 0 0 0	(Kamińska et al., 2008)
224.	$\text{HSO}^+ + \text{e}^- \rightarrow \text{H} + \text{SO}$ $\rightarrow \text{HS} + \text{O}$ $\rightarrow \text{H} + \text{S} + \text{O}$	1.0E-7 5.0E-8 5.0E-8	-0.5 -0.5 -0.5	0 0 0	Capture rate theory
225.	$\text{HCS}^+ + \text{e}^- \rightarrow \text{S} + \text{CH}$ $\rightarrow \text{H} + \text{CS}$ $\rightarrow \text{H} + \text{C} + \text{S}$	7.86E-7 1.84E-7 0	-0.57 -0.57	0 0	(Montaigne et al., 2005)
226.	$\text{H}_3\text{CS}^+ + \text{e}^- \rightarrow \text{H} + \text{H}_2\text{CS}$ $\rightarrow \text{H} + \text{H} + \text{HCS}$ $\rightarrow \text{H} + \text{H}_2 + \text{CS}$ $\rightarrow \text{CH}_2 + \text{SH}$ $\rightarrow \text{H}_2\text{S} + \text{CH}$	2.2E-7 2.2E-7 2.2E-7 3.8E-8 1.5E-8	-0.78 -0.78 -0.78 -0.78 -0.78	0 0 0 0 0	(Hamberg et al., 2007)
227.	$\text{CH}_3\text{SH}_2^+ + \text{e}^- \rightarrow \text{CH}_3 + \text{H}_2\text{S}$	8.0E-8	-0.59	0	(Geppert et al., 2006)

# A. SUMMARY OF SULPHUR COMPOUNDS REACTIONS REVIEW

Table A.1 – continued from previous page

N°	Reaction	$\alpha$	$\beta$	$\gamma$	Comments
	$\rightarrow \text{CH}_3 + \text{SH} + \text{H}$	4.5E-7	-0.59	0	
	$\rightarrow \text{CH}_2 + \text{H} + \text{H}_2\text{S}$	1.9E-7	-0.59	0	
	$\rightarrow \text{CH}_3\text{SH} + \text{H}$	2.7E-8	-0.59	0	
	$\rightarrow \text{CH}_3\text{S} + \text{H}_2$	5.3E-8	-0.59	0	
	$\rightarrow \text{H}_2\text{CS} + \text{H}_2 + \text{H}$	5.9E-8	-0.59	0	
228.	$\text{HC}_2\text{S}^+ + \text{e}^-$				
	$\rightarrow \text{H} + \text{C}_2\text{S}$	1.5E-7	-0.5	0	See appendix A of
	$\rightarrow \text{CH} + \text{CS}$	7.5E-8	-0.5	0	<a href="#">Vidal et al. (2017)</a>
	$\rightarrow \text{C}_2\text{H} + \text{S}$	7.5E-8	-0.5	0	
229.	$\text{H}_2\text{C}_2\text{S}^+ + \text{e}^-$				
	$\rightarrow \text{H} + \text{HCCS}$	1.5E-7	-0.5	0	See appendix A of
	$\rightarrow \text{H} + \text{H} + \text{C}_2\text{S}$	1.0E-8	-0.5	0	<a href="#">Vidal et al. (2017)</a>
	$\rightarrow \text{CH}_2 + \text{CS}$	1.5E-7	-0.5	0	
230.	$\text{CH}_3\text{CS}^+ + \text{e}^-$				
	$\rightarrow \text{H} + \text{H}_2\text{CCS}$	1.5E-7	-0.5	0	See appendix A of
	$\rightarrow \text{CH}_3 + \text{CS}$	1.5E-7	-0.5	0	<a href="#">Vidal et al. (2017)</a>
231.	$\text{NH}_3\text{CHS}^+ + \text{e}^-$				
	$\rightarrow \text{NH}_3 + \text{CS} + \text{H}$	2.0E-7	-0.5	0	See appendix A of
	$\rightarrow \text{H} + \text{NH}_2\text{CHS}$	1.0E-7	-0.5	0	<a href="#">Vidal et al. (2017)</a>
	$\rightarrow \text{H}_2\text{S} + \text{HCN} + \text{H}$	1.0E-7	-0.5	0	
232.	$\text{HC}_3\text{S}^+ + \text{e}^-$				
	$\rightarrow \text{H} + \text{C}_3\text{S}$	1.0E-7	-0.5	0	See appendix A of
	$\rightarrow \text{C}_2\text{H} + \text{CS}$	1.0E-7	-0.5	0	<a href="#">Vidal et al. (2017)</a>
	$\rightarrow \text{CH} + \text{C}_2\text{S}$	1.0E-7	-0.5	0	
233.	$\text{H}_2\text{C}_3\text{S}^+ + \text{e}^-$				
	$\rightarrow \text{H} + \text{HC}_3\text{S}$	1.0E-7	-0.5	0	See appendix A of
	$\rightarrow \text{CH}_2 + \text{C}_2\text{S}$	1.0E-7	-0.5	0	<a href="#">Vidal et al. (2017)</a>
	$\rightarrow \text{C}_2\text{H}_2 + \text{CS}$	1.0E-7	-0.5	0	
234.	$\text{HC}_4\text{S}^+ + \text{e}^-$				
	$\rightarrow \text{H} + \text{C}_4\text{S}$	1.0E-7	-0.5	0	See appendix A of
	$\rightarrow \text{CH} + \text{C}_3\text{S}$	1.0E-7	-0.5	0	<a href="#">Vidal et al. (2017)</a>
	$\rightarrow \text{C}_2\text{H} + \text{C}_2\text{S}$	1.0E-7	-0.5	0	
	$\rightarrow \text{l-C}_3\text{H} + \text{CS}$	1.0E-7	-0.5	0	
	$\rightarrow \text{C}_4\text{H} + \text{S}$	1.0E-7	-0.5	0	
235.	$\text{HNCS}^+ + \text{e}^-$				
	$\rightarrow \text{HNC} + \text{S}$	1.0E-7	-0.5	0	See appendix A of
	$\rightarrow \text{HCN} + \text{S}$	5.0E-7	-0.5	0	<a href="#">Vidal et al. (2017)</a>
	$\rightarrow \text{NH} + \text{CS}$	1.5E-7	-0.5	0	
236.	$\text{HCNS}^+ + \text{e}^-$				
	$\rightarrow \text{S} + \text{HCN}$	1.5E-7	-0.5	0	See appendix A of
	$\rightarrow \text{CH} + \text{NS}$	1.5E-7	-0.5	0	<a href="#">Vidal et al. (2017)</a>
237.	$\text{HSCN}^+ + \text{e}^-$				
	$\rightarrow \text{HS} + \text{CN}$	1.5E-7	-0.5	0	See appendix A of
	$\rightarrow \text{S} + \text{HCN}$	1.5E-7	-0.5	0	<a href="#">Vidal et al. (2017)</a>
238.	$\text{H}_2\text{NCS}^+ + \text{e}^-$				
	$\rightarrow \text{HNCS} + \text{H}$	1.7E-7	-0.5	0	See appendix A of
	$\rightarrow \text{HSCN} + \text{H}$	1.3E-7	-0.5	0	<a href="#">Vidal et al. (2017)</a>
	$\rightarrow \text{NH}_2 + \text{CS}$	3.0E-7	-0.5	0	
239.	$\text{HNCSH}^+ + \text{e}^-$				
	$\rightarrow \text{HNCS} + \text{H}$	1.5E-7	-0.5	0	Similar reasons than for
	$\rightarrow \text{HSCN} + \text{H}$	1.5E-7	-0.5	0	$\text{H}_2\text{NCS}^+ + \text{e}^-$
	$\rightarrow \text{HNC} + \text{SH}$	1.5E-7	-0.5	0	
	$\rightarrow \text{HCN} + \text{SH}$	1.5E-7	-0.5	0	
240.	$\text{H}_2\text{SCN}^+ + \text{e}^-$				
	$\rightarrow \text{HSCN} + \text{H}$	1.6E-7	-0.5	0	Similar reasons than for
	$\rightarrow \text{HNCS} + \text{H}$	1.4E-7	-0.5	0	$\text{H}_2\text{NCS}^+ + \text{e}^-$
	$\rightarrow \text{H}_2\text{S} + \text{CN}$	2.0E-7	-0.5	0	
	$\rightarrow \text{H} + \text{SH} + \text{CN}$	2.0E-7	-0.5	0	
241.	$\text{H}_2\text{CNS}^+ + \text{e}^-$				
	$\rightarrow \text{HCNS} + \text{H}$	1.0E-7	-0.5	0	See appendix A of
	$\rightarrow \text{CH}_2 + \text{NS}$	3.0E-7	-0.5	0	<a href="#">Vidal et al. (2017)</a>

Table A.1 – continued from previous page

N°	Reaction	$\alpha$	$\beta$	$\gamma$	Comments
	$\rightarrow \text{H} + \text{HCN} + \text{S}$	2.0E-7	-0.5	0	
242.	$\text{HCNSH}^+ + \text{e}^-$				
	$\rightarrow \text{HCNS} + \text{H}$	1.0E-7	-0.5	0	See appendix A of
	$\rightarrow \text{HCN} + \text{SH}$	3.0E-7	-0.5	0	Vidal et al. (2017)
	$\rightarrow \text{H} + \text{CN} + \text{SH}$	2.0E-7	-0.5	0	
243.	$\text{NH}_2\text{CHSH}^+ + \text{e}^-$				
	$\rightarrow \text{NH}_2\text{CHS} + \text{H}$	1.5E-7	-0.5	0	See appendix A of
	$\rightarrow \text{NH}_2 + \text{H}_2\text{CS}$	1.5E-7	-0.5	0	Vidal et al. (2017)
	$\rightarrow \text{NH}_3 + \text{HCS}$	1.5E-7	-0.5	0	
	$\rightarrow \text{NH}_3 + \text{H} + \text{CS}$	1.5E-7	-0.5	0	
244.	$\text{NH}_3\text{CH}_2\text{SH}^+ + \text{e}^-$				
	$\rightarrow \text{NH}_2\text{CH}_2\text{SH} + \text{H}$	1.0E-7	-0.5	0	See appendix A of
	$\rightarrow \text{NH}_3 + \text{CH}_2\text{SH}$	1.0E-7	-0.5	0	Vidal et al. (2017)
	$\rightarrow \text{NH}_3 + \text{H}_2\text{CS} + \text{H}$	4.0E-7	-0.5	0	
<b>GRAIN SURFACE REACTIONS</b>					
245.	$\text{C} + \text{s-H}_2\text{S}$	$\rightarrow \text{s-H}_2\text{CS}$	1.0	0	0 (Ruaud et al., 2015)
246.	$\text{s-H} + \text{s-S}$	$\rightarrow \text{s-HS}$	1.0	0	0 See appendix A of Vidal et al. (2017)
247.	$\text{s-H} + \text{s-HS}$	$\rightarrow \text{s-H}_2\text{S}$	1.0	0	0 See appendix A of Vidal et al. (2017)
248.	$\text{s-H} + \text{s-H}_2\text{S}$	$\rightarrow \text{s-H}_2 + \text{s-HS}$	1.0	0	860 (Kurylo et al., 1971; Peng et al., 1999).
249.	$\text{s-H} + \text{s-CS}$	$\rightarrow \text{s-HCS}$	1.0	0	1000 See appendix A of Vidal et al. (2017)
250.	$\text{s-H} + \text{s-HCS}$	$\rightarrow \text{s-H}_2\text{CS}$	1.0	0	0 See appendix A of
		$\rightarrow \text{s-H}_2 + \text{s-CS}$	0		Vidal et al. (2017)
251.	$\text{s-H} + \text{s-H}_2\text{CS}$	$\rightarrow \text{s-CH}_3\text{S}$	0.5	0	1200 See appendix A of
		$\rightarrow \text{s-CH}_2\text{SH}$	0.5	0	800 Vidal et al. (2017)
		$\rightarrow \text{s-H}_2 + \text{s-HCS}$	0		
252.	$\text{s-H} + \text{s-CH}_3\text{S}$	$\rightarrow \text{s-CH}_3\text{SH}$	1.0	0	0 See appendix A of Vidal et al. (2017)
253.	$\text{s-H} + \text{s-CH}_2\text{SH}$	$\rightarrow \text{s-CH}_3\text{SH}$	1.0	0	0 See appendix A of Vidal et al. (2017)
254.	$\text{s-H} + \text{s-CH}_3\text{SH}$	$\rightarrow \text{s-CH}_2\text{SH} + \text{s-H}_2$	0		
		$\rightarrow \text{s-CH}_3\text{S} + \text{s-H}_2$	0.5	0	800 (Kerr et al., 2015)
		$\rightarrow \text{s-CH}_3 + \text{s-H}_2\text{S}$	0.5	0	1600 (Martin et al., 1988)
255.	$\text{s-H} + \text{s-HNCS}$	$\rightarrow \text{s-NH}_2\text{CS}$	0.4	0	3600 See appendix A of
		$\rightarrow \text{s-HNCSH}$	0.4	0	2600 Vidal et al. (2017)
		$\rightarrow \text{s-HNCHS}$	0.2	0	5400
		$\rightarrow \text{s-HNC} + \text{s-SH}$	0	0	2600
256.	$\text{s-H} + \text{s-HSCN}$	$\rightarrow \text{s-HSCHN}$	0.3	0	4000 See appendix A of
		$\rightarrow \text{s-HNCSH}$	0.5	0	4000 Vidal et al. (2017)
		$\rightarrow \text{s-HCN} + \text{s-SH}$	0.2	0	4000
		$\rightarrow \text{s-HNC} + \text{s-SH}$	0	0	4000
		$\rightarrow \text{s-H}_2\text{S} + \text{s-CN}$	0		
257.	$\text{s-H} + \text{s-NH}_2\text{CS}$	$\rightarrow \text{s-NH}_2\text{CHS}$	0.6	0	0 See appendix A of
		$\rightarrow \text{s-H}_2 + \text{s-HNCS}$	0.4	0	0 Vidal et al. (2017)
258.	$\text{s-H} + \text{s-HNCSH}$	$\rightarrow \text{s-HNCHSH}$	0.6	0	0 See appendix A of
		$\rightarrow \text{s-HNCS} + \text{s-H}_2$	0.3	0	0 Vidal et al. (2017)
		$\rightarrow \text{s-HSCN} + \text{s-H}_2$	0.1	0	0
259.	$\text{s-H} + \text{s-HNCHS}$	$\rightarrow \text{s-NH}_2\text{CHS}$	0.3	0	0 See appendix A of



# A. SUMMARY OF SULPHUR COMPOUNDS REACTIONS REVIEW

Table A.1 – continued from previous page

N°	Reaction	$\alpha$	$\beta$	$\gamma$	Comments	
	$\rightarrow$ s-HNCHSH	0.3	0	0	Vidal et al. (2017)	
	$\rightarrow$ s-HNCS + s-H <sub>2</sub>	0.4	0	0		
260.	s-H + s-HSCHN	$\rightarrow$ s-HNCHSH	0.6	0	0	See appendix A of
	$\rightarrow$ s-HSCN + s-H <sub>2</sub>	0.4	0	0	Vidal et al. (2017)	
261.	s-H + s-NH <sub>2</sub> CHS	$\rightarrow$ s-NH <sub>2</sub> CH <sub>2</sub> S	1	0	1000	Same as H + H <sub>2</sub> CS reaction
262.	s-H + s-HNCHSH	$\rightarrow$ s-NH <sub>2</sub> CHSH	1	0	1000	Same as H + H <sub>2</sub> CS reaction
263.	s-H + s-NH <sub>2</sub> CH <sub>2</sub> S	$\rightarrow$ s-NH <sub>2</sub> CH <sub>2</sub> SH	1	0	0	See appendix A of Vidal et al. (2017)
264.	s-H + s-NH <sub>2</sub> CHSH	$\rightarrow$ s-NH <sub>2</sub> CH <sub>2</sub> SH	1	0	0	See appendix A of Vidal et al. (2017)
265.	s-H + s-SO	$\rightarrow$ s-HSO	1	0	0	We supposed no barrier for H addition by comparison with H + O <sub>2</sub> reaction.
266.	s-H + s-HSO	$\rightarrow$ s-HSOH	0			See appendix A of
	$\rightarrow$ s-H <sub>2</sub> SO	0			Vidal et al. (2017)	
	$\rightarrow$ s-HS + s-OH	1.0	0	0		
	$\rightarrow$ s-H <sub>2</sub> + s-SO	0				
	$\rightarrow$ s-HS + s-H <sub>2</sub> O	0				
	$\rightarrow$ s-O + s-H <sub>2</sub> S	0				
267.	s-H + s-C <sub>2</sub> S	$\rightarrow$ s-HCCS	1.0	0	0	See appendix A of Vidal et al. (2017)
268.	s-H + s-HCCS	$\rightarrow$ s-H <sub>2</sub> CCS	1.0	0	0	See appendix A of Vidal et al. (2017)
269.	s-H + s-C <sub>3</sub> S	$\rightarrow$ s-HC <sub>3</sub> S	1.0	0	800	See appendix A of Vidal et al. (2017)
270.	s-H + s-HC <sub>3</sub> S	$\rightarrow$ s-H <sub>2</sub> C <sub>3</sub> S	1.0	0	0	See appendix A of Vidal et al. (2017)
271.	s-N + s-HS	$\rightarrow$ s-H + s-NS	1.0	0	0	See appendix A of Vidal et al. (2017)
272.	s-N + s-NS	$\rightarrow$ s-S + s-N <sub>2</sub>	1.0	0	0	See appendix A of Vidal et al. (2017)
273.	s-N + s-HCS	$\rightarrow$ s-HNCS	0.5	0	0	See appendix A of
	$\rightarrow$ s-HSCN	0.5	0	0	Vidal et al. (2017)	
274.	s-NH + s-CS	$\rightarrow$ s-HNCS	1.0	0	1200	See appendix A of Vidal et al. (2017)
275.	s-NH + s-HCS	$\rightarrow$ s-NHCHS	1.0	0	0	
276.	s-NH <sub>2</sub> + s-CS	$\rightarrow$ s-NH <sub>2</sub> CS	1.0	0	800	See appendix A of Vidal et al. (2017)
277.	s-NH <sub>2</sub> + s-HCS	$\rightarrow$ s-NH <sub>2</sub> CHS	1.0	0	0	See appendix A of Vidal et al. (2017)
278.	s-O + s-HS	$\rightarrow$ s-HSO	1.0	0	0	See appendix A of Vidal et al. (2017)
279.	s-O + s-SO	$\rightarrow$ s-SO <sub>2</sub>	1.0	0	0	See appendix A of Vidal et al. (2017)
280.	s-O + s-HCS	$\rightarrow$ s-H + s-OCS	0.6	0	0	See appendix A of
	$\rightarrow$ s-HS + s-CO	0.4	0	0	Vidal et al. (2017)	

Table A.1 – continued from previous page

N°	Reaction	$\alpha$	$\beta$	$\gamma$	Comments
281.	s-O + s-NS $\rightarrow$ s-S + s-NO	1.0	0	0	See appendix A of <a href="#">Vidal et al. (2017)</a>
282.	s-S + s-HCO $\rightarrow$ s-H + s-OCS	0.6	0	0	<a href="#">(Rice et al., 1993)</a>
	$\rightarrow$ s-HS + s-CO	0.4	0	0	<a href="#">(Rice and Chabalowski, 1994)</a>
283.	s-OH + s-CH <sub>3</sub> SH $\rightarrow$ s-CH <sub>2</sub> SH + s-H <sub>2</sub> O	0			<a href="#">(Atkinson et al., 2004)</a>
	$\rightarrow$ s-CH <sub>3</sub> S + s-H <sub>2</sub> O	1.0	0	0	



# B | INITIAL PARAMETERS OF THE RADIATION HYDRODYNAMIC MODELS

In this appendix, I present a summary of the dataset of RHD models from [Vaytet and Haugbolle \(2017\)](#) that I use in chapter 4. In table A.1, the models of the reference dataset that I obtained in section 4.2.2.1 are displayed in black font, while the discarded models ( $T_0 = 5\text{K}$ ) are displayed in red. For each model, the table gives the five initial physical parameters of collapse (IPPC) of interest:  $M_0$ ,  $T_0$ ,  $R_0$ ,  $\rho_0$  and  $t_{\text{ff}}$ .

Table B.1: Summary of the dataset of RHD models and their respective IPPC.

Model n°	$M_0$ ( $M_\odot$ )	$T_0$ (K)	$R_0$ (AU)	$\rho_0$ (part.cm <sup>-3</sup> )	$t_{\text{ff}}$ (kyrs)
1	0.2	5	3000	2.99E+06	27.26
2	0.5	5	3000	7.46E+06	17.26
3	0.5	10	3000	7.46E+06	17.26
4	0.5	15	3000	7.46E+06	17.26
5	1.0	5	3000	1.49E+07	12.20
6	1.0	10	3000	1.49E+07	12.20
7	1.0	15	3000	1.49E+07	12.20
8	1.0	20	3000	1.49E+07	12.20
9	1.0	25	3000	1.49E+07	12.20
10	1.0	30	3000	1.49E+07	12.20
11	2.0	5	3000	2.99E+07	8.63
12	2.0	10	3000	2.99E+07	8.63
13	2.0	15	3000	2.99E+07	8.63
14	2.0	20	3000	2.99E+07	8.63
15	2.0	25	3000	2.99E+07	8.63
16	2.0	30	3000	2.99E+07	8.63
17	4.0	5	3000	5.97E+07	6.10
18	4.0	10	3000	5.97E+07	6.10
19	4.0	15	3000	5.97E+07	6.10

Table B.1 – continued from previous page

Model n°	$M_0$ ( $M_\odot$ )	$T_0$ (K)	$R_0$ (AU)	$\rho_0$ (part.cm <sup>-3</sup> )	$t_{\text{ff}}$ (kyrs)
20	4.0	20	3000	5.97E+07	6.10
21	4.0	25	3000	5.97E+07	6.10
22	4.0	30	3000	5.97E+07	6.10
23	6.0	5	3000	8.96E+07	4.98
24	6.0	10	3000	8.96E+07	4.98
25	6.0	15	3000	8.96E+07	4.98
26	6.0	20	3000	8.96E+07	4.98
27	6.0	25	3000	8.96E+07	4.98
28	6.0	30	3000	8.96E+07	4.98
29	8.0	5	3000	1.19E+08	4.31
30	8.0	10	3000	1.19E+08	4.31
31	8.0	15	3000	1.19E+08	4.31
32	8.0	20	3000	1.19E+08	4.31
33	8.0	25	3000	1.19E+08	4.31
34	8.0	30	3000	1.19E+08	4.31
35	0.5	5	5000	1.61E+06	37.13
36	0.5	10	5000	1.61E+06	37.13
37	1.0	5	5000	3.23E+06	26.25
38	1.0	10	5000	3.23E+06	26.25
39	1.0	15	5000	3.23E+06	26.25
40	1.0	20	5000	3.23E+06	26.25
41	2.0	5	5000	6.45E+06	18.56
42	2.0	10	5000	6.45E+06	18.56
43	2.0	15	5000	6.45E+06	18.56
44	2.0	20	5000	6.45E+06	18.56
45	2.0	25	5000	6.45E+06	18.56
46	2.0	30	5000	6.45E+06	18.56
47	4.0	5	5000	1.29E+07	13.13
48	4.0	10	5000	1.29E+07	13.13
49	4.0	15	5000	1.29E+07	13.13
50	4.0	20	5000	1.29E+07	13.13
51	4.0	25	5000	1.29E+07	13.13
52	4.0	30	5000	1.29E+07	13.13
53	6.0	5	5000	1.94E+07	10.72
54	6.0	10	5000	1.94E+07	10.72
55	6.0	15	5000	1.94E+07	10.72
56	6.0	20	5000	1.94E+07	10.72
57	6.0	25	5000	1.94E+07	10.72
58	6.0	30	5000	1.94E+07	10.72
59	8.0	5	5000	2.58E+07	9.28

Table B.1 – continued from previous page

Model n°	$M_0$ ( $M_\odot$ )	$T_0$ (K)	$R_0$ (AU)	$\rho_0$ (part.cm <sup>-3</sup> )	$t_{\text{ff}}$ (kyrs)
60	8.0	10	5000	2.58E+07	9.28
61	8.0	15	5000	2.58E+07	9.28
62	8.0	20	5000	2.58E+07	9.28
63	8.0	25	5000	2.58E+07	9.28
64	8.0	30	5000	2.58E+07	9.28
65	0.5	5	7500	4.78E+05	68.20
66	1.0	5	7500	9.56E+05	48.23
67	1.0	10	7500	9.56E+05	48.23
68	2.0	5	7500	1.91E+06	34.10
69	2.0	10	7500	1.91E+06	34.10
70	2.0	15	7500	1.91E+06	34.10
71	2.0	20	7500	1.91E+06	34.10
72	2.0	25	7500	1.91E+06	34.10
73	4.0	5	7500	3.82E+06	24.11
74	4.0	10	7500	3.82E+06	24.11
75	4.0	15	7500	3.82E+06	24.11
76	4.0	20	7500	3.82E+06	24.11
77	4.0	25	7500	3.82E+06	24.11
78	4.0	30	7500	3.82E+06	24.11
79	6.0	5	7500	5.74E+06	19.69
80	6.0	10	7500	5.74E+06	19.69
81	6.0	15	7500	5.74E+06	19.69
82	6.0	20	7500	5.74E+06	19.69
83	6.0	25	7500	5.74E+06	19.69
84	6.0	30	7500	5.74E+06	19.69
85	8.0	5	7500	7.65E+06	17.05
86	8.0	10	7500	7.65E+06	17.05
87	8.0	15	7500	7.65E+06	17.05
88	8.0	20	7500	7.65E+06	17.05
89	8.0	25	7500	7.65E+06	17.05
90	8.0	30	7500	7.65E+06	17.05
91	1.0	5	12000	2.33E+05	97.61
92	2.0	5	12000	4.67E+05	69.02
93	2.0	10	12000	4.67E+05	69.02
94	2.0	15	12000	4.67E+05	69.02
95	4.0	5	12000	9.34E+05	48.80
96	4.0	10	12000	9.34E+05	48.80
97	4.0	15	12000	9.34E+05	48.80
98	4.0	20	12000	9.34E+05	48.80
99	4.0	25	12000	9.34E+05	48.80

Table B.1 – continued from previous page

Model n°	$M_0$ ( $M_\odot$ )	$T_0$ (K)	$R_0$ (AU)	$\rho_0$ (part.cm <sup>-3</sup> )	$t_{\text{ff}}$ (kyrs)
100	4.0	30	12000	9.34E+05	48.80
101	6.0	5	12000	1.40E+06	39.85
102	6.0	10	12000	1.40E+06	39.85
103	6.0	15	12000	1.40E+06	39.85
104	6.0	20	12000	1.40E+06	39.85
105	6.0	25	12000	1.40E+06	39.85
106	6.0	30	12000	1.40E+06	39.85
107	8.0	5	12000	1.87E+06	34.51
108	8.0	10	12000	1.87E+06	34.51
109	8.0	15	12000	1.87E+06	34.51
110	8.0	20	12000	1.87E+06	34.51
111	8.0	25	12000	1.87E+06	34.51
112	8.0	30	12000	1.87E+06	34.51
113	1.0	5	20000	5.04E+04	209.00
114	2.0	5	20000	1.01E+05	148.51
115	2.0	10	20000	1.01E+05	148.51
116	4.0	5	20000	2.02E+05	105.01
117	4.0	10	20000	2.02E+05	105.01
118	4.0	15	20000	2.02E+05	105.01
119	4.0	20	20000	2.02E+05	105.01
120	6.0	5	20000	3.03E+05	85.74
121	6.0	10	20000	3.02E+05	85.74
122	6.0	15	20000	3.02E+05	85.74
123	6.0	20	20000	3.02E+05	85.74
124	6.0	25	20000	3.02E+05	85.74
125	6.0	30	20000	3.02E+05	85.74
126	8.0	5	20000	4.03E+05	74.25
127	8.0	10	20000	4.03E+05	74.25
128	8.0	15	20000	4.03E+05	74.25
129	8.0	20	20000	4.03E+05	74.25
130	8.0	25	20000	4.03E+05	74.25
131	8.0	30	20000	4.03E+05	74.25
132	2.0	5	30000	2.98E+04	272.83
133	4.0	5	30000	5.97E+04	192.92
134	4.0	10	30000	5.97E+04	192.92
135	6.0	5	30000	8.96E+04	157.52
136	6.0	10	30000	8.96E+04	157.52
137	6.0	15	30000	8.96E+04	157.52
138	6.0	20	30000	8.96E+04	157.52
139	8.0	5	30000	1.19E+05	136.41

---

Table B.1 – continued from previous page

Model n <sup>o</sup>	$M_0$ ( $M_\odot$ )	$T_0$ (K)	$R_0$ (AU)	$\rho_0$ (part.cm <sup>-3</sup> )	$t_{\text{ff}}$ (kyrs)
140	8.0	10	30000	1.19E+05	136.41
141	8.0	15	30000	1.19E+05	136.41
142	8.0	20	30000	1.19E+05	136.41
143	8.0	25	30000	1.19E+05	136.41

---





# C | CORRELATIONS IN THE HOT CORE REGION

Hereafter I present an extensive description of the correlations between the species of the network and the initial physical parameters of collapse (IPPC) in the Hot Corino Region (HCR) defined in section 4.3.1.2. Table C.1 displays the species which are best correlated with the IPPC  $T_0$ ,  $R_0$ ,  $\rho_0$  and  $t_{\text{ff}}$ , *ie* with a Spearman's coefficient of  $|\rho_S| > 0.6$ . I do not display the results for  $M_0$  since no significant correlations were found (see section 4.3.1.2).

Table C.1: Summary of the species in the HCR which are best correlated with the IPPC  $T_0$ ,  $R_0$ ,  $\rho_0$  and  $t_{\text{ff}}$ , *ie* with a Spearman's coefficient of  $|\rho_S| > 0.6$ .

$T_0$		$R_0$		$\rho_0$		$t_{\text{ff}}$	
Species	$\rho_S$	Species	$\rho_S$	Species	$\rho_S$	Species	$\rho_S$
HCOOH	0.953	H <sub>2</sub> CCS	0.910	e <sup>-</sup>	0.830	H <sub>2</sub> CCS	0.983
NH <sub>2</sub> CHO	0.940	HC <sub>4</sub> N	0.891	HCl	0.809	c <sup>-</sup> H <sub>2</sub> C <sub>3</sub> O	0.953
C <sub>3</sub> H <sub>6</sub> OH <sup>+</sup>	0.939	c <sup>-</sup> H <sub>2</sub> C <sub>3</sub> O	0.887	Si	0.793	CH <sub>3</sub> CHS	0.95
CH <sub>3</sub> NH <sub>2</sub> <sup>+</sup>	0.924	H <sub>2</sub> C <sub>3</sub> S	0.878	OH <sup>-</sup>	0.782	CCl	0.95
CH <sub>3</sub> NH <sub>2</sub>	0.919	CH <sub>3</sub> CHS	0.866	CH <sub>3</sub> <sup>+</sup>	0.776	HC <sub>4</sub> N	0.948
NH <sub>2</sub> CH <sub>2</sub> O <sup>+</sup>	0.915	HC <sub>6</sub> N	0.861	NH <sub>3</sub> <sup>+</sup>	0.769	H <sub>2</sub> C <sub>3</sub> S	0.937
H <sub>2</sub> NC <sup>+</sup>	0.913	C <sub>3</sub> S	0.858	OH <sup>+</sup>	0.737	HCCS	0.933
PH <sub>2</sub>	0.912	CCl	0.850	NH <sub>2</sub> <sup>+</sup>	0.737	HC <sub>6</sub> N	0.924
HCOOH <sup>+</sup>	0.896	H <sub>2</sub> C <sub>2</sub> S <sup>+</sup>	0.849	H	0.737	C <sub>4</sub> S	0.918
CH <sub>3</sub> OCH <sub>3</sub>	0.893	c <sup>-</sup> H <sub>2</sub> C <sub>3</sub> OH <sup>+</sup>	0.847	H <sub>2</sub> <sup>+</sup>	0.729	C <sub>3</sub> S	0.917
H <sub>3</sub> C <sub>4</sub> NH <sup>+</sup>	0.888	CH <sub>3</sub> C <sub>6</sub> H	0.847	Cl	0.719	H <sub>2</sub> C <sub>2</sub> S <sup>+</sup>	0.907
CH <sub>3</sub> O <sub>2</sub> <sup>+</sup>	0.875	HCCS	0.846	H <sub>2</sub> O <sup>+</sup>	0.710	c <sup>-</sup> H <sub>2</sub> C <sub>3</sub> OH <sup>+</sup>	0.906
C <sub>2</sub> H <sub>6</sub> CO <sup>+</sup>	0.874	HC <sub>8</sub> N	0.843	OH	0.709	CH <sub>3</sub> C <sub>6</sub> H	0.902
CH <sub>3</sub> COCH <sub>3</sub>	0.874	C <sub>5</sub> O	0.841	PH <sub>3</sub> <sup>+</sup>	0.691	CH <sub>2</sub> NH	0.9
CH <sub>3</sub> C <sub>3</sub> N	0.861	CH <sub>3</sub> CS <sup>+</sup>	0.838	C <sub>10</sub> <sup>-</sup>	0.687	C <sub>6</sub> H <sub>6</sub>	0.899
SiH <sub>4</sub>	0.857	C <sub>6</sub> H <sub>6</sub>	0.833	FeH	0.683	H <sub>2</sub> CSiCH	0.895
C <sub>2</sub> H <sub>6</sub>	0.856	C <sub>4</sub> S	0.833	F	0.657	CH <sub>3</sub> CHSH <sup>+</sup>	0.894
H <sub>2</sub> CCO	0.847	H <sub>2</sub> C <sub>3</sub> O	0.831	HC <sub>3</sub> NH <sup>+</sup>	0.657	HC <sub>8</sub> N	0.893
C <sub>7</sub> O	0.843	CH <sub>2</sub> CHCHCH <sub>2</sub>	0.831	C <sub>5</sub> N	0.656	CH <sub>3</sub> CS <sup>+</sup>	0.887
C <sub>2</sub> H <sub>6</sub> <sup>+</sup>	0.840	CH <sub>3</sub> CHSH <sup>+</sup>	0.824	CH <sub>3</sub> OH <sub>2</sub> <sup>+</sup>	0.653	H <sub>2</sub> C <sub>3</sub> O	0.886
CH <sub>3</sub> OCH <sub>3</sub> <sup>+</sup>	0.838	HCCNC	0.823	CH <sub>3</sub>	0.651	CH <sub>2</sub> CHCHCH <sub>2</sub>	0.884
C <sub>4</sub> H <sub>3</sub> <sup>+</sup>	0.836	C <sub>2</sub> H <sub>3</sub> CO <sup>+</sup>	0.816	I <sup>-</sup> C <sub>3</sub> H <sub>3</sub> <sup>+</sup>	0.647	HCSi	0.875
HCN	0.835	H <sub>2</sub> CSiCH	0.812	H <sup>+</sup>	0.646	C <sub>5</sub> O	0.874

Table C.1 – continued from previous page

$T_0$		$R_0$		$\rho_0$		$t_{\text{ff}}$	
Species	$\rho_S$	Species	$\rho_S$	Species	$\rho_S$	Species	$\rho_S$
C <sub>2</sub> O <sup>+</sup>	0.834	C <sub>5</sub> H <sub>2</sub>	0.811	C <sub>3</sub> H <sub>8</sub>	0.629	C <sub>5</sub> H <sub>3</sub>	0.867
CH <sub>3</sub> CN <sup>+</sup>	0.833	CH <sub>3</sub> C <sub>4</sub> H	0.801	C <sub>3</sub> H <sub>4</sub> <sup>+</sup>	0.625	C <sub>2</sub> H <sub>3</sub> CO <sup>+</sup>	0.867
CH <sub>2</sub> CN <sup>+</sup>	0.814	C <sub>5</sub> H <sub>3</sub>	0.799	SiO	0.620	c <sup>-</sup> HCCHSi	0.867
HCCP	0.812	C <sub>4</sub> H <sub>2</sub>	0.798	He <sup>+</sup>	0.605	C <sub>5</sub> H <sub>2</sub>	0.864
HNSi	0.808	C <sub>5</sub> H <sub>4</sub>	0.795	NH <sub>2</sub>	0.603	C <sub>4</sub> H <sub>2</sub>	0.862
C <sub>2</sub> HO <sup>+</sup>	0.808	c <sup>-</sup> HCCHSi	0.789	H <sub>3</sub> <sup>+</sup>	0.602	HCCNC	0.862
PH	0.806	CH <sub>2</sub> NH	0.781	-	-	GRAIN0	0.846
GRAIN <sup>-</sup>	0.805	HC <sub>4</sub> S <sup>+</sup>	0.778	-	-	HC <sub>4</sub> S <sup>+</sup>	0.845
CCP	0.795	C <sub>4</sub> N	0.776	-	-	C <sub>6</sub> H <sub>3</sub>	0.842
CH <sub>3</sub> NH <sub>3</sub> <sup>+</sup>	0.793	HCSi	0.776	-	-	CH <sub>3</sub> C <sub>4</sub> H	0.836
CCO	0.790	CH <sub>2</sub> CHC <sub>2</sub> H	0.772	-	-	SiS	0.822
HC <sub>7</sub> O <sup>+</sup>	0.772	C <sub>6</sub> H <sub>3</sub>	0.768	-	-	C <sub>8</sub> H <sub>3</sub>	0.818
H <sub>2</sub> SiO	0.769	C <sub>3</sub> <sup>-</sup>	0.761	-	-	C <sub>4</sub> S <sup>+</sup>	0.816
FeH	0.764	HCNCC	0.758	-	-	CH <sub>2</sub> CHC <sub>2</sub> H	0.816
H <sub>2</sub> NCO <sup>+</sup>	0.759	HNC	0.757	-	-	NaH <sub>2</sub> O <sup>+</sup>	0.813
PCH <sub>2</sub> <sup>+</sup>	0.747	C <sub>4</sub> S <sup>+</sup>	0.753	-	-	HONC	0.802
CCN	0.742	GRAIN0	0.753	-	-	C <sub>5</sub> H <sub>4</sub>	0.791
CP	0.742	CCS	0.749	-	-	C <sub>7</sub> H <sub>3</sub>	0.789
HCCO	0.739	C <sub>8</sub> H <sub>3</sub>	0.748	-	-	C <sub>4</sub> N	0.788
C <sub>2</sub> H <sub>5</sub> OH <sub>2</sub> <sup>+</sup>	0.738	HC <sub>5</sub> N	0.747	-	-	l <sup>-</sup> SiC <sub>3</sub>	0.783
HCP	0.738	CH <sub>2</sub> CHCN	0.746	-	-	HCCCHS	0.779
C <sub>2</sub> H <sub>5</sub> OH <sup>+</sup>	0.727	HCCCHS	0.744	-	-	C <sub>6</sub> H <sub>2</sub>	0.778
CH <sub>3</sub> CO <sup>+</sup>	0.723	Na <sup>+</sup>	0.744	-	-	HCNCC	0.778
CH <sub>3</sub> CH <sub>2</sub> OH	0.721	C <sub>6</sub> H <sub>2</sub>	0.740	-	-	HNC	0.773
C <sub>9</sub> O	0.718	SiS	0.739	-	-	C <sub>9</sub> H <sub>3</sub>	0.773
CH <sub>3</sub> CN	0.713	NaH <sub>2</sub> O <sup>+</sup>	0.738	-	-	c <sup>-</sup> SiC <sub>2</sub>	0.773
C <sub>4</sub> H <sub>7</sub> <sup>+</sup>	0.712	c <sup>-</sup> SiC <sub>2</sub>	0.728	-	-	CH <sub>2</sub> CHCN	0.772
CH <sub>3</sub> OCH <sub>4</sub> <sup>+</sup>	0.697	C <sub>7</sub> H <sub>2</sub>	0.722	-	-	CCS	0.769
CO <sub>2</sub>	0.689	C <sub>8</sub> H <sub>2</sub>	0.721	-	-	HC <sub>3</sub> S	0.767
C <sub>3</sub> H <sub>9</sub> <sup>+</sup>	0.687	C <sub>7</sub> H <sub>3</sub>	0.713	-	-	C <sub>3</sub> <sup>-</sup>	0.767
OCN	0.682	HC <sub>3</sub> S <sup>+</sup>	0.712	-	-	Na <sup>+</sup>	0.763
H <sub>2</sub> S <sub>2</sub> <sup>+</sup>	0.681	C <sub>9</sub> H <sub>3</sub>	0.712	-	-	SiC <sub>3</sub> H	0.76
HNCO	0.681	H <sub>2</sub> C <sub>5</sub> N <sup>+</sup>	0.712	-	-	t <sup>-</sup> C <sub>3</sub> H <sub>2</sub>	0.759
SiN	0.680	SiC	0.710	-	-	C <sub>3</sub> H <sub>7</sub>	0.752
H <sub>2</sub>	0.679	HCCSi	0.706	-	-	SiC	0.752
CH <sub>3</sub> CNH <sup>+</sup>	0.677	HC <sub>3</sub> S	0.706	-	-	C <sub>7</sub> H <sub>2</sub>	0.751
H <sub>3</sub> S <sub>3</sub> <sup>+</sup>	0.674	t <sup>-</sup> C <sub>3</sub> H <sub>2</sub>	0.703	-	-	HC <sub>5</sub> N	0.75
C <sub>9</sub> H <sub>4</sub> <sup>+</sup>	0.673	HONC	0.698	-	-	C <sub>8</sub> H <sub>2</sub>	0.75
HCN <sup>+</sup>	0.669	C <sub>3</sub> H <sub>3</sub> N <sup>+</sup>	0.698	-	-	HCNOH <sup>+</sup>	0.729
HCS <sub>2</sub> <sup>+</sup>	0.663	l <sup>-</sup> SiC <sub>3</sub>	0.697	-	-	H <sub>2</sub> CNO <sup>+</sup>	0.726
CH	0.651	C <sub>3</sub> H <sub>3</sub> NH <sup>+</sup>	0.687	-	-	HC <sub>3</sub> S <sup>+</sup>	0.722
O <sub>2</sub> <sup>+</sup>	0.650	SiC <sub>3</sub> H	0.681	-	-	C <sub>3</sub> H <sub>5</sub>	0.714
HNC <sup>+</sup>	0.650	C <sub>6</sub> H <sub>4</sub>	0.672	-	-	C <sub>3</sub> H <sub>3</sub> N <sup>+</sup>	0.713
HCNH <sup>+</sup>	0.646	C <sub>9</sub> N	0.671	-	-	Na	0.713
HC <sub>2</sub> NCH <sup>+</sup>	0.644	HCCCHSH <sup>+</sup>	0.670	-	-	HCCSi	0.709
CN	0.640	C <sub>8</sub> H <sub>4</sub> <sup>+</sup>	0.669	-	-	H <sub>2</sub> C <sub>5</sub> N <sup>+</sup>	0.7
C <sub>2</sub> H <sub>3</sub> <sup>+</sup>	0.638	C <sub>9</sub> H <sub>2</sub>	0.654	-	-	C <sub>3</sub> H <sub>3</sub> NH <sup>+</sup>	0.699

Table C.1 – continued from previous page

$T_0$		$R_0$		$\rho_0$		$t_{\text{ff}}$	
Species	$\rho_s$	Species	$\rho_s$	Species	$\rho_s$	Species	$\rho_s$
NH <sup>+</sup>	0.637	HC <sub>7</sub> N	0.651	-	-	HC <sub>3</sub> O	0.694
C	0.636	HC <sub>3</sub> O	0.651	-	-	C <sub>9</sub> N	0.688
H <sub>2</sub> CCO <sup>+</sup>	0.636	HCNOH <sup>+</sup>	0.644	-	-	C <sub>8</sub> H <sub>4</sub> <sup>+</sup>	0.687
HSO <sub>2</sub> <sup>+</sup>	0.635	H <sub>2</sub> CNO <sup>+</sup>	0.642	-	-	MgH	0.686
HNCS <sup>+</sup>	0.635	C <sub>8</sub> H <sub>4</sub>	0.638	-	-	Fe	0.684
C <sub>6</sub> N	0.632	HC <sub>9</sub> N	0.636	-	-	HCCCHSH <sup>+</sup>	0.679
CS <sub>2</sub>	0.631	Na	0.635	-	-	C <sub>9</sub> H <sub>2</sub>	0.664
c <sup>-</sup> C <sub>3</sub> H <sub>2</sub> <sup>+</sup>	0.629	NC <sub>4</sub> N	0.616	-	-	HCNO	0.655
C <sub>2</sub> H <sub>2</sub> <sup>+</sup>	0.629	C <sub>3</sub> H <sub>5</sub>	0.614	-	-	SiH	0.637
H <sub>3</sub> C <sub>6</sub> NH <sup>+</sup>	0.627	C <sub>3</sub> H <sub>7</sub>	0.606	-	-	SiH <sub>2</sub>	0.636
MgH <sub>2</sub>	0.625	-	-	-	-	NH <sub>2</sub> CH <sub>2</sub> O	0.633
SO <sub>2</sub>	0.624	-	-	-	-	H <sub>2</sub> CS	0.633
HNCOH <sup>+</sup>	0.620	-	-	-	-	C <sub>6</sub> H <sub>4</sub>	0.624
CH <sub>2</sub> NH <sub>2</sub>	0.617	-	-	-	-	N <sub>2</sub> O	0.624
C <sub>3</sub> P	0.617	-	-	-	-	HC <sub>7</sub> N	0.614
HSS	0.608	-	-	-	-	SiC <sub>2</sub> CH <sub>3</sub>	0.611
H <sub>2</sub> CO <sup>+</sup>	0.607	-	-	-	-	CH <sub>2</sub> SH	0.607
C <sub>2</sub> H <sub>4</sub> <sup>+</sup>	0.606	-	-	-	-	HC <sub>9</sub> N	0.602
C <sub>10</sub>	0.606	-	-	-	-	-	-
H <sub>2</sub> C <sub>6</sub> N <sup>+</sup>	0.604	-	-	-	-	-	-
H <sub>2</sub> CCN	0.602	-	-	-	-	-	-
-	-	-	-	HC <sub>9</sub> N	-0.603	-	-
-	-	-	-	CH <sub>2</sub> SH	-0.606	-	-
-	-	-	-	SiC <sub>2</sub> CH <sub>3</sub>	-0.611	-	-
-	-	-	-	HC <sub>7</sub> N	-0.615	-	-
-	-	-	-	N <sub>2</sub> O	-0.624	-	-
-	-	-	-	C <sub>6</sub> H <sub>4</sub>	-0.625	-	-
-	-	-	-	H <sub>2</sub> CS	-0.630	-	-
-	-	-	-	NH <sub>2</sub> CH <sub>2</sub> O	-0.633	-	-
-	-	-	-	SiH <sub>2</sub>	-0.635	-	-
-	-	-	-	SiH	-0.636	-	-
-	-	-	-	HCNO	-0.654	-	-
-	-	-	-	C <sub>9</sub> H <sub>2</sub>	-0.664	-	-
-	-	-	-	HCCCHSH <sup>+</sup>	-0.677	-	-
-	-	-	-	Fe	-0.683	-	-
-	-	-	-	MgH	-0.685	-	-
-	-	-	-	C <sub>8</sub> H <sub>4</sub> <sup>+</sup>	-0.687	-	-
-	-	-	-	C <sub>9</sub> N	-0.688	-	-
-	-	-	-	HC <sub>3</sub> O	-0.692	-	-
-	-	-	-	C <sub>3</sub> H <sub>3</sub> NH <sup>+</sup>	-0.700	-	-
-	-	-	-	H <sub>2</sub> C <sub>5</sub> N <sup>+</sup>	-0.700	-	-
-	-	-	-	HCCSi	-0.711	-	-
-	-	-	-	C <sub>3</sub> H <sub>5</sub>	-0.712	-	-
-	-	-	-	Na	-0.712	-	-
-	-	-	-	C <sub>3</sub> H <sub>3</sub> N <sup>+</sup>	-0.714	-	-
-	-	-	-	HC <sub>3</sub> S <sup>+</sup>	-0.720	-	-
-	-	-	-	H <sub>2</sub> CNO <sup>+</sup>	-0.725	-	-

# C. CORRELATIONS IN THE HOT CORE REGION

Table C.1 – continued from previous page

$T_0$		$R_0$		$\rho_0$		$t_{\text{ff}}$	
Species	$\rho_S$	Species	$\rho_S$	Species	$\rho_S$	Species	$\rho_S$
-	-	-	-	HCNOH <sup>+</sup>	-0.728	-	-
-	-	-	-	C <sub>7</sub> H <sub>2</sub>	-0.749	-	-
-	-	-	-	C <sub>8</sub> H <sub>2</sub>	-0.749	-	-
-	-	-	-	HC <sub>5</sub> N	-0.751	-	-
-	-	-	-	C <sub>3</sub> H <sub>7</sub>	-0.751	-	-
-	-	-	-	SiC	-0.754	-	-
-	-	-	-	t <sup>-</sup> C <sub>3</sub> H <sub>2</sub>	-0.759	-	-
-	-	-	-	SiC <sub>3</sub> H	-0.761	-	-
-	-	-	-	Na <sup>+</sup>	-0.763	-	-
-	-	-	-	HC <sub>3</sub> S	-0.765	-	-
-	-	-	-	C <sub>3</sub> <sup>-</sup>	-0.767	-	-
-	-	-	-	CCS	-0.768	-	-
-	-	-	-	CH <sub>2</sub> CHCN	-0.773	-	-
-	-	-	-	C <sub>9</sub> H <sub>3</sub>	-0.773	-	-
-	-	-	-	HNC	-0.773	-	-
-	-	-	-	c <sup>-</sup> SiC <sub>2</sub>	-0.775	-	-
-	-	-	-	C <sub>6</sub> H <sub>2</sub>	-0.777	-	-
-	-	-	-	HCCCHS	-0.777	-	-
H <sub>2</sub> CS	-0.605	-	-	HCNCC	-0.779	-	-
HNO	-0.608	-	-	I <sup>-</sup> SiC <sub>3</sub>	-0.784	-	-
OCS <sup>+</sup>	-0.612	-	-	C <sub>7</sub> H <sub>3</sub>	-0.789	-	-
SiC <sub>2</sub> CH <sub>3</sub>	-0.613	-	-	C <sub>4</sub> N	-0.789	-	-
SiH	-0.621	-	-	C <sub>5</sub> H <sub>4</sub>	-0.792	-	-
H <sub>3</sub> CS <sup>+</sup>	-0.626	-	-	HONC	-0.801	-	-
HONC	-0.634	-	-	NaH <sub>2</sub> O <sup>+</sup>	-0.814	-	-
H <sub>2</sub> CO	-0.635	-	-	C <sub>4</sub> S <sup>+</sup>	-0.816	-	-
NaOH	-0.661	-	-	CH <sub>2</sub> CHC <sub>2</sub> H	-0.817	-	-
HOCS <sup>+</sup>	-0.670	-	-	C <sub>8</sub> H <sub>3</sub>	-0.818	-	-
H <sub>2</sub> O	-0.676	-	-	SiS	-0.821	-	-
HCNO	-0.697	-	-	CH <sub>3</sub> C <sub>4</sub> H	-0.837	-	-
SiC <sub>3</sub> H <sub>5</sub>	-0.705	-	-	C <sub>6</sub> H <sub>3</sub>	-0.842	-	-
PCH <sub>3</sub> <sup>+</sup>	-0.713	-	-	HC <sub>4</sub> S <sup>+</sup>	-0.845	-	-
H <sub>2</sub> S	-0.717	-	-	GRAIN0	-0.846	-	-
CH <sub>3</sub> O	-0.736	-	-	C <sub>4</sub> H <sub>2</sub>	-0.862	H <sub>3</sub> <sup>+</sup>	-0.602
CH <sub>3</sub> CHO	-0.756	-	-	HCCNC	-0.862	NH <sub>2</sub>	-0.604
CH <sub>3</sub> OH	-0.760	-	-	C <sub>5</sub> H <sub>2</sub>	-0.863	He <sup>+</sup>	-0.605
MgH	-0.762	-	-	c <sup>-</sup> HCCHSi	-0.867	SiO	-0.618
Fe	-0.764	-	-	C <sub>2</sub> H <sub>3</sub> CO <sup>+</sup>	-0.867	C <sub>3</sub> H <sub>4</sub> <sup>+</sup>	-0.624
H <sub>2</sub> CNS <sup>+</sup>	-0.791	-	-	C <sub>5</sub> H <sub>3</sub>	-0.867	C <sub>3</sub> H <sub>8</sub>	-0.631
HCNSH <sup>+</sup>	-0.791	-	-	HCSi	-0.874	H <sup>+</sup>	-0.646
HOCN	-0.801	-	-	C <sub>5</sub> O	-0.875	I <sup>-</sup> C <sub>3</sub> H <sub>3</sub> <sup>+</sup>	-0.646
NHCHO	-0.801	-	-	CH <sub>2</sub> CHCHCH <sub>2</sub>	-0.885	CH <sub>3</sub>	-0.651
CO	-0.802	-	-	H <sub>2</sub> C <sub>3</sub> O	-0.886	CH <sub>3</sub> OH <sub>2</sub> <sup>+</sup>	-0.653
CH <sub>5</sub> <sup>+</sup>	-0.806	-	-	CH <sub>3</sub> CS <sup>+</sup>	-0.887	C <sub>5</sub> N	-0.656
CH <sub>2</sub> SH	-0.810	-	-	CH <sub>3</sub> CHSH <sup>+</sup>	-0.892	HC <sub>3</sub> NH <sup>+</sup>	-0.656
SiH <sub>2</sub>	-0.810	-	-	HC <sub>8</sub> N	-0.893	F	-0.657
CH <sub>4</sub> <sup>+</sup>	-0.812	-	-	H <sub>2</sub> CSiCH	-0.895	FeH	-0.684

Table C.1 – continued from previous page

$T_0$		$R_0$		$\rho_0$		$t_{\text{ff}}$	
Species	$\rho_s$	Species	$\rho_s$	Species	$\rho_s$	Species	$\rho_s$
HSCN	-0.823	-	-	C <sub>6</sub> H <sub>6</sub>	-0.899	C <sub>10</sub> <sup>-</sup>	-0.687
HSCHN	-0.823	-	-	CH <sub>2</sub> NH	-0.900	PH <sub>3</sub> <sup>+</sup>	-0.692
NS	-0.835	-	-	CH <sub>3</sub> C <sub>6</sub> H	-0.903	OH	-0.709
NS <sup>+</sup>	-0.840	-	-	H <sub>2</sub> C <sub>2</sub> S <sup>+</sup>	-0.907	H <sub>2</sub> O <sup>+</sup>	-0.711
P	-0.841	-	-	c <sup>-</sup> H <sub>2</sub> C <sub>3</sub> OH <sup>+</sup>	-0.907	Cl	-0.718
HNS <sup>+</sup>	-0.841	-	-	C <sub>4</sub> S	-0.917	H <sub>2</sub> <sup>+</sup>	-0.729
HOCHN	-0.849	PH <sub>3</sub> <sup>+</sup>	-0.600	C <sub>3</sub> S	-0.917	H	-0.737
OCS	-0.869	CH <sub>3</sub> <sup>+</sup>	-0.616	HC <sub>6</sub> N	-0.924	NH <sub>2</sub> <sup>+</sup>	-0.737
SiH <sub>3</sub>	-0.872	C <sub>5</sub> N	-0.617	HCCS	-0.933	OH <sup>+</sup>	-0.737
SiCH <sub>3</sub>	-0.878	SiO	-0.617	H <sub>2</sub> C <sub>3</sub> S	-0.937	NH <sub>3</sub> <sup>+</sup>	-0.769
HCNS	-0.890	HC <sub>3</sub> NH <sup>+</sup>	-0.618	HC <sub>4</sub> N	-0.948	CH <sub>3</sub> <sup>+</sup>	-0.776
NH <sub>3</sub>	-0.902	OH <sup>-</sup>	-0.640	CH <sub>3</sub> CHS	-0.949	OH <sup>-</sup>	-0.781
HSSH	-0.943	e <sup>-</sup>	-0.711	CCl	-0.950	Si	-0.793
CH <sub>4</sub>	-0.970	Si	-0.733	c <sup>-</sup> H <sub>2</sub> C <sub>3</sub> O	-0.954	HCl	-0.809
CH <sub>2</sub> OH	-0.978	HCl	-0.736	H <sub>2</sub> CCS	-0.983	e <sup>-</sup>	-0.83



# D | CONSTRAINTS ON THE IPPC FOR EACH SOURCES

In this appendix, I display the detailed results of the application of the method described in section 4.3.2.1 to all the sources considered in table 4.2 with the exception of IRAS 16293-2422, which results are displayed in table 4.4. Hence, the following tables are the same as table 4.4 but for respectively L1448-I2, L1448-C, N1333-I2, N1333-I4A, N1333-I4B, L1527, VLA1623, L483, L723, L1157, and L1551-I5. In these table, IC stands for InConclusive and ND means that no data were available. Upper and lower limits are only defined within their corresponding IPPC range of values (see table 4.1). In red are contradictory results, and in blue the final constraints on the IPPC of the source.  $e$  is the uncertainty factor.

Table D.1: Summary of the application of the method to Jørgensen et al. (2004)'s observations of L1448-I2.

Species	$M_0$ ( $M_\odot$ )	$T_0$ (K)	$R_0$ (AU)	$\rho_0$ (part.cm <sup>-3</sup> )	$t_{\text{ff}}$ (kyrs)	$\chi^2$	$N_L$	$e$
CO	IC	$\leq 20$	IC	IC	IC	ND	4	3
CS	IC	IC	IC	IC	IC	ND	3	10
SO	IC	IC	IC	$\leq 8.96\text{E}+07$	$\geq 4.98$	ND	1	10
HCO <sup>+</sup>	IC	IC	IC	$\leq 2.58\text{E}+07$	$\geq 9.28$	ND	1	10
N <sub>2</sub> H <sup>+</sup>	$\geq 1$	$\geq 20$	IC	$\geq 8.96\text{E}+04$	$\leq 157.52$	ND	1	10
HCN	IC	IC	IC	$\leq 8.96\text{E}+07$	$\geq 4.98$	ND	1	10
HNC	IC	IC	IC	IC	IC	ND	2	3
CN	IC	IC	IC	$\leq 5.97\text{E}+07$	$\geq 6.10$	0.13	4	3
HC <sub>3</sub> N	IC	IC	IC	$\leq 5.97\text{E}+07$	$\geq 6.10$	ND	1	10
Constraints	[1 ; 8]	[10 ; 20]	[3000 ; 30000]	[8.96E+04 ; 2.58E+07]	[9.28 ; 157.52]			



Table D.2: Summary of the application of the method to Jørgensen et al. (2004, 2005)'s observations of L1448-C.

Species	$M_0 (M_\odot)$	$T_0$ (K)	$R_0$ (AU)	$\rho_0$ (part.cm <sup>-3</sup> )	$t_{\text{ff}}$ (kyrs)	$\chi^2$	$N_L$	$e$
CO	IC	15	IC	$\geq 8.96\text{E}+04$	$\leq 157.52$	2.1	4	3
CS	IC	IC	$\geq 5000$	$\leq 5.74\text{E}+06$	$\geq 19.69$	2.6	2	3
SO	IC	IC	IC	$\leq 8.96\text{E}+07$	$\geq 4.98$	ND	1	10
HCO <sup>+</sup>	IC	IC	IC	IC	IC	0.21	4	3
N <sub>2</sub> H <sup>+</sup>	IC	$\geq 20$	IC	$\geq 8.96\text{E}+04$	$\leq 157.52$	ND	1	10
HCN	$\geq 1$	IC	IC	$\leq 8.96\text{E}+07$	$\geq 4.98$	2.5	3	3
HNC	IC	IC	IC	$\leq 8.96\text{E}+07$	$\geq 4.98$	ND	2	3
CN	IC	IC	IC	$\leq 1.94\text{E}+07$	$\geq 10.72$	2.4	4	3
HC <sub>3</sub> N	IC	IC	IC	$\leq 5.97\text{E}+07$	$\geq 6.10$	ND	1	10
H <sub>2</sub> CO	IC	IC	$\geq 5000$	$\leq 7.65\text{E}+06$	$\geq 17.05$	1.2	3	3
CH <sub>3</sub> OH	IC	IC	IC	IC	IC	ND	1	10
Constraints	[1 ; 8]	15	[5000 ; 30000]	[8.96E+04 ; 5.74E+06]	[19.69 ; 157.52]			

Table D.3: Summary of the application of the method to Jørgensen et al. (2004, 2005)'s observations of N1333-I2.

Species	$M_0 (M_\odot)$	$T_0$ (K)	$R_0$ (AU)	$\rho_0$ (part.cm <sup>-3</sup> )	$t_{\text{ff}}$ (kyrs)	$\chi^2$	$N_L$	$e$
CO	IC	$\leq 15$	IC	IC	IC	3.9	4	3
CS	IC	IC	$\geq 5000$	$\leq 3.82\text{E}+06$	$\geq 24.11$	0.91	2	3
SO	$\geq 1$	$\leq 25$	IC	$\leq 8.96\text{E}+07$	$\geq 4.98$	1.3	2	3
HCO <sup>+</sup>	4	10	30000	$5.98\text{E}+04$	192.92	0.59	4	3
N <sub>2</sub> H <sup>+</sup>	$\geq 1$	$\geq 20$	IC	$\geq 8.96\text{E}+04$	$\leq 157.52$	ND	1	10
HCN	IC	IC	IC	$\leq 8.96\text{E}+07$	$\geq 4.98$	7.1	3	3
HNC	IC	IC	IC	$\leq 8.96\text{E}+07$	$\geq 4.98$	ND	2	3
CN	IC	IC	IC	$\leq 5.97\text{E}+07$	$\geq 6.10$	2.3	4	3
HC <sub>3</sub> N	IC	IC	IC	$\leq 2.98\text{E}+07$	$\geq 8.63$	ND	1	10
H <sub>2</sub> CO	IC	IC	IC	$\leq 8.96\text{E}+07$	$\geq 4.98$	0.63	3	3
CH <sub>3</sub> OH	IC	IC	IC	IC	IC	20.4	8	10
CH <sub>3</sub> CN	$\geq 2$	IC	IC	$\leq 8.96\text{E}+07$	$\geq 4.98$	8.5	4	3
Constraints	4	10	30000	$5.98\text{E}+04$	192.92			

Table D.4: Summary of the application of the method to Jørgensen et al. (2004, 2005)'s observations of N1333-I4A.

Species	$M_0 (M_\odot)$	$T_0$ (K)	$R_0$ (AU)	$\rho_0$ (part.cm <sup>-3</sup> )	$t_{\text{ff}}$ (kyrs)	$\chi^2$	$N_L$	$e$
CO	IC	$\leq 20$	IC	IC	IC	0.7	4	3
CS	IC	IC	IC	$\leq 5.97\text{E}+07$	$\geq 6.10$	0.019	2	3
SO	$\geq 1$	$\leq 25$	IC	$\leq 8.96\text{E}+07$	$\geq 4.98$	0.66	2	3
HCO <sup>+</sup>	$\geq 2$	$\leq 20$	$\geq 20000$	$\leq 2.01\text{E}+05$	$\geq 105.01$	1.2	3	3
N <sub>2</sub> H <sup>+</sup>	$\geq 1$	$\geq 20$	IC	$\geq 8.96\text{E}+04$	$\leq 157.52$	ND	1	10
HCN	IC	IC	IC	$\leq 8.96\text{E}+07$	$\geq 4.98$	18	3	10
HNC	IC	IC	IC	IC	IC	ND	2	3
CN	IC	IC	IC	IC	IC	1.4	4	3
HC <sub>3</sub> N	IC	IC	IC	$\leq 8.96\text{E}+07$	$\geq 4.98$	ND	1	10
H <sub>2</sub> CO	IC	IC	IC	$\leq 8.96\text{E}+07$	$\geq 4.98$	0.59	3	3
CH <sub>3</sub> OH	$\geq 2$	10	$\geq 5000$	$\leq 2.58\text{E}+07$	$\geq 9.28$	4.5	7	3
Constraints	[2 ; 8]	10	[20000 ; 30000]	[5.98E+04 ; 2.01E+05]	[105.01 ; 192.92]			

Table D.5: Summary of the application of the method to Jørgensen et al. (2004, 2005)'s observations of N1333-I4B.

Species	$M_0$ ( $M_\odot$ )	$T_0$ (K)	$R_0$ (AU)	$\rho_0$ (part.cm $^{-3}$ )	$t_{\text{ff}}$ (kyrs)	$\chi^2$	$N_L$	$e$
CO	IC	$\leq 20$	IC	IC	IC	0.3	4	3
CS	IC	IC	IC	$\leq 5.97\text{E}+07$	$\geq 6.10$	1.1	2	3
SO	$\geq 1$	$\leq 25$	IC	$\leq 8.96\text{E}+07$	$\geq 4.98$	0.82	2	3
HCO $^+$	$\geq 2$	$\leq 20$	$\geq 20000$	$\leq 1.20\text{E}+05$	$\geq 136.41$	2.7	2	3
N $_2$ H $^+$	$\geq 1$	$\geq 20$	IC	$\geq 8.96\text{E}+04$	$\leq 157.52$	ND	1	10
HCN	IC	IC	IC	$\leq 8.96\text{E}+07$	$\geq 4.98$	1.9	3	3
HNC	IC	IC	IC	$\leq 8.96\text{E}+07$	$\geq 4.98$	ND	2	3
CN	IC	IC	IC	$\leq 8.96\text{E}+07$	$\geq 4.98$	1.5	4	3
HC $_3$ N	IC	IC	IC	$\leq 8.96\text{E}+07$	$\geq 4.98$	ND	1	10
H $_2$ CO	$\geq 1$	IC	$\geq 7500$	$\leq 9.56\text{E}+05$	$\geq 48.23$	6.2	3	3
CH $_3$ OH	2	10	20000	1.01E+05	148.51	11.4	7	10
Constraints	2	10	20000	1.01E+05	148.51			

Table D.6: Summary of the application of the method to Jørgensen et al. (2004, 2005)'s observations of L1527.

Species	$M_0$ ( $M_\odot$ )	$T_0$ (K)	$R_0$ (AU)	$\rho_0$ (part.cm $^{-3}$ )	$t_{\text{ff}}$ (kyrs)	$\chi^2$	$N_L$	$e$
CO	IC	$\leq 15$	IC	$\geq 8.96\text{E}+04$	$\leq 157.52$	1.0	4	3
CS	IC	IC	IC	$\leq 8.96\text{E}+07$	$\geq 4.98$	2.9	4	3
SO	IC	IC	IC	$\leq 8.96\text{E}+07$	$\geq 4.98$	1.4	2	3
HCO $^+$	$\geq 2$	$\leq 20$	$\geq 20000$	$\leq 1.20\text{E}+05$	$\geq 136.41$	0.41	5	3
N $_2$ H $^+$	$\geq 1$	IC	IC	IC	IC	ND	1	10
HCN	IC	IC	IC	$\leq 8.96\text{E}+07$	$\geq 4.98$	ND	1	10
HNC	IC	IC	IC	$\leq 8.96\text{E}+07$	$\geq 4.98$	ND	2	3
CN	IC	IC	IC	$\leq 1.94\text{E}+07$	$\geq 10.72$	0.93	4	3
HC $_3$ N	$\geq 1$	IC	IC	$\leq 2.99\text{E}+07$	$\geq 8.62$	ND	1	10
H $_2$ CO	IC	IC	$\geq 5000$	$\leq 7.65\text{E}+06$	$\geq 17.05$	7.7	3	3
Constraints	[2 ; 8]	[10 ; 15]	[20000 ; 30000]	[8.96E+04 ; 1.20E+05]	[136.41;157.52]			

Table D.7: Summary of the application of the method to Jørgensen et al. (2004, 2005)'s observations of VLA1623.

Species	$M_0$ ( $M_\odot$ )	$T_0$ (K)	$R_0$ (AU)	$\rho_0$ (part.cm $^{-3}$ )	$t_{\text{ff}}$ (kyrs)	$\chi^2$	$N_L$	$e$
CO	IC	15	IC	$\geq 8.96\text{E}+04$	$\leq 157.52$	0.01	4	3
CS	IC	IC	$\geq 5000$	$\leq 3.82\text{E}+06$	$\geq 24.11$	2.6	2	3
SO	$\geq 1$	$\leq 25$	$\leq 20000$	[3.02E+05 ; 8.96E+07]	[4.98 ; 85.74]	1.6	3	3
HCO $^+$	IC	IC	IC	IC	IC	2.0	3	3
N $_2$ H $^+$	$\geq 1$	$\geq 20$	IC	$\geq 8.96\text{E}+04$	$\leq 157.52$	ND	1	10
HCN	IC	IC	IC	$\leq 8.96\text{E}+07$	$\geq 4.98$	ND	1	10
HNC	IC	IC	IC	$\leq 8.96\text{E}+07$	$\geq 4.98$	ND	2	3
CN	IC	IC	IC	$\leq 2.98\text{E}+07$	$\geq 8.62$	2.0	4	3
HC $_3$ N	IC	IC	IC	$\leq 2.98\text{E}+07$	$\geq 8.62$	ND	1	10
H $_2$ CO	IC	IC	$\geq 5000$	$\leq 7.65\text{E}+06$	$\geq 17.05$	0.061	3	3
CH $_3$ OH	IC	IC	IC	IC	IC	ND	1	10
Constraints	[1 ; 8]	15	[5000 ; 20000]	[3.02E+05 ; 7.65E+06]	[17.05 ; 85.74]			

Table D.8: Summary of the application of the method to Jørgensen et al. (2004, 2005)'s observations of L483.

Species	$M_0 (M_\odot)$	$T_0$ (K)	$R_0$ (AU)	$\rho_0$ (part.cm <sup>-3</sup> )	$t_{ff}$ (kyrs)	$\chi^2$	$N_L$	$e$
CO	IC	$\leq 20$	IC	IC	IC	1.1	4	3
CS	IC	IC	IC	$\leq 8.96E+07$	$\geq 4.98$	1.7	2	3
SO	IC	IC	IC	$\leq 8.96E+07$	$\geq 4.98$	ND	1	10
HCO <sup>+</sup>	[2 ; 4]	10	$\geq 20000$	$\leq 1.01E+05$	$\geq 148.51$	0.63	4	3
N <sub>2</sub> H <sup>+</sup>	$\geq 1$	$\geq 20$	IC	$\geq 8.96E+04$	$\leq 157.52$	ND	1	10
HCN	IC	IC	IC	$\leq 8.96E+07$	$\geq 4.98$	1.0	3	3
HNC	IC	IC	IC	$\leq 8.96E+07$	$\geq 4.98$	ND	2	3
CN	IC	IC	IC	$\leq 2.99E+07$	$\geq 8.63$	2.3	4	3
HC <sub>3</sub> N	IC	IC	IC	$\leq 5.97E+07$	$\geq 6.10$	ND	1	10
H <sub>2</sub> CO	IC	IC	$\geq 5000$	$\leq 1.61E+06$	$\geq 37.13$	ND	1	10
Constraints	[2 ; 4]	10	[20000 ; 30000]	[5.98E+04 ; 1.01E+05]	[148.51 ; 192.92]			

Table D.9: Summary of the application of the method to Jørgensen et al. (2004, 2005)'s observations of L723.

Species	$M_0 (M_\odot)$	$T_0$ (K)	$R_0$ (AU)	$\rho_0$ (part.cm <sup>-3</sup> )	$t_{ff}$ (kyrs)	$\chi^2$	$N_L$	$e$
CO	IC	$\leq 20$	IC	IC	IC	2.5	4	3
CS	IC	IC	IC	$\leq 8.96E+07$	$\geq 4.98$	13	2	10
SO	$\geq 1$	IC	IC	$\leq 8.96E+07$	$\geq 4.98$	ND	1	10
HCO <sup>+</sup>	4	10	30000	5.98E+04	192.92	0.61	3	3
N <sub>2</sub> H <sup>+</sup>	$\geq 1$	$\geq 20$	IC	$\geq 8.96E+04$	$\leq 157.52$	ND	1	10
HCN	IC	IC	IC	$\leq 8.96E+07$	$\geq 4.98$	ND	1	10
HNC	IC	IC	IC	$\leq 8.96E+07$	$\geq 4.98$	ND	2	3
CN	IC	IC	IC	$\leq 2.99E+07$	$\geq 8.63$	1.8	4	3
HC <sub>3</sub> N	$\geq 1$	IC	IC	$\leq 2.99E+07$	$\geq 8.63$	ND	1	10
H <sub>2</sub> CO	IC	IC	IC	$\leq 8.96E+07$	$\geq 4.98$	ND	1	10
Constraints	4	10	30000	5.98E+04	192.92			

Table D.10: Summary of the application of the method to Jørgensen et al. (2004, 2005)'s observations of L1157.

Species	$M_0 (M_\odot)$	$T_0$ (K)	$R_0$ (AU)	$\rho_0$ (part.cm <sup>-3</sup> )	$t_{ff}$ (kyrs)	$\chi^2$	$N_L$	$e$
CO	IC	$\leq 20$	IC	IC	IC	3.3	4	3
CS	IC	IC	IC	IC	IC	ND	1	10
SO	$\geq 1$	IC	IC	$\leq 8.96E+07$	$\geq 4.98$	0.25	3	3
HCO <sup>+</sup>	$\geq 2$	$\leq 20$	$\geq 20000$	$\leq 1.20E+05$	$\geq 136.41$	0.29	2	3
N <sub>2</sub> H <sup>+</sup>	$\geq 1$	$\geq 20$	IC	$\geq 8.96E+04$	$\leq 157.52$	ND	1	10
HCN	IC	IC	IC	IC	IC	ND	1	10
HNC	IC	IC	IC	IC	IC	ND	2	3
CN	IC	IC	IC	IC	IC	1.1	4	3
HC <sub>3</sub> N	IC	IC	IC	$\leq 8.96E+07$	$\geq 4.98$	ND	1	10
H <sub>2</sub> CO	IC	IC	IC	IC	IC	3.9	3	3
Constraints	[2 ; 8]	[10 ; 20]	[20000 ; 30000]	[8.96E+04 ; 1.20E+05]	[136.41 ; 157.52]			

Table D.11: Summary of the application of the method to Jørgensen et al. (2004)'s observations of L1551-I5.

Species	$M_0$ ( $M_\odot$ )	$T_0$ (K)	$R_0$ (AU)	$\rho_0$ (part.cm $^{-3}$ )	$t_{\text{ff}}$ (kyrs)	$\chi^2$	$N_L$	$e$
CO	IC	$\leq 15$	IC	IC	IC	1.3	4	3
CS	IC	IC	IC	$\leq 8.96\text{E}+07$	$\geq 4.98$	0.64	4	3
SO	$\geq 1$	IC	IC	$\leq 8.96\text{E}+07$	$\geq 4.98$	0.95	2	3
HCO $^+$	[2 ; 4]	10	$\geq 20000$	$\leq 1.01\text{E}+05$	$\geq 148.51$	1.3	2	3
N $_2$ H $^+$	$\geq 1$	$\geq 20$	IC	$\geq 8.96\text{E}+04$	$\leq 157.52$	ND	1	10
HNC	IC	IC	IC	$\leq 8.96\text{E}+07$	$\geq 4.98$	ND	2	3
HC $_3$ N	IC	IC	IC	$\leq 5.97\text{E}+07$	$\geq 6.10$	ND	1	10
Constraints	[2 ; 4]	10	[20000 ; 30000]	[8.96E+04 ; 1.01E+05]	[148.51 ; 157.52]			



# E | ACRONYMS AND SYMBOLS

Table E.1: Table of acronyms

Acronyms	Definition
BE	Bonnor-Ebert
COMs	Complex Organic Molecules
CR	Cosmic Ray
DFT	Density Functional Theory
DR	Dissociative Recombination
EDC	Evolved Dark Cloud
ER	Envelope Region
FHSC	First HydroStatic Core
HCR	Hot Core Region
IC	InConclusive
IPPC	Initial Physical Parameters of Collapse
IR	InfraRed
IRAM	Institut de RadioAstronomie Millimétrique
ISM	InterStellar Medium
KIDA	KInetic Database for Astrochemistry
LEDC	Low Evolved Dark Cloud
MP2	2nd order Møller-Plesset method
ND	No Data
PMC	Parent Molecular Cloud
PA	Percentage of Agreement
QCISD	Quadratic Configuration Interaction Calculation with Single and Double excitations and a triples excitation contribution
RHD	Radiation HydroDynamical
SHSC	Second HydroStatic Core
TH	Too High
TR	Transitional Region
UV	Ultra Violet

Table E.2: Table of symbols

Symbols	Definitions	Units (when relevant)
$\alpha$	Pre-exponential factor of the Arrhenius law	$\text{cm}^3.\text{s}^{-1}$
$\alpha_p$	Dipole polarizability	$\text{cm}^3$
$\beta$	Factor for the Arrhenius-Kooij law	-
$\gamma$	Factor for the Arrhenius-Kooij law ( $=E_A$ in that case) or the Su-Chesnavich capture approach rate constant expressions	-
$\gamma_D$	Density contrast	-
$\delta_{is}$	Dirac function assessing the match between source $s$ and IPPC value $y_i$	-
$\epsilon$	Recombination efficiency	-
$\epsilon_M$	Mass ratio	-
$\zeta_{\text{CR}}$	CR ionization rate	$\text{s}^{-1}$
$\kappa_{ij}$	Efficiency of the reaction between species $i$ and $j$	-
$\mu$	Mean atomic weight	-
$\mu_D$	Dipole moment	statC.cm
$\xi$	Dimensionless radius of the BE sphere	-
$\rho$	Density of the BE sphere	$\text{g.cm}^{-3}$
$\rho_0$	Initial external density of the BE sphere	$\text{g.cm}^{-3}$ or $\text{part.cm}^{-3}$
$\rho_c$	Initial central density of the BE sphere	$\text{g.cm}^{-3}$
$\rho_S$	Spearman's correlation coefficient	-
$\sigma_g$	Cross section of a grain	$\text{cm}^2$
$\sigma_i$	Uncertainty in observation $i$	$\text{K.km.s}^{-1}$
$\chi^2$	$\chi^2$ statistic	-
$A_V$	Visual extinction	mag
b-X	Species X in the grains bulk	-
$c_s$	Isothermal sound speed	$\text{m.s}^{-1}$
$D$	Distance of disagreement	-
$D_{\text{min}}$	Minimum of distance of disagreement	-
$d_s$	Density of chemisorption sites on a grain	$\text{sites.cm}^{-2}$
$e$	Uncertainty factor	-
$e^-$	Electron	-
$E_A$	Activation energy/barrier	K
$E_D$	Diffusion energy	K
$F_{\text{mod}}$	Modeled integrated line intensity	$\text{K.km.s}^{-1}$
$F_{\text{obs}}$	Observed integrated line intensity	$\text{K.km.s}^{-1}$
$G$	Gravitational constant	$\text{m}^3.\text{kg}^{-1}.\text{s}^{-2}$
$k$	Rate constant	$\text{cm}^3.\text{s}^{-1}$

Symbols	Definitions	Units (when relevant)
$k_B$	Boltzmann constant	$\text{m}^2.\text{kg}.\text{s}^{-2}.\text{K}^{-1}$
$m_H$	Hydrogen atom mass	g
$M_0$	Initial prestellar core mass	$M_\odot$
$M_{\text{BE}}$	Mass of the critical BE sphere	$M_\odot$
$n(X)$	Concentration of species X	$\text{part}.\text{cm}^{-3}$
$n_g$	Number density of grains	$\text{part}.\text{cm}^{-3}$
$n_H$	Total proton density	$\text{part}.\text{cm}^{-3}$
$N_{\text{bulk}}$	Number of bulk mono-layer	-
$N_L$	Number of observed lines	-
$N_{\text{ML}}$	Total number of mono-layer on grains	-
$N_{\text{surf}}$	Number of surface mono-layer	-
$N_{\text{obs}}$	Number of observed species	-
$N_s$	Number of sources	-
$N_y(s)$	Number of IPPC values constrained for source s	-
$P_{\text{abs}}$	Probability of absorption of each mono-layer of ice	-
$P_0$	External pressure of the prestellar core	-
$r$	Radius	AU
$r_c$	Characteristic radius	AU
$r_g$	Grains core radius	$\mu\text{m}$
$R_0$	Initial radius of the BE sphere	AU
$R_c$	Radius of the innermost cell of the Lagrangian grid	AU
$R_{\text{HC}}$	Hot core radius	AU
$s$	Source	-
$S$	Sticking coefficient	-
s-X	Species X on the grains surface	-
$t$	Time	kyrs
$t_{\text{BF}}$	Best-fit time	kyrs
$t_f$	Final time of collapse	kyrs
$t_{\text{ff}}$	Free-fall time	kyrs
$T$	Temperature	K
$T_0$	Initial temperature of the BE sphere	K
$T_{\text{gas}}$	Gas temperature	K
$T_m$	Transitional temperature for the expressions ionpol1-2	K
$v$	Reaction rate	$\text{part}.\text{cm}^{-3}.\text{s}^{-1}$
$v_H$	Thermal velocity of hydrogen atoms	$\text{cm}.\text{s}^{-1}$
X	Species	-
[X]	Abundance of species X	-



Symbols	Definitions	Units (when relevant)
$[X]_{\text{ini}}$	Elemental abundance of species X	-
$[X]_{\text{obs}}$	Observed abundance of species X	-

# F | INTRODUCTION

## F.1 REVISITER LA CHIMIE ...

### F.1.1 Généralités

L'espace n'est pas vide. Même le milieu le moins dense de la galaxie, qui remplit l'espace entre les étoiles, appelé milieu interstellaire (ci-après MIS), est en réalité composé de gaz et de poussières, dont les fractions massiques représentent respectivement 99% et 1% de la masse totale du MIS (Lequeux, 2005; Draine, 2011). Le gaz interstellaire est sous forme ionique, atomique et moléculaire et est principalement composé des éléments les plus légers de l'Univers, à savoir l'hydrogène (H) et l'hélium (He), représentant respectivement 70% et 28% de la masse totale du MIS. Les éléments plus lourds tels que le carbone (C), l'azote (N), l'oxygène (O), le soufre (S), le magnésium (Mg), le fer (Fe), le silicium (Si) ou l'argon (Ar) ne représentent que 2% de la masse totale du MIS (voir la figure F.1). La poussière interstellaire est quant à elle principalement composée de silicates, de carbone amorphe et de glaces. Cette composition évolue au travers de différentes phases caractérisées par l'état de sa matière constitutive. La discipline dédiée à l'étude de cette évolution chimique du MIS est appelée l'astrochimie.

L'astrochimie est l'une des nombreuses branches de l'astrophysique. Elle consiste en l'étude des éléments chimiques qui composent l'Univers, au carrefour de l'astronomie et de la chimie. En particulier, elle se concentre sur la formation et la destruction des molécules, ainsi que leurs interactions avec les radiations, les grains de poussière interstellaires et entre elles. L'astrochimie s'inscrit dans le contexte plus général de l'astrobiologie, qui étudie l'origine des composants moléculaires nécessaires à la Vie dans les environnements extraterrestres. Dans ce contexte, les études astrochimiques se concentrent principalement sur les différentes structures du processus de formation des systèmes stellaires, en utilisant trois domaines principaux de la recherche: la spectroscopie, la chimie expérimentale et la modélisation chimique.

### F.1.2 Le modèle de chimie NAUTILUS

Le modèle chimique NAUTILUS calcule l'évolution temporelle des abondances chimiques dans des conditions physiques données en résolvant un système d'équations

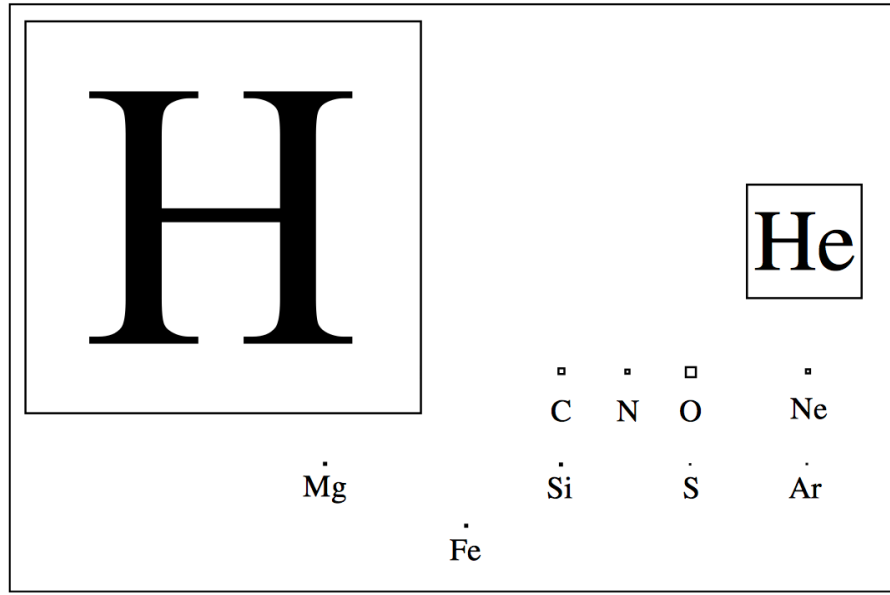


Figure F.1: Le "tableau périodique de l'astronome" (McCall, 2001)

différentielles. Le modèle utilise l'approche «rate equations», qui consiste à considérer que l'évolution du système est continue et déterministe, c'est-à-dire que l'état du système à un instant donné peut être déduit de son état initial. Le modèle peut simuler une chimie à 3 phases comprenant la chimie en phase gazeuse, à la surface des grains et dans le manteau des grains, ainsi que les échanges possibles entre ces différentes phases (Ruaud et al., 2016). Les processus pris en compte dans le modèle sont décrits ci-après.

### F.1.2.1 Chimie en phase gazeuse

#### F.1.2.1.1 Reactions bimoléculaires

Pour une réaction en phase gazeuse entre les espèces  $i$  et  $j$ , la constante de vitesse correspondante  $k_{ij}$  est calculée en utilisant la loi d'Arrhenius-Kooij:

$$k_{ij} = \alpha_{ij} \left( \frac{T_{\text{gas}}}{300\text{K}} \right)^{\beta} \exp\left( \frac{-E_{A,ij}}{T_{\text{gas}}} \right) \quad (\text{F.1})$$

où  $\alpha_{ij}$  et  $\beta$  sont des constantes de la réaction,  $T_{\text{gas}}$  est la température du gaz, en K, et  $E_{A,ij}$  est l'énergie d'activation de la réaction, en K. Cette dernière est l'énergie nécessaire au système pour surmonter la barrière d'activation de la réaction. Par conséquent, seules les collisions impliquant une énergie cinétique suffisante peuvent sur-

monter cette barrière et entraîner une réaction.  $\alpha_{ij}$ ,  $\beta$  et  $E_{A,ij}$  sont obtenus en ajustant des mesures de laboratoire à différentes températures. Dans plusieurs cas, l'équation (F.1) peut être simplifiée car  $\beta = 0$  ou, comme c'est le cas pour la plupart des réactions ion-neutre, les réactions ne comportent pas de barrière d'activation, *ie*  $E_{A,ij} = 0$ .

#### F.1.2.1.2 Photodissociation et photoionisation

Le modèle prend en compte les deux principaux phénomènes responsables de la photodissociation et de la photoionisation des espèces en phase gazeuse :

- l'interaction directe entre les espèces et les rayons cosmiques (RC),
- l'interaction directe avec les photons UV, provenant du champ de rayonnement interstellaire ou induit par les RC (voir Prasad and Tarafdar, 1983).

L'efficacité de ces phénomènes dépend principalement du taux d'ionisation par les RC  $\zeta_{RC}$ , en  $s^{-1}$ , et de l'extinction visuelle  $A_V$ , en mag, qui quantifie l'absorption et la diffusion du champ électromagnétique par le gaz et les grains de poussière, *ie* détermine l'opacité du milieu considéré au rayonnement.

#### F.1.2.2 Chimie sur les grains

Le modèle NAUTIUS considère des grains avec des noyaux de silicate et un rayon  $r_g = 0.1\mu m$ . L'adsorption de molécules sur un grain nu forme des mono-couches de glace qui s'empilent successivement. Le nombre total de monocouches est  $N_{ML} = N_{surf} + N_{bulk}$  où  $N_{surf}$  est le nombre de mono-couches de surface, c'est-à-dire les couches externes pouvant interagir avec la phase gazeuse, et  $N_{bulk}$  est le nombre de mono-couches du manteau. Le maximum total de mono-couches sur la surface est défini par  $N_{surf,max} = 2$ . Sur les mono-couches externes, sont considérés des sites qui représentent les petites zones sur lesquelles les espèces peuvent être adsorbées et où des réactions chimiques peuvent se produire. Une densité de  $d_s = 1.5 \times 10^{15}$  sites par  $cm^2$  est prise en compte dans le modèle. Ci-dessous est décrite la modélisation de la chimie des grains dans le modèle 3 phases de NAUTILUS. Tous les processus décrits sont résumés à la figure F.2.

##### F.1.2.2.1 Accrétion et diffusion

Le mécanisme d'accrétion des espèces chimiques sur la surface des grains est celui décrit dans Hasegawa et al. (1992). Le taux d'accrétion d'une espèce dépend principalement de la densité de grains dans le milieu, de leur section géométrique transverse, ainsi que du coefficient de collage. Ce dernier est pris égal à 1 pour toutes les espèces sauf H et  $H_2$ , pour lesquelles le formalisme est celui dérivé expérimentalement par Chaabouni et al. (2012).

Concernant la diffusion des espèces à la surface des grains après leur accrétion, le modèle prend en compte la diffusion thermique. Ce mécanisme dépend de l'énergie de diffusion de l'espèce, c'est-à-dire l'énergie qu'il faut apporter à l'espèce pour passer d'un site à un autre. Ces énergies sont calculées en tant que fraction des énergies de liaison respectives des espèces, c'est-à-dire l'énergie nécessaire à ces espèces pour désorber de la surface des grains. Pour la surface, la valeur de ce rapport est de 0,4, comme le suggèrent les expériences et les travaux théoriques réalisés sur H (voir Ru-[aud et al., 2016](#)), CO et CO<sub>2</sub> (voir [Karssemeijer and Cuppen, 2014](#)). Cette valeur est ensuite généralisée à toutes les espèces à la surface des grains.

Une fois qu'une espèce entre dans le manteau des grains, le modèle considère que sa diffusion est contrôlée par la diffusion de la glace d'eau, comme le montre le travail théorique de [Ghesquière et al. \(2015\)](#). Ainsi, pour les espèces qui ont une énergie de diffusion  $E_D < E_D^{\text{H}_2\text{O}}$ , leurs énergies de diffusion dans le manteau est prise égale à  $E_D^{\text{H}_2\text{O}}$ . De plus, le rapport entre les énergies de diffusion et de liaison est pris égal à 0,8 dans le manteau (voir [Ru-\[aud et al., 2016\]\(#\)](#)).

#### F.1.2.2.2 Réactions à la surface des grains

Le mécanisme principal considéré dans le modèle pour les réactions à la surface des grains est le mécanisme Langmuir-Hinshelwood, qui considère qu'une réaction entre deux espèces se produit selon les étapes suivantes :

1. l'adsorption des deux réactifs à la surface des grains,
2. la diffusion d'un (ou des deux) réactif(s) sur la surface,
3. la réaction entre les deux réactifs lors de leur rencontre sur un même site de grains.

Ce mécanisme dépend principalement de la probabilité de réaction entre les espèces  $i$  et  $j$ ,  $\kappa_{ij}$ . Ce coefficient est pris égal à 1 si la réaction entre les deux espèces est sans barrière, ainsi, dans ce cas, les espèces réagiront toujours lors de leur rencontre. Cependant, si la réaction a une barrière d'activation  $E_{A,ij} > 0$ , alors la concurrence entre réaction et diffusion (ou désorption) de l'un des réactifs est envisagée, comme le suggèrent [Chang et al. \(2007\)](#) et [Garrod and Pauly \(2011\)](#). Dans ce cas, la réaction se produit si l'énergie d'activation de la réaction est inférieure aux énergies de diffusion des deux réactifs.

Dans le manteau des grains, les réactions se produisent via le même mécanisme. Cependant,  $\kappa_{ij}$  est divisé par le nombre de mono-couches constituant le manteau, en considérant que l'efficacité de la diffusion dans le manteau diminue lorsque l'épaisseur de celui-ci augmente.

L'autre mécanisme de réaction considéré est le mécanisme Eley-Rideal qui peut être décomposé en :

1. l'adsorption d'un des réactifs à la surface des grains,
2. la collision directe entre une espèce en phase gazeuse (deuxième réactif) et celle adsorbée,
3. la réaction possible entre les deux réactifs sur le site des grains où la collision s'est produite.

On peut noter que ce mécanisme ne peut se produire qu'à la surface des grains (pas dans le manteau), où les espèces adsorbées sont en contact direct avec la phase gazeuse. De plus, ce mécanisme est moins fréquent que le mécanisme Langmuir-Hinshelwood, mais peut toujours jouer un rôle important dans la formation d'espèces spécifiques lorsque le réactif adsorbé est très abondant (voir [Ruaud et al., 2015](#)).

#### F.1.2.2.3 Dissociation

Comme pour la phase gazeuse, la chimie des grains prend en compte la photodissociation directe par photons UV ainsi que la photodissociation induite par les photons UV secondaires introduits par [Prasad and Tarafdar \(1983\)](#). Ces processus sont efficaces à la surface et dans le manteau des grains. En effet, la probabilité d'absorption de chaque mono-couche de glace est faible ( $P_{\text{abs}} \approx 0.007$  photons/mono-couches, [Anderson and van Dishoeck, 2008](#)). Cette hypothèse est donc raisonnable étant donné que le nombre moyen de mono-couches de glace sur les grains est de 100 mono-couches et que, par conséquent, seulement 0,7% des photons entrant en collision avec la surface seraient absorbés avant d'atteindre le noyau des grains.

#### F.1.2.2.4 Désorption

Les processus de désorption pris en compte dans le modèle sont :

- la désorption thermique, *ie* l'évaporation, qui dépend de la température des grains et de l'énergie de liaison des espèces considérées,
- la désorption due au chauffage ponctuel des grains par les RC, qui induit une désorption thermique. Ce mécanisme dépend de la fraction de temps que le grain passe à la température due à l'impact des RC, et du taux de désorption thermique à cette température,
- la désorption chimique, qui prend en compte pour les réactions exothermiques qu'une partie de l'énergie libérée peut provoquer la désorption de leurs produits. Le formalisme utilisé dans le modèle pour ce processus est celui décrit dans [Garrod et al. \(2007\)](#). Ils ont estimé que la fraction des produits désorbés en phase

gazeuse dépend de leurs énergies de liaison, de l'enthalpie de la réaction et de la fraction de l'énergie libérée perdue à la surface. Dans le modèle utilisé ici, les paramètres sont sélectionnés pour donner une efficacité d'évaporation d'environ 1% pour toutes les espèces,

- la photodésorption, qui est un processus non thermique qui se produit après l'absorption d'un photon UV par la surface. Comme recommandé par [Bertin et al. \(2012\)](#), un taux de photodésorption unique est utilisé pour toutes les espèces de la surface.

Tous les processus décrits ci-dessus sont résumés sur la figure F.2.

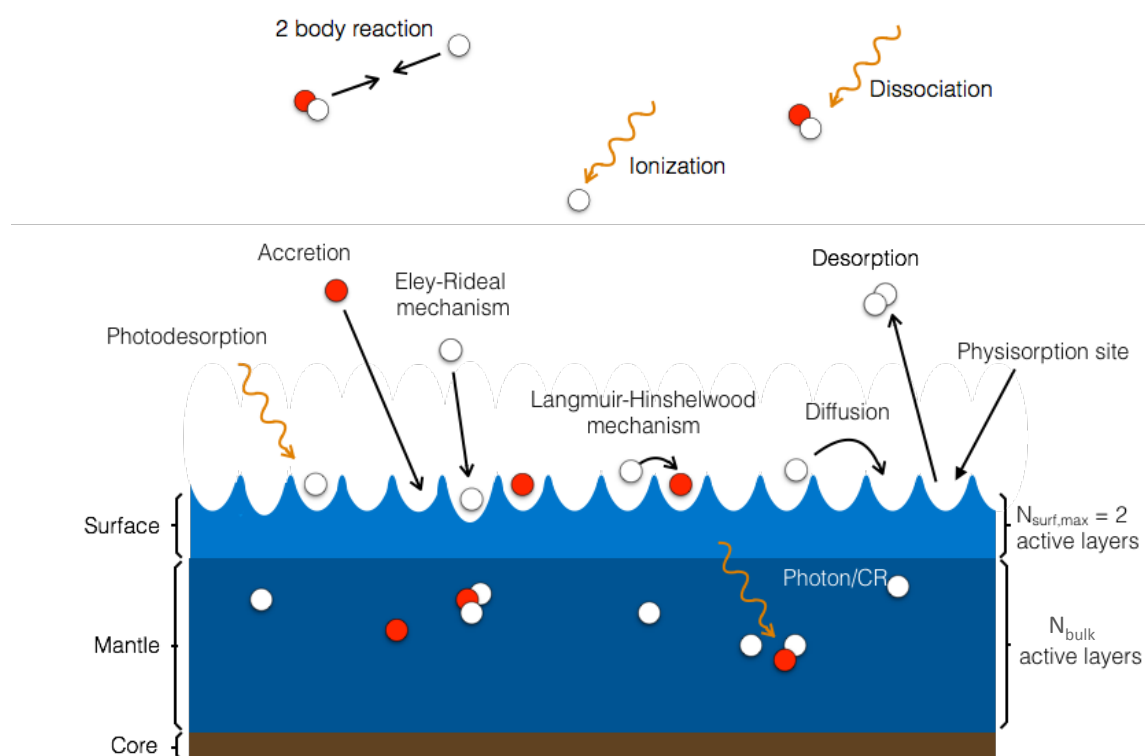


Figure F.2: Résumé des processus chimiques pris en compte dans le modèle 3 phases NAUTILUS ([Ruaud et al., 2016](#)).

## F.2 ...DE LA FORMATION STELLAIRE

En plus de permettre la formation de planètes, d'eau liquide et de la Vie, les étoiles jouent un rôle majeur dans l'Univers. Ce rôle consiste à former, détruire et redistribuer la matière interstellaire tout au long de leur cycle de vie. La figure F.3 illustre ce cycle de la matière interstellaire à travers la formation, la vie et la mort des étoiles. Dans ce qui suit, chaque étape de ce cycle est présentée, avec un accent particulier sur la formation des étoiles, sujet d'intérêt de cette thèse.

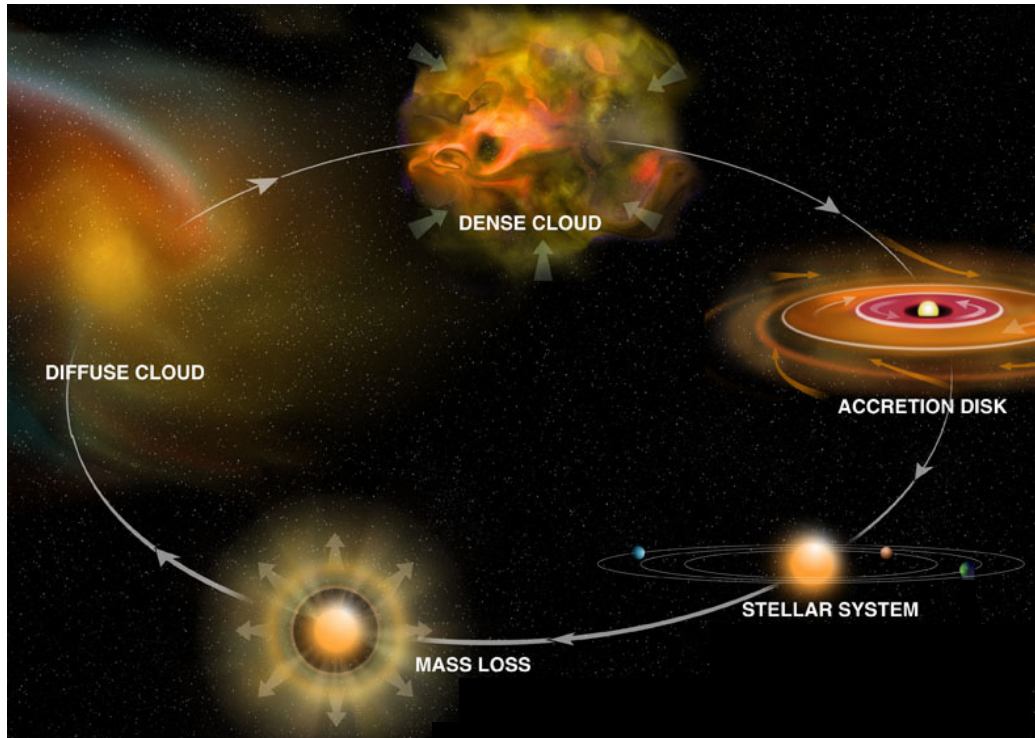


Figure F.3: Le cycle de la matière interstellaire. Credits: Bill Saxton, NRAO/AUI/NSF.

### F.2.1 Des nuages diffus aux nuages denses

Les nuages diffus sont définis comme des objets du MIS où la densité est de  $n_H \in [100 ; 500] \text{ part.cm}^{-3}$  et  $T_{\text{gas}} \in [30 ; 100] \text{ K}$  (Snow and McCall, 2006). Dans ces régions, la densité est suffisamment élevée pour atténuer le champ de rayonnement interstellaire ( $A_V > 0,2$ ) et  $\text{H}_2$  peut s'accumuler sans être instantanément photodissocié. Sous effets dynamiques, un tel nuage diffus peut se condenser en un nuage dense. Ces nuages denses sont presque opaques au champ de rayonnement interstellaire ( $A_V > 5$ ), ce qui permet au carbone de rester sous forme moléculaire (préférentiellement sous forme de CO). Cette opacité est due à la forte densité de grains de poussière. Les nuages denses sont donc caractérisés par de fortes densités de protons ( $n_H > 10^4 \text{ part.cm}^{-3}$ ), ce qui implique également des températures basses ( $T_{\text{gas}} \in [10 ; 50] \text{ K}$ , voir Snow and McCall, 2006). On peut noter que l'opacité de tels nuages à la lumière visuelle est la raison pour laquelle ils sont également appelés nuages sombres, comme ils seront nommés ci-après. De part leurs conditions physiques propices à la chimie, les nuages sombres sont des régions où la chimie du gaz et des grains est particulièrement efficace, permettant à leur composition chimique d'évoluer de manière significative au cours de leur vie, dont la durée est de quelques millions d'années.



## F.2.2 Effondrement et formation stellaire

Les détails du processus de formation des étoiles sont encore mal contraints, car ils impliquent de nombreux mécanismes physiques différents sur une vaste gamme d'échelles spatiales. Cependant, les principales étapes de sa progression sont connues. En termes de masse, il existe deux types d'étoiles: les étoiles de faible masse ( $\leq 10 M_{\odot}$ ) et celles de grande masse ( $> 10 M_{\odot}$ ). Le processus de formation des étoiles de grande masse reste une question ouverte :

- elles pourraient se former à partir du même processus que les étoiles de faible masse, sauf que cela se produirait beaucoup plus rapidement, car les effets gravitationnels sont beaucoup plus importants que pour les étoiles de faible masse,
- elles pourraient se former à partir de la fusion de coeurs d'étoiles de faible masse en formation, car les étoiles de grande masse se forment généralement en groupes denses.

Dans ce qui suit et pour des raisons de clarté, seul le processus de formation commun aux deux types d'étoiles est décrit.

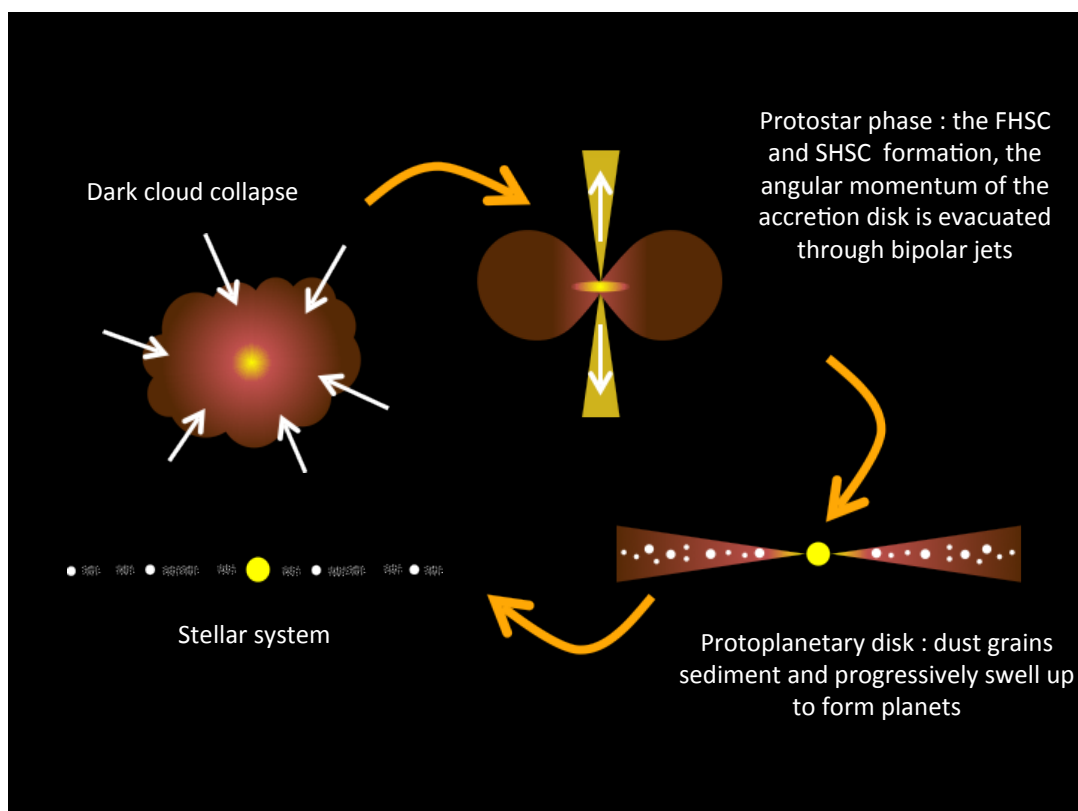


Figure F.4: Les étapes de la formation stellaire.

La figure F.4 présente une vue détaillée des différentes étapes de la formation stellaires. Lorsque les coeurs prestellaires qui se forment dans les nuages sombres deviennent suffisamment grands pour devenir gravitationnellement instables, ils commencent à s'effondrer sur eux-mêmes. Généralement, ces effondrements sont causées par des événements très énergiques, tels que la collision de deux nuages sombres ou même de galaxies, ou une explosion de supernovae à proximité qui envoie de la matière choquée dans le nuage à très grande vitesse.

Les coeurs prestellaires sont initialement optiquement minces et le nuage s'effondre isothermiquement, l'énergie issue de la compression étant évacuée par rayonnement. L'efficacité de ce refroidissement radiatif diminue lorsque la densité du nuage augmente en son centre. Lorsqu'il ne peut plus s'équilibrer avec la caléfaction compressive, l'évolution de la matière au centre du nuage devient adiabatique et un coeur hydrostatique, appelé premier coeur hydrostatique, ou premier coeur de Larson (Larson, 1969), est formé au centre. La proto-étoile est née. Pendant une courte période (<1000 ans, voir par exemple Vaytet and Haugbolle, 2017), le premier coeur continuera à accréter le matériel de son enveloppe, augmentant ainsi sa masse, sa densité et sa température. Lorsque sa température atteint  $\approx 2000$  K, la dissociation des molécules  $H_2$  à l'intérieur du coeur est déclenchée. En raison de la nature endothermique de ce processus, une deuxième phase d'effondrement commence. Lorsque la plupart des molécules  $H_2$  sont scindées, le deuxième effondrement cesse et un coeur beaucoup plus dense et compact, appelé le deuxième coeur de Larson (Larson, 1969) apparaît. Ce coeur continue d'accréter lentement de la matière pendant quelques centaines de milliers d'années, jusqu'à ce que sa température soit suffisamment élevée pour déclencher les réactions nucléaires et que la proto-étoile devienne une jeune étoile.

Au cours de tout ce processus, le matériel entourant la proto-étoile évolue également. Lorsque l'effondrement commence, le nuage se transforme progressivement en un disque d'accrétion en rotation autour de la proto-étoile (voir figure F.4). Lorsque le premier coeur de Larson est formé, le moment angulaire de ce disque est évacué par la formation de jets bipolaires qui forment des chocs dans l'enveloppe environnante. Les hautes températures de ces régions de chocs sont très propices à la chimie en phase gazeuse dont les produits peuvent retomber sur le disque d'accrétion. Ce dernier perd l'essentiel de sa masse lors des deux effondrements, jusqu'à la formation de la jeune étoile. Ensuite, le disque est nommé disque proto-planétaire, car c'est dans celui-ci que les grains de poussière et le gaz vont sédimenter et grossir progressivement pour finalement former des planètes. Le système stellaire est alors né.

Le cycle de vie des étoiles présente un intérêt particulier pour les astrochimistes car il régit la chimie du MIS. En effet, les nombreux processus et conditions physiques qui peuvent être trouvés au cours de ce cycle sont responsables de la création, de la redistribution et de la destruction de toutes les molécules qui composent l'Univers.

Plus précisément, le processus de formation des étoiles joue un rôle primordial dans ce cycle, dans la mesure où il permet la formation de molécules complexes telles que les molécules complexes organiques (MCO), censées être la clé pour comprendre comment la vie est apparue sur Terre.

### F.3 OBJECTIFS ET ORGANISATION DE LA THÈSE

L'objectif de cette thèse est d'apporter un regard nouveau sur la chimie de la formation stellaire à l'aide des améliorations récentes du modèle chimique NAUTILUS, telles que le modèle à 3 phases ou le processus de compétition entre réaction et diffusion/désorption. Plus particulièrement, je me concentre sur les points suivants :

1. la problématique de déplétion du soufre dans les nuages sombres,
2. la chimie du soufre dans les coeurs chauds,
3. contraindre les paramètres physiques initiaux des coeurs prestellaires de faibles masse à partir d'une base de donnée de modèles physico-chimiques.

Les 3 prochains chapitres présentent respectivement chacune de ces études et leurs résultats. Notez que les deux premières études présentées ci-après ont été publiées (Vidal et al., 2017; Vidal and Wakelam, 2018). Le dernier chapitre conclut cette thèse.

# G | RÉSUMÉ, CONCLUSIONS ET PERSPECTIVES

Les études astrochimiques de la formation stellaire présentent un intérêt particulier car elles permettent de mieux comprendre l'évolution de la composition chimique de l'Univers, du milieu interstellaire diffus à la formation de systèmes stellaires et à la vie qu'ils peuvent abriter. Les progrès récents en matière de modélisation chimique, et en particulier une meilleure compréhension de la chimie des grains, permettent maintenant d'apporter de nouvelles contraintes sur la chimie de la formation stellaire.

L'objectif de cette thèse était de d'apporter un regard neuf sur la chimie de la formation stellaire en utilisant les améliorations récentes du modèle chimique NAUTILUS, comme le modèle à 3 phases ou le processus de compétition entre réaction et diffusion/désorption. Dans ce but, je me suis d'abord concentré sur la chimie du soufre durant différentes étapes de la formation stellaire, de son évolution dans les nuages sombres aux coeurs chauds. J'ai ensuite décidé de développer une méthode permettant de dériver les paramètres physiques initiaux de l'effondrement de coeurs prestellaires, en utilisant une base de données de modèles physico-chimiques d'effondrement comparés à des observations de proto-étoiles de Classe 0.

## SOUFRE DANS LES NUAGES SOMBRES

La première étude de ma thèse consistait en une revision du réseau chimique soufré et une évaluation de son effet sur la modélisation du soufre dans les nuages sombres. Pour ce faire, j'ai ajouté (ou révisé dans le cas de réactions) 46 espèces soufrées au réseau chimique, ainsi que 478 réactions en phase gazeuse, 305 réactions à la surface des grains et 147 réactions dans le manteau des grains. J'ai ensuite effectué plusieurs modèles 0D avec des conditions physiques typiques des nuages sombres. Les résultats de ces modèles m'ont permis d'étudier la chimie des réservoirs de soufre et des espèces soufrées nouvellement implémentées. J'ai également étudié les espèces soufrées dont la chimie était la plus sensible aux modifications du réseau.

Dans une deuxième partie, j'ai évalué l'efficacité du nouveau réseau soufré à reproduire les observations de nuages sombres, en particulier pour déterminer si le nou-

veau modèle pourrait inférer de nouvelles indications sur le problème de déplétion du soufre ces objets. Pour ce faire, j'ai comparé les résultats du modèle aux observations effectuées dans le nuage sombre TMC-1 (CP) et dans les glaces autour de la proto-étoile W33A en utilisant quatre abondances élémentaires de soufre différentes, allant de sa valeur "déplétée" couramment utilisée ( $[S]_{\text{ini}} = 8 \times 10^{-8}$ ) à sa valeur cosmique ( $[S]_{\text{ini}} = 1.5 \times 10^{-5}$ ). Les résultats ont montrés que le modèle chimique NAUTILUS ne nécessitait plus de déplétion de l'abondance élémentaire de soufre pour reproduire les observations d'espèces soufrées dans les nuages sombres. En particulier, les observations peuvent être reproduites en utilisant comme abondance élémentaire de soufre sa valeur cosmique ou une valeur trois fois plus faible ( $[S]_{\text{ini}} = 5 \times 10^{-6}$ ). Comme la plupart des estimations de l'abondance cosmique de soufre se situent entre ces deux valeurs, le modèle chimique NAUTILUS devient le premier modèle chimique à ne pas nécessiter de déplétion supplémentaire en soufre. Ce résultat m'a ensuite permis d'apporter de nouvelles réponses sur les réservoirs de soufre dans les nuages sombres. Au vue des résultats du modèle utilisé avec l'abondance élémentaire cosmique de soufre, les réservoirs de soufre dans les nuages sombres sont:

- $S^+$  en phase gazeuse du début de la simulation jusqu'à  $2.8 \times 10^3$  ans (forme élémentaire du soufre),
- Le soufre atomique en phase gazeuse entre  $2.8 \times 10^3$  et  $4.6 \times 10^5$  ans, contenant entre 25 et 88% de la quantité totale de soufre, en fonction de l'âge du nuage. Durant cette période, le CS contient également une quantité importante de soufre, entre 9 et 16%.
- HS et  $H_2S$  dans le manteau des grains pour les nuages plus vieux, contenant au total plus de 51% de la quantité totale de soufre, atteignant plus de 80% à des périodes  $\geq 2.7 \times 10^6$  ans. Ce réservoir partagé montre une légère préférence pour HS entre 3 et 10% de la quantité totale de soufre, en fonction de l'âge du nuage. Ce résultat est conforme à la limite supérieure sur l'abondance de  $H_2S$  dans les glaces dérivée des observations.

Les résultats ci-dessus sont également vrais pour une abondance élémentaire de soufre de  $[S]_{\text{ini}} = 5 \times 10^{-6}$  (3 fois déplétée), qui permet également de reproduire les observations des espèces soufrées dans les nuages sombres. De plus, ces réservoirs de soufre sont en accord avec l'hypothèse communément admise que les réservoirs de soufre dans les nuages sombres sont soit sous forme gazeuse non observable (telle que le soufre atomique), soit piégés dans les glaces des grains sous forme de  $H_2S$  en raison de l'hydrogénation successive du soufre atomique adsorbé à la surface des grains. Cependant, les réservoirs que j'ai trouvés ne sont pas encore observables, notamment parce que les instruments actuels ne possèdent pas la sensibilité nécessaire pour observer le HS et le  $H_2S$  dans les glaces des grains.

---

**Perspectives :** La possibilité de reproduire les observations d'espèces soufrées dans les nuages sombres en utilisant comme abondance élémentaire son abondance cosmique ouvre la voie à de nombreuses études possibles sur le soufre dans les régions de formation stellaire. Cependant, pour confirmer mes résultats, de meilleures contraintes observationnelles sur  $\text{H}_2\text{S}$  dans les glaces sont nécessaires. Par exemple, étant donné que le  $\text{H}_2\text{S}$  solide devrait être libéré en phase gazeuse lors des étapes suivantes de la formation stellaire, des observations pourraient être effectuées dans des régions telles que les chocs ou les disques protoplanétaires pour confirmer le rôle de  $\text{H}_2\text{S}$  comme réservoir de soufre. Le futur lancement du James Webb Space Telescope (JWST) devrait permettre une meilleure caractérisation des réservoirs de soufre dans les nuages sombres. Plus important encore, les effets de l'amélioration du modèle ainsi que de son réseau de soufre prouvent l'importance de continuer à actualiser les modèles et les réseaux chimiques afin d'assurer une modélisation astrochimique correcte.

## SOUFRE DANS LES COEURS CHAUDS

Au cours de la deuxième partie de ma thèse, j'ai effectué une étude de la chimie du soufre dans les coeurs chauds à la lumière des résultats obtenus dans des nuages sombres. Un objectif secondaire était d'évaluer les conséquences des simplifications géométriques et dynamiques couramment utilisée pour modéliser de tels objets. Pour ce faire, j'ai d'abord mené une étude approfondie de la chimie des principales espèces soufrées observées dans les coeurs chauds avec des modèles 0D. J'ai utilisé deux compositions pré-effondrement : un nuage sombre évolué et un moins évolué. Ensuite, j'ai présenté et comparé les résultats de deux types de modèles (1D statique et 0D dynamique), afin de mettre en évidence la sensibilité de la chimie au choix du modèle utilisé dans les études astrochimiques, en particulier pour les coeurs chauds.

Dans un premier temps, mon étude approfondie des espèces soufrées a mis en avant cinq résultats principaux :

1. La quantité totale d'oxygène réactif dans la phase gazeuse dépend de manière critique de la composition pré-effondrement (cf. tableau 3.4), ainsi que de la température du coeur chaud;
2. La composition chimique en soufre dans les coeurs chauds dépend également grandement de la composition pré-effondrement, principalement en raison de son lien avec celle de l'oxygène, du carbone et de l'hydrogène, qui participent tous activement à la chimie du soufre dans un tel environnement;
3. La composition chimique en soufre dans les coeurs chauds dépend beaucoup de la température, en partie parce qu'elle est directement et indirectement liée aux hydrocarbures évaporés des glaces et à leurs principaux produits de destruction  $\text{CH}_2$  et  $\text{CH}_3$ ;

4. J'ai trouvé des chemins efficaces de formation de  $\text{H}_2\text{S}$  en phase gazeuse qui pourraient être responsables de sa surestimation dans la plupart des modèles de coeurs chauds effectués. Les études sur la chimie en phase gazeuse de cette espèce doivent être poursuivies pour assurer la pertinence du réseau.
5. J'ai trouvé un accord entre les modèles avec une composition pré-effondrement évoluée et les observations dans Orion KL, ainsi qu'avec l'un des modèles avec une composition pré-effondrement moins évoluée et les observations dans le coeur chaud d'IRAS 16293-2422. Ces résultats suggèrent qu'en utilisant comme abondance élémentaire de soufre son abondance cosmique, le modèle chimique NAUTILUS peut non seulement reproduire les observations dans les nuages sombres, mais également dans les coeurs chauds.

Dans un deuxième temps, mon études des modèles 1D statiques et 0D dynamiques a conduit aux résultats suivants:

1. La composition chimique du nuage parent est un paramètre clé pour les modèles 1D statiques de la chimie du soufre dans les coeurs chauds. En effet, les abondances calculées montrent qu'elle peut impliquer des différences allant jusqu'à six ordres de grandeur pour une espèce donnée dans le coeur chaud. Cependant, la composition pré-effondrement ne semble avoir que peu d'impact sur la composition chimique de l'enveloppe. Enfin, le modèle 1D montre qu'un coeur chaud formé à partir d'un nuage parent jeune serait pauvre en  $\text{H}_2\text{S}$  et riche en  $\text{SO}_2$ , tandis qu'un coeur chaud formé à partir d'un nuage parent plus évolué serait riche en  $\text{H}_2\text{S}$  et  $\text{H}_2\text{CS}$ .
2. Les modèles dynamiques 0D étudié dans cette étude n'ont révélé que de faibles différences entre les résultats des compositions chimiques pré-effondrement moins évoluées et évoluées, avec une faible dépendance de la chimie du soufre dans les coeur chaud à la composition pré-effondrement. En effet, dans les deux cas, le modèle prédit des abondances élevées de  $\text{H}_2\text{S}$  et  $\text{OCS}$  et de faibles abondances de  $\text{SO}_2$  et de  $\text{SO}$ . Toutefois, ce résultat pourrait être dû à un temps d'effondrement assez long dans le modèle, qui laisserait suffisamment de temps pour que le soufre soit adsorbé sur les grains pour former principalement ces espèces avant leur évaporation. On s'attend à ce que, pour un temps d'effondrement plus court, les différences entre les deux cas de composition pré-effondrement soient plus grandes.

Enfin, la comparaison entre les modèles 1D statiques et 0D dynamiques a montré de grandes différences entre les abondances calculées, pouvant aller jusqu'à six ordres de grandeur dans le coeur chaud. Ce résultat met en évidence la sensibilité au choix des modèles dans les études astrochimiques, en particulier lorsque l'on compare les résultats avec les observations, ou avec les résultats d'autres articles. Je recommande à l'avenir l'utilisation de modèles dynamiques pour la modélisation d'objets tel que les

---

coeurs chauds, ces modèles étant plus réalistes que les modèles statiques.

**Perspectives :** Mon étude approfondie des principales espèces soufrées dans les coeurs chauds peut servir de référence pour les futures modélisations de la chimie du soufre dans ces régions. Les variations des compositions chimiques avec la composition pré-effondrement et la température donnent des éléments de réponses sur les raisons des différentes compositions chimiques en molécules soufrées observées dans les coeurs chauds, et devraient faire l'objet de futures études. De plus, les travaux futurs devraient mettre l'accent sur l'importance du temps d'effondrement, car il pourrait également expliquer la grande variété d'abondances d'espèces soufrées observées dans les coeurs chauds.

## CONTRAINTES SUR LES PARAMÈTRES PHYSIQUES INITIAUX DES COEURS PRESTELLAIRE DE FAIBLES MASSES

Pour la dernière partie de ma thèse, j'ai travaillé sur l'étude chimique de la formation de proto-étoiles de Classe 0, avec pour but de contraindre leurs paramètres physiques initiaux d'effondrement (PPIE). L'étude était basée sur une base de donnée de 110 modèles physiques 1D hydrodynamiques et radiatifs de l'effondrement de coeur prestellaire de faibles masses, au travers de la formation du premier et du second coeur de Larson. À partir de cette base de donnée, j'ai extrait les résultats de 16 cellules de matériel par modèle, conformément au domaine de validité du modèle chimique NAUTILUS, que j'ai traitées indépendamment les unes des autres à des fins statistiques. J'ai ensuite effectué des modèles chimiques dynamiques 0D sur chacune des 1760 cellules ainsi sélectionnées.

L'idée initiale de mon étude étant d'utiliser un ensemble de données aussi volumineux pour déduire des résultats statistiques, j'ai d'abord essayé de trouver des traceurs possibles des PPIE en étudiant leurs corrélations respectives avec chacune des distributions d'abondance des espèces présentes dans le réseau chimique. Pour ce faire, j'ai défini deux régions physiques dans l'enveloppe protostellaire à partir de la distribution d'abondance de l'eau: la Région Enveloppe (RE) et la Région Coeur Chaud (RCC). Comme les corrélations obtenues dans la RE étaient peu concluantes, j'ai axé mon étude sur les corrélations dans la RCC. Malgré le fait que je n'ai trouvé aucune corrélation satisfaisante avec  $M_0$ , mon étude montre que, pour les quatre PPIE  $T_0$ ,  $R_0$ ,  $\rho_0$  et  $t_{ff}$ , de nombreuses espèces sont candidates. J'ai présenté les résultats de quatre de ces candidats traceurs des PPIE observés dans IRAS 16293-2422 à la lumière de leurs chimie respective:  $\text{CH}_3\text{CN}$ ,  $\text{H}_2\text{CS}$ , NS et OCS.  $\text{H}_2\text{CS}$  s'est avéré être un traceur possible pour le temps d'effondrement et la densité initiale, tandis que les trois autres espèces sont des traceurs possibles de la température initiale du coeur prestellaire parent.



Pour la RE, j'ai développé une méthode simple de comparaison des distributions d'abondance avec les observations. De cette méthode, j'ai pu contraindre les PPIE pour 12 proto-étoiles de Classe 0 à partir de l'observation de 7 à 19 espèces dans leurs enveloppes respectives. De plus, toutes les contraintes ont été obtenues avec un pourcentage d'accord entre espèces supérieur à 85%, ce qui inspire confiance dans la méthode et ses résultats. Les résultats spécifiques obtenus pour chaque source pourraient être d'un grand intérêt pour la modélisation future de leur chimie respective. En étudiant les résultats pour chaque PPIE, j'ai également pu déduire les probabilités suivantes pour les proto-étoiles de faibles masses. Il convient de noter que ces probabilités sont définies à partir de l'échantillon de 12 sources que j'ai utilisé et pourraient donc évoluer en utilisant un plus grand échantillon:

- La probabilité pour qu'une proto-étoile de faible masse se forme à partir de coeurs prestellaires de masses  $\leq 1 M_{\odot}$  semble être de seulement 5%, alors que l'intervalle privilégié  $[2; 4] M_{\odot}$  atteint une probabilité de 68%. L'intervalle le plus externe  $[6; 8] M_{\odot}$  correspond à une probabilité totale de 26% et pourrait donc correspondre à un nombre non négligeable de proto-étoiles de faibles masses,
- Les températures initiales, qui sont les PPIE les mieux contraintes, sont efficacement contraintes entre 10 et 15 K, toutes les sources concordant avec l'une ou ces deux valeurs. Par conséquent, la probabilité totale que des sources de faibles masses se forment dans des coeur prestellaire avec de telles températures atteint 94%. Ce résultat suggère que, même si cela est théoriquement possible, une étoile de faible masse aurait tendance à ne pas se former à partir de coeurs prestellaires plus chauds ( $T_0 \geq 20$  K),
- Les rayons initiaux sont également bien contraints avec la méthode en raison de leur corrélation avec les densités initiales. Le résultat montre que les étoiles de faible masse se forment préférentiellement dans de vastes coeurs prestellaires de  $R_0 \geq 20000$  AU, avec une probabilité de 77%. Cette limite est toutefois très dépendante du modèle car les valeurs choisies pour  $R_0$  dans la base de données d'origine sont très espacée lorsqu'elles sont supérieures à 7500 AU,
- Enfin, le résultat le plus intéressant concernant les densités initiales et les temps d'effondrement est que les étoiles de faible masse semblent avoir une probabilité très faible (0,8%) de se former dans des coeurs prestellaires de densités supérieures à  $10^7 \text{ part.cm}^{-3}$  ( $t_{\text{ff}} < 17$  kans). De plus, 70% des étoiles de faible masse semblent naître dans des coeurs prestellaires dont la densité est comprise dans l'intervalle  $[5.97 \times 10^4 ; 2.02 \times 10^5] \text{ part.cm}^{-3}$  (respectivement  $t_{\text{ff}} \in [105.01 ; 192.92]$  kans). Enfin, le fait que les valeurs possibles obtenues pour toutes les sources s'étendent entre quelques  $10^4$  et  $10^6 \text{ part.cm}^{-3}$  (20 à 192 kans pour le temps d'effondrement) laisse à penser que les étoiles de faible masse peuvent se former dans des coeurs prestellaires avec des densités différentes.

---

Un autre résultat intéressant de cette étude est que deux des sources (IRAS 16293-2422 et VLA1623) ont des contraintes sur  $R_0$ ,  $\rho_0$  et  $t_{ff}$  dans des intervalles qui ne sont pas favorisé par la méthode, suggérant qu'elles pourraient être des représentantes d'un type spécifique de proto-étoiles se formant à partir de coeurs prestellaires de tailles moyennes ayant des densités plus élevées (respectivement un temps d'effondrement plus petit) que la majorité des proto-étoiles de faible masse considérés dans mon échantillon.

**Perspectives :** Cette dernière étude démontre le potentiel de modélisations chimiques à grande échelle, notamment la possibilité d'apporter de nouvelles contraintes à la formation d'étoiles de faible masse, ainsi que de déterminer de nouveaux traceurs chimiques de paramètres physiques. En ce qui concerne les traceurs des PPIE trouvés, l'observation simultanée à haute résolution angulaire de  $\text{CH}_3\text{CN}$ ,  $\text{NS}$  et  $\text{OCS}$  dans des enveloppes protostellaires pourrait permettre de déduire leurs températures initiales respectives d'effondrement  $T_0$ . De plus, j'ai utilisé ici uniquement les données au temps final du modèle physico-chimique, et d'autres résultats pourraient être trouvés en utilisant les données à des temps différents. Par exemple, on pourrait rechercher des traceurs chimiques du stade de premier coeur de Larson, ce qui aiderait à confirmer les diverses observations de candidats possibles pour ces objets, et donc d'apporter de nouvelles contraintes sur leurs paramètres physico-chimiques. Dans ce but, j'ai soumis un projet d'observations avec l'interféromètre du Plateau de Bure qui est actuellement observé. De plus, à mesure que de plus en plus d'observations de proto-étoiles sont effectuées, des études devraient être menées pour élargir l'échantillon de sources que j'ai utilisées et ainsi affiner les probabilités. Enfin, l'amélioration constante des modèles et des observations chimiques devrait permettre de constituer des bases de données plus volumineuses et de préciser les résultats présentés.



# H | PUBLICATIONS

## Joint publications:

- [1] **Vidal, T. H. G.**, and Wakelam, V. (2018). A new look at sulphur chemistry in hot cores and corinos. *MNRAS*, 474 (4), 5575-5587.
- [2] **Vidal, T. H. G.**, Loison, J.-C., Jaziri, A. Y., Ruaud, M., Gratier, P., and Wakelam, V. (2017). On the reservoir of sulphur in dark clouds: chemistry and elemental abundance reconciled. *MNRAS*, 469 (1), 435-447.

## Publications list:

- [1] Vastel, C., Quénard, D., Le Gal, R., Wakelam, V., Andrianasolo, A., Caselli, P., **Vidal, T. H. G.**, Ceccarelli, C., Lefloch, B., and Bachiller, R. (2018). Sulphur chemistry in the L1544 pre-stellar core. *MNRAS*, 478 (4), 5519-5537.
- [2] Fuente, A., Goicoechea, J. R., Pety, J., Le Gal, R., Martín-Doménech, R., Gratier, P., Guzmán, V., Roueff, E., Loison, J.-C.; Muñoz Caro, G. M., Wakelam, V., Gerin, M., Riviere-Marichalar, P., and **Vidal, T. H. G.** (2017). First detection of interstellar S<sub>2</sub>H. *ApJ*, 851 (L49).
- [3] Le Gal, R., Herbst, E., Dufour, G., Gratier, P., Ruaud, M., **Vidal, T. H. G.**, and Wakelam, V. (2017). A new study of the chemical structure of the Horsehead nebula: the influence of grain-surface chemistry. *A&A*, 605 (A88).
- [4] Majumdar, L., Gratier, P., **Vidal, T. H. G.**, Wakelam, V., Loison, J.-C., Hickson, K. M., and Caux, E. (2016). Detection of CH<sub>3</sub>SH in protostar IRAS 16293-2422. *MNRAS*, 458 (2), 1859-1865.
- [5] Idoughi, R., **Vidal, T. H. G.**, Foucher, P.-Y., Gagnon, M.-A., and Briottet, X. (2016). Background radiance estimation for gas plume quantification for airborne hyperspectral thermal imaging. *Journal of Spectroscopy*, 2016 (6), 1-17.



# A new look at sulphur chemistry in hot cores and corinos

Thomas H. G. Vidal<sup>★</sup> and Valentine Wakelam

*Laboratoire d'astrophysique de Bordeaux, Univ. Bordeaux, CNRS, B18N, allée Geoffroy Saint-Hilaire, F-33615 Pessac, France*

Accepted 2017 November 28. Received 2017 November 28; in original form 2017 September 8

## ABSTRACT

Sulphur-bearing species are often used to probe the evolution of hot cores because their abundances are particularly sensitive to physical and chemical variations. However, the chemistry of sulphur is not well understood in these regions, notably because observations of several hot cores have displayed a large variety of sulphur compositions, and because the reservoir of sulphur in dense clouds, in which hot cores form, is still poorly constrained. In order to help disentangle its complexity, we present a fresh comprehensive review of sulphur chemistry in hot cores along with a study of sulphur's sensibility to temperature and pre-collapse chemical composition. In parallel, we analyse the discrepancies that result from the use of two different types of models (static and dynamic) in order to highlight the sensitivity to the choice of model to be used in astrochemical studies. Our results show that the pre-collapse chemical composition is a critical parameter for sulphur chemistry in hot cores and that it could explain the different sulphur compositions observed. We also report that differences in abundances for a given species between the static and dynamic models can reach six orders of magnitude in the hot core, which reveals the key role of the choice of model in astrochemical studies.

**Key words:** astrochemistry – methods: numerical – stars: abundances – stars: formation – stars: protostars – ISM: molecules.

## 1 INTRODUCTION

Hot cores have been defined as small ( $<0.1$  pc), dense ( $n_{\text{H}} > 2 \times 10^7 \text{ cm}^{-3}$ ) and warm ( $T > 100$  K) regions surrounding high-mass protostars in their early phase of formation (see for example, Kurtz et al. 2000; van der Tak 2004). Because of their high temperatures, these regions are characterized by the sublimation of icy mantles of dust grain. Therefore, they present high abundances of hydrogenated molecules, such as water ( $\text{H}_2\text{O}$ ), hydrogen sulfide ( $\text{H}_2\text{S}$ ) or complex organic molecules such as methanol ( $\text{CH}_3\text{OH}$ ; see Schöier et al. 2002, and references therein). These molecules are originally synthesized on dust grains in the cold dense cloud from which the protostar has formed. Once evaporated in the hot core, they undergo further gas-phase chemical reactions (Wakelam et al. 2004b; Garrod & Herbst 2006; Herbst & van Dishoeck 2009). It is now generally admitted that low-mass protostars present the same kind of physico-chemical structure called ‘hot corinos’ (Ceccarelli, Hollenbach & Tielens 1996; Ivezić & Elitzur 1997). They differ from their high-mass counterparts mainly in size and, consequently, in infall time-scale, which could perhaps affect the chemical composition. Because our Sun is a low-mass star, the chemistry that takes place in these ‘small’ hot cores is important for understanding the history of the material from which planetary systems such as ours are formed. In this paper, we use the expression ‘hot core’ as

a generic term to designate the hot and dense regions surrounding both high-mass and low-mass protostars.

To model the chemistry of hot cores, several types of simulations exist in the literature (see for instance, Charnley 1997; Hatchell et al. 1998; Garrod & Herbst 2006; Wakelam, Hersant & Herpin 2011; Hincelin et al. 2016). Ranging from simple zero-dimensional static gas-phase models to complex three-dimensional gas-grain models, different assumptions are made for each type of model, regarding for instance the age of the parent cloud or its free-fall time. These numerous approaches to hot core chemistry and the different hypotheses they imply raise the question of the uniformity of the results obtained by these models.

Sulphur-bearing species are often used to probe the evolution of hot cores because their abundance is particularly sensitive to physical and chemical variations. For example, the ratios  $\text{SO}_2/\text{SO}$ ,  $\text{SO}_2/\text{H}_2\text{S}$  and  $\text{OCS}/\text{H}_2\text{S}$  have been proposed as chemical clocks in these regions (Charnley 1997; Hatchell et al. 1998; Wakelam et al. 2011), SO is often used to trace small-scale heating process, such as shocked regions (Viti et al. 2001; Podio et al. 2015) or the centrifugal barrier (Sakai et al. 2014), and OCS can efficiently trace the infalling-rotating envelope (Oya et al. 2016).

Hence, the modelling of sulphur chemistry in such hot and dense regions is crucial for a better understanding of the star formation process. Moreover, such models can uncover new information on the main form of sulphur in dense clouds. Indeed, the gas-phase abundance of atomic sulphur in the diffuse medium is observed to be constant with cloud density, around its cosmic value of  $10^{-5}$

<sup>★</sup> E-mail: [thomas.vidal@u-bordeaux.fr](mailto:thomas.vidal@u-bordeaux.fr)

(see for instance, Jenkins 2009). However, in dense clouds, the total abundance of detected S-bearing molecules only accounts for 0.1 per cent of the cosmic abundance of atomic sulphur (Tieftfrunk et al. 1994; Charnley 1997). Furthermore, for most chemical models, assuming an initial abundance of sulphur as high as its cosmic value results in predicted abundances of observable S-bearing species much higher than the observed abundances. Consequently, modellers usually assume a depleted abundance of sulphur compared to its cosmic value. Therefore, the main reservoirs of sulphur in dense clouds, and consequently in hot cores, are still uncertain.

Let us add to these uncertainties the fact that the observation of S-bearing species in hot cores is also a puzzling issue, as a large variety of sulphur compositions have been observed towards different hot cores and therefore no global trend has yet been found (see fig. 5 of Woods et al. 2015, and references therein). However, a given set of hot cores can present similar sulphur composition (see for example, Minh 2016), which would suggest similar evolutionary stages.

Recent studies have put forward evidence in favour of the long-lasting idea that because hydrogenation is the most effective chemical process in icy grain mantles,  $\text{H}_2\text{S}$  could be the sought-for main reservoir of sulphur in dense clouds (see Minh et al. 1990; Charnley 1997). Holdship et al. (2016) studied the properties of  $\text{H}_2\text{S}$  in the low-mass protostar L1157-B1 and showed that a significant fraction of the sulphur is likely to be locked into the form of  $\text{H}_2\text{S}$  prior to evaporation of the grain mantles in the hot corino. Moreover, we reported the first chemical model able to reproduce observed abundances of S-bearing species in dense clouds, using as an initial abundance of sulphur its cosmic abundance (or three times depleted; see Vidal et al. 2017). In this previous paper, we showed that the main form of sulphur in dense clouds critically depends on the age of the cloud. We proposed that this reservoir could be atomic sulphur for clouds of ages  $< 5 \times 10^5$  yr, or a shared reservoir between HS and  $\text{H}_2\text{S}$  in the grain mantles for older clouds.

In this current paper, we aim to present a comprehensive study of the modelling of S-bearing species in hot cores. In particular, we try to determine how the history (i.e. the pre-collapsing chemical composition) of a hot core affects sulphur chemistry, and how important is the choice of the type of model used for hot cores studies. Hence, we study the evolution of the abundances of the main S-bearing species observed in a hot core, as given by different types of simulations using several physico-chemical parameters. In Section 2, we present the gas grain model as well as the different types of simulations we run. In Section 3, we present the results of our hot core simulations for sulphur chemistry. We discuss these results regarding the issues we want to address in the final section.

## 2 MODEL DESCRIPTION

In order to conduct a comprehensive study of the sulphur chemistry in hot cores, as well as highlighting the discrepancies between the different models commonly used in the literature, we use three types of simulations:

- (i) zero-dimensional simulations for which we consider constant physical parameters throughout the simulation time;
- (ii) one-dimensional static simulations for which each cell of the spatial grid evolves with constant physical parameter as a zero-dimensional model;
- (iii) zero-dimensional dynamic simulations for which each cell of the spatial grid evolves with time-dependant physical parameters.

For all the simulations, we use the latest version of the time-dependent gas-grain NAUTILUS V-1.1 chemical model (Ruaud,

Wakelam & Hersant 2016). In the following, we describe the chemical model, and then we give the parameters of the parent cloud model we use to obtain the same pre-collapsing chemical composition for all hot cores models. Afterwards, we describe the different parameters we use for each simulation.

### 2.1 Chemical model

The NAUTILUS chemical model computes the evolution of chemical abundances for a given set of physical and chemical parameters. It can simulate a three-phase chemistry including gas-phase, grain-surface and grain-bulk chemistry, along with the possible exchanges between the different phases (Ruaud et al. 2016). These exchanges are: the adsorption of gas-phase species on to grain surfaces, the thermal and non-thermal desorption of species from the grain surface into the gas phase, and the surface–bulk and bulk–surface exchange of species. The chemical desorption process used in the model is the one depicted in Garrod, Wakelam & Herbst (2007). They considered that for each surface reaction leading to a single product, a part of the energy released by the reaction can contribute to the desorption of the product in the gas phase using the Rice–Ramsperger–Kessel theory. The fraction of the product desorbed in the gas phase depends on the binding energy of the product to the surface, the enthalpy of the reaction, and the fraction of the released energy that is lost to the surface. In our case, we use an  $\alpha$  parameter of 0.001, which produces approximately a 1 per cent efficiency evaporation for all species. Moreover, the grain chemistry takes into account the standard direct photodissociation by photons along with the photodissociation induced by secondary UV photons introduced by Prasad & Tarafdar (1983). These processes are effective on the surface as well as in the bulk of the grains. The model also takes into account the newly implemented competition between reaction, diffusion and evaporation, as suggested by Chang, Cuppen & Herbst (2007) and Garrod & Pauly (2011). The diffusion energies of each species are computed as a fraction of their binding energies. We take for the surface a value of this ratio of 0.4 as suggested by experiments and theoretical work made on H (see Ruaud et al. 2016, and reference therein), CO and  $\text{CO}_2$  (see Karssemeijer & Cuppen 2014). This value is then extrapolated to every species on the surface. For the bulk, we take a value of 0.8 (see also Ruaud et al. 2016).

Given the high-temperature regimes encountered in this study, we use the ad hoc formation mechanism for  $\text{H}_2$  described in Harada, Herbst & Wakelam (2010). They consider that the formation rate of  $\text{H}_2$  can be written as

$$\frac{dn(\text{H}_2)}{dt} = \frac{1}{2} n_{\text{H}} v_{\text{H}} n_{\text{g}} \sigma_{\text{g}} S(T) \epsilon, \quad (1)$$

where  $n_{\text{H}}$  and  $v_{\text{H}}$  are the number density and thermal velocity of hydrogen atoms, respectively, in  $\text{cm}^{-3}$  and  $\text{cm s}^{-1}$ ,  $n_{\text{g}}$  is the number density of grains in  $\text{cm}^{-3}$ ,  $\sigma_{\text{g}}$  is the cross-section of a grain in  $\text{cm}^2$ ,  $S$  is the sticking coefficient for a hydrogen atom as a function of temperature and  $\epsilon$  is the recombination efficiency. For our study, we use for the recombination efficiency the results from Cazaux et al. (2005), and for the sticking coefficient the expression derived by Chaabouni et al. (2012).

The reference chemical networks are *kida.uva.2014* (see Wakelam et al. 2015a) for the gas phase and that described in Ruaud et al. (2016) for the grains. To this we added the sulphur network detailed in Vidal et al. (2017) (including the reactions given in Druard & Wakelam 2012), as well as the chemical schemes for carbon chains proposed in Wakelam et al. (2015b), Loison et al. (2016, 2017) and

**Table 1.** Initial abundances. In the  $n_i/n_H$  column,  $a(b)$  stands for  $a \times 10^b$ . References are: 1, Wakelam & Herbst (2008); 2, Jenkins (2009); 3, Hincelin et al. (2011); 4, low-metal abundances from Graedel, Langer & Frerking (1982); 5, depleted value from Neufeld, Wolfire & Schilke (2005).

Element	$n_i/n_H$	References
H <sub>2</sub>	0.5	
He	0.09	1
N	6.2(−5)	2
O	2.4(−4)	3
C <sup>+</sup>	1.7(−4)	2
S <sup>+</sup>	1.5(−5)	2
Si <sup>+</sup>	8.0(−9)	4
Fe <sup>+</sup>	3.0(−9)	4
Na <sup>+</sup>	2.0(−9)	4
Mg <sup>+</sup>	7.0(−9)	4
P <sup>+</sup>	2.0(−10)	4
Cl <sup>+</sup>	1.0(−9)	4
F	6.7(−9)	5

Hickson, Wakelam & Loison (2016). Note that all abundances in this paper are expressed with respect to the total H density.

## 2.2 Parent cloud parameters

In order to model the chemistry of a given hot core, one must consider as an initial condition the chemical composition of its parent cloud before it collapses. Moreover, if we want to be able to compare the outputs of our different types of simulations, it makes sense to use the same initial chemical composition. Hence, we begin to run a simulation with the commonly used dark cloud physical parameters: a gas and dust temperature of 10 K, an atomic hydrogen total density of  $2 \times 10^4 \text{ cm}^{-3}$ , a cosmic ionization rate of  $1.3 \times 10^{-17} \text{ s}^{-1}$  and a visual extinction of 15 mag. Our set of initial abundances is summarized in Table 1. We start with all species in their atomic (or ionized) form, except for hydrogen, which is assumed to be entirely in its molecular form. As our model does not require additional depletion of sulphur from its cosmic value to reproduce dark cloud observations (Vidal et al. 2017), we choose to use it as an initial abundance of sulphur.

We show that the evolution time of the parent cloud is critical for the sulphur reservoirs (Vidal et al. 2017) and the same kind of results is observed for oxygen in our simulations. Hence, in order to study the importance of the chemical history of the parent cloud on the hot core composition, we use the outputs of the parent cloud simulation at two different final times for all our simulations:  $10^5$  and  $10^6$  yr. Both these ages are acceptable for dark clouds and allow us to obtain two very different chemical compositions of the cloud before it collapses. On the one hand, in the case of the less evolved dark cloud (hereafter LEDC), most of the oxygen and sulphur are still in the gas phase in atomic form (42 and 61 per cent of their total amount, respectively), or in the form of CO (26 per cent) and CS (15 per cent), respectively. The remainder is, for both species, locked in icy grain bulks, mainly in the form of H<sub>2</sub>O, HS and H<sub>2</sub>S. On the other hand, in the case of the evolved dark cloud (hereafter EDC), more than 95 per cent of the oxygen is locked in the ices mainly in the form of H<sub>2</sub>O (53 per cent) and H<sub>2</sub>CO (9 per cent). As for sulphur, more than 90 per cent is locked in the ices, including its main reservoirs HS (35 per cent) and H<sub>2</sub>S (26 per cent). The two pre-collapse cloud compositions are summarized in Table 2. For more details on the time evolution of the abundances of the

**Table 2.** Description of the pre-collapse dark cloud oxygen and sulphur composition. The prefix ‘b-’ denotes the bulk species.

LEDC	
Oxygen	Sulphur
O (42 per cent)	S (61 per cent)
CO (26 per cent)	CS (15 per cent)
b-H <sub>2</sub> O (22 per cent)	b-HS (6 per cent)
b-O (1 per cent)	b-H <sub>2</sub> S (5 per cent)
EDC	
Oxygen	Sulphur
b-H <sub>2</sub> O (53 per cent)	b-HS (35 per cent)
b-H <sub>2</sub> CO (9 per cent)	b-H <sub>2</sub> S (26 per cent)
b-CO (8 per cent)	b-NS (17 per cent)
b-CH <sub>3</sub> OH (7 per cent)	b-S (8 per cent)

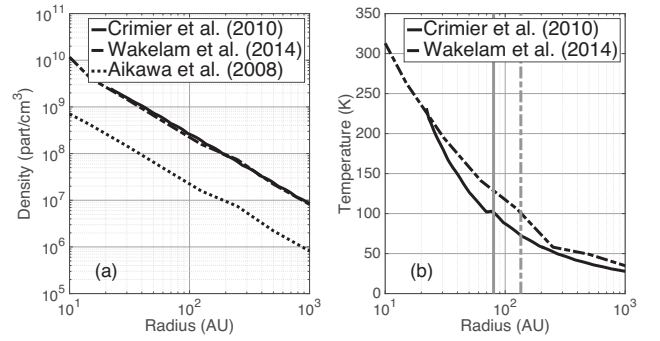


**Figure 1.** Radial structure of the one-dimensional static and zero-dimensional dynamic models at the final time for (a) density, for which we plot the initial structure from Aikawa et al. (2008) as reference, and (b) temperature, for which we plot the limit of the hot core ( $T > 100$  K) for the one-dimensional static ( $R_{\text{HC}} = 80$  au, solid grey vertical line) and zero-dimensional dynamic ( $R_{\text{HC}} = 135$  au, dashed grey vertical line) models.

main S-bearing species in the parent cloud, see fig. 1 of Vidal et al. (2017).

## 2.3 Zero-dimensional simulation parameters

For this study, we begin to run zero-dimensional simulations with the main purpose of obtaining a comprehensive look at sulphur chemistry in hot cores. As Charney (1997) showed the important role of temperature on sulphur chemistry in such environments, we present calculations for a typical hot core density of  $2 \times 10^7 \text{ cm}^{-3}$ , and two temperature regimes of 100 and 300 K. Hence, we obtain four zero-dimensional simulations with different pre-evaporative compositions (EDC and LEDC) and temperatures (100 and 300 K).

## 2.4 One-dimensional static simulation parameters

The one-dimensional model used in this paper follows the physical structure for the envelope of the low-mass protostar IRAS 16293–2422 from Crimier et al. (2010), which was constrained through multiwavelength dust and molecular observations. Indeed, this protostar is believed to have a hot core within  $\sim 150$  au around its centre (see Schöier et al. 2002). The density and temperature radial evolutions are shown in Figs 1(a) and (b), respectively (solid lines). For this model, the spatial limit of the hot core ( $T > 100$  K) is located at  $R_{\text{HC}} = 80$  au (solid grey line in Fig. 1b).



**Table 3.** Summary of the simulations designations and physical parameters.

Simulation	Physical parameter	Pre-collapse evolution time
Zero-dimensional static models		
0DS100LEDC	$T = 100 \text{ K}, n_{\text{H}} = 2 \times 10^7 \text{ cm}^{-3}$	$10^5 \text{ yr}$
0DS300LEDC	$T = 300 \text{ K}, n_{\text{H}} = 2 \times 10^7 \text{ cm}^{-3}$	$10^5 \text{ yr}$
0DS100EDC	$T = 100 \text{ K}, n_{\text{H}} = 2 \times 10^7 \text{ cm}^{-3}$	$10^6 \text{ yr}$
0DS300EDC	$T = 300 \text{ K}, n_{\text{H}} = 2 \times 10^7 \text{ cm}^{-3}$	$10^6 \text{ yr}$
One-dimensional static models		
1DSLEDC	Structure from Crimier et al. (2010)	$10^5 \text{ yr}$
1DSEDC	Structure from Crimier et al. (2010)	$10^6 \text{ yr}$
Zero-dimensional dynamic models		
0DDLDC	Modified structure from Aikawa et al. (2008)	$10^5 \text{ yr}$
0DDEDC	Modified structure from Aikawa et al. (2008)	$10^6 \text{ yr}$

### 2.5 Zero-dimensional dynamic simulation parameters

The structure we use for our dynamic simulation is the same as in Aikawa et al. (2008), Wakelam et al. (2014) and Majumdar et al. (2016), and it was computed from the radiation hydrodynamic (RHD) model of Masunaga & Inutsuka (2000). It initially starts from a parent cloud with a central density of  $\sim 6 \times 10^4 \text{ cm}^{-3}$ , a radius of  $4 \times 10^4 \text{ au}$  and a total mass of  $3.852 M_{\odot}$ . Then the model follows the collapse of the pre-stellar core, which eventually forms a protostellar core after  $2.5 \times 10^5 \text{ yr}$ . Finally, the protostar grows by mass accretion from the envelope for  $9.3 \times 10^4 \text{ yr}$ . As in Wakelam et al. (2014), we have multiplied by 10 all the densities of the simulations in order for the final physical structure of the dynamic model to be similar to the one-dimensional structure of Crimier et al. (2010). The consequence of this modification is discussed in Section 4.1 (see also section 4.5 of Wakelam et al. 2014). Fig. 1(a) shows the resulting final density radial evolution (dashed line) as well as the previous one (dotted line), and Fig. 1(b) shows the final temperature radial evolution (dashed line). For this model, the spatial limit of the hot core ( $T > 100 \text{ K}$ ) is located at  $R_{\text{HC}} = 135 \text{ au}$  (dashed grey line in Fig. 1b).

The designations and physical parameters of all the simulations presented in this paper are summarized in Table 3.

## 3 RESULTS

### 3.1 Zero-dimensional models

In this section, we aim to perform a comprehensive study of sulphur chemistry in environments such as hot cores. In particular, we want to address the importance of the temperature as well as the pre-collapse chemical composition using the four zero-dimensional simulations defined in Section 2.3. Sulphur chemistry in the hot gas phase is known to be intertwined with the distribution of reactive oxygen: O, O<sub>2</sub> and OH (Charnley 1997; Esplugues et al. 2014; Wakelam et al. 2004b). Hence, we begin with a description of the chemistry of these species, and then we study the chemistry of the main S-bearing species observed towards hot and dense objects: SO, SO<sub>2</sub>, H<sub>2</sub>S, OCS, CS and H<sub>2</sub>CS.

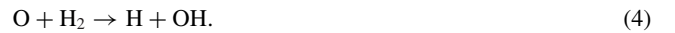
#### 3.1.1 Oxygen chemistry

The left, middle and right panels of Fig. 2 show the abundances of O, O<sub>2</sub> and OH, respectively, for the LEDC (top) and EDC (bottom) pre-collapse compositions. For atomic oxygen in the 0DS100LEDC case (see Fig. 2a), the temperature is not high enough for all the

mantle of grain to evaporate and O reacts mainly with the S-bearing species available in the gas phase. It initially reacts with CS, which is the second most abundant S-bearing species in the gas phase, to form S and CO. As the abundance of CS consequently decreases, O is then mainly destroyed through formation of SO and SO<sub>2</sub>:



In the 0D300LEDC case (see Fig. 2a), the temperature of the core is high enough for mantle hydrocarbons ( $\text{H}_x\text{C}_n$ ) to evaporate. They participate in the consumption of O by forming mainly CO, causing the O abundance to decrease much faster than in the 0D100LEDC case. However, the most efficient reaction at this temperature is



Towards the end ( $t > 10^6 \text{ yr}$ ), the abundance of atomic oxygen increases again from the reaction



as well as photodissociation by secondary UV photons of SO and SO<sub>2</sub>.

With the pre-collapse composition of the EDC, contrary to the LEDC, most of the oxygen is trapped in grain mantle, mainly under the form of H<sub>2</sub>O, H<sub>2</sub>CO and CO (see Table 2). Hence, little atomic oxygen is available in the gas phase even after sublimation of the grain mantle, which explains the fact that its initial abundance in both EDC cases is lower by two orders of magnitude compared to LEDC cases. In the 0DS100EDC case (see Fig. 2d), the temperature of the corino is hot enough to sublimate light species, especially HS and NS, which are two of the sulphur reservoirs in the pre-collapse composition. These species react rapidly with O to form SO and NO for  $10^4 \text{ yr}$ . After this time, it is HCNS that reacts mainly with atomic oxygen through the following reactions:



The global increase of abundance of O at the end of the simulation is due to reaction (5).

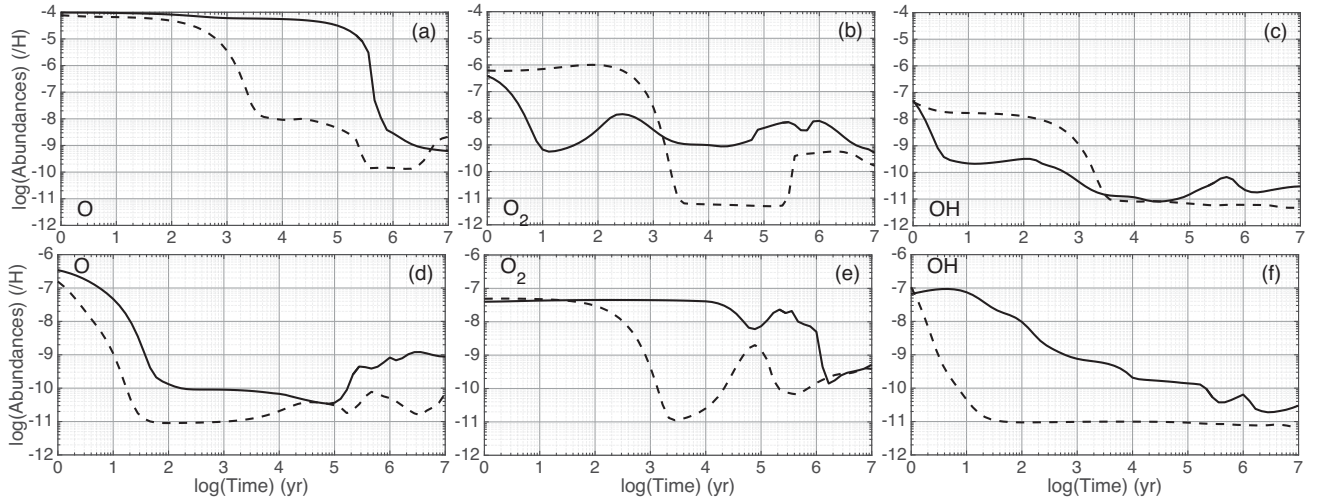


**Figure 2.** Abundances of O, O<sub>2</sub> and OH relative to H as a function of time for hot core conditions:  $n_H = 2 \times 10^7 \text{ cm}^{-3}$  and  $T = 100 \text{ K}$  (solid line) or  $300 \text{ K}$  (dashed line), and for LEDC (top panel) and EDC (bottom panel) pre-collapse compositions.

In the 0D300EDC case (see Fig. 2d), most of the sublimated hydrocarbons efficiently form CH<sub>3</sub>, which consumes O in the first 100 yr following



Afterwards, O abundance increases slowly, mainly from the reaction



In both 0DS100LEDC and 0DS300LEDC models, dioxygen chemistry is strongly linked with S and OH chemistry via



At 100 K (see Fig. 2b), atomic carbon initially destroys O<sub>2</sub> faster than it is created by reaction (12) through



Then, atomic sulphur consumes both O<sub>2</sub> and OH (see Fig. 2c) within a time-scale of 1000 yr, respectively via reaction (11) and



Afterwards, the chemistries of both species are linked by reaction (12). The short increase of both abundances near 10<sup>6</sup> yr is mainly due to the formation of OH via electronic recombination of HOCS<sup>+</sup> and HSO<sub>2</sub><sup>+</sup>.

At 300 K however (see Fig. 2b), atomic carbon is initially rapidly consumed by the two evaporated hydrocarbons C<sub>4</sub>H<sub>2</sub> and C<sub>2</sub>H<sub>2</sub>, and does not destroy O<sub>2</sub> as efficiently as at 100 K. Instead, OH is formed rapidly via reaction (4) (see Fig. 2c), which causes the O<sub>2</sub> abundance to increase through reaction (12) in the first 100 yr. Then, O<sub>2</sub> and OH are consumed in a few 1000 yr, respectively, by reaction (11) and



It should be noted that the increase in O<sub>2</sub> abundance near 10<sup>5</sup> yr is due to the following ion-neutral reactions:



In the EDC cases, atomic oxygen is not abundant enough in the gas phase for reaction (12) to be efficient. Hence, there is no evident link between O<sub>2</sub> and OH chemistries as in the LEDC cases. For the 0D100EDC model (see Fig. 2e), the abundance of dioxygen first slowly grows for a few 100 yr from the reaction:



O<sub>2</sub>H is also destroyed by H to form OH, and when there is not enough left in the gas phase, HCO then reacts with O<sub>2</sub> causing its abundance to decrease after a few 1000 yr. Moreover, reaction (11) also becomes efficient after 10<sup>4</sup> yr and O<sub>2</sub> abundance starts to drop at this time. The increase near 10<sup>5</sup> yr is mainly due to reaction (17).

In the 0D300EDC case (see Fig. 2e), the CH<sub>3</sub> formed from the evaporated hydrocarbon destroys efficiently O<sub>2</sub> for a few 1000 yr via



Afterwards, the abundance of O<sub>2</sub> globally increases from the following reactions:



OH abundance generally decreases in both EDC models. For the 0D100EDC case (see Fig. 2f), this decrease is mainly due to



As for the 0D300EDC case (see Fig. 2f), it is mainly due to reactions (15) and (23).

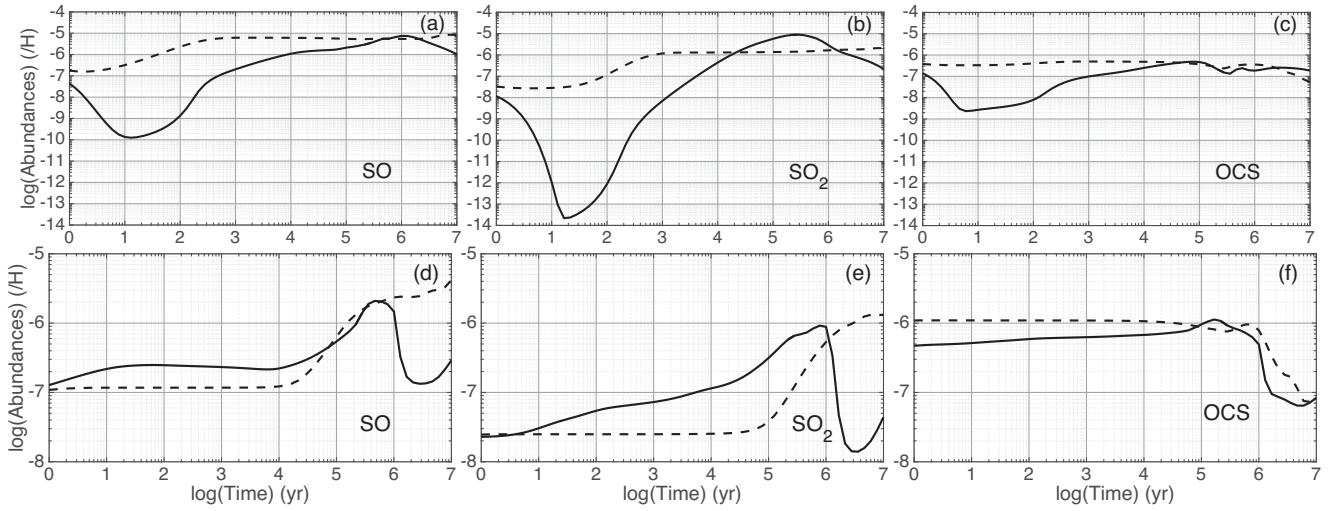


**Figure 3.** Abundances of SO, SO<sub>2</sub> and OCS relative to H as a function of time for hot core conditions:  $n_H = 2 \times 10^7 \text{ cm}^{-3}$  and  $T = 100 \text{ K}$  (solid line) and  $300 \text{ K}$  (dashed line), and for LDC (top panel) and EDC (bottom panel) pre-collapse compositions.

### 3.1.2 Sulphur chemistry

In the following, we take a comprehensive look at the chemistry of the main neutral S-bearing species detected in hot cores, namely SO, SO<sub>2</sub>, OCS, H<sub>2</sub>S, H<sub>2</sub>CS and CS.

#### SO, SO<sub>2</sub> and OCS in the LDC cases

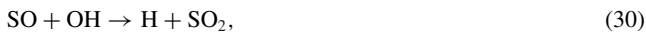
Fig. 3 displays the abundances of SO, SO<sub>2</sub> and OCS in both the LDC (top panels) and EDC (bottom panels) cases. In the 0DS100LDC case, these three species are initially destroyed by atomic carbon, which explains their respective drops in the first 10 yr of the simulation:



SO abundance then grows, first mainly from reaction (14), then reactions (2) and (11) (see Fig. 3a). After  $10^6$  yr, as only a small amount of reactive oxygen remains in the gas phase, SO is no longer efficiently produced. It is instead mainly destroyed by CH through



SO<sub>2</sub> is linked with SO mainly by reaction (3), as well as

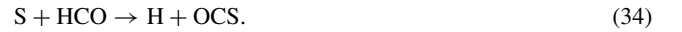


which is only efficient when OH is abundant enough in the gas phase (i.e. at the very beginning of the simulation; see Fig. 2c). Hence, SO<sub>2</sub> abundance grows from 10 yr to a few  $10^5$  yr from these

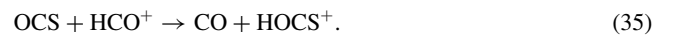
reactions (see Fig. 3b). Afterwards, SO<sub>2</sub> is destroyed by H<sub>3</sub><sup>+</sup> and C<sup>+</sup> following



After its consumption by atomic carbon, OCS is also efficiently formed until  $10^5$  yr from HCO and HCS (see Fig. 3c):



For the remainder of the simulation, HCO<sup>+</sup> is formed efficiently from reaction of H<sub>3</sub><sup>+</sup> with CO, and reacts with OCS:



However, OCS abundance remains stable at this time because of reaction (28).

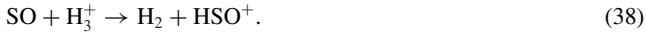
In the 0DS300LDC case, C<sub>4</sub>H<sub>2</sub> and C<sub>2</sub>H<sub>2</sub> thermally desorb from the grain mantle. Both these species react initially with atomic carbon with reaction rates higher of more than two orders of magnitude than those of reactions (24), (25), (26) and (27) preventing SO, SO<sub>2</sub> and OCS from abrupt initial consumptions. Therefore, SO and SO<sub>2</sub> form rapidly from reactions (11), (14) and (30) (see Figs 3a and b). When the abundance of reactive oxygen drops around  $10^3$  yr, their abundances will undergo only small variations. Indeed, as the main reactions ruling SO chemistry are no longer efficient because of the lack of reactive oxygen in the gas phase, reactions that recycle SO via HSO<sup>+</sup> allow its abundances to reach a quasi-static regime until the end of the simulation. For instance, because of the high temperature, the high abundances of evaporated H<sub>2</sub>O and CO render efficient the two following reactions:



**Table 4.** Description of the reactive oxygen composition in the gas phase at the first time-step of the hot core simulations (post-collapse). The values display the percentage relative to the total abundance of oxygen.

LEDC	
100 K	300 K
41 per cent	33 per cent
EDC	
100 K	300 K
0.1 per cent	<0.09 per cent

The SO thus formed is then put back in  $\text{HSO}^+$ :



As a result, the  $\text{SO}_2$  abundance shows only a small increase during the final part of the simulation, mainly due to reaction (30).

The OCS abundance does not vary much in the ODS300LEDC case (see Fig. 3c). When atomic oxygen is still abundant in the gas phase, OCS is mainly formed through reaction (33). Afterwards OCS is destroyed by secondary UV photons to form S and CO, and by  $\text{H}_3^+$  through

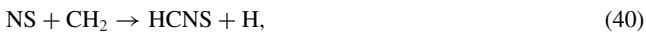


$\text{HOCS}^+$  then recombines electronically to form either CS and OCS, which explains why the latter abundance decreases slowly.

#### SO, $\text{SO}_2$ and OCS in the EDC cases

The bottom panel of Fig. 3 displays the abundances of SO,  $\text{SO}_2$  and OCS in both EDC cases. On the one hand, it appears that the chemistry of these species does not depend as much on the temperature as in the LEDC cases. This can be explained by the poor abundance of reactive oxygen, especially atomic oxygen, in the gas phase in the EDC cases compared with the LEDC cases. Table 4 displays the amount of reactive oxygen (relative to that of total oxygen) in the gas phase at the first time-step of each hot core simulation. It shows that in the LEDC cases at least 33 per cent of the total amount of oxygen is under reactive form in the gas phase, against at most 0.1 per cent in the EDC cases.

On the other hand, the chemistry of SO,  $\text{SO}_2$  and OCS looks relatively inert, except for the last part of the simulation ( $t > 10^5$  yr). Indeed, in the ODS100EDC case, SO and  $\text{SO}_2$  (see Figs 3d and e) are at first slowly formed through reactions (14) and (30), respectively. As the abundance of HCNS grows from the evaporated NS (accumulated on the grain during the dense parent cloud phase; see Table 2) through



the abundance of SO grows steeper from  $10^4$  yr because of reaction (6). Finally, after  $10^6$  yr, SO is consumed by CH through reactions (28) and (29). The strong link of  $\text{SO}_2$  with SO via reaction (30), coupled with reaction (31), makes its abundance drop at the same time. Regarding OCS (see Fig. 3f), its abundance grows at first in the ODS100EDC case from reaction (22), then from reaction (34) after  $10^4$  yr. Towards the end of the simulation, as for SO and  $\text{SO}_2$ , OCS is destroyed by CH via



In the ODS300EDC case, the chemistry of SO,  $\text{SO}_2$  and OCS differs from the ODS100EDC case in two main ways. First, the abundance

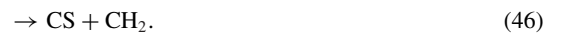
of OH decreases much faster in the ODS300EDC case (see Fig. 2f), diminishing even more the quantity of reactive oxygen in the gas phase, causing the abundances of SO,  $\text{SO}_2$  and OCS to remain relatively constant during at least the first  $10^5$  yr of the simulation. Secondly, CH is much less abundant at 300 K (by two to three orders of magnitude) because it is effectively destroyed by evaporated  $\text{H}_2\text{O}$  and  $\text{C}_2\text{H}_2$ :



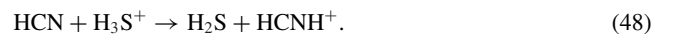
Hence, SO and  $\text{SO}_2$  abundances continue to increase at the end of the simulation (see Figs 3d and e) and do not decrease as in the ODS100EDC case. However, the lack of CH does not prevent the late-time decrease of OCS (see Fig. 3f), which is ruled by the same reactions as in the ODS300LEDC case, namely its photodissociation by secondary UV photon and reaction (39).

#### $\text{H}_2\text{S}$ , $\text{H}_2\text{CS}$ and CS in the LEDC cases

Fig. 4 is the same as Fig. 3 but for  $\text{H}_2\text{S}$ ,  $\text{H}_2\text{CS}$  and CS. In the ODS100LEDC case, as for SO,  $\text{SO}_2$  and OCS,  $\text{H}_2\text{S}$  and  $\text{H}_2\text{CS}$  (see Figs 4a and b) are both initially destroyed by atomic carbon via the following reactions:



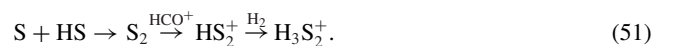
The following increase in  $\text{H}_2\text{S}$  abundance is mainly due to two coupled reactions:



Indeed,  $\text{CH}_2\text{SH}$  evaporates slowly from the grain surface in the physical conditions of the simulation. Reacting with atomic nitrogen via reaction (47), it forms both  $\text{H}_2\text{S}$  and HCN. The latter then also forms  $\text{H}_2\text{S}$ . The combination of these two reactions explains the steep increase in  $\text{H}_2\text{S}$  abundance between 10 and  $10^5$  yr. Afterwards, it decreases from the following ion-neutral reactions:



Towards the end of the simulation,  $\text{H}_2\text{S}$  is efficiently produced by the electronic recombination of  $\text{H}_3\text{S}_2^+$ , provided by the following reaction mechanism:



This mechanism is made efficient by the increase of the abundance of HS during this period of time.

$\text{H}_2\text{CS}$  gas-phase chemistry at 100 K (in both LEDC and EDC cases; see Figs 4b and e, respectively) is intertwined with its grain



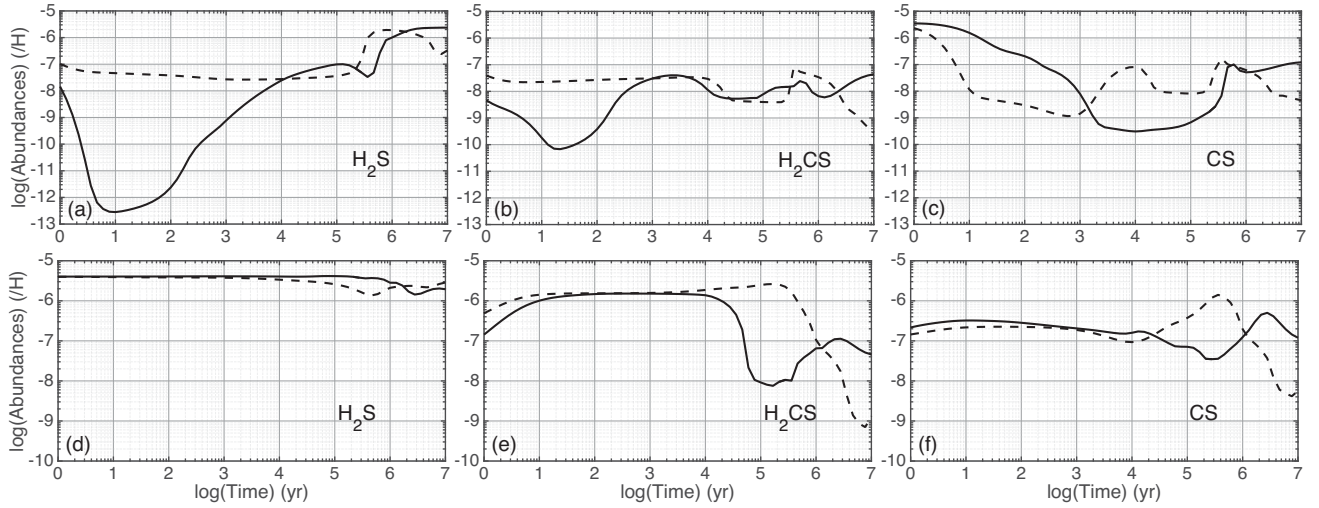
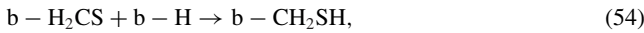


**Figure 4.** Abundances of  $\text{H}_2\text{S}$ ,  $\text{H}_2\text{CS}$  and  $\text{CS}$  relative to  $\text{H}$  as a function of time for hot core conditions:  $n_{\text{H}} = 2 \times 10^7 \text{ cm}^{-3}$  and  $T = 100 \text{ K}$  (solid line) and  $300 \text{ K}$  (dashed line), and for LDC (top panel) and EDC (bottom panel) pre-collapse compositions.

chemistry because the temperature is not high enough for its complete thermal desorption from grain ices. Hence, after its destruction by atomic carbon,  $\text{H}_2\text{CS}$  grows from



Then its abundance decreases from destruction by  $\text{HCNH}^+$  in the gas phase, as well as by hydrogenation in the grain bulk. Indeed, the latter contributes to the depletion of  $\text{H}_2\text{CS}$  from the gas phase at this time because the chemistry has reached adsorption/desorption equilibrium. The reactions in question are, respectively,

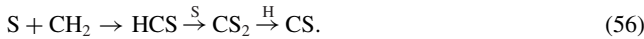


where the prefix ‘b-’ denotes the bulk species. Afterwards,  $\text{H}_2\text{CS}$  abundance increases again, mainly from the electronic recombination of  $\text{H}_3\text{CS}^+$  and reaction (52).

Contrary to the other S-bearing species studied in this paper,  $\text{CS}$  is not destroyed by atomic carbon during the early phase of the simulation (see Fig. 4c). It is instead destroyed during a longer period of time (approximately  $10^4 \text{ yr}$ ) by atomic oxygen, contributing efficiently to lock gas-phase oxygen into  $\text{CO}$  via



$\text{CS}$  abundance then grows mainly from reaction (25) as well as from the following reaction mechanism:



As previously observed, atomic carbon is preferentially consumed by evaporated hydrocarbon in the ODS300LDC case and therefore has a limited impact on sulphur chemistry compared to the ODS100LDC case. Hence,  $\text{H}_2\text{S}$  (see Fig. 4a) is first destroyed by atomic hydrogen and oxygen for  $10^3 \text{ yr}$  via

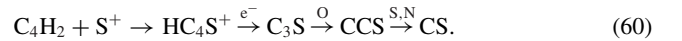


$\text{H}_2\text{S}$  is after formed by the electronic recombination of  $\text{H}_3\text{S}_2^+$  provided by a similar reaction mechanism as (51), except that instead of  $\text{HCO}^+$ , it is the  $\text{H}_3\text{O}^+$  ion that mainly reacts with  $\text{S}_2$  to form  $\text{HS}_2^+$ . Indeed,  $\text{H}_3\text{O}^+$  is much more abundant in the gas phase at  $300 \text{ K}$  than at  $100 \text{ K}$  because it comes mainly from  $\text{H}_2\text{O}$ , which is totally evaporated from grain at this temperature. Furthermore, it is  $\text{H}_3\text{O}^+$  that destroys  $\text{H}_2\text{S}$  at the end of the simulation:

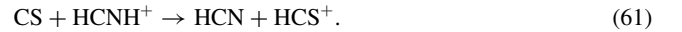


At  $300 \text{ K}$ ,  $\text{H}_2\text{CS}$  is fully depleted from the grain surface and bulk and is affected only by gas-phase chemistry (see Fig. 4b). Partially consumed by atomic carbon during the first  $10 \text{ yr}$ , it is then formed mainly through reaction (52) and destroyed by reaction (53).

In the ODS300LDC case,  $\text{CS}$  is also initially destroyed by atomic oxygen via reaction (55) (see Fig. 4c), but for a shorter time than in the ODS100LDC case. The increase in its abundance at  $10^3 \text{ yr}$  is mostly due to a reaction mechanism starting from the evaporated  $\text{C}_4\text{H}_2$ :



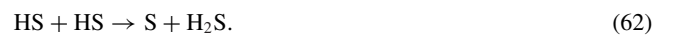
Then  $\text{CS}$  is mainly destroyed by  $\text{HCNH}^+$  via



Finally, the last increase in its abundance is due to the reaction mechanism (56).

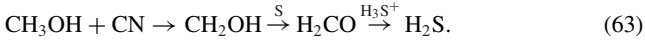
#### *$\text{H}_2\text{S}$ , $\text{H}_2\text{CS}$ and $\text{CS}$ in the EDC cases*

In the EDC cases and prior to collapse,  $\text{H}_2\text{S}$  in icy grain bulk is the second reservoir of sulphur, containing 26 per cent of the total amount of sulphur (see Table 2). Hence, its abundance in both EDC cases is generally higher than in the LDC cases. Moreover, in the ODS100EDC case (see Fig. 4d),  $\text{H}_2\text{S}$  initially forms efficiently from its abundant reservoirs counterpart  $\text{HS}$  via



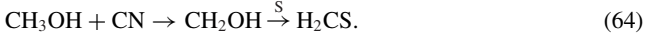
It is also produced during most of the simulation from the slow evaporation of methanol, which is the fourth reservoir of oxygen

in the EDC case (see Table 2), and through the following reaction mechanism:



Towards the end,  $\text{H}_2\text{S}$  is destroyed via reaction (49).

In the 0DS100EDC case (see Fig. 4e),  $\text{H}_2\text{CS}$  is first formed via reaction (52) as well as from methanol slow depletion with the following reaction mechanism, similar to reaction (63):



As in the 0DS100LEDC case,  $\text{H}_2\text{CS}$  chemistry is afterwards linked with its grain chemistry via reactions (53) and (54), making its abundance drop at  $10^5$  yr. At the end of the simulation,  $\text{H}_2\text{CS}$  abundance increases again from reaction (52) and electronic recombination of  $\text{H}_3\text{CS}^+$ .

Because of the small amount of reactive oxygen in the EDC cases compared to the LEDC cases (see Table 4), CS is not destroyed by atomic oxygen at the beginning of the simulation (see Fig. 4e). At 100 K, it is instead formed rapidly via



with HCS coming from the small fraction of  $\text{H}_2\text{S}$  destroyed by reaction (44). Afterwards, CS is destroyed for a few  $10^5$  yr by OH and HS via reaction 22 and



When  $\text{CS}_2$  abundance is high enough, it is hydrogenated back into CS, causing the abundance of the latter to grow again at the end of the simulation.

In the 0DS300EDC case, all the methanol is directly depleted in the gas phase and rapidly forms  $\text{CH}_3$  through many different reactions. Hence, as  $\text{CH}_3$  abundance is rapidly much higher than in the 0DS100EDC case,  $\text{H}_2\text{S}$  is mainly destroyed at 300 K via (see Fig. 4d)



This high abundance of  $\text{CH}_3$  in the gas phase also causes  $\text{H}_2\text{CS}$  to be efficiently formed for a few  $10^5$  yr by reaction (52) (see Fig. 4e). Afterwards, as in the 0DS300LEDC case, the steep decrease of its abundance is mainly due to reaction (53).

Finally, CS chemistry in the 0DS300EDC case is similar to the 0DS100EDC case, except for the fact that OH abundance at 300 K is much lower than at 100 K (see Fig. 4f). Hence, CS is mainly destroyed by reaction (66). Moreover, as  $\text{CS}_2$  abundance grows faster at 300 K than at 100 K, the peak in CS abundance happens sooner in the 0DS300LEDC case. At the end, CS is destroyed like  $\text{H}_2\text{CS}$ , by  $\text{HCNH}^+$  via reaction (61).

### 3.1.3 Comparisons to observations

The species studied in this section have been detected in many hot cores and corinos, and their respective observed abundances present differences among sources that can go as high as three orders of magnitude (see for example, table 5 of Wakelam et al. 2004a, and references therein). These variations are often explained by differences among the ages of the sources, or among the temperatures of their respective hot cores or corinos (see discussion in Herpin et al. 2009). Therefore, it would be complex, as well as out of the scope of the present study, to quantitatively compare our results to observations. Qualitatively, however, we can raise the two following points.

(i) The total amount of sulphur observed in massive hot cores generally accounts only for a small part of its cosmic abundance (around 0.1 per cent; see Hatchell et al. 1998; van der Tak 2004; Wakelam et al. 2004a; Herpin et al. 2009), which contrasts with our modelling results where most of the sulphur appears to be in the form of SO,  $\text{SO}_2$ ,  $\text{H}_2\text{S}$  and OCS at the ages that are expected for such objects. Uncertainties on massive hot core observations due to the fact that they are mostly very distant sources, and therefore not spatially resolved, as well as uncertainties on our high-temperature network could explain these discrepancies. However, among this type of source, the hot core of Orion KL presents a high abundance of  $\text{H}_2\text{S}$  of  $2.5 \times 10^{-6}$ , accounting for more than 15 per cent of the total amount of sulphur (Minh et al. 1990), as well as higher abundances of SO and  $\text{SO}_2$  than in other massive hot cores (Sutton et al. 1995). It appears that, even if our models fail to reproduce the observed abundances of these molecules for most massive hot core observations, both our EDC models can reproduce the Orion KL abundances of  $\text{H}_2\text{S}$ , SO and  $\text{SO}_2$  within one order of magnitude in a range of time acceptable for this structure, between  $10^4$  and  $10^6$  yr. However, in this range of time, the models tend to overestimate the abundances of OCS, CS and  $\text{H}_2\text{CS}$ , which suggests that work still has to be done regarding the modelling of the chemistry of these species.

(ii) The only hot corinos towards which all the S-bearing species studied in this paper have been observed is IRAS 16293–2422. The observed abundances of SO,  $\text{SO}_2$ , OCS,  $\text{H}_2\text{CS}$  and  $\text{H}_3\text{S}$  in the dense inner part of its envelope ( $\leq 150$  au; see table 7 of Schöier et al. 2002) can be reproduced within one order of magnitude by both our LEDC models in a range of time compatible with that derived by Schöier et al. (2002), between a few  $10^3$  and a few  $10^4$  yr. This result would suggest that IRAS 16293–2422 has formed in a parent cloud that would have collapsed at an age of approximately  $10^5$  yr.

These results suggest that, following our previous paper (Vidal et al. 2017), our model can reproduce observations of S-bearing molecules in  $\text{H}_2\text{S}$ -rich hot cores and in hot corinos using – as an initial abundance of sulphur – its cosmic abundance. However, work still has to be conducted regarding our high-temperature network, especially for OCS,  $\text{H}_2\text{CS}$  and CS.

### 3.2 One-dimensional static models

In this section, we study the results of the two one-dimensional static simulations whose parameters are described in Section 2.4 and Table 3. The goal is to evaluate the impact of the pre-collapse chemical composition of the parent cloud on the computed abundances of the main S-bearing species SO,  $\text{SO}_2$ , OCS,  $\text{H}_2\text{S}$ ,  $\text{H}_2\text{CS}$  and CS. Both LEDC and EDC simulations were run for a period of  $3.5 \times 10^5$  yr so as to make the results comparable to those of the zero-dimensional dynamic simulations presented in Section 3.3.

Fig. 5 displays the abundances of each of these species for both 1DSLEDC (solid lines) and 1DSEDC (dashed lines) pre-collapse compositions. For a radius greater than 300 au, which corresponds to the outermost and coldest ( $T < 50$  K) part of the envelope of the protostar, most considered species present only small local differences in their abundances between the LEDC and EDC cases. Only  $\text{SO}_2$  presents significant differences that can go to more than three orders of magnitude while other species display differences smaller than one order of magnitude (see Fig. 5b).

In the inner part of the envelope ( $R < 300$  au) where the temperature goes from 50 to 200 K (see the right panel of Fig. 1), all

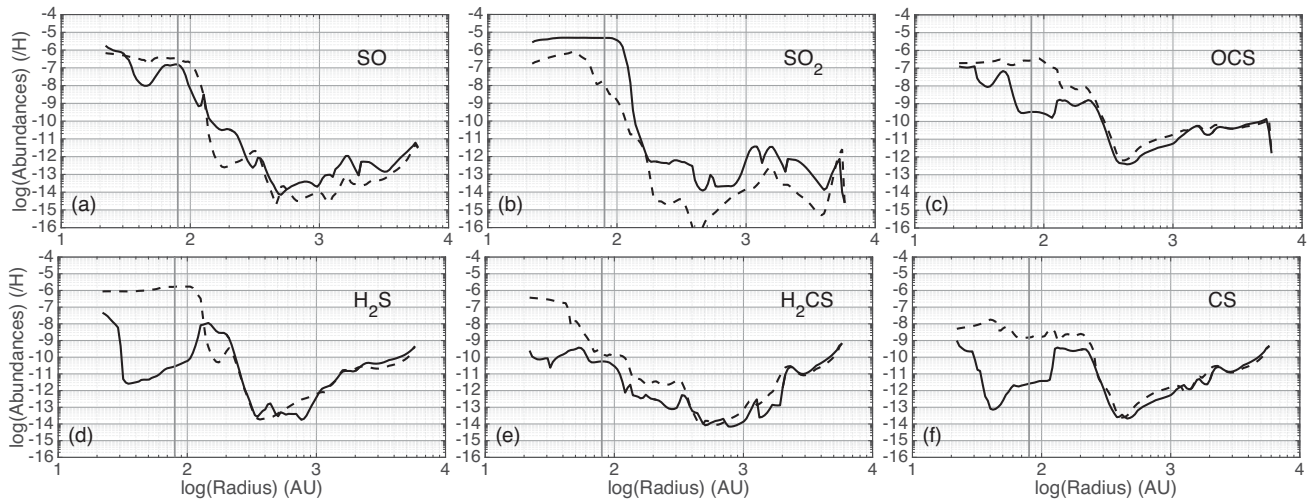


**Figure 5.** Abundances of SO, SO<sub>2</sub> and OCS (top panel) and H<sub>2</sub>S, H<sub>2</sub>CS and CS (bottom panel), relative to H as a function of the radius to the star IRAS 16293–2422 according to the one-dimensional structure of Crimier et al. (2010), for the LEDC (solid line) and EDC (dashed line) pre-collapse compositions. Both models were run for a period of  $3.5 \times 10^5$  yr so the results would be comparable to those of the zero-dimensional dynamic simulations. The vertical grey line represent the hot core spatial limit  $R_{\text{HC}} = 80$  au,  $T > 100$  K.

species abundances show significant differences between the LEDC and EDC pre-collapse compositions. These differences can go from two to more than six orders of magnitude. Within the hot core limits (delimited by a vertical grey line in Fig. 5 at  $R_{\text{HC}} < 80$  au,  $T > 100$  K), the species that are most sensitive to the pre-collapse composition appear to be H<sub>2</sub>S, H<sub>2</sub>CS, and CS with differences of more than three orders of magnitude (see Figs 5d, e and f, respectively). For H<sub>2</sub>S, these differences are explained by its dependence on the parent cloud evolution time. Indeed, in the EDC case, H<sub>2</sub>S in icy grain bulk is the second reservoir of sulphur in the pre-collapse composition, containing 26 per cent of the total amount of sulphur, whereas in the LEDC case, it only contains 5 per cent (see Table 2). Hence, in the inner part of the envelope and the hot core, where the temperature is high enough for H<sub>2</sub>S thermal desorption, its abundance is much higher than in the LEDC case. Moreover, Fig. 4 shows that, in that case, H<sub>2</sub>S is not efficiently destroyed in the gas phase. Regarding H<sub>2</sub>CS, this species efficiently forms at high temperature in the gas phase from CH<sub>3</sub>, via reaction (52), which is much more abundant in the EDC case because of evaporated methanol and hydrocarbons accumulated on the grains during the parent cloud evolution. Finally, in the EDC case, CS is not as efficiently destroyed in the gas phase as in the LEDC case (see Fig. 4) because of the low abundance of reactive oxygen (see Table 4).

We can finally highlight that our one-dimensional static models show that the pre-collapse composition of the parent cloud appears to be critical for the sulphur-bearing species in hot core physical conditions. Indeed, we can see from Fig. 5 that a hot core that formed from a young parent cloud will be poor in H<sub>2</sub>S and rich in SO<sub>2</sub>, while a hot core formed from a more evolved parent cloud would be rich in H<sub>2</sub>S and H<sub>2</sub>CS.

### 3.3 Zero-dimensional dynamic model

In this section, we carry out the same study as in the previous section but for the zero-dimensional dynamic simulations ODDLEDC and ODDEDC described in Section 2.5 and Table 3.

Fig. 6 is the same as Fig. 5 but for the zero-dimensional dynamic simulations. In this figure, it is particularly striking that the pre-collapse chemical composition of the parent cloud appears to

have little or no effect on the abundances of the considered S-bearing species. Only SO presents a significant difference in the hot core (delimited by a vertical grey line in Fig. 6 at  $R_{\text{HC}} < 135$  au,  $T > 100$  K), and even this difference is no more than a factor of 7 (see Fig. 6a). A possible explanation for this lack of differences would be that the free-fall time considered in these simulations is long enough for both models to evolve towards the same chemical composition. Indeed, if the initial pre-collapse chemical composition has enough time to evolve in an environment cold enough for species not to evaporate, it will tend towards a state similar to the EDC case (i.e. with an evolved grain surface and bulk chemistry), notably with most of the sulphur transformed into H<sub>2</sub>S and OCS on the grains. Hence, the hot core chemical composition of both ODDLEDC and ODDEDC would be very similar.

Moreover, the modification we made to the density profile of the model would tend to accelerate the chemistry and adsorption of species on the grains and therefore reduce the chemical time-scale. We expect that by using the original model of Aikawa et al. (2008) we would obtain more differences and thus a more important impact of the pre-collapse chemical composition on the hot core chemistry.

## 4 DISCUSSION

### 4.1 Modification of the density profile of the dynamic model

In order to evaluate the impact of the modification of the density radial profile for our zero-dimensional dynamic model on sulphur chemistry, we run the ODDLEDC and ODDEDC cases, but this time using the original physical structure of Aikawa et al. (2008). Fig. 7 is therefore the same as Fig. 6, but for the models run with the original density structure of Aikawa et al. (2008). As expected, the results displays larger differences between the LEDC and EDC pre-collapse compositions cases, which can be explained by a slower chemistry due to lower density. Moreover, as discussed in Wakelam et al. (2014), lower densities tend to decrease adsorption of species on grains (and consequently depletion), and therefore enhance gas-phase chemistry at low temperature, which explains why the abundances of the studied species are higher in the envelope in the original structure case. However, the resulting abundances



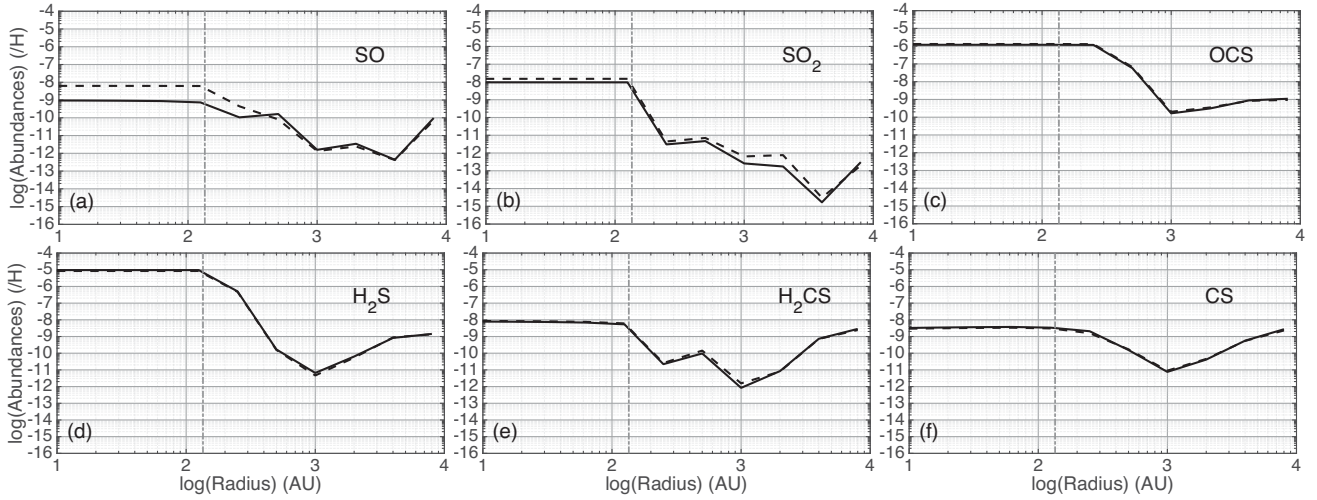


**Figure 6.** Abundances of SO, SO<sub>2</sub> and OCS (top panel) and H<sub>2</sub>S, H<sub>2</sub>CS and CS (bottom panel), relative to H as a function of the radius to the star IRAS 16293–2422 according to the modified structure of Aikawa et al. (2008), for the LEDC (solid line) and EDC (dashed line) pre-collapse compositions. The vertical grey dashed line represents the hot core spatial limit  $R_{\text{HC}} = 135$  au,  $T > 100$  K.

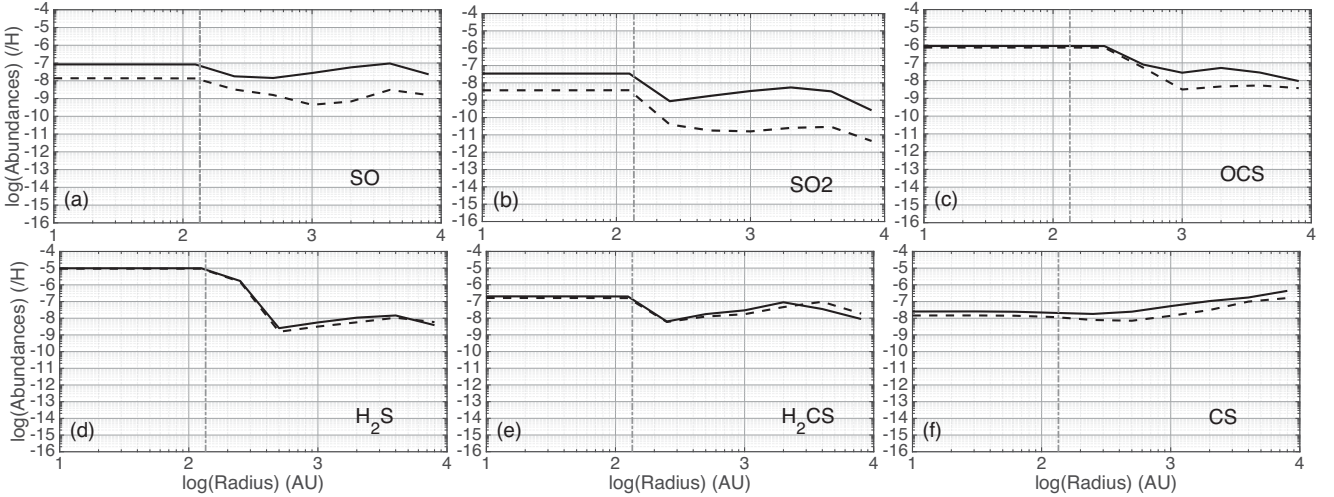


**Figure 7.** Abundances of SO, SO<sub>2</sub> and OCS (top panel) and H<sub>2</sub>S, H<sub>2</sub>CS and CS (bottom panel), relative to H as a function of the radius to the star IRAS 16293–2422 according to the original structure of Aikawa et al. (2008), for the LEDC (solid line) and EDC (dashed line) pre-collapse compositions. The vertical grey dashed line represents the hot core spatial limit  $R_{\text{HC}} = 135$  au,  $T > 100$  K.

in the hot core do not change drastically (at most slightly more than one order of magnitude) and are even the same for OCS and H<sub>2</sub>S (see Figs 7c and d, respectively). As discussed in Section 3.3, this could be explained by a long free-fall time, which would give the chemistry enough time for H<sub>2</sub>S and OCS to accumulate on the grains before thermal depletion in the hot core. More complete studies of the effect of density and free-fall time on the chemistry of a collapsing envelopes and hot cores will be conducted in the future.

#### 4.2 H<sub>2</sub>S and the initial abundance of sulphur

This study was conducted in light of the previous results we obtained regarding the sulphur reservoir in dark clouds (Vidal et al. 2017), namely that depending on the age of the cloud, the reservoir of sulphur could be either atomic sulphur in the gas phase (LED case) or H<sub>2</sub>S and HS in icy grain bulk nearly equally sharing more than 55 per cent of the total amount of sulphur (EDC case). Another

result was that the NAUTILUS model could reproduce the S-bearing observations in the dark cloud TMC-1 using as an initial abundance of sulphur its cosmic abundance, or three times depleted. Hence, throughout this paper, we present results obtained using the cosmic abundance of sulphur of  $1.5 \times 10^{-5}$  (Jenkins 2009). With this initial abundance of sulphur, the H<sub>2</sub>S abundances obtained in the hot core in the dynamic simulation with the modified as well as the original structure from Aikawa et al. (2008) is as high as  $10^{-5}$ . Such a high abundance of H<sub>2</sub>S is not consistent with the abundance derived from the observation of IRAS 16293–2422 ( $2.7 \times 10^{-7}$ ; see Wakelam et al. 2004a). On the one hand, to understand why the model overestimates the H<sub>2</sub>S abundance, we ran all the models presented in this paper with an initial abundance of  $5 \times 10^{-6}$ . It should be noted that it only changes the presented results quantitatively, linearly diminishing the abundances of the studied species by approximately a factor of 3. Regarding H<sub>2</sub>S in the dynamical case, this initial depletion of sulphur allows an estimation of its abundance in the hot



**Table 5.** Comparison of the abundances obtained in the LEDC case, where  $a(b)$  stands for  $a \times 10^b$ .

Species	$(n_i/n_H)_{\text{1DLEDC}}$	$(n_i/n_H)_{\text{0DLEDC}}$
<i>R</i> = 50 au (hot core)		
SO	5.7(−8)	9.0(−10)
SO <sub>2</sub>	1.4(−5)	9.5(−9)
OCS	3.0(−7)	1.2(−6)
H <sub>2</sub> S	1.2(−11)	9.5(−6)
H <sub>2</sub> CS	7.4(−10)	7.6(−9)
CS	1.2(−12)	3.3(−9)
<i>R</i> = 500 au (envelope)		
SO	2.3(−14)	1.6(−10)
SO <sub>2</sub>	1.2(−13)	4.7(−12)
OCS	2.2(−12)	5.8(−8)
H <sub>2</sub> S	1.1(−13)	1.7(−10)
H <sub>2</sub> CS	2.7(−14)	1.4(−10)
CS	1.2(−13)	1.7(−10)

core to be slightly overestimated around  $3 \times 10^{-6}$ , but it could be considered in accordance with the observations (within a margin of one order of magnitude).

On the other hand, the overestimation of H<sub>2</sub>S that we find could be a result of the efficient formation path due to slowly evaporating CH<sub>2</sub>SH and CH<sub>3</sub>OH at 100 K studied in Section 3.1. This contradicts previous theoretical and laboratory studies that predict that in the high-temperature gas phase, the H<sub>2</sub>S evaporated from grain ices is preferentially destroyed to form SO and SO<sub>2</sub>, or molecules with two S atoms, such as H<sub>2</sub>S<sub>2</sub> or HS<sub>2</sub> (Charnley 1997; Wakelam et al. 2004b; Druard & Wakelam 2012; Esplugues et al. 2014; Martín-Doménech et al. 2016). Hence, this result could suggest missing efficient destruction gas-phase reactions in the H<sub>2</sub>S chemistry in our network.

### 4.3 Sensitivity to the type of simulation

One goal of this paper is to highlight the differences that can appear when using two types of simulations to model the same hot core. In order to do so, we have used a one-dimensional static model and a zero-dimensional dynamic model of IRAS 16293–2422. Our results show that our one-dimensional model favours a hot core sulphur chemistry dominated by SO<sub>2</sub> and SO in the LEDC case and by H<sub>2</sub>S in the EDC case, while our zero-dimensional dynamic model displays in both cases high abundances of H<sub>2</sub>S and OCS and low abundances of SO<sub>2</sub> and SO. Table 5 displays the abundances obtained for both types of models in the LEDC case, at 50 au (in the hot core) and at 500 au (in the envelope). In light of the difference in abundance that exists for a given species between the two type of models, we can easily make a conclusion about the sensitivity to the type of simulation used to compute the chemistry of a hot core and its collapsing envelope. Especially in the hot core, these differences can reach as much as six orders of magnitude, rendering critical the choice of model used to compare results with possible observations or related works.

### 4.4 Importance of the pre-collapse chemical composition

The observations of S-bearing species in hot cores are still a puzzling issue, as a large variety of sulphur compositions have been observed towards different hot cores and therefore no global trend has yet been found (see fig. 5 of Woods et al. 2015, and refer-

ences therein). However, a given set of hot cores can present similar sulphur compositions (see for example, Minh 2016), which would suggest similar evolutionary stages. In this paper we have investigated the importance of the pre-collapse chemical composition on the hot core chemistry of S-bearing species. Our results on zero-dimensional and one-dimensional simulations (Sections 3.1 and 3.2) support the fact that, given the fast evolution of sulphur chemistry in the parent cold clouds, the pre-collapse chemical composition is a critical parameter for hot core simulations. This could partially explain the absence of a global trend for sulphur compositions in observed hot cores from different parent clouds, as well as supporting the fact that for parent clouds that collapse at similar ages and physical environments, hot cores can have similar sulphur compositions. However, the study of our dynamical simulation (Section 3.3) raises the question of the role of the free-fall time on sulphur evolution, which would also explain the similar composition of different hot cores, especially those where H<sub>2</sub>S and OCS are found to be more abundant than the other species (see for example, Herpin et al. 2009).

## 5 CONCLUSIONS

In this paper, we aimed to take a comprehensive look at the chemistry of sulphur in hot cores. In order to do so, we have conducted an extensive study with simple zero-dimensional models of the chemistry of the main S-bearing species observed towards hot cores, namely SO, SO<sub>2</sub>, OCS, H<sub>2</sub>S, H<sub>2</sub>CS and CS. We have presented and compared the results from two types of simulations (one-dimensional static and zero-dimensional dynamic), in order to highlight the sensitivity of chemistry to the choice of model used in astrochemical studies.

Our zero-dimensional extensive study revealed four main results:

- (i) The total amount of reactive oxygen in the gas phase depends critically on the pre-collapse composition of the hot core (see Table 4) as well as the temperature.
- (ii) Sulphur chemistry in hot and dense gas also depends greatly on the pre-collapse composition, mainly because of its impact on reactive atomic oxygen, carbon and hydrogen, which all participate actively in most of the sulphur chemistry in such environments.
- (iii) Sulphur chemistry in hot and dense gas depends greatly on the temperature, partly because it is directly and indirectly linked with hydrocarbon evaporated from grain ices, and their main destruction products CH<sub>2</sub> and CH<sub>3</sub>.
- (iv) We found efficient paths of formation of gas-phase H<sub>2</sub>S that could be responsible for its overestimation in most of our hot core results. Studies of the gas-phase chemistry of this species need to be continued to ensure the relevance of our network.

Our study of the one-dimensional static and zero-dimensional dynamic models led to the following conclusions:

- (i) The pre-collapse chemical composition of the parent cloud is a key parameter for one-dimensional static simulations of sulphur chemistry in hot cores. Indeed, the computed abundances showed that it can imply differences up to six orders of magnitude for a given species in the hot core. However, the pre-collapse composition appears to have only a small impact on the chemical composition of the envelope. Finally, our one-dimensional model shows that a hot core that was formed from a young parent cloud will be poor in H<sub>2</sub>S and rich in SO<sub>2</sub>, while a hot core formed from a more evolved parent cloud would be rich in H<sub>2</sub>S and H<sub>2</sub>CS.

(ii) The zero-dimensional dynamic simulations conducted in this paper have revealed only small differences between the results of the less evolved and the evolved pre-collapse chemical composition, showing only a weak dependence of the hot core sulphur chemistry on the pre-collapse composition. Indeed, for both cases, the model predicts high abundances of  $\text{H}_2\text{S}$  and  $\text{OCS}$  and low abundances of  $\text{SO}_2$  and  $\text{SO}$ . However, this result is thought to be due to the long free-fall time used in our model, which would allow enough time for sulphur to be adsorbed on to grains and to form mainly  $\text{H}_2\text{S}$  and  $\text{OCS}$  in the envelope before thermal depletion. We expect that for a shorter free-fall time the differences between the two pre-collapse composition cases would be larger. Future work will focus on this importance of the free-fall time, as along with the pre-collapse chemical composition, it could explain the large variety of abundances of S-bearing species observed in hot cores.

The comparison between the one-dimensional static and zero-dimensional dynamic models has displayed large differences between the computed abundances, which can be as high as six orders of magnitude in the hot core. This result highlights the sensitivity to the choice of simulations in astrochemical studies, especially when comparing results with observations, or with results from other papers.

## ACKNOWLEDGEMENTS

This work has been funded by the European Research Council (Starting Grant 3DICE, grant agreement 336474). The authors are also grateful to the CNRS programme, Physique et Chimie du Milieu Interstellaire (PCMI), for partial funding of their work.

## REFERENCES

- Aikawa Y., Wakelam V., Garrod R. T., Herbst E., 2008, *ApJ*, 674, 984  
 Cazaux S., Caselli P., Tielens A. G. G. M., LeBourlot J., Walmsley M., 2005, *J. Phys. Conf. Ser.*, 6, 155  
 Ceccarelli C., Hollenbach D. J., Tielens A. G. G. M., 1996, *ApJ*, 471, 400  
 Chaabouni H., Bergeron H., Baouche S., Dulieu F., Matar E., Congiu E., Gavilan L., Lemaire J. L., 2012, *A&A*, 538, A128  
 Chang Q., Cuppen H. M., Herbst E., 2007, *A&A*, 469, 973  
 Charnley S. B., 1997, *ApJ*, 481, 396  
 Crimier N., Ceccarelli C., Maret S., Bottinelli S., Caux E., Kahane C., Lis D. C., Olofsson J., 2010, *A&A*, 519, A65  
 Druard C., Wakelam V., 2012, *MNRAS*, 426, 354  
 Esplugues G. B., Viti S., Goicoechea J. R., Cernicharo J., 2014, *A&A*, 567, A95  
 Garrod R. T., Herbst E., 2006, *A&A*, 457, 927  
 Garrod R. T., Pauly T., 2011, *ApJ*, 735, 15  
 Garrod R. T., Wakelam V., Herbst E., 2007, *A&A*, 467, 1103  
 Graedel T. E., Langer W. D., Frerking M. A., 1982, *ApJS*, 48, 321  
 Harada N., Herbst E., Wakelam V., 2010, *ApJ*, 721, 1570  
 Hatchell J., Thompson M. A., Millar T. J., MacDonald G. H., 1998, *A&A*, 338, 713  
 Herbst E., van Dishoeck E. F., 2009, *ARA&A*, 47, 427  
 Herpin F., Marseille M., Wakelam V., Bontemps S., Lis D. C., 2009, *A&A*, 504, 853  
 Hickson K. M., Wakelam V., Loison J.-C., 2016, *Molecular Astrophysics*, 3, 1  
 Hincelin U., Wakelam V., Hersant F., Guilloteau S., Loison J. C., Honvault P., Troe J., 2011, *A&A*, 530, A61  
 Hincelin U., Commerçon B., Wakelam V., Hersant F., Guilloteau S., Herbst E., 2016, *ApJ*, 822, 12  
 Holdship J. et al., 2016, *MNRAS*, 463, 802  
 Ivezić Z., Elitzur M., 1997, *MNRAS*, 287, 799  
 Jenkins E. B., 2009, *ApJ*, 700, 1299  
 Karssemeijer L. J., Cuppen H. M., 2014, *A&A*, 569, A107  
 Kurtz S., Cesaroni R., Churchwell E., Hofner P., Walmsley C. M., 2000, in Mannings V., Boss A. P., Russell S. S., eds, *Protostars and Planets IV*. Univ. Arizona Press, Tuscon, AZ, p. 299  
 Loison J.-C. et al., 2016, *MNRAS*, 456, 4101  
 Loison J.-C. et al., 2017, *MNRAS*, 470, 4075  
 Majumdar L., Gratier P., Vidal T., Wakelam V., Loison J.-C., Hickson K. M., Caux E., 2016, *MNRAS*, 458, 1859  
 Martín-Doménech R., Jiménez-Serra I., Muñoz Caro G. M., Müller H. S. P., Occhiogrosso A., Testi L., Woods P. M., Viti S., 2016, *A&A*, 585, A112  
 Masunaga H., Inutsuka S.-i., 2000, *ApJ*, 531, 350  
 Minh Y. C., 2016, *J. Phys. Conf. Ser.*, 728, 052007  
 Minh Y. C., Irvine W. M., McGonagle D., Ziurys L. M., 1990, *ApJ*, 360, 136  
 Neufeld D. A., Wolfire M. G., Schilke P., 2005, *ApJ*, 628, 260  
 Oya Y., Sakai N., López-Sepulcre A., Watanabe Y., Ceccarelli C., Lefloch B., Favre C., Yamamoto S., 2016, *ApJ*, 824, 88  
 Podio L. et al., 2015, *A&A*, 581, A85  
 Prasad S. S., Tarafdar S. P., 1983, *ApJ*, 267, 603  
 Ruaud M., Wakelam V., Hersant F., 2016, *MNRAS*, 459, 3756  
 Sakai N. et al., 2014, *Nature*, 507, 78  
 Schöier F. L., Jørgensen J. K., van Dishoeck E. F., Blake G. A., 2002, *A&A*, 390, 1001  
 Sutton E. C., Peng R., Danchi W. C., Jaminet P. A., Sandell G., Russell A. P. G., 1995, *ApJS*, 97, 455  
 Tieftrunk A., Pineau des Forets G., Schilke P., Walmsley C. M., 1994, *A&A*, 289, 579  
 van der Tak F. F. S., 2004, in Burton M. G., Jayawardhana R., Bourke T. L., eds, *Proc. IAU Symp. Vol. 221, Star Formation at High Angular Resolution*. Kluwer, Dordrecht, p. 59  
 Vidal T. H. G., Loison J.-C., Jaziri A. Y., Ruaud M., Gratier P., Wakelam V., 2017, *MNRAS*, 469, 435  
 Viti S., Caselli P., Hartquist T. W., Williams D. A., 2001, *A&A*, 370, 1017  
 Wakelam V., Herbst E., 2008, *ApJ*, 680, 371  
 Wakelam V., Castets A., Ceccarelli C., Lefloch B., Caux E., Pagani L., 2004a, *A&A*, 413, 609  
 Wakelam V., Caselli P., Ceccarelli C., Herbst E., Castets A., 2004b, *A&A*, 422, 159  
 Wakelam V., Hersant F., Herpin F., 2011, *A&A*, 529, A112  
 Wakelam V., Vastel C., Aikawa Y., Coutens A., Bottinelli S., Caux E., 2014, *MNRAS*, 445, 2854  
 Wakelam V. et al., 2015a, *ApJS*, 217, 20  
 Wakelam V., Loison J.-C., Hickson K. M., Ruaud M., 2015b, *MNRAS*, 453, L48  
 Woods P. M., Occhiogrosso A., Viti S., Kaňuchová Z., Palumbo M. E., Price S. D., 2015, *MNRAS*, 450, 1256

This paper has been typeset from a  $\text{\LaTeX}$  file prepared by the author.



# On the reservoir of sulphur in dark clouds: chemistry and elemental abundance reconciled

Thomas H. G. Vidal,<sup>1</sup>★ Jean-Christophe Loison,<sup>2,3</sup> Adam Yassin Jaziri,<sup>1</sup>  
Maxime Ruaud,<sup>1</sup> Pierre Gratier<sup>1</sup> and Valentine Wakelam<sup>1</sup>

<sup>1</sup>Laboratoire d'astrophysique de Bordeaux, Univ. Bordeaux, CNRS, B18N, allée Geoffroy Saint-Hilaire, F-33615 Pessac, France

<sup>2</sup>Univ. Bordeaux, ISM, UMR 5255, F-33400 Talence, France

<sup>3</sup>CNRS, ISM, UMR 5255, F-33400 Talence, France

Accepted 2017 March 31. Received 2017 March 31; in original form 2016 June 28

## ABSTRACT

Sulphur-bearing species are often used to probe the physical structure of star-forming regions of the interstellar medium, but the chemistry of sulphur in these regions is still poorly understood. In dark clouds, sulphur is supposed to be depleted under a form that is still unknown despite numerous observations and chemical modelling studies that have been performed. In order to improve the modelling of sulphur chemistry, we propose an enhancement of the sulphur chemical network using experimental and theoretical literature. We test the effect of the updated network on the outputs of a three-phases gas–grain chemical model for dark cloud conditions using different elemental sulphur abundances. More particularly, we focus our study on the main sulphur reservoirs as well as on the agreement between model predictions and the abundances observed in the dark cloud TMC-1 (CP). Our results show that depending on the age of the observed cloud, the reservoir of sulphur could either be atomic sulphur in the gas phase or HS and H<sub>2</sub>S in icy grain bulks. We also report the first chemical model able to reproduce the abundances of observed S-bearing species in TMC-1 (CP) using as elemental abundance of sulphur its cosmic value.

**Key words:** astrochemistry – methods: numerical – stars: formation – ISM: abundances – ISM: clouds – ISM: molecules.

## 1 INTRODUCTION

Since the first detection of an S-bearing molecule in the interstellar medium (CS; Penzias et al. 1971), sulphur has become a subject of interest for many astrochemists. S-bearing molecules are indeed often used to probe the physical structure of star-forming regions (Lada, Bally & Stark 1991; Plume et al. 1997; Viti et al. 2001; Sakai et al. 2014; Podio et al. 2015) and have been proposed as chemical clocks for hot cores (Charnley 1997; Hatchell et al. 1998; Wakelam et al. 2004). But sulphur chemistry in the dense interstellar medium has also been at the centre of a puzzling issue for many years, namely the sulphur depletion problem (Ruffle et al. 1999). Unlike most of the other elements, in the diffuse medium, the gas-phase abundance of atomic sulphur is observed to be constant with cloud density, around its cosmic value of a few 10<sup>−5</sup> (see for instance Jenkins 2009). However, in dark clouds the total abundance of detected S-bearing molecules only accounts for 0.1 per cent of the cosmic abundance of atomic sulphur (Tieftrunk et al. 1994; Charnley 1997). Therefore, the main reservoirs of sulphur in dark clouds are still un-

known. One could argue that sulphur is in its atomic form, that is, non-observable. However, assuming an elemental abundance of sulphur in chemical models as high as its cosmic value produces predicted abundances of observable S-bearing molecules much higher than the observed one. Consequently, modellers usually assume that the elements (sulphur but other heavy elements as well) are depleted compared to their cosmic reference values and they use the so-called depleted abundance of sulphur of a few 10<sup>−8</sup> (Wakelam & Herbst 2008).

The main hypothesis to explain this missing sulphur is that it is depleted on to interstellar grains. In cometary ices, which are thought to present chemical similarities with the ices processed during hot core formation (Irvine et al. 2000), H<sub>2</sub>S is the most abundant S-bearing molecule, at the level of 1.5 per cent compared to water (Bockelée-Morvan et al. 2000). More recently, Holdship et al. (2016) studied the properties of H<sub>2</sub>S in the low-mass protostar L1157-B1 and found that a significant fraction of the sulphur is likely to be locked into the form of H<sub>2</sub>S on the grains. Chemical models also predict that, in the dense interstellar medium, atomic sulphur would stick on grains and be mostly hydrogenated to form H<sub>2</sub>S. To this day, however, only OCS (Palumbo, Geballe & Tielens 1997) and SO<sub>2</sub> (Boogert et al. 1997) have been likely identified

\* E-mail: [thomas.vidal@u-bordeaux.fr](mailto:thomas.vidal@u-bordeaux.fr)

in icy grain bulks in dense molecular clouds surrounding high-mass protostars and their estimated total abundance does not account for the missing sulphur. Upper limits for the column density of  $\text{H}_2\text{S}$  in icy grain bulks have been derived by Smith (1991), notably towards the line of sight of three late-type field stars lying behind the Taurus dark cloud, but these are also too low for  $\text{H}_2\text{S}$  to be the reservoir of sulphur in dark clouds.

Laboratory experiments coupled with chemical models have recently brought new insight into the problem by studying the irradiation of  $\text{H}_2\text{S}$  interstellar ice analogues by energetic protons and UV photons by Garozzo et al. (2010) and Jiménez-Escobar & Muñoz Caro (2011). Both studies found that solid  $\text{H}_2\text{S}$  was easily destroyed to form other species such as OCS,  $\text{SO}_2$ ,  $\text{CS}_2$  and  $\text{H}_2\text{S}_2$ . Subsequently, a corresponding network was proposed by Druard & Wakelam (2012) to reproduce these experiments but the authors showed that sulphur was converted into other forms, mostly  $\text{H}_2\text{S}_2$  and  $\text{H}_2\text{S}_3$ , at higher temperatures ( $> 20$  K) than those found in dark clouds (around 10 K).

In this paper, we propose an enhancement of the sulphur chemical network for dark cloud simulations motivated by the recent observations of HNCS and HSCN in TMC-1 (CP) (Adande et al. 2010) and of  $\text{CH}_3\text{SH}$  in IRAS 16293–2422 (Majumdar et al. 2016). Our network also includes the network proposed by Druard & Wakelam (2012). We test the effect of the updated network on the outputs of a gas–grain chemical model for dark cloud conditions using different sulphur elemental abundances. More particularly, we focus our study on the main sulphur reservoirs as well as on the agreement between model predictions and the abundances observed in the dark cloud TMC-1 (CP). The gas–grain model we used as well as the modifications of the chemical network are presented in Sections 2 and 3. Sections 4 and 5 describe our new modelling results and include comparisons with the previous version of the network as well as comparisons with observations in the dark cloud TMC-1 (CP). We discuss and conclude on our results in the last section.

## 2 MODEL

The model we use to assess the impact of our new network on the predicted S-bearing species abundances of dark clouds, is the latest version of the NAUTILUS chemical model, described in Ruaud, Wakelam & Hersant (2016). This model allows us to compute the evolution of chemical abundances for a given set of physical and chemical parameters. Recently updated, it simulates a three-phases chemistry including gas-phase, grain surface and grain bulk chemistries, along with the possible exchanges between the phases. These exchanges are: the adsorption of gas-phase species on to grain surfaces, the thermal and non-thermal desorption of species from the grain surface into the gas phase and the surface-bulk and bulk-surface exchange of species. Our reference model for this paper uses the formulation of chemical desorption processes depicted in Garrod, Wakelam & Herbst (2007). They consider that for each surface reactions leading to a single product, a part of the energy released by the reaction can contribute to the desorption of the product in the gas phase using the Rice–Ramsperger–Kessel theory. The fraction of the product desorbed in the gas phase depends on the binding energy of the product to the surface, the enthalpy of the reaction and the fraction of the released energy that is lost to the surface. In our case, we use an  $\alpha$  parameter of 0.001, which produces approximately a 1 per cent efficiency evaporation for all species. Moreover, the grain chemistry takes into account the standard direct photodissociation by UV photons along with the photodissociation induced by secondary UV photons introduced by Prasad & Tarafdar

**Table 1.** Initial abundances.

Element	$n_i/n_{\text{H}}^a$	References
$\text{H}_2$	0.5	
He	0.09	1
N	6.2(−5)	2
O	2.4(−4)	3
$\text{C}^+$	1.7(−4)	2
$\text{S}^+$	8.0(−8)	4
$\text{Si}^+$	8.0(−9)	4
$\text{Fe}^+$	3.0(−9)	4
$\text{Na}^+$	2.0(−9)	4
$\text{Mg}^+$	7.0(−9)	4
$\text{P}^+$	2.0(−10)	4
$\text{Cl}^+$	1.0(−9)	4
F	6.7(−9)	5

<sup>a</sup> $a(b)$  stands for  $a \times 10^b$ .

References: (1) Wakelam & Herbst (2008), (2) Jenkins (2009), (3) Hincelin et al. (2011), (4) low metal abundances from Graedel, Langer & Frerking (1982) and (5) depleted value from Neufeld, Wolfire & Schilke (2005).

(1983). These processes are effective on the surface as well as in the bulk of the grains. The model also takes into account the newly implemented competition between reaction, diffusion and evaporation as suggested by Chang, Cuppen & Herbst (2007) and Garrod & Pauly (2011). The diffusion energies of each species are computed as a fraction of their binding energies. We take for the surface a value of this ratio of 0.4 as suggested by experiments and theoretical work made on H (see Ruaud et al. 2016, and reference therein), CO and  $\text{CO}_2$  (see Karssemeijer & Cuppen 2014). This value is then extrapolated to every species on the surface. For the bulk, we take a value of 0.8 (see also Ruaud et al. 2016). The reference (gas phase and grains) network is *kida.uva.2014* (see Wakelam et al. 2015a), the same one as in Ruaud et al. (2016).

The set of physical parameters used throughout this paper is the commonly used dark cloud parameter configuration, namely a gas and dust temperature of 10 K, an atomic hydrogen total density of  $2 \times 10^4 \text{ cm}^{-3}$ , a cosmic ionization rate of  $1.3 \times 10^{-17} \text{ s}^{-1}$  and a visual extinction of 15 mag. All abundances are expressed with respect to the total H density. Our set of initial abundances is summarized in Table 1. We start with all species in their atomic (or ionized) form, except for hydrogen which is assumed to be entirely in its molecular form.

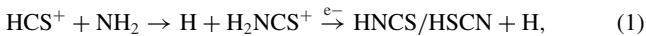
## 3 MODIFICATION OF THE SULPHUR NETWORK

To update the sulphur chemistry network, we first examine the existing KIDA network (*kida.uva.2014*; Wakelam et al. 2015a) looking systematically at the possible reactions between S and  $\text{S}^+$  with the most abundant species in dense molecular clouds ( $\text{CO}$ ,  $\text{CH}_4$ ,  $\text{C}_2\text{H}_2$ ,  $\text{c-C}_3\text{H}_2$ ) as well as the potential reactions between sulphur compounds and the most abundant reactive species in molecular clouds ( $\text{C}$ ,  $\text{C}^+$ , H, N, O, OH, CN). We found that various neutral reactions were missing from KIDA (or other data bases) such as  $\text{C} + \text{H}_2\text{S}$ ,  $\text{C} + \text{H}_2\text{CS}$  and  $\text{S} + \text{l,c-C}_3\text{H}$ . When previous experimental or theoretical studies exist, we use them to update the KIDA data base when necessary. However, there are relatively few kinetics data for the reactions of sulphur compounds. To estimate the unknown rate



constants to be used in the network, we use a methodology developed in appendix A (see supplementary material online) including new DFT and ab-initio calculations on the reactions  $\text{H} + \text{CS}$ ,  $\text{H} + \text{H}_2\text{CS}$ ,  $\text{H} + \text{C}_2\text{S}$ ,  $\text{H} + \text{HNCS}$ ,  $\text{H} + \text{HSCN}$ ,  $\text{NH} + \text{CS}$ ,  $\text{NH}_2 + \text{CS}$ ,  $\text{C}_2\text{H}_3 + \text{CS}$ ,  $\text{O} + \text{C}_3\text{S}$ ,  $\text{S} + \text{c-C}_3\text{H}_3^+$ ,  $\text{S} + \text{c-C}_3\text{H}_2$ ,  $\text{N} + \text{HCS}$ . All calculations have been performed for gas-phase reactions. The hydrogenation reaction barriers are used in the surface chemistry without changes. The rate constant of the  $\text{NH} + \text{CS}$ ,  $\text{NH}_2 + \text{CS}$ ,  $\text{C}_2\text{H}_3 + \text{CS}$ ,  $\text{O} + \text{C}_3\text{S}$  reactions are presented in appendix B (see supplementary material online). It should be noted that there are often large uncertainties on rate constant values and branching ratios for the sulphur chemical network. This is particularly true for the branching ratios of dissociative recombination (DR). Most of them are deduced from general rules, developed in appendix A, by analogy with similar oxygenated compounds, but DR of  $\text{HCS}^+$  leads mainly to  $\text{S} + \text{CH}$  (Montaigne et al. 2005), while DR of  $\text{HCO}^+$  leads mainly to  $\text{H} + \text{CO}$  (Hamberg et al. 2014). This may be critical for  $\text{H}_2\text{CS}$  (and also  $\text{HC}_3\text{S}$ ) production if DR of  $\text{CH}_3\text{SH}^+$  leads mainly to C-S bond breaking in contrast to DR of  $\text{CH}_2\text{OH}^+$  which preserves the C-O bond (Hamberg et al. 2007).

In this work, we introduce three isomers for HNCS (HNCS, HSCN, HCNS) and five for the protonated forms. We use the work of Gronowski & Kolos (2014) to describe the ionic chemistry but, unlike them, we do not consider the  $\text{CSH}^+$  isomer but only the  $\text{HCS}^+$  one. Indeed, the  $\text{CSH}^+ \rightarrow \text{HCS}^+$  isomerization barrier is only  $5.4 \text{ kJ mol}^{-1}$  (Puzzarini 2005) and as the reaction producing  $\text{CSH}^+$  ( $\text{CS} + \text{H}_3^+$ ) is exothermic by  $78 \text{ kJ mol}^{-1}$ , most of the  $\text{CSH}^+$  should isomerize into  $\text{HCS}^+$ . The comparison with  $\text{HOC}^+$  is not relevant, as the  $\text{COH}^+/\text{HCO}^+$  isomerization barrier is equal to  $150 \text{ kJ mol}^{-1}$  (Nobes & Radom 1981). We carefully searched for other reactions producing HNCS isomers, performing various theoretical calculations on the H-H-C-N-S system. For the  $\text{NH}_2 + \text{CS}$  reaction, we found a small barrier ( $+3.0 \text{ kJ mol}^{-1}$ ) at the CCSD(T)/cc-pVQZ//MP2/cc-pVTZ level (this barrier being submerged by  $-2.4 \text{ kJ mol}^{-1}$  at the M06-2X/cc-pVTZ level but this method is thought to be less precise and usually slightly underestimates barrier values). We calculate the rate constant for this reaction using the CCSD(T) values leading to a negligible value at low temperature. We also include various reactions on the grain surface. Indeed, it appears that the s-N + s-HCS reaction is, alongside the following reaction mechanism:



the main source of HNCS isomers. The first step of this reaction is very likely N-C bond formation without a barrier through the pairing up of free electrons of the N atom and the HCS radical leading to  $\text{HC(N)S}$  formation. This species is indeed the transition state linking HNCS and HSCN. The branching ratio between HNCS and HSCN formation can be deduced from statistical theory. HNCS/HSCN production is estimated to be proportional to the density of vibrational states of each isomer near the effective barrier to isomerization in a similar manner to  $\text{HCN}/\text{HNC}$  formation in DR of  $\text{HCNH}^+$  (Herbst, Terzieva & Talbi 2000). Using the MESMER program (Glowacki et al. 2012) for the calculations of the ro-vibrational density of states near the isomerization barrier (see appendix A).

For the loss reactions, we consider no barrier for the reactions of HNCS isomers with carbon atoms taking into account the high reactivity of carbon atoms with unsaturated closed shell molecules (see table 1 in Loison et al. 2014). We neglect the reactions of HNCS isomers with H, N and O atoms in the gas phase either from M06-2X/cc-pVTZ calculations (see appendix A) or by com-

**Table 2.** Table of the 46 S-bearing species added to the network.

Neutrals	
$\text{CS}_2$	HNCS
$\text{H}_2\text{S}_3^a$	HSCN
$\text{S}_3^a$	$\text{H}_2\text{C}_3\text{S}$
$\text{S}_4^a$	HNCHS
$\text{S}_5^a$	HSCHN
$\text{S}_6^a$	HNCSH
$\text{S}_7^a$	$\text{NH}_2\text{CHS}$
$\text{S}_8^a$	$\text{H}_2\text{C}_2\text{S}$
$\text{HC}_3\text{S}$	$\text{NH}_2\text{CS}$
$\text{HC}_2\text{S}$	$\text{NH}_2\text{CH}_2\text{S}$
$\text{CH}_3\text{S}$	$\text{NH}_2\text{CH}_2\text{SH}$
$\text{CH}_3\text{SH}$	HSO
$\text{CH}_2\text{SH}$	HNCHSH
HCNS	$\text{NH}_2\text{CHSH}$
Ions	
$\text{CS}_2^+$	$\text{HSCN}^+$
$\text{HCS}_2^+$	$\text{H}_2\text{CNS}^+$
$\text{H}_2\text{C}_2\text{S}^+$	$\text{H}_2\text{NCS}^+$
$\text{H}_2\text{C}_3\text{S}^+$	$\text{H}_2\text{SCN}^+$
$\text{CH}_3\text{S}^+$	$\text{HCNSH}^+$
$\text{CH}_3\text{SH}^+$	$\text{HNCSH}^+$
$\text{CH}_3\text{SH}_2^+$	$\text{CH}_3\text{CS}^+$
$\text{HCNS}^+$	$\text{NH}_2\text{CHSH}^+$
$\text{HNCS}^+$	$\text{NH}_3\text{CH}_2\text{SH}^+$

<sup>a</sup>These species are not allowed to evaporate in the gas phase (see text).

parison with similar reactions with HNCO isomers. For  $\text{He}^+$  and  $\text{H}^+$  reactions with HNCS isomers we consider, by comparison with similar reactions (Anicich 2003), a charge transfer mechanism as the main process leading to highly excited species followed by dissociation. For  $\text{C}^+$  reactions with HNCS isomers, the charge exchange is usually a minor channel (Anicich 2003). We consider then that these reactions lead mainly to the most exothermic exit channel involving the fewest steps. For protonation reactions, we use the work of Gronowski & Kolos (2014) leading to five  $\text{H}_2\text{NCS}^+$  isomers. The DR rate constant of the five  $\text{H}_2\text{NCS}^+$  isomers is assumed to be equal to the ion-electron collision rate estimated to be equal to  $3 \times 10^{-7} \times (T/300)^{-0.5}$  considering the size of the cations (Florescu-Mitchell & Mitchell 2006; Fournier et al. 2013). For the branching ratio of the DR of  $\text{H}_2\text{NCS}^+$  and  $\text{HNCSH}^+$ , a critical parameter for the HNCS/HSCN ratio, we follow the same procedure as used for the DR of  $\text{HCNH}^+$  (Herbst et al. 2000) using the MESMER program for the calculations of the ro-vibrational density of states near the isomerization barrier (see appendix A). Then, the DR reactions of  $\text{H}_2\text{NCS}^+$  and  $\text{HNCSH}^+$  leads to similar amounts of HNCS and HSCN.

Overall, we added (or reviewed in the case of reactions) 46 S-bearing species to the network along with 478 reactions in the gas phase, 305 reactions on the grain surface and 147 reactions in the grain bulk (see the table in appendix B). The newly introduced species are listed in Table 2. Among these species,  $\text{H}_2\text{S}_3$  and  $\text{S}_n$  ( $n = 3$  to 8) are only present on the grains, that is, they are formed on the surfaces and not allowed to evaporate (see also Druard & Wakelam 2012). At 10 K, these species are not efficiently formed so we do not want to add any gas-phase routes for these species as this chemistry is not known. It should be noted that our enhanced network includes the chemical schemes for carbon chains proposed

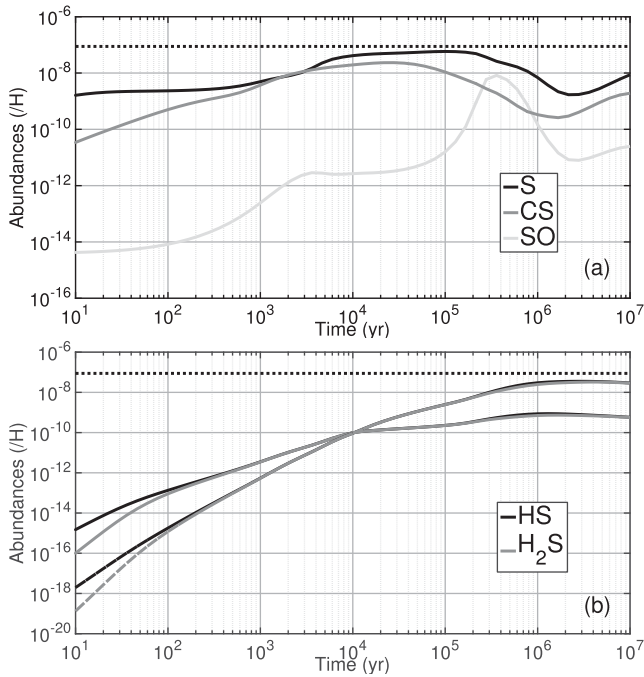


**Figure 1.** Abundances of main sulphur-bearing species relative to H as a function of time for dark cloud physical conditions: (a) in the gas phase, (b) on the grain surface (solid line) and bulk (dashed line). The dotted line represents the elemental abundance of sulphur (here,  $X_{\text{ini}} = 8 \times 10^{-8}$ ).

in Wakelam et al. (2015b), Loison et al. (2016), Hickson, Wakelam & Loison (2016b) and Loison et al. (in preparation).

#### 4 IMPACT OF THE NEW NETWORK ON THE CHEMICAL MODEL OF DARK CLOUDS

In this section, we highlight the impact of our enhanced sulphur network on the outputs of the NAUTILUS chemical code, configured for dark cloud physical conditions. We first present the abundance evolution of the most abundant sulphur-bearing species we obtain from the model in this configuration. Then we highlight our results on the newly implemented sulphur-bearing species. Finally, we compare the outputs obtained with our new network with those obtained with the nominal network for the same model configuration.

##### 4.1 Abundances of the main sulphur-bearing species

In the following, we study the abundances of the main sulphur-bearing species obtained with our enhanced network, both in the gas phase and on the grains. We choose these species since they contain more than 5 per cent of the elemental sulphur at one point in our simulation.

###### 4.1.1 Main gas-phase species: S, CS and SO

Fig. 1(a) shows the time evolution of the main sulphur-bearing species in the gas phase: atomic sulphur (S), carbon monosulphide (CS) and sulphur monoxide (SO). In our simulation, sulphur is initially in the form of  $\text{S}^+$  and between  $7.7 \times 10^3$  and  $4.6 \times 10^5$  yr, S becomes the main sulphur reservoir (including species on grains). During this period, its abundance reaches a maximum at  $10^5$  yr when it contains up to 73 per cent of the elemental sulphur. The growth of the atomic S abundance up to this maximum seems to be

mainly caused by the electronic recombination mechanisms of  $\text{S}^+$ , as well as of  $\text{CS}^+$  and  $\text{HCS}^+$ . The last two are related to  $\text{S}^+$  by the following reaction mechanism:

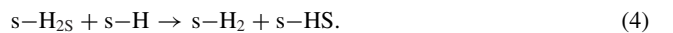


This mechanism is therefore very efficient because CH is rapidly formed by electronic recombination of  $\text{CH}_2^+$  which is itself formed by the ion-neutral reaction between elemental species  $\text{C}^+$  and  $\text{H}_2$ . Later, S is consumed by reactions with  $\text{H}_3^+$ ,  $\text{CH}_3$ , OH and  $\text{O}_2$ , which efficiently produce SO causing the peak in its abundance at  $3.6 \times 10^5$  yr. The CS abundance follows closely the atomic sulphur one, first growing from numerous reactions, including notably the electronic recombination of  $\text{HCS}^+$ ,  $\text{C}_2\text{S}^+$  and  $\text{HC}_3\text{S}^+$  and destruction of  $\text{C}_2\text{S}$  and by atomic carbon. It reaches a maximum between  $10^4$  and  $10^5$  yr, becoming the second main reservoir of sulphur, containing up to 29 per cent of the initial sulphur. However, CS does not accumulate, in contrast to CO, as the hydrogenation of CS followed by DR of  $\text{HCS}^+$  produce much more  $\text{S} + \text{CH}$  than  $\text{H} + \text{CS}$  (Montaigne et al. 2005).

It should be noted that we cannot reproduce the observed CS/ $\text{HCS}^+$  ratio for TMC-1 of 26 (Gratier et al. 2016) at early time but the agreement become better, if not perfect, for longer age. Although  $\text{HCS}^+$  and CS are linked through protonation reaction and DR, other reactions are involved in the chemistry of these species. Before  $4.6 \times 10^3$  yr, CS is mainly formed by DR of  $\text{HCS}^+$  and  $\text{HCS}^+$  is formed by reaction 2. At longer time neutral reactions such as  $\text{S} + \text{CH} \rightarrow \text{CS} + \text{H}$  plays also a role. Comparing our model results with the observed abundance of CS of  $6.5 \times 10^{-9}$  (Gratier et al. 2016), the problem is very likely an overestimation of the CS abundance, which can come from wrong branching ratios of the  $\text{HCS}^+$  DR (we currently use the measured values from Montaigne et al. 2005), wrong observational estimations of CS (for example, underestimation of CS due to saturation of CS lines), or an additional loss not producing  $\text{HCS}^+$ . A potentially new sink for CS may be the  $\text{O} + \text{CS}$  reaction. We currently use the rate from Lilenfeld & Richardson (1977) determined in the 150–300 K range leading to a negligible rate at 10 K. However, the work of Gonzalez et al. (1996) may suggest a non-negligible rate at low temperature.

###### 4.1.2 Main species on grains: HS and $\text{H}_2\text{S}$

On the grains, it appears that the most abundant species are the hydrosulphide radical (HS) and hydrogen sulphide ( $\text{H}_2\text{S}$ ). The abundances of those species, both on the surface (solid line) and in the bulk (dashed line), are depicted in Fig. 1(b). At times prior to 100 years, both species are formed on the surface by the successive hydrogenation of atomic sulphur physisorbed on the grains. Once the species are formed, they begin to sink into the bulk. After a hundred years, both species continue to form on the surface and eventually enter into a loop created by the two following reactions:



Reaction (4) has a barrier and should not be efficient under dark cloud physical conditions. However, it becomes efficient in our model because of the reaction-diffusion competition whose main effect is to increase the rates of reactions with activation barrier through tunnelling (Ruud et al. 2016). Therefore, this cycle enabled by the reaction-diffusion competition and supplied in HS by the hydrogenation of S on the grains, keeps increasing at equal rates

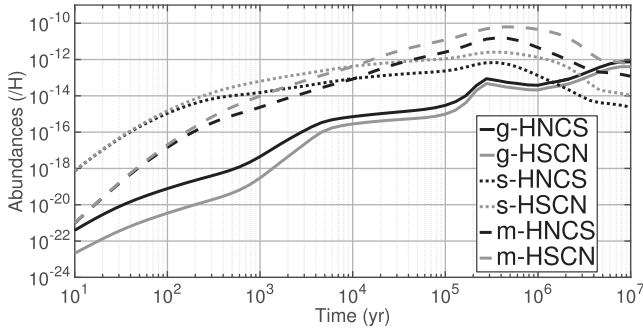


**Figure 2.** Abundances of HNCS (black) and HSCN (grey) relative to H as a function of time for dark cloud physical conditions in the gas phase (solid line), on the grain surface (dotted line) and in the grain bulk (dashed line).

the abundances of the two species during the rest of the simulation. For this model, we have assumed a barrier of  $E_a = 860$  K but there remains uncertainties in this value. The gas-phase reaction  $H + H_2S$  has been measured in a wide range of temperature from 190 up to 2237 K (Kurylo, Peterson & Braun 1971; Peng, Hu & Marshall 1999; Yoshimura et al. 1992). The rate constant shows strong non-Arrhenius behaviour at low temperature likely due to the importance of tunnelling. Peng et al. (1999) performed theoretical calculations of the barrier of the reaction equal to 1330 at DFT level and 1930 K at QCISD(T) level. Considering these uncertainties, we have used the experimental value of Kurylo et al. (1971), which is the one measured at the lower temperature (in the 190–464 K range). We also tested the higher values by Peng et al. (1999) but it did not change significantly the results shown in this paper.

As HS and  $H_2S$  keep on sinking into the bulk, their abundances in the latter eventually becomes higher than at the surface. At approximately  $6 \times 10^5$  yr and until  $10^7$  yr, HS and  $H_2S$  (in the bulk) are the main reservoirs of sulphur, sharing more than 80 per cent of the initial sulphur nearly equally divided between the two species, with a slight excess for HS. It should be noted that during this period of time, the 20 per cent of the initial sulphur remaining is mostly divided between atomic S in the gas phase and in the bulk, as well as NS in the bulk.

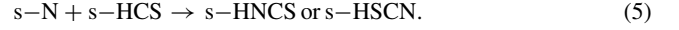
## 4.2 Abundances of the newly implemented S-bearing species

Our enhanced sulphur network includes the addition of 45 new S-bearing species. Among those species, we now present the results of our calculations for HNCS, the species around which most of our new network has been built, and  $CH_3SH$ , which was recently detected in the envelope of the low-mass protostar IRAS 16293–2422 (Majumdar et al. 2016).

### 4.2.1 HNCS and HSCN

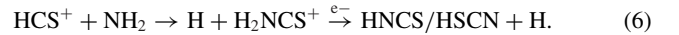
Isothiocyanic acid HNCS is the most stable among possible CHNS isomers. It has been very well studied since its first detection in Sgr B2 by Frerking, Linke & Thaddeus (1979), and has since been detected in the dark cloud TMC-1 (CP) (Adande et al. 2010). In contrast, thiocyanic acid HSCN is highly unstable and is about a factor of 3 less abundant in Sgr B2 than HNCS (Halfen et al. 2009), and has been also detected in TMC-1 (CP) with a similar abundance to HNCS (Adande et al. 2010). Fig. 2 shows the time evolution of their abundances in the three phases of the model (in the gas phase, on the grain surface and in the grain bulk) for dark cloud conditions. It should be noted that our network for HNCS and

HSCN is an improved version of the one proposed in Gronowski & Kolos (2014), which itself is a revised version of the network proposed in Adande et al. (2010). It appears from our simulations that both species are essentially produced at the surface of the grains where their main formation reaction is

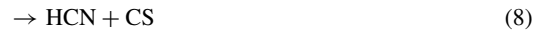
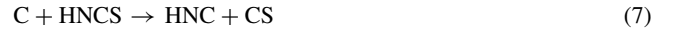


HNCS and HSCN abundances on the grain surface are also regulated by hydrogenation loops similar to the one described in Section 4.1.2: for HNCS with HNCSH and  $NH_2CS$ , and for HSCN with HNCSH and HSCHN. It should be noted that the hydrogenation of HSCN is calculated to be much less efficient than the hydrogenation of HNCS (see appendix A). At times  $> 2.8 \times 10^5$  yr, as less and less atomic N is available, abundances of both species decrease on the surface. For HNCS, it happens through the chemical desorption of the products of its hydrogenation, HNCSH and  $NH_2CS$ . For HSCN, it happens through its successive hydrogenations. Moreover, as the chemistry of both species is not efficient in the bulk, its abundance increase in this phase is primarily due to sinking from the surface.

In the gas phase, HNCS and HSCN abundances increase efficiently from chemical desorption from the grains following reaction (5), as well as from the following reaction mechanism:



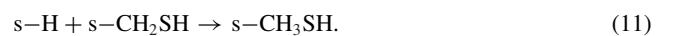
Consequently, after  $2.8 \times 10^5$  yr, as reaction (5) is less efficient because there is less N available, reaction (6) then becomes the main formation pathway of HNCS and HSCN in the gas phase. They are also predicted to be efficiently destroyed by atomic C via:



The depletion of atomic C on grains after  $10^5$  yr then explains the increase in the gas-phase abundance gradients for both species at this time.

### 4.2.2 $CH_3SH$

Numerous previous detections of methyl mercaptan  $CH_3SH$  in hot cores such as Sgr B2 (Linke, Frerking & Thaddeus 1979), G327.3–0.6 (Gibb et al. 2000) and Orion KL (Kolesniková et al. 2014) suggest that this species initially forms in the ices and then evaporates in hot cores. More recently, Majumdar et al. (2016) presented the detection of  $CH_3SH$  in IRAS 16293–2422 and proposed an associated chemical network to explain its observed abundance. This work is included in our enhanced sulphur network and has been completed, notably regarding grain chemistry. Fig. 3 shows the time evolution of the  $CH_3SH$  abundance. It appears from our results that  $CH_3SH$  is mainly formed on the grain surface and is released into the gas phase by chemical desorption in dark cloud conditions. The main formation processes on the grains are:



Moreover, similarly to HNCS, it seems that  $CH_3SH$  chemistry in the grain bulk is relatively inert, which throughout the simulation explains its accumulation in this phase from sinking from the grain surface.



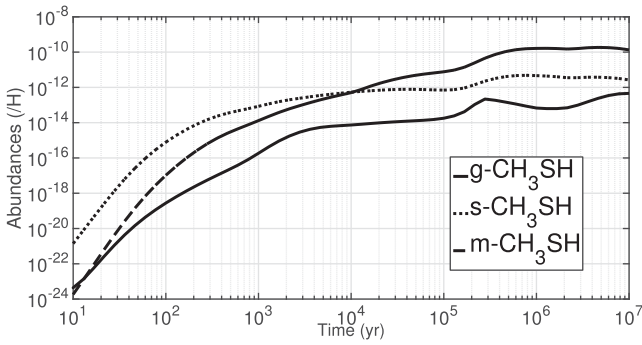


**Figure 3.** Abundance of  $\text{CH}_3\text{SH}$  relative to H as a function of time for dark cloud physical conditions in the gas phase (solid line), on the grain surface (dotted line) and in the grain bulk (dashed line).

As said above, the gas-phase chemistry of  $\text{CH}_3\text{SH}$  is essentially ruled by its chemical desorption from the grain surface during the entire simulation. As for  $\text{HNCS}$ , it should be noted that it is consumed by atomic C at times  $< 2.8 \times 10^5$  yr following:



However, after this time, in contrast to  $\text{HNCS}$ , gas-phase  $\text{CH}_3\text{SH}$  is still produced from grain surface chemistry and chemical desorption, which can be explained by the fact that the CS abundance in the gas phase remains high, and gradually depletes to form  $\text{CH}_3\text{SH}$  through successive hydrogenations. Moreover, as the hydrogen atom abundance remains relatively constant on the grain surface during the simulation, due to cosmic ray interactions with  $\text{H}_2$ ,  $\text{CH}_3\text{SH}$  is efficiently produced in contrast to  $\text{HNCS}$  and  $\text{HSCN}$  as nitrogen atomic strongly decreases.

### 4.3 Comparison with the previous version of the network

We now highlight the differences between the nominal model (hereafter Model A) and Model B, which takes into account our enhanced sulphur network. It should be noted that Model A already includes the reactions between HS and  $\text{H}_2\text{S}$  studied in Section 4.1.2, as well as the reaction–diffusion competition mechanism, two key parameters for sulphur chemistry. As our calculations show that numerous S-bearing species are impacted by the changes we made to the network, we present here only a selection of these species ( $\text{C}_3\text{S}$ ,  $\text{H}_2\text{CS}$ ,  $\text{HCS}$ ,  $\text{H}_2\text{S}$ , HS and SO). We selected these molecules because they present a difference between Models A and B of more than one order of magnitude in the time period between  $10^5$  and  $10^6$  yr and because their abundances rise above  $10^{-12}$  during this period. Indeed, the estimated ages of well-studied dark clouds such as TMC-1 or L134N are thought to correspond to this time period (see discussion in Agúndez & Wakelam 2013). Hence, an abundance of  $10^{-12}$  is considered as the detection limit for species in the gas phase.

#### 4.3.1 $\text{C}_3\text{S}$

Fig. 4 shows the comparison of the abundances of  $\text{C}_3\text{S}$  calculated for Models A and B, both in the gas phase and in the grain bulk. It can be seen that our new network induces differences for this species that can reach up to two orders of magnitude in the gas phase and four orders of magnitude in the grain bulk at times around  $10^5$  yr. In both models,  $\text{C}_3\text{S}$  is mainly formed in the gas phase by the reaction:

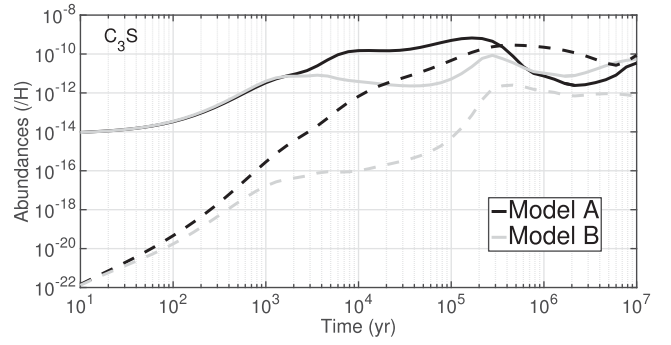


**Figure 4.** Comparison of the abundances of  $\text{C}_3\text{S}$  relative to H as a function of time for dark cloud physical conditions in the gas phase (solid line) and in the grain bulk (long dashed line).

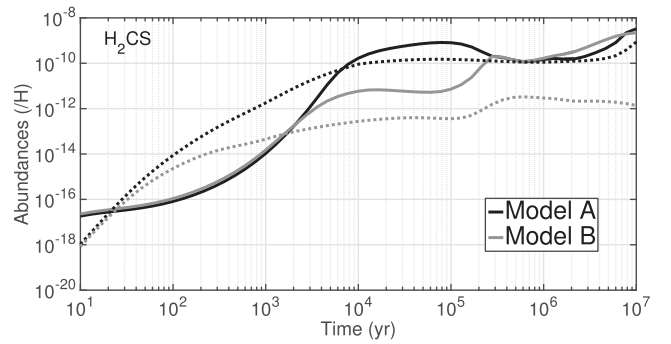


**Figure 5.** Comparison of the abundances of  $\text{H}_2\text{CS}$  relative to H as a function of time for dark cloud physical conditions in the gas phase (solid line) and on the grain surface (dotted line).

$\text{HC}_3\text{S}^+$  being efficiently produced through reactions of atomic sulphur with  $\text{c,l-C}_3\text{H}_2^+$  and  $\text{c,l-C}_3\text{H}_3^+$ . We thus consider that the decrease of its abundance in the grain bulk in Model B (as compared to Model A) is a direct result of its decrease in the gas phase. This decrease is due to the following added reaction:



This reaction becomes efficient in Model B at times  $> 10^3$  yr when the abundance of atomic C in the gas phase reaches  $10^{-4}$ . Finally, after  $10^4$  yr, while in Model A the abundance of  $\text{C}_3\text{S}$  continues to increase because of reaction (13), in Model B the small peak at  $2.8 \times 10^5$  yr is due to the reaction:



Reaction (15) becomes more efficient than reaction (14) at this time because depletion is more efficient for atomic carbon ( $\sim 10^5$  yr) than for atomic oxygen ( $\sim 8 \times 10^5$  yr). It should be noted that branching ratios for the DR of  $\text{HC}_3\text{S}^+$  are unknown and our network may overestimate  $\text{C}_3\text{S}$  production leading to an overestimation of its abundance.

#### 4.3.2 $\text{H}_2\text{CS}$

The abundance of  $\text{H}_2\text{CS}$  in the gas phase presents a similar change in its evolution between Models A and B (see Fig. 5). Its main reaction of formation in both models is the electronic recombination of  $\text{H}_3\text{CS}^+$ :



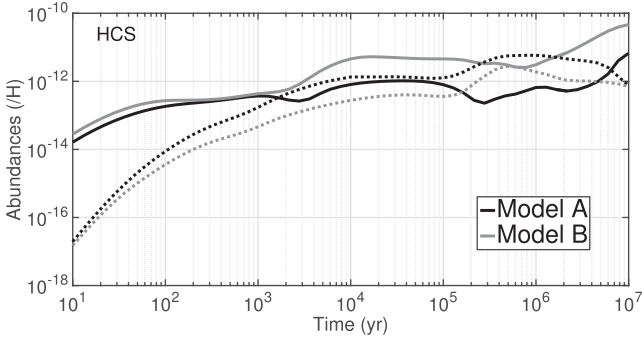


Figure 6. Same as Fig. 5 but for HCS.

$\text{H}_3\text{CS}^+$  being efficiently produced through  $\text{S}^+ + \text{CH}_4$  reaction.  $\text{H}_2\text{CS}$  is less efficiently formed in Model B after  $10^3$  yr because, like  $\text{C}_3\text{S}$ , it is consumed by atomic C via the following two reactions:



These reactions induce differences in the  $\text{H}_2\text{CS}$  abundance of more than two orders of magnitude between  $10^4$  and  $10^5$  yr. As atomic carbon is depleted on the grains, these reactions become less efficient after  $10^5$  yr and the abundance of  $\text{H}_2\text{CS}$  increases again through reaction (16).

In contrast to  $\text{C}_3\text{S}$ ,  $\text{H}_2\text{CS}$  is also efficiently formed on the grain surface in both models by the hydrogenation of HCS. However, in Model B, two hydrogenation processes of  $\text{H}_2\text{CS}$  have been added, which cause its abundance at the grain surface to drop compared to Model A by more than two orders of magnitude. Those processes are:



which also lead to the formation of  $\text{CH}_3\text{SH}$ . Moreover, as already noted, the branching ratios for the DR of  $\text{H}_3\text{CS}^+$  are unknown and may lead mainly to breaking of the C-S bond which will strongly limit the  $\text{H}_2\text{CS}$  abundance.

#### 4.3.3 HCS

Fig. 6 shows the time evolution of the HCS abundance in the gas phase in both Models A and B. We can see in this figure that the overall effect of our enhanced network on this species is to increase its abundance in the gas phase above the detection level of  $10^{-12}$ . This potential observability of HCS in dark clouds will be discussed later. In Model A, HCS is mainly formed by the two following reactions:



However, in Model B two new reactions show a higher HCS production efficiency. Those reactions are:

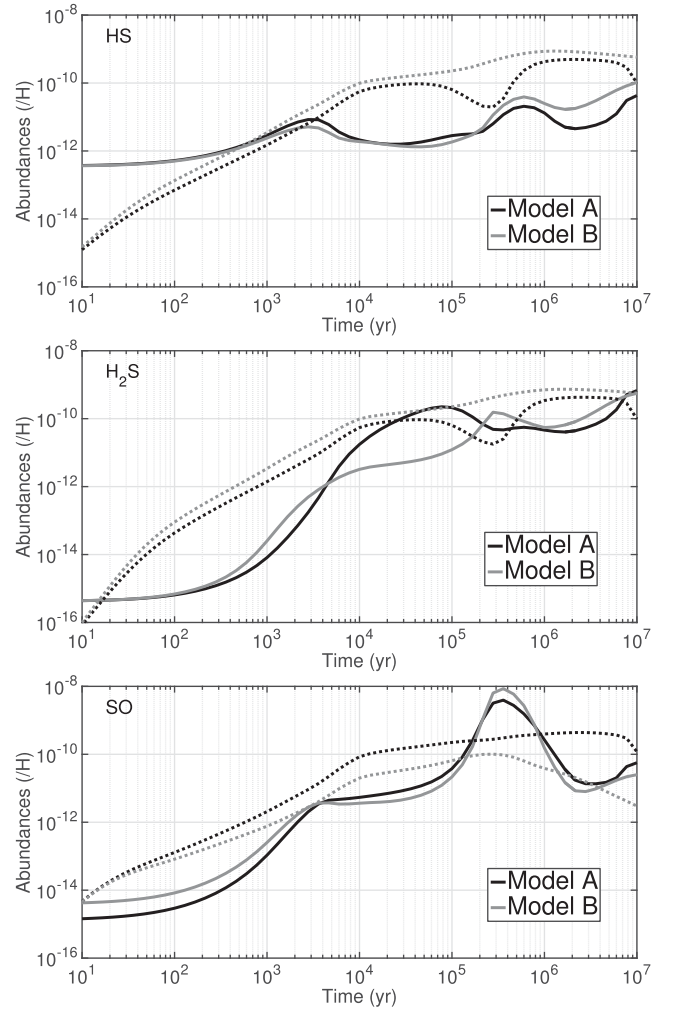


Figure 7. Comparison of the abundances of HS,  $\text{H}_2\text{S}$  and SO, relative to H as a function of time for dark cloud physical conditions in the gas phase (solid line) and on the grain surface (dotted line).

It should be noted that HCS is also formed at the grain surface by the hydrogenation of CS, and that its abundance in this phase is decreased in Model B because of numerous added reactions with atomic O and N, the latter forming the newly implemented species HNCS on the grains.

#### 4.3.4 HS, $\text{H}_2\text{S}$ and SO

We choose to describe the changes brought by our new model to HS,  $\text{H}_2\text{S}$  and SO abundances together, notably on the grain surface, because they are correlated.

On the one hand, in the gas phase, among those three species, the only one that presents a significant difference in Model B (compared to Model A) is  $\text{H}_2\text{S}$  (see Fig. 7). This difference (that reaches more than one order of magnitude) appears between  $5 \times 10^3$  and  $3 \times 10^5$  yr and is mainly due to the fact that reaction (24) slows down the increase of  $\text{H}_2\text{S}$  during this period of time. Besides this change, gas-phase  $\text{H}_2\text{S}$  is efficiently formed in both models on the grain surface by the hydrogenation of HS (reaction 4) enabled by the reaction–diffusion competition, followed by desorption.

On the other hand, our modifications of the network bring about a new reaction mechanism on the grain surface that causes several

**Table 3.** Observed abundances of S-bearing species in TMC-1 (CP).

Species	$n_i/n_H^a$	References
OCS	1.1(−9)	1
NS	4.0(−10)	2
CS	6.5(−9)	3
HCS <sup>+</sup>	2.5(−10)	3
H <sub>2</sub> CS	2.6(−9)	3
C <sub>2</sub> S	5.0(−9)	3
C <sub>3</sub> S	7.0(−10)	3
SO	1.0(−8)	4
SO <sub>2</sub>	1.5(−10)	5
HNCS	4.15(−12)	6
HSCN	6.3(−12)	6

<sup>a</sup> $a(b)$  stands for  $a \times 10^b$ .

References (1) Matthews et al. (1987), (2) McGonagle, Irvine &amp; Ohishi (1994), (3) Gratier et al. (2016), (4) Lique, Cernicharo &amp; Cox (2006), (5) Cernicharo et al. (2011) and (6) Adande et al. (2010).

changes to the abundances of HS, H<sub>2</sub>S and SO:



From Model A to Model B, the main effects of this reaction mechanism are:

- (i) to globally increase the grain surface abundance of HS because of the added path (26),
- (ii) to globally increase the grain surface abundance of H<sub>2</sub>S because of the loop described in Section 4.1.2, and hence its abundance in the gas phase (except during the time period described above),
- (iii) to globally decrease the grain surface abundance of SO which is, in our enhanced network, successively hydrogenated to form HSO then HS.

## 5 COMPARISON WITH OBSERVATIONS

In this section, we compare our modelling results with observations of sulphur bearing species in dense molecular clouds. We use the method of the so-called distance of disagreement described in Wakelam, Herbst & Selsis (2006) and which is computed as follows:

$$D(t) = \frac{1}{N_{\text{obs}}} \sum_i |\log[n(X)_{\text{obs},i}] - \log[n(X)_i(t)]|, \quad (27)$$

where  $n(X)_{\text{obs},i}$  and  $n(X)_i(t)$  are the observed abundances (relative to H) of the  $i$ th species and the modelled ones at time  $t$ , respectively.  $N_{\text{obs}}$  is the total number of observed species considered. The minimum of function  $D$  (hereafter noted  $D_{\text{min}}$ ) is then the minimum average difference (in magnitude) between modelled and observed abundances. We call the time for which this minimum is obtained the ‘best fit’ time (hereafter noted  $t_{\text{BF}}$ ), which consequently is the estimated age of the observed object according to the model.

We detail the observed abundances we use for S-bearing species in Table 3, and for other species we use table 4 of Agúndez & Wakelam (2013) and reference therein.

**Table 4.** Results of the comparison of Models A and B with observations in the dark cloud TMC-1 (CP).

Model	$D_{\text{min}}$	$t_{\text{BF}}$ (yr)	Fraction of reproduced molecules
A	0.908	$2.8 \times 10^5$	64 per cent
B	0.766	$2.8 \times 10^5$	67 per cent

### 5.1 Comparison with Models A and B

In order to validate our enhanced sulphur network, we compare the results of both Models A and B with the observations of the well-studied TMC-1 (CP) dark cloud for which numerous observational constraints are available. Indeed, more than 60 gas-phase species have been detected in this source, and upper limits on the abundance of 7 more are available (see a review of these species in Adande et al. 2010; Agúndez & Wakelam 2013). For the calculation of the corresponding distance of disagreement for both models, we take into account 58 of the 64 detected species because six of them are not implemented in one or either of the two networks (nominal and enhanced). Using equation (27), we find a similar level of agreement between Models A and B, with however a slightly better agreement with observations for Model B with  $D_{\text{min}} = 0.766$  (against  $D_{\text{min}} = 0.908$  for Model A), giving a ‘best fit’ time of  $2.8 \times 10^5$  yr, same as Model A. At this time, and assuming that the observed abundances were reproduced by the model when the difference between the two was smaller than one order of magnitude, the fractions of reproduced molecules are 64 and 67 per cent, respectively, for Model A and Model B. A summary of these results is shown in Table 4.

For both models, five of the nine S-bearing species taken into account in the comparison are reproduced: OCS, CS, C<sub>3</sub>S, SO and SO<sub>2</sub>, and Model B gives a slightly better agreement than Model A for these species. The similarity of the results comes from the fact that Model A includes the reaction–diffusion competition as well as the hydrogenation loop described in Section 4.1.2, both key parameters for sulphur chemistry. Moreover, considering only the 58 species taken into account in Model A, Model B reproduces only two more species than Model A which are carbon chains. However, the goal of this paper is to evaluate the efficiency of our enhanced network (Model B) to reproduce S-bearing species abundances, which should be done by considering all the species it takes into account. Therefore, we hereafter choose to exclude Model A from our study and focus only on Model B.

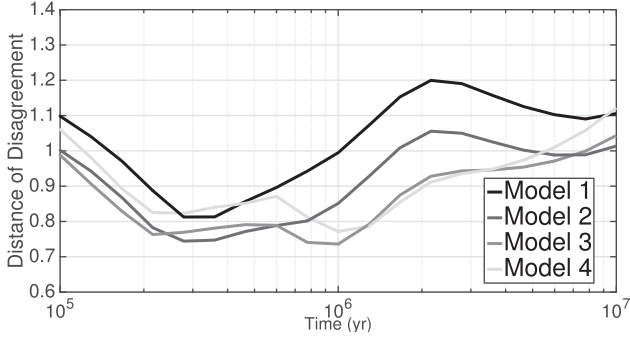
### 5.2 Variation of the elemental sulphur abundance

In order to assess the issue of sulphur depletion in chemical simulations of dark clouds with our enhanced network, we run the model for four different values of the elemental sulphur abundance and compare the results with observations to determine which one leads to better agreement with the observed species abundances. These values vary from the so-called depleted one ( $8 \times 10^{-8}$ ), which is commonly used by chemical models to reproduce observations and which we used previously in this paper, to the cosmic one ( $1.5 \times 10^{-5}$ ), which is considered to be the real elemental abundance of sulphur for dark cloud formation. The different values of the sulphur elemental abundances used and the labels of their associated models are summarized in Table 5. Apart from sulphur, the other species elemental abundances we use are those reported in Table 1.

In the following, we first compare for each model our calculated abundances of gas-phase species with those determined from the

**Table 5.** Set of elemental sulphur abundances.

Model	$n(S)_{\text{ini}}^a$
1	8(−8)
2	5(−7)
3	5(−6)
4	1.5(−5)

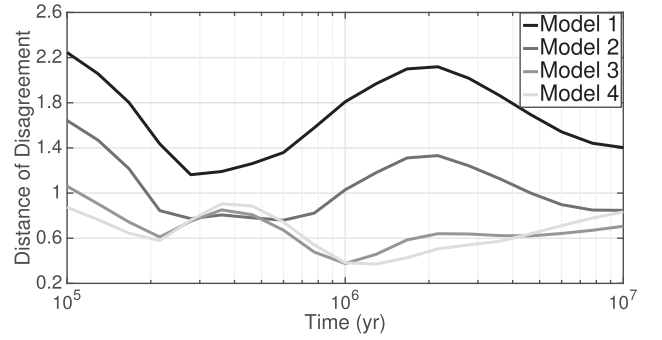
<sup>a</sup>  $a(b)$  stands for  $a \times 10^b$ .**Figure 8.** Comparison of the distances of disagreement for Models 1, 2, 3 and 4 considering 61 detected species in TMC-1 (CP).

well-studied dark cloud TMC-1 (CP). The only sulphur-bearing species observed on ice being OCS and SO<sub>2</sub> in the molecular cloud surrounding the deeply embedded protostar W33A, we then compare the modelled abundances of these species on the grains with the observed ones.

### 5.2.1 Comparison with all observed gas-phase species in TMC-1 (CP)

To assess the overall agreement of our enhanced network with observations, we compute the distance of disagreement for Models 1, 2, 3 and 4 with the 61 observed species that are taken into account in this network. Fig. 8 displays these distances of disagreement between 10<sup>5</sup> and 10<sup>7</sup> yr, the time period when the minimum values are reached. On the one hand, it appears that Model 3 is the best model in that it presents the distance of disagreement with the lowest minimum of  $D_3(t_{\text{BF}}) = 0.736$  with  $t_{\text{BF}} = 10^6$  yr which is still a reasonable estimated age for TMC-1 (CP). Moreover at that time, 44 of the 61 species considered (72 per cent) are reproduced by the model within a factor of 10. This result means that the elemental sulphur abundance which our new model theoretically needs to best reproduce the observations is around  $X(S)_{\text{ini}} = 5 \times 10^{-6}$ . Model 4 also reproduce 44 of the 61 species at its ‘best fit’ time but its minima of distance of disagreement is slightly higher than Model 3 (0.772).

On the other hand, Fig. 8 shows that the maximum difference between the distances of disagreement of the four models is lower than 0.3. Hence, for a given time, the average of the differences of abundances between two models (for a same species) is lower than a factor of 2. The distance of disagreement is thus not very sensitive to the elemental sulphur abundance. This result can be explained by the fact that among the 61 observed species we consider for the calculations, only 11 of them are S-bearing species.

**Figure 9.** Comparison of the distances of disagreement for Models 1, 2, 3 and 4 considering only the 11 detected S-bearing species in TMC-1 (CP).

### 5.2.2 Comparison with observed S-bearing gas-phase species in TMC-1 (CP)

Considering the low sensitivity of the distance of disagreement (61 observed species) to the elemental sulphur abundance and because our improvement of the network concerns mainly the sulphur chemistry, we also assess the efficiency of our enhanced network by checking its agreement with only the observations of the S-bearing species detected in TMC-1 (CP). Fig. 9 is the same as Fig. 8 but considering only the 11 detected S-bearing gas-phase species in TMC-1 (CP). Those species are OCS, NS, HCS<sup>+</sup>, CS, H<sub>2</sub>CS, CCS, C<sub>3</sub>S, SO, SO<sub>2</sub> (see Agúndez & Wakelam 2013, for a review), HNCS and HSCN (Adande et al. 2010). As expected, the distances of disagreement are much more sensitive to the elemental sulphur abundance than in the previous case, with differences going up to an average order of magnitude of 1.6 at some time steps. Moreover, the figure shows that the distance of disagreement for Models 1 and 2 never goes down to 0.7, whereas the other two present their minima under 0.4. Models 1 and 2 are therefore the ‘worst’ models, which means the depleted elemental sulphur abundance of  $8 \times 10^{-8}$  and  $5 \times 10^{-7}$  do not allow the model to reproduce the observations of S-bearing species with our enhanced network.

However, at the times of their respective minimums, Models 3 and 4 reproduce all the S-bearing molecules considered. Model 4 is the one that presents the distance of disagreement with the lowest minimum of  $D_4(t_{\text{BF}}) = 0.371$  with  $t_{\text{BF}} = 1.3 \times 10^6$  yr. Furthermore, Model 3 allows us to obtain a minimum of the distance of disagreement that is nearly equal to the one found for Model 4, namely  $D_3(t_{\text{BF}}) = 0.376$  with  $t_{\text{BF}} = 10^6$  yr. In both cases, the time of ‘best fit’ is in the acceptable range for the age of TMC-1 (CP). These results suggest that our model is able to reproduce the observations of S-bearing species in TMC-1 (CP) using the cosmic elemental abundance of sulphur  $X(S)_{\text{ini}} = 1.5 \times 10^{-5}$  or an abundance three times lower.

### 5.2.3 The case of HNCS and HSCN

As our enhanced network was mainly built around HNCS and its isomers, it is important to check that our results fit well with the observations of these species. Adande et al. (2010) identified the  $7_{0,7} \rightarrow 6_{0,6}$  and  $8_{0,8} \rightarrow 7_{0,7}$  transitions of HNCS and HSCN towards TMC-1 (CP) and were able to derive a corresponding ratio  $\frac{[\text{HNCS}]}{[\text{HSCN}]} = 1.4 \pm 0.7$  and abundances for HNCS and HSCN of, respectively,  $4.15 \times 10^{-12}$  and  $3 \times 10^{-12}$ . Fig. 10 shows the simulated abundances of HNCS and HSCN in the case of the cosmic elemental abundance for sulphur (Model 4) as well as their observed abundances in TMC-1 (CP) (horizontal dashed lines). At



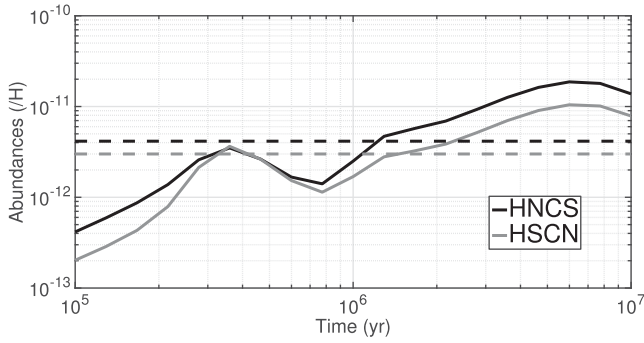


**Figure 10.** Comparison of the simulated gas-phase abundances of HNCS and HSCN with the observed ones in TMC-1 (CP) (horizontal dashed lines), relative to H.

$t_{\text{BF}} = 1.3 \times 10^6$  yr, we obtain a ratio of 1.68 that seems to fit well with the observed value. Moreover, the figure shows that at this time, the differences between the observed and calculated abundances of HNCS and HSCN are less than a factor 1.2 and 1.1, respectively, which confirms the efficiency of the network to model the chemistry of HNCS. It should be noted that Model 3 also allows us to reproduce well the observed abundance of HNCS and HSCN at  $t_{\text{BF}} = 10^6$  yr.

#### 5.2.4 Comparison with observed S-bearing species on grains towards W33A

Only two solid S-bearing species have been detected in icy grain bulks: OCS (Palumbo et al. 1997) and  $\text{SO}_2$  (Boogert et al. 1997). Both species have been detected towards the deeply embedded protostar W33A and we can therefore use the results of our models in the dark cloud configuration to compare with these observations. In order to do so, we have to compare for a given species its observed abundance ( $7 \times 10^{-8}$  and  $6.2 \times 10^{-7}$  for OCS and  $\text{SO}_2$ , respectively) with the sum of its simulated abundances on the grain surface and in the grain bulk. For both species, Fig. 11 displays the comparison between their simulated total abundances for our four models in icy grain bulks and their observed ones between  $10^5$  and  $10^7$  yr. The age of the giant molecular cloud W33 is indeed supposed to lie in that time frame (Messineo et al. 2015).

Fig. 11(a) shows that both Models 3 and 4 reproduce the observed abundance of OCS in icy grain bulks, at  $7.74 \times 10^5$  and  $2.15 \times 10^6$  yr, respectively. Moreover, considering the fact that most of the young stellar objects detected in W33 have an estimated age of a few million years (see e.g. Messineo et al. 2015), the most favoured model is Model 4. Regarding  $\text{SO}_2$ , Fig. 11(b) shows that the model for which its modelled abundance in icy grain bulks comes the closest to its observed one is Model 4. Both comparisons suggest once again that our enhanced network needs an elemental sulphur abundance close to the cosmic one in order to best reproduce the observations. Note that we assume here that the detections of OCS and  $\text{SO}_2$  ices are real although the two species are not in the list of ‘firmly detected’ species of Boogert, Gerakines & Whittet (2015). The *JWST* mission may give us more constraints on this matter.

### 5.3 Impacts of the use of the cosmic abundance of sulphur on the reservoirs

In Section 4, we studied the chemistry of the main S-bearing species using the elemental abundances listed in Table 1, more particularly

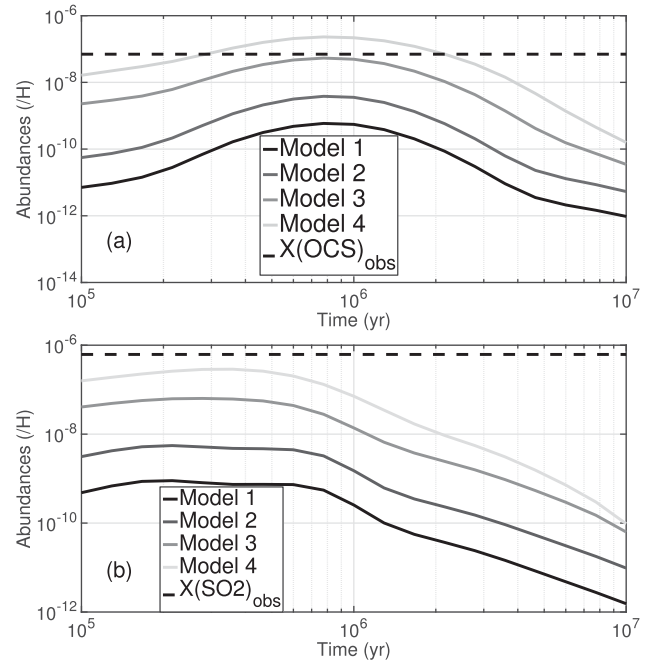


**Figure 11.** Comparison of the calculated abundances in icy grain bulks of OCS (a) and  $\text{SO}_2$  (b) for Models 1, 2, 3 and 4 (solid lines) with the observed one towards W33A (dashed lines).

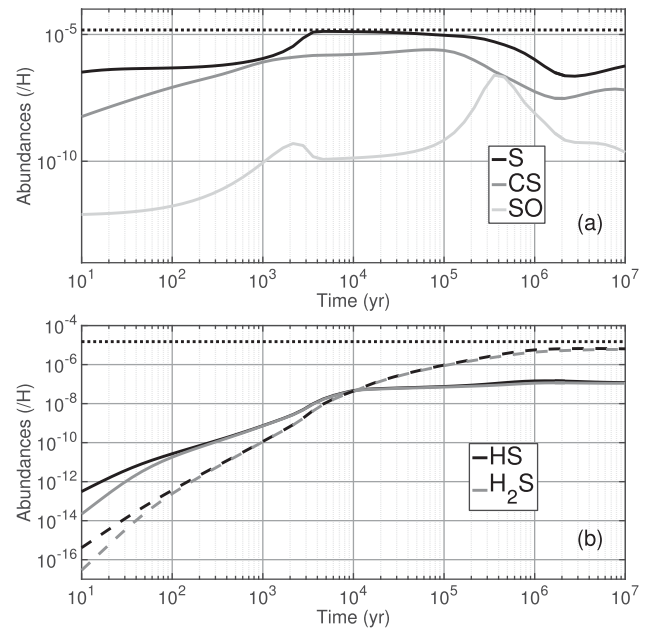


**Figure 12.** Abundances of main sulphur-bearing species relative to H as a function of time for dark cloud physical conditions: (a) in the gas phase, (b) on the grain surface (solid line) and bulk (dashed line). The dotted line represents the elemental abundance of sulphur (here,  $X_{\text{ini}} = 1.5 \times 10^{-5}$ ).

the depleted abundance of sulphur of  $X(\text{S})_{\text{ini}} = 8 \times 10^{-8}$ . Now that we determined that in order to reproduce S-bearing species observations in dark clouds, our model needs an elemental abundance of sulphur close to the cosmic one, we need to assess the impact of the use of such an abundance on the results.

Fig. 12 is the same as Fig. 1 but for an elemental abundance of sulphur of  $X_{\text{ini}} = 1.5 \times 10^{-5}$ . What appears is that the differences are mainly quantitative and that the chemistry stays the same as

described in Section 4, with the exception of the two following points.

(i) Adsorption of atomic S on the grain is much more efficient with  $X_{\text{ini}} = 1.5 \times 10^{-5}$ , which cause its abundance to drop much sooner than for  $X(S)_{\text{ini}} = 8 \times 10^{-8}$ , near  $3 \times 10^3$  yr. However, atomic S still stays the main reservoir of sulphur between  $2.8 \times 10^3$  and  $4.6 \times 10^5$ , containing at its maximum 88 per cent of the initial sulphur.

(ii) With  $X_{\text{ini}} = 1.5 \times 10^{-5}$ , we can no longer consider SO as a main sulphur-bearing species as defined in Section 4. Indeed, at  $3.6 \times 10^5$  yr, time when its abundance peaks, it now only contains less than 2 per cent of the initial sulphur.

Hence, our results regarding the reservoirs of sulphur in dark clouds stay the same (with the exception of SO).

## 6 DISCUSSIONS AND CONCLUSIONS

### 6.1 About the elemental abundance of sulphur

The comparison of our enhanced model with the gas-phase observations in TMC-1 (CP) (see Section 5) favours the use of an elemental abundance of sulphur between  $X(S)_{\text{ini}} = 5 \times 10^{-6}$  and  $X(S)_{\text{ini}} = 1.5 \times 10^{-5}$ . As most of the estimations of the cosmic abundance of sulphur lie between these two values (Federman et al. 1993; Sofia, Cardelli & Savage 1994; Tiefert et al. 1994; Ruffle et al. 1999; Shalabiea 2001), our model does not require additional depletion of sulphur. Moreover, our results on the comparison with the observations of OCS and SO<sub>2</sub> in icy grain bulks towards W33A confirm that a cosmic abundance of sulphur as the elemental sulphur abundance in our model is required to reproduce the observed abundances of these two species.

### 6.2 About the reservoirs of sulphur

Two main hypotheses exist to explain the observed depletion of sulphur in dark clouds: either the sulphur is in an as yet undiscovered form in the gas phase, which could be atomic sulphur, or it could be locked in icy grain bulks. The latter hypothesis is supported by the observation of H<sub>2</sub>S as the most important S-bearing species in cometary ices (Bockelée-Morvan et al. 2000), which are thought to present chemical similarities with the ices processed during hot cores formation (Irvine et al. 2000). Moreover, as hydrogenation is the most effective process in grains chemistry, models often predict that when sulphur atoms stick on the grain, they will consequently form H<sub>2</sub>S (Garrod et al. 2007). However, H<sub>2</sub>S has never been detected in dark cloud ices. Additionally, upper limits to its column density towards three high-mass protostars and three late-type stars lying behind TMC-1 (CP) have been derived from observations by Smith (1991). These limits, despite large uncertainties, are believed to be too small to account for the missing sulphur in dark clouds and alternative hypotheses have recently been proposed (Jiménez-Escobar & Muñoz Caro 2011; Druard & Wakelam 2012; Martín-Doménech et al. 2016).

As seen in Section 4.1, the results of simulations with our enhanced sulphur network seem to support both of the main hypotheses about the reservoirs of sulphur, depending on the age of the observed dark cloud. Indeed, according to our results, if the age of the cloud is less than  $5 \times 10^5$  yr then atomic sulphur in the gas phase is the main reservoir of sulphur. However, if the age of the cloud is greater, then our results show that because of hydrogenation of sulphur on the grain surface (the cycle between HS and H<sub>2</sub>S enabled by

the reaction–diffusion competition and the accumulation of these species in the bulk), the reservoirs of sulphur are nearly equally HS and H<sub>2</sub>S in the grain bulk. The upper limit to the abundance of H<sub>2</sub>S in ices provided by the observations is between  $3 \times 10^{-7}$  and  $3 \times 10^{-6}$  (assuming an abundance of H<sub>2</sub>O in ices of  $10^{-4}$  and based on Smith 1991). It should be noted that these upper limits are derived using the infrared transition strengths obtained by Ferraro, Sill & Fink (1980) which has been obtained in pure H<sub>2</sub>S ice. The intensity strengths can be notably different in interstellar ice analogues. As the total abundances of H<sub>2</sub>S on the grains in Models 3 and 4 at the time of ‘best fit’  $10^6$  yr are, respectively,  $1.5 \times 10^{-6}$  and  $4.4 \times 10^{-6}$ , it appears that our enhanced network results are in agreement with the upper limits of Smith (1991) and therefore in favour of a joint HS and H<sub>2</sub>S sulphur reservoir in icy grain bulks in dark clouds. This result is in agreement with the results depicted in appendix E of Furuya et al. (2015). Indeed, they also find that HS and H<sub>2</sub>S are likely to be the main reservoirs of sulphur, notably due to the same hydrogenation loop described in equation (4). Constraints on the icy grain bulk abundance of HS would be useful to validate this hypothesis. However, the  $v = 0 \rightarrow v = 1$  transition of HS lies around  $2599 \text{ cm}^{-1}$  in the gas phase (Bernath, Amano & Wong 1983) and has never been observed in ice. The calculated IR strength (at DFT or MP2 level using Gaussian) is three orders of magnitude less efficient than water and four order of magnitude less efficient than OCS. Subsequently, even if solid HS is the reservoir of sulphur in dark clouds, the lack of sensibility of IR detection may prevent its observation.

### 6.3 About the observability of HCS

In order to assess the observability of HCS in the gas phase of TMC-1 (CP) (see Section 4.3.3), we proceed using a local thermodynamic equilibrium calculation of the HCS emission spectrum in the 3- and 2-mm atmospheric windows with  $T_{\text{ex}} = 10$  K, a column density of HCS of  $1 \times 10^{12} \text{ cm}^{-2}$  (corresponding to a gas-phase abundance of HCS of approximately  $10^{-10}$  as obtained with Model 4 in the time frame between  $10^5$  and  $10^7$  yr), assuming a wide source (no beam dilution) and a linewidth of  $1 \text{ km s}^{-1}$ . We estimate that the brightest line would be the one at  $80\,553.516 \text{ MHz}$  with a main beam temperature of 2 mK. This result infers that for a  $5\sigma$  detection of HCS in the gas phase, it would take more than a thousand hours of observations with the IRAM 30 m. We therefore conclude that HCS is unlikely to be detected in the gas phase in dark clouds even if its abundance grows notably above  $10^{-12}$  in our simulations.

## ACKNOWLEDGEMENTS

This work has been founded by the European Research Council (Starting Grant 3DICE, grant agreement 336474). The authors are grateful to the CNRS programme ‘Physique et Chimie du Milieu Interstellaire’ (PCMI) for partial funding of their work.

## REFERENCES

- Adande G. R., Halfen D. T., Ziurys L. M., Quan D., Herbst E., 2010, *ApJ*, 725, 561
- Agúndez M., Wakelam V., 2013, *Chem. Rev.*, 113, 8710
- Anicich V. G., 2003, JPL Technical Report, JPL-Publ-03-19, NASA, Washington, DC
- Baulch D. et al., 2005, *J. Phys. Chem. Ref. Data*, 34, 757
- Benson S., 1976, *Thermochemical Kinetics: Methods for the Estimation of Thermochemical Data and Rate Parameters*, 2nd edn. Wiley, New York

- Bernath P., Amano T., Wong M., 1983, *J. Mol. Spectrosc.*, 98, 20
- Bockelée-Morvan D. et al., 2000, *A&A*, 353, 1101
- Boogert A. C. A., Schutte W. A., Helmich F. P., Tielens A. G. G. M., Wooden D. H., 1997, *A&A*, 317, 929
- Boogert A. C. A., Gerakines P. A., Whittet D. C. B., 2015, *ARA&A*, 53, 541
- Cernicharo J. et al., 2011, *A&A*, 531, A103
- Chabot M. et al., 2010, *A&A*, 524, A39
- Chang Q., Cuppen H. M., Herbst E., 2007, *A&A*, 469, 973
- Charnley S. B., 1997, *ApJ*, 481, 396
- Druard C., Wakelam V., 2012, *MNRAS*, 426, 354
- Federman S. R., Sheffer Y., Lambert D. L., Gilliland R. L., 1993, *ApJ*, 413, L51
- Ferraro J. R., Sill G., Fink U., 1980, *Appl. Spectrosc.*, 34, 525
- Florescu-Mitchell A. I., Mitchell J. B. A., 2006, *Phys. Rep.*, 430, 277
- Fournier J. A., Shuman N. S., Melko J. J., Ard S. G., Viggiano A. A., 2013, *J. Chem. Phys.*, 138, 154201
- Frerking M. A., Linke R. A., Thaddeus P., 1979, *ApJ*, 234, L143
- Furuya K., Aikawa Y., Hincelin U., Hassel G. E., Bergin E. A., Vasyunin A. I., Herbst E., 2015, *A&A*, 584, A124
- Galland N., Caralp F., Rayez M.-T., Hannachi Y., Loison J.-C., Dorthé G., Bergeat A., 2001, *J. Phys. Chem. A*, 105, 9893
- Galland N., Caralp F., Hannachi Y., Bergeat A., Loison J.-C., 2003, *J. Phys. Chem. A*, 107, 5419
- Garozzo M., Fulvio D., Kanuchova Z., Palumbo M. E., Strazzulla G., 2010, *A&A*, 509, A67
- Garrod R., Herbst E., 2006, *A&A*, 457, 927
- Garrod R. T., Pauly T., 2011, *ApJ*, 735, 15
- Garrod R. T., Wakelam V., Herbst E., 2007, *A&A*, 467, 1103
- Georgievskii Y., Klippenstein S. J., 2005, *J. Chem. Phys.*, 122, 194103
- Georgievskii Y., Klippenstein S. J., 2007, *J. Phys. Chem. A*, 111, 3802
- Gibb E., Nummelin A., Irvine W. M., Whittet D. C. B., Bergman P., 2000, *ApJ*, 545, 309
- Glowacki D. R., Liang C.-H., Morley C., Pilling M. J., Robertson S. H., 2012, *J. Phys. Chem. A*, 116, 9545
- Gonzalez M., Hijazo J., Novoa J. J., Sayos R., 1996, *J. Chem. Phys.*, 105, 10999
- Graedel T. E., Langer W. D., Frerking M. A., 1982, *ApJS*, 48, 321
- Gratier P., Majumdar L., Ohishi M., Roueff E., Loison J. C., Hickson K. M., Wakelam V., 2016, *ApJS*, 225, 25
- Gronowski M., Kolos R., 2014, *ApJ*, 792, 89
- Halfen D. T., Ziurys L. M., Brünken S., Gottlieb C. A., McCarthy M. C., Thaddeus P., 2009, *ApJ*, 702, L124
- Hama T., Watanabe N., 2013, *Chem. Rev.*, 113, 8783
- Hamberg M. et al., 2007, *Mol. Phys.*, 105, 899
- Hamberg M. et al., 2014, *J. Phys. Chem. A*, 118, 6034
- Hasegawa T. I., Herbst E., Leung C. M., 1992, *ApJS*, 82, 167
- Hatchell J., Thompson M. A., Millar T. J., MacDonald G. H., 1998, *A&A*, 338, 713
- Herbst E., Terzieva R., Talbi D., 2000, *MNRAS*, 311, 869
- Hickson K., Loison J., Cavalié T., Hébrard E., Dobrijevic M., 2014, *A&A*, 572, A58
- Hickson K. M., Loison J.-C., Nunez-Reyes D., Méreau R., 2016a, *J. Phys. Chem. Lett.*, preprint ([arXiv:1608.08877](https://arxiv.org/abs/1608.08877))
- Hickson K. M., Wakelam V., Loison J.-C., 2016b, *Mol. Astrophys.*, 3, 1
- Hincelin U., Wakelam V., Hersant F., Guilloteau S., Loison J. C., Honvault P., Troe J., 2011, *A&A*, 530, A61
- Hippler H., Viskolcz B., 2002, *Phys. Chem. Chem. Phys.*, 4, 4663
- Holdship J. et al., 2016, *MNRAS*, 463, 802
- Irvine W. M., Schloerb F. P., Crovisier J., Fegley B., Jr, Mumma M. J., 2000, *Protostars and Planets IV*. Univ. Arizona Press, Tucson, AZ, p. 1159
- Jenkins E. B., 2009, *ApJ*, 700, 1299
- Jiménez-Escobar A., Muñoz Caro G. M., 2011, *A&A*, 536, A91
- Karssemeijer L. J., Cuppen H. M., 2014, *A&A*, 569, A107
- Kolesníková L., Tercero B., Cernicharo J., Alonso J. L., Daly A. M., Gordon B. P., Shipman S. T., 2014, *ApJ*, 784, L7
- Korth M., Grimme S., 2009, *J. Chem. Theory Comput.*, 5, 993
- Kurylo M. J., Peterson N. C., Braun W., 1971, *J. Chem. Phys.*, 54, 943
- Lada E. A., Bally J., Stark A. A., 1991, *ApJ*, 368, 432
- Leonori F., Occhiogrosso A., Balucani N., Bucci A., Petrucci R., Casavecchia P., 2011, *J. Phys. Chem. Lett.*, 3, 75
- Leonori F., Balucani N., Nevrlý V., Bergeat A., Falcinelli S., Vanuzzo G., Casavecchia P., Cavallotti C., 2015, *J. Phys. Chem. C*, 119, 14632
- Lilenfeld H. V., Richardson R. J., 1977, *J. Chem. Phys.*, 67, 3991
- Linke R. A., Frerking M. A., Thaddeus P., 1979, *ApJ*, 234, L139
- Lique F., Cernicharo J., Cox P., 2006, *ApJ*, 653, 1342
- Loison J.-C., Wakelam V., Hickson K. M., Bergeat A., Méreau R., 2014, *MNRAS*, 437, 930
- Loison J.-C. et al., 2016, *MNRAS*, 456, 4101
- McGonagle D., Irvine W. M., Ohishi M., 1994, *ApJ*, 422, 621
- Majumdar L., Gratier P., Vidal T., Wakelam V., Loison J.-C., Hickson K. M., Caux E., 2016, *MNRAS*, 458, 1859
- Martín-Doménech R., Jiménez-Serra I., Muñoz Caro G. M., Müller H. S. P., Occhiogrosso A., Testi L., Woods P. M., Viti S., 2016, *A&A*, 585, A112
- Matthews H. E., MacLeod J. M., Broten N. W., Madden S. C., Friberg P., 1987, *ApJ*, 315, 646
- Mendes M. B. et al., 2012, *ApJ*, 746, L8
- Messineo M. et al., 2015, *ApJ*, 805, 110
- Montaigne H. et al., 2005, *ApJ*, 631, 653
- Neufeld D. A., Wolfire M. G., Schilke P., 2005, *ApJ*, 628, 260
- Nobes R. H., Radom L., 1981, *Chem. Phys.*, 60, 1
- Oehlers C., Wagner H. G., Ziemer H., Temps F., Dobe S., 2000, *J. Phys. Chem. A*, 104, 10500
- Palumbo M. E., Geballe T. R., Tielens A. G. G. M., 1997, *ApJ*, 479, 839
- Peng J., Hu X., Marshall P., 1999, *J. Phys. Chem. A*, 103, 5307
- Penzias A. A., Solomon P. M., Wilson R. W., Jefferts K. B., 1971, *ApJ*, 168, L53
- Peters P. S., Duffot D., Wiesenfeld L., Toubin C., 2013, *J. Chem. Phys.*, 139, 164310
- Plessis S., Carrasco N., Dobrijevic M., Pernot P., 2012, *Icarus*, 219, 254
- Plume R., Jaffe D. T., Evans N. J., II, Martín-Pintado J., Gómez-González J., 1997, *ApJ*, 476, 730
- Podio L. et al., 2015, *A&A*, 581, A85
- Prasad S. S., Tarafdar S. P., 1983, *ApJ*, 267, 603
- Puzzarini C., 2005, *J. Chem. Phys.*, 123, 024313
- Reiter D., Janev R., 2010, *Contrib. Plasma Phys.*, 50, 986
- Rice B. M., Chabalowski C. F., 1994, *J. Phys. Chem.*, 98, 9488
- Rice B. M., Cartland H. E., Chabalowski C. F., 1993, *Chem. Phys. Lett.*, 211, 283
- Ruad M., Wakelam V., Hersant F., 2016, *MNRAS*, 459, 3756
- Ruffle D. P., Hartquist T. W., Caselli P., Williams D. A., 1999, *MNRAS*, 306, 691
- Sabbah H., Biennier L., Sims I. R., Georgievskii Y., Klippenstein S. J., Smith I. W., 2007, *Science*, 317, 102
- Sakai N. et al., 2014, *Nature*, 507, 78
- Sander S. et al., 2011, *JPL Technical Report*, JPL-Publ-10-6, NASA, Washington, DC
- Scott G. B., Fairley D. A., Freeman C. G., McEwan M. J., Anicich V. G., 1999, *J. Phys. Chem. A*, 103, 1073
- Scott G. B., Milligan D. B., Fairley D. A., Freeman C. G., McEwan M. J., 2000, *J. Chem. Phys.*, 112, 4959
- Shalabiea O. M., 2001, *A&A*, 370, 1044
- Shannon R. J., Blitz M. A., Goddard A., Heard D. E., 2013, *Nature Chem.*, 5, 745
- Smith R. G., 1991, *MNRAS*, 249, 172
- Smith I. W., 2006, *Angew. Chem. Int. Ed.*, 45, 2842
- Smith I. W. M., 2011, *ARA&A*, 49, 29
- Sofia U. J., Cardelli J. A., Savage B. D., 1994, *ApJ*, 430, 650
- Tieftrunk A., Pineau des Forets G., Schilke P., Walmsley C. M., 1994, *A&A*, 289, 579
- Tielens A., Hagen W., 1982, *A&A*, 114, 245
- Viti S., Caselli P., Hartquist T. W., Williams D. A., 2001, *A&A*, 370, 1017
- Wagner A. F., Bowman J. M., 1987, *J. Phys. Chem.*, 91, 5314
- Wakelam V., Herbst E., 2008, *ApJ*, 680, 371
- Wakelam V., Caselli P., Ceccarelli C., Herbst E., Castets A., 2004, *A&A*, 422, 159

- Wakelam V., Herbst E., Selsis F., 2006, *A&A*, 451, 551  
 Wakelam V. et al., 2010, *Space Sci. Rev.*, 156, 13  
 Wakelam V. et al., 2012, *ApJS*, 199, 21  
 Wakelam V. et al., 2015a, *ApJS*, 217, 20  
 Wakelam V., Loison J.-C., Hickson K. M., Ruaud M., 2015b, *MNRAS*, 453, L48  
 Wang H., Eyre J., Dorfman L. M., 1973, *J. Chem. Phys.*, 59, 5199  
 Wierzejewska M., Moc J., 2003, *J. Phys. Chem. A*, 107, 11209  
 Woods P. M., Occhiogrosso A., Viti S., Kaňuchová Z., Palumbo M. E., Price S. D., 2015, *MNRAS*, 450, 1256  
 Woon D. E., Herbst E., 2009, *ApJS*, 185, 273  
 Yoshimura M., Koshi M., Matsui H., Kamiya K., Umeyama H., 1992, *Chem. Phys. Lett.*, 189, 199  
 Zhao Y., Truhlar D. G., 2008, *J. Chem. Theory Comput.*, 4, 1849

## SUPPORTING INFORMATION

Supplementary data are available at [MNRAS](#) online.

**Supplementary material (file for review).pdf**

**Supplementary material (online).pdf**

Please note: Oxford University Press is not responsible for the content or functionality of any supporting materials supplied by the authors. Any queries (other than missing material) should be directed to the corresponding author for the article.

This paper has been typeset from a  $\text{\LaTeX}$  file prepared by the author.





# BIBLIOGRAPHY

- Adams, N. G., Smith, D., and Paulson, J. F. (1980). An experimental survey of the reactions of  $\text{NH}_n$  + ions ( $n=0$  to 4) with several diatomic and polyatomic molecules at 300 K. *The Journal of Chemical Physics*, 72(1):288–297.
- Adande, G. R., Halfen, D. T., Ziurys, L. M., Quan, D., and Herbst, E. (2010). Observations of the  $[\text{HNCS}]/[\text{HSCN}]$  Ratio in Sgr B2 and TMC-1: Evidence for Low-temperature Gas-phase Chemistry. *ApJ*, 725:561–570.
- Adriaens, D., Goumans, T., Catlow, C., and Brown, W. (2010). Computational study of carbonyl sulphide formation on model interstellar dust grains. *The Journal of Physical Chemistry C*, 114(4):1892–1900.
- Agúndez, M. and Wakelam, V. (2013). Chemistry of Dark Clouds: Databases, Networks, and Models. *Chemical Reviews*, 113:8710–8737.
- Aikawa, Y., Wakelam, V., Garrod, R. T., and Herbst, E. (2008). Molecular Evolution and Star Formation: From Prestellar Cores to Protostellar Cores. *ApJ*, 674:984–996.
- Andersson, S. and van Dishoeck, E. F. (2008). Photodesorption of water ice. A molecular dynamics study. *A&A*, 491:907–916.
- Anicich, V. G. (2003). An index of the literature for bimolecular gas phase cation-molecule reaction kinetics. *JPL Publication*.
- Atkinson, R., Baulch, D., Cox, R., Crowley, J., Hampson, R., Hynes, R., Jenkin, M., Rossi, M., and Troe, J. (2004). IUPAC Task Group on atmospheric chemical kinetic data evaluation. *Atmos. Chem. Phys*, 4:1461–1738.
- Bauer, W., Becker, K., and Meuser, R. (1985). Laser induced fluorescence studies on  $\text{C}_2\text{O}$  and CH radicals. *Berichte der Bunsengesellschaft für physikalische Chemie*, 89(3):340–341.
- Belau, L., Wheeler, S. E., Ticknor, B. W., Ahmed, M., Leone, S. R., Allen, W. D., Schaefer, H. F., and Duncan, M. A. (2007). Ionization thresholds of small carbon clusters: tunable VUV experiments and theory. *Journal of the American Chemical Society*, 129(33):10229–10243.
- Bernath, P., Amano, T., and Wong, M. (1983). Observation of the  $v=1\rightarrow 0$  band of SH ( $x=2\pi$ ) with a difference frequency laser. *Journal of Molecular Spectroscopy*, 98(1):20–26.

- Bertin, M., Fayolle, E. C., Romanzin, C., Öberg, K. I., Michaut, X., Moudens, A., Philippe, L., Jeseck, P., Linnartz, H., and Fillion, J.-H. (2012). UV photodesorption of interstellar CO ice analogues: from subsurface excitation to surface desorption. *Physical Chemistry Chemical Physics (Incorporating Faraday Transactions)*, 14:9929.
- Blitz, M. A., McKee, K. W., and Pilling, M. J. (2000). Temperature dependence of the reaction of OH with SO. *Proceedings of the Combustion Institute*, 28(2):2491–2497.
- Bockelée-Morvan, D., Lis, D. C., Wink, J. E., Despois, D., Crovisier, J., Bachiller, R., Benford, D. J., Biver, N., Colom, P., Davies, J. K., Gérard, E., Germain, B., Houde, M., Mehringer, D., Moreno, R., Paubert, G., Phillips, T. G., and Rauer, H. (2000). New molecules found in comet C/1995 O1 (Hale-Bopp). Investigating the link between cometary and interstellar material. *A&A*, 353:1101–1114.
- Bonnor, W. B. (1956). Boyle’s Law and gravitational instability. *MNRAS*, 116:351.
- Boogert, A. C. A., Gerakines, P. A., and Whittet, D. C. B. (2015). Observations of the icy universe. *ARAA*, 53:541–581.
- Boogert, A. C. A., Schutte, W. A., Helmich, F. P., Tielens, A. G. G. M., and Wooden, D. H. (1997). Infrared observations and laboratory simulations of interstellar CH<sub>4</sub> and SO<sub>2</sub>. *A&A*, 317:929–941.
- Bradley, J. N., Trueman, S. P., Whytock, D. A., and Zaleski, T. A. (1973). Electron spin resonance study of the reaction of hydrogen atoms with hydrogen sulphide. *Journal of the Chemical Society, Faraday Transactions 1: Physical Chemistry in Condensed Phases*, 69:416–425.
- Butkovskaya, N. and Setser, D. (1999). Product branching fractions and kinetic isotope effects for the reactions of OH and OD radicals with CH<sub>3</sub>SH and CH<sub>3</sub>SD. *The Journal of Physical Chemistry A*, 103(35):6921–6929.
- Cazaux, S., Caselli, P., Tielens, A. G. G. M., LeBourlot, J., and Walmsley, M. (2005). Molecular Hydrogen formation on grain surfaces. In Saija, R. and Cecchi-Pestellini, C., editors, *Journal of Physics Conference Series*, volume 6 of *Journal of Physics Conference Series*, pages 155–160.
- Ceccarelli, C., Hollenbach, D. J., and Tielens, A. G. G. M. (1996). Far-Infrared Line Emission from Collapsing Protostellar Envelopes. *ApJ*, 471:400.
- Cernicharo, J., Spielfiedel, A., Balança, C., Dayou, F., Senent, M.-L., Feautrier, N., Faure, A., Cressiot-Vincent, L., Wiesenfeld, L., and Pardo, J. R. (2011). Collisional excitation of sulfur dioxide in cold molecular clouds. *A&A*, 531:A103.
- Chaabouni, H., Bergeron, H., Baouche, S., Dulieu, F., Matar, E., Congiu, E., Gavilan, L., and Lemaire, J. L. (2012). Sticking coefficient of hydrogen and deuterium on silicates under interstellar conditions. *A&A*, 538:A128.

- Chaabouni, H., Diana, S., Nguyen, T., and Dulieu, F. (2018). Thermal desorption of formamide and methylamine from graphite and amorphous water ice surfaces. *A&A*, 612:A47.
- Chang, Q., Cuppen, H. M., and Herbst, E. (2007). Gas-grain chemistry in cold interstellar cloud cores with a microscopic Monte Carlo approach to surface chemistry. *A&A*, 469:973–983.
- Charnley, S. B. (1997). Sulfuretted Molecules in Hot Cores. *ApJ*, 481:396–405.
- Cheng, B.-M., Eberhard, J., Chen, W.-C., and Yu, C.-h. (1997). Photoionization efficiency spectrum and ionization energy of HSO studied by discharge flow-photoionization mass spectrometry. *The Journal of chemical physics*, 106(23):9727–9733.
- Coutens, A., Jørgensen, J. K., van der Wiel, M. H. D., Müller, H. S. P., Lykke, J. M., Bjerkeli, P., Bourke, T. L., Calcutt, H., Drozdovskaya, M. N., Favre, C., Fayolle, E. C., Garrod, R. T., Jacobsen, S. K., Ligterink, N. F. W., Öberg, K. I., Persson, M. V., van Dishoeck, E. F., and Wampfler, S. F. (2016). The ALMA-PILS survey: First detections of deuterated formamide and deuterated isocyanic acid in the interstellar medium. *A&A*, 590.
- Crimier, N., Ceccarelli, C., Maret, S., Bottinelli, S., Caux, E., Kahane, C., Lis, D. C., and Olofsson, J. (2010). The solar type protostar IRAS16293-2422: new constraints on the physical structure. *A&A*, 519:A65.
- Cupitt, L. and Glass, G. (1975). Reactions of SH with atomic oxygen and hydrogen. *Int. J. Chem. Kinet.:(United States)*, 7(Suppl 1).
- Decker, B. K. and Macdonald, R. G. (2001). Channeling of products in the hot atom reaction  $\text{H} + (\text{CN})_2 \rightarrow \text{HCN}/\text{HNC} + \text{CN}$  and in the reaction of CN with  $\text{CH}_3\text{SH}$ . *The Journal of Physical Chemistry A*, 105(28):6817–6825.
- Deeyamulla, M. and Husain, D. (2006). Kinetic studies of atomic carbon, C [2p2 (3P)], with small sulfur-containing molecules by time-resolved atomic resonance absorption spectroscopy in the vacuum ultra-violet. *Journal of Photochemistry and Photobiology A: Chemistry*, 184(3):347–353.
- Dorthe, G., Caubet, P., Vias, T., Barrere, B., and Marchais, J. (1991). Fast flow studies of atomic carbon kinetics at room temperature. *The Journal of Physical Chemistry*, 95(13):5109–5116.
- Draine, B. T. (2011). *Physics of the Interstellar and Intergalactic Medium*.
- Drozdovskaya, M. N., van Dishoeck, E. F., Jørgensen, J. K., Calmonte, U., van der Wiel, M. H. D., Coutens, A., Calcutt, H., Müller, H. S. P., Bjerkeli, P., Persson, M. V.,

- Wampfler, S. F., and Altwegg, K. (2018). The ALMA-PILS survey: the sulphur connection between protostars and comets: IRAS 16293-2422 B and 67P/Churyumov-Gerasimenko. *A&A*, 476:4949–4964.
- Druard, C. and Wakelam, V. (2012). Polysulphanes on interstellar grains as a possible reservoir of interstellar sulphur. *MNRAS*, 426:354–359.
- Ebert, R. (1955). Über die Verdichtung von H I-Gebieten. Mit 5 Textabbildungen. *Zeitschrift für Astrophysik*, 37:217.
- Ellingson, B. A. and Truhlar, D. G. (2007). Explanation of the unusual temperature dependence of the atmospherically important  $\text{OH} + \text{H}_2\text{S} \rightarrow \text{H}_2\text{O} + \text{HS}$  reaction and prediction of the rate constant at combustion temperatures. *Journal of the American Chemical Society*, 129(42):12765–12771.
- Eshchenko, G., Köcher, T., Kerst, C., and Temps, F. (2002). Formation of HCNO and HCN in the 193 nm photolysis of  $\text{H}_2\text{CCO}$  in the presence of NO. *Chemical physics letters*, 356(1-2):181–187.
- Esplugues, G. B., Viti, S., Goicoechea, J. R., and Cernicharo, J. (2014). Modelling the sulphur chemistry evolution in Orion KL. *A&A*, 567:A95.
- Ewig, F., Rhäsa, D., and Zellner, R. (1987). Kinetics, energetics and OH product yield of the reaction  $\text{CH}_3\text{O} + \text{O} (3\text{P}) \rightarrow \text{CH}_3\text{O}^* \rightarrow \text{products}$ . *Berichte der Bunsengesellschaft für physikalische Chemie*, 91(7):708–717.
- Fayolle, E. C., Öberg, K. I., Cuppen, H. M., Visser, R., and Linnartz, H. (2011). Laboratory  $\text{H}_2\text{O}:\text{CO}_2$  ice desorption data: entrapment dependencies and its parameterization with an extended three-phase model. *A&A*, 529:A74.
- Federman, S. R., Sheffer, Y., Lambert, D. L., and Gilliland, R. L. (1993). Detection of boron, cobalt, and other weak interstellar lines toward Zeta Ophiuchi. *ApJL*, 413:L51–L54.
- Fehsenfeld, F. and Ferguson, E. (1973). Atmospheric atomic sulfur ion reactions. *Journal of Geophysical Research*, 78(10):1699–1701.
- Ferraro, J. R., Sill, G., and Fink, U. (1980). Infrared intensity measurements of cryo-deposited thin films of  $\text{NH}_3$ ,  $\text{NH}_4\text{HS}$ ,  $\text{H}_2\text{S}$ , and assignments of absorption bands. *Applied Spectroscopy*, 34(5):525–533.
- Fikri, M., Meyer, S., Roggenbuck, J., and Temps, F. (2002). An experimental and theoretical study of the product distribution of the reaction  $\text{CH}_2 (x^3\text{B}_1) + \text{NO}$ . *Faraday discussions*, 119:223–242.
- Flores, J., Estevez, C., Carballeira, L., and Juste, I. P. (2001). A theoretical study of the  $\text{S} + \text{C}_2\text{H}$  reaction: Potential energy surfaces and dynamics. *The Journal of Physical Chemistry A*, 105(19):4716–4725.

- Flores, J., Martinez-Nunez, E., Vazquez, S., and Gomez, F. (2002). A theoretical study of the dynamics of the S + c-C<sub>3</sub>H reaction. *The Journal of Physical Chemistry A*, 106(37):8811–8819.
- Frerking, M. A., Linke, R. A., and Thaddeus, P. (1979). Interstellar isothiocyanic acid. *ApJL*, 234:L143–L145.
- Furuya, K., Aikawa, Y., Hincelin, U., Hassel, G. E., Bergin, E. A., Vasyunin, A. I., and Herbst, E. (2015). Water deuteration and ortho-to-para nuclear spin ratio of H<sub>2</sub> in molecular clouds formed via the accumulation of H I gas. *A&A*, 584:A124.
- Galland, N., Caralp, F., Rayez, M.-T., Hannachi, Y., Loison, J.-C., Dorthe, G., and Bergeat, A. (2001). Reaction of carbon atoms, C (2p<sup>2</sup>, 3P), with hydrogen sulfide, H<sub>2</sub>S (XA1): Overall rate constant and product channels. *The Journal of Physical Chemistry A*, 105(43):9893–9900.
- Garozzo, M., Fulvio, D., Kanuchova, Z., Palumbo, M. E., and Strazzulla, G. (2010). The fate of S-bearing species after ion irradiation of interstellar icy grain mantles. *A&A*, 509:A67.
- Garrod, R. T. and Herbst, E. (2006). Formation of methyl formate and other organic species in the warm-up phase of hot molecular cores. *A&A*, 457:927–936.
- Garrod, R. T. and Pauly, T. (2011). On the Formation of CO<sub>2</sub> and Other Interstellar Ices. *ApJ*, 735:15.
- Garrod, R. T., Wakelam, V., and Herbst, E. (2007). Non-thermal desorption from interstellar dust grains via exothermic surface reactions. *A&A*, 467:1103–1115.
- Geppert, W. D., Hamberg, M., Thomas, R. D., Österdahl, F., Hellberg, F., Zhaunerchyk, V., Ehlerding, A., Millar, T., Roberts, H., Semaniak, J., et al. (2006). Dissociative recombination of protonated methanol. *Faraday discussions*, 133:177–190.
- Gerin, M., Pety, J., Fuente, A., Cernicharo, J., Commerçon, B., and Marcelino, N. (2015). Nascent bipolar outflows associated with the first hydrostatic core candidates Barnard 1b-N and 1b-S. *A&A*, 577.
- Ghesquière, P., Mineva, T., Talbi, D., Theulé, P., Noble, J. A., and Chiavassa, T. (2015). Diffusion of molecules in the bulk of a low density amorphous ice from molecular dynamics simulations. *Physical Chemistry Chemical Physics (Incorporating Faraday Transactions)*, 17:11455–11468.
- Gibb, E., Nummelin, A., Irvine, W. M., Whittet, D. C. B., and Bergman, P. (2000). Chemistry of the Organic-Rich Hot Core G327.3-0.6. *ApJ*, 545:309–326.
- Gingerich, K. A., Finkbeiner, H. C., and Schmude Jr, R. W. (1994). Enthalpies of formation of small linear carbon clusters. *Journal of the American Chemical Society*, 116(9):3884–3888.

- Graedel, T. E., Langer, W. D., and Frerking, M. A. (1982). The kinetic chemistry of dense interstellar clouds. *ApJS*, 48:321–368.
- Gratier, P., Majumdar, L., Ohishi, M., Roueff, E., Loison, J. C., Hickson, K. M., and Wakelam, V. (2016). A New Reference Chemical Composition for TMC-1. *ApJS*, 225:25.
- Gronowski, M. and Kolos, R. (2014). A theoretical study on the interstellar synthesis of  $\text{H}_2\text{NCS}^+$  and  $\text{HNCSH}^+$  cations. *ApJ*, 792(2):89.
- Grotheer, H.-H., Riecktr, G., Walter, D., and Just, T. (1989). Reactions of hydroxymethyl and hydroxyethyl radicals with molecular and atomic oxygen. In *Symposium (International) on Combustion*, volume 22, pages 963–972. Elsevier.
- Halfen, D. T., Ziurys, L. M., Brünken, S., Gottlieb, C. A., McCarthy, M. C., and Thaddeus, P. (2009). Detection of a New Interstellar Molecule: Thiocyanic Acid HSCN. *ApJL*, 702:L124–L127.
- Hamberg, M., Geppert, W. D., Thomas, R. D., Zhaunerchyk, V., Österdahl, F., Ehlerding, A., Kaminska, M., Semaniak, J., Ugglas, M. a., Källberg, A., et al. (2007). Experimental determination of dissociative recombination reaction pathways and absolute reaction cross-sections of  $\text{CH}_2\text{OH}^+$ ,  $\text{CD}_2\text{OD}^+$  and  $\text{CD}_2$ . *Molecular Physics*, 105(5-7):899–906.
- Harada, N., Herbst, E., and Wakelam, V. (2010). A New Network for Higher-temperature Gas-phase Chemistry. I. A Preliminary Study of Accretion Disks in Active Galactic Nuclei. *ApJ*, 721:1570–1578.
- Hasegawa, T. I., Herbst, E., and Leung, C. M. (1992). Models of gas-grain chemistry in dense interstellar clouds with complex organic molecules. *ApJS*, 82:167–195.
- Hatchell, J., Thompson, M. A., Millar, T. J., and MacDonald, G. H. (1998). Sulphur chemistry and evolution in hot cores. *A&A*, 338:713–722.
- Herbst, E. (2006). Astrochemistry and Star Formation: Successes and Challenges. In Roeser, S., editor, *Reviews in Modern Astronomy*, volume 19 of *Reviews in Modern Astronomy*, page 167.
- Herbst, E. and van Dishoeck, E. F. (2009). Complex Organic Interstellar Molecules. *ARAA*, 47:427–480.
- Herpin, F., Marseille, M., Wakelam, V., Bontemps, S., and Lis, D. C. (2009). S-bearing molecules in massive dense cores. *A&A*, 504:853–867.
- Hickson, K. M., Wakelam, V., and Loison, J.-C. (2016). Methylacetylene ( $\text{CH}_3\text{CCH}$ ) and propene ( $\text{C}_3\text{H}_6$ ) formation in cold dense clouds: A case of dust grain chemistry. *Molecular Astrophysics*, 3:1–9.

- Hincelin, U., Commerçon, B., Wakelam, V., Hersant, F., Guilloteau, S., and Herbst, E. (2016). Chemical and Physical Characterization of Collapsing Low-mass Prestellar Dense Cores. *ApJ*, 822:12.
- Hincelin, U., Wakelam, V., Hersant, F., Guilloteau, S., Loison, J. C., Honvault, P., and Troe, J. (2011). Oxygen depletion in dense molecular clouds: a clue to a low O<sub>2</sub> abundance? *A&A*, 530:A61.
- Hochlaf, M., Nicolas, C., and Poisson, L. (2007). Photoionization of C<sub>4</sub> molecular beam: Ab initio calculations. *The Journal of chemical physics*, 127(1):014310.
- Holdship, J., Viti, S., Jimenez-Serra, I., Lefloch, B., Codella, C., Podio, L., Benedettini, M., Fontani, F., Bachiller, R., Tafalla, M., and Ceccarelli, C. (2016). H<sub>2</sub>S in the L1157-B1 Bow Shock. *MNRAS*.
- Hollenbach, D. and Salpeter, E. E. (1971). Surface Recombination of Hydrogen Molecules. *ApJ*, 163:155.
- Hunter, E. P. L. and Lias, S. G. (1998). Evaluated Gas Phase Basicities and Proton Affinities of Molecules: An Update. *Journal of Physical and Chemical Reference Data*, 27:413–656.
- Husain, D. and Ioannou, A. X. (1999). Collisional removal of atomic carbon, C [2p<sup>2</sup> (3P<sup>J</sup>)], by aldehydes and ketones, investigated by time-resolved atomic resonance absorption spectroscopy in the vacuum ultra-violet. *Journal of Photochemistry and Photobiology A: Chemistry*, 129(1-2):1–7.
- Hynes, A. and Wine, P. (1987). Kinetics of the hydroxyl radical+ methyl mercaptan reaction under atmospheric conditions. *Journal of Physical Chemistry*, 91(13):3672–3676.
- Irvine, W. M., Schloerb, F. P., Crovisier, J., Fegley, Jr., B., and Mumma, M. J. (2000). Comets: a Link Between Interstellar and Nebular Chemistry. *Protostars and Planets IV*, page 1159.
- Ivezic, Z. and Elitzur, M. (1997). Self-similarity and scaling behaviour of infrared emission from radiatively heated dust - I. Theory. *MNRAS*, 287:799–811.
- Jaber Al-Edhari, A., Ceccarelli, C., Kahane, C., Viti, S., Balucani, N., Caux, E., Faure, A., Lefloch, B., Lique, F., Mendoza, E., Quenard, D., and Wiesenfeld, L. (2017). History of the solar-type protostar IRAS 16293-2422 as told by the cyanopolyynes. *A&A*, 597.
- Jenkins, E. B. (2009). A Unified Representation of Gas-Phase Element Depletions in the Interstellar Medium. *ApJ*, 700:1299–1348.
- Jiménez-Escobar, A. and Muñoz Caro, G. M. (2011). Sulfur depletion in dense clouds and circumstellar regions. I. H<sub>2</sub>S ice abundance and UV-photochemical reactions in the H<sub>2</sub>O-matrix. *A&A*, 536:A91.



- Jørgensen, J. K., Schöier, F. L., and van Dishoeck, E. F. (2004). Molecular inventories and chemical evolution of low-mass protostellar envelopes. *A&A*, 416:603–622.
- Jørgensen, J. K., Schöier, F. L., and van Dishoeck, E. F. (2005). H<sub>2</sub>CO and CH<sub>3</sub>OH abundances in the envelopes around low-mass protostars. *A&A*, 437:501–515.
- Jørgensen, J. K., van der Wiel, M. H. D., Coutens, A., Lykke, J. M., Müller, H. S. P., van Dishoeck, E. F., Calcutt, H., Bjerkeli, P., Bourke, T. L., Drozdovskaya, M. N., Favre, C., Fayolle, E. C., Garrod, R. T., Jacobsen, S. K., Öberg, K. I., Persson, M. V., and Wampfler, S. F. (2016). The ALMA Protostellar Interferometric Line Survey (PILS). First results from an unbiased submillimeter wavelength line survey of the Class 0 protostellar binary IRAS 16293-2422 with ALMA. *A&A*, 595.
- Jourdain, J., Bras, G. L., and Combourieu, J. (1979). Kinetic study of some elementary reactions of sulfur compounds including reactions of S and SO with OH radicals. *International Journal of Chemical Kinetics*, 11(6):569–577.
- Kamińska, M., Vigren, E., Zhaunerchyk, V., Geppert, W., Roberts, H., Walsh, C., Millar, T., Danielsson, M., Hamberg, M., Thomas, R., et al. (2008). Dissociative recombination of D<sub>3</sub>S<sup>+</sup>: Product branching fractions and absolute cross sections. *The Astrophysical Journal*, 681(2):1717.
- Karssemeijer, L. J. and Cuppen, H. M. (2014). Diffusion-desorption ratio of adsorbed CO and CO<sub>2</sub> on water ice. *A&A*, 569:A107.
- Kerr, K. E., Alecu, I. M., Thompson, K. M., Gao, Y., and Marshall, P. (2015). Experimental and computational studies of the kinetics of the reaction of atomic hydrogen with methanethiol. *The Journal of Physical Chemistry A*, 119(28):7352–7360.
- Kolesníková, L., Tercero, B., Cernicharo, J., Alonso, J. L., Daly, A. M., Gordon, B. P., and Shipman, S. T. (2014). Spectroscopic Characterization and Detection of Ethyl Mercaptan in Orion. *ApJL*, 784:L7.
- Kurtz, S., Cesaroni, R., Churchwell, E., Hofner, P., and Walmsley, C. M. (2000). Hot Molecular Cores and the Earliest Phases of High-Mass Star Formation. *Protostars and Planets IV*, pages 299–326.
- Kurylo, M. J., Peterson, N. C., and Braun, W. (1971). Absolute rate of the reaction H + H<sub>2</sub>S. *The Journal of Chemical Physics*, 54(3):943–946.
- Lada, E. A., Bally, J., and Stark, A. A. (1991). An unbiased survey for dense cores in the LYND 1630 molecular cloud. *ApJ*, 368:432–444.
- Lander, D., Unfried, K. G., Glass, G. P., and Curl, R. (1990). Rate constant measurements of ethynyl radical with methane, ethane, ethylene, deuterium, and carbon monoxide. *Journal of Physical Chemistry*, 94(20):7759–7763.

- Larson, R. B. (1969). Numerical calculations of the dynamics of collapsing proto-star. *MNRAS*, 145:271.
- Le Picard, S. D. and Canosa, A. (1998). Measurement of the rate constant for the association reaction  $\text{CH} + \text{N}_2$  at 53 K and its relevance to Triton's atmosphere. *Geophysical research letters*, 25(4):485–488.
- Lequeux, J. (2005). *The Interstellar Medium*.
- Lilenfeld, H. and Richardson, R. (1977). Temperature dependence of the rate constant for the reaction between carbon monosulfide and atomic oxygen. *The Journal of Chemical Physics*, 67(9):3991–3997.
- Lin, Y.-L., Wang, N.-S., and Lee, Y.-P. (1985). Temperature dependence of the rate constant for the reaction  $\text{OH} + \text{H}_2\text{S}$  in He,  $\text{N}_2$ , and  $\text{O}_2$ . *International journal of chemical kinetics*, 17(11):1201–1214.
- Linke, R. A., Frerking, M. A., and Thaddeus, P. (1979). Interstellar methyl mercaptan. *ApJL*, 234:L139–L142.
- Lique, F., Cernicharo, J., and Cox, P. (2006). The Excitation of SO in Cold Molecular Clouds: TMC-1. *ApJ*, 653:1342–1352.
- Loison, J.-C., Agúndez, M., Marcelino, N., Wakelam, V., Hickson, K. M., Cernicharo, J., Gerin, M., Roueff, E., and Guélin, M. (2016). The interstellar chemistry of  $\text{H}_2\text{C}_3\text{O}$  isomers. *MNRAS*, 456:4101–4110.
- Loison, J.-C., Agúndez, M., Wakelam, V., Roueff, E., Gratier, P., Marcelino, N., Reyes, D. N., Cernicharo, J., and Gerin, M. (2017). The interstellar chemistry of  $\text{C}_3\text{H}$  and  $\text{C}_3\text{H}_2$  isomers. *MNRAS*, 470:4075–4088.
- Loison, J.-C., Halvick, P., Bergeat, A., Hickson, K. M., and Wakelam, V. (2012). Review of ocs gas-phase reactions in dark cloud chemical models. *Monthly Notices of the Royal Astronomical Society*, 421(2):1476–1484.
- Lu, C.-W., Wu, Y.-J., Lee, Y.-P., Zhu, R., and Lin, M. (2004). Experimental and theoretical investigations of rate coefficients of the reaction  $\text{S}(3\text{P}) + \text{O}_2$  in the temperature range 298–878 K. *The Journal of chemical physics*, 121(17):8271–8278.
- Lykke, J. M., Coutens, A., Jørgensen, J. K., van der Wiel, M. H. D., Garrod, R. T., Müller, H. S. P., Bjerke, P., Bourke, T. L., Calcutt, H., Drozdovskaya, M. N., Favre, C., Fayolle, E. C., Jacobsen, S. K., Öberg, K. I., Persson, M. V., van Dishoeck, E. F., and Wampfler, S. F. (2017). The ALMA-PILS survey: First detections of ethylene oxide, acetone and propanal toward the low-mass protostar IRAS 16293-2422. *A&A*, 597.
- Maiti, B., Schatz, G. C., and Lendvay, G. (2004). Importance of intersystem crossing in the  $\text{S}(3\text{P}, 1\text{D}) + \text{H}_2 \rightarrow \text{SH} + \text{H}$  reaction. *The Journal of Physical Chemistry A*, 108(41):8772–8781.

- Majumdar, L., Gratier, P., Andron, I., Wakelam, V., and Caux, E. (2017). A study of singly deuterated cyclopropenylidene  $c\text{-C}_3\text{HD}$  in the protostar IRAS 16293-2422. *MNRAS*, 467:3525–3532.
- Majumdar, L., Gratier, P., Vidal, T., Wakelam, V., Loison, J.-C., Hickson, K. M., and Caux, E. (2016). Detection of  $\text{CH}_3\text{SH}$  in protostar IRAS 16293-2422. *MNRAS*, 458:1859–1865.
- Martin, D., Jourdain, J., and Le Bras, G. (1988). Kinetics and mechanism for the reactions of H atoms with  $\text{CH}_3\text{SH}$  and  $\text{C}_2\text{H}_5\text{SH}$ . *International journal of chemical kinetics*, 20(11):897–907.
- Martín-Doménech, R., Jiménez-Serra, I., Muñoz Caro, G. M., Müller, H. S. P., Occhiogrosso, A., Testi, L., Woods, P. M., and Viti, S. (2016). The sulfur depletion problem: upper limits on the  $\text{H}_2\text{S}_2$ ,  $\text{HS}'_2$ , and  $\text{S}_2$  gas-phase abundances toward the low-mass warm core IRAS 16293-2422. *A&A*, 585:A112.
- Masunaga, H. and Inutsuka, S.-i. (2000). A Radiation Hydrodynamic Model for Protostellar Collapse. II. The Second Collapse and the Birth of a Protostar. *ApJ*, 531:350–365.
- Matthews, H. E., MacLeod, J. M., Broten, N. W., Madden, S. C., and Friberg, P. (1987). Observations of OCS and a search for OC $3\text{S}$  in the interstellar medium. *ApJ*, 315:646–653.
- Maureira, M. J., Arce, H. G., Dunham, M. M., Pineda, J. E., Fernández-López, M., Chen, X., and Mardones, D. (2017). Kinematics of a Young Low-mass Star-forming Core: Understanding the Evolutionary State of the First-core Candidate L1451-mm. *ApJ*, 838.
- McCall, B. J. (2001). *Spectroscopy of trihydrogen(+) in laboratory and astrophysical plasmas*. PhD thesis, Department of Chemistry and Department of Astronomy and Astrophysics, University of Chicago, 5735 S. Ellis Ave., Chicago, IL 60637.
- McGonagle, D., Irvine, W. M., and Ohishi, M. (1994). Nitrogen sulfide in quiescent dark clouds. *ApJ*, 422:621–625.
- Messineo, M., Clark, J. S., Figer, D. F., Kudritzki, R.-P., Najarro, F., Rich, R. M., Menten, K. M., Ivanov, V. D., Valenti, E., Trombely, C., Chen, C.-H. R., and Davies, B. (2015). Massive Stars in the W33 Giant Molecular Complex. *ApJ*, 805:110.
- Millar, T., Adams, N., Smith, D., Lindinger, W., and Villinger, H. (1986). The chemistry of  $\text{SH}^+$  in shocked interstellar gas. *Monthly Notices of the Royal Astronomical Society*, 221(3):673–678.
- Milligan, D. B. and McEwan, M. J. (2000).  $\text{H}_3^+ + \text{O}$ : an experimental study. *Chemical Physics Letters*, 319(5-6):482–485.

- Minh, Y. C. (2016). Sulfur-bearing molecules observed in the massive star-forming regions, DR21(OH) and G33.92+0.11. In *Journal of Physics Conference Series*, volume 728 of *Journal of Physics Conference Series*, page 052007.
- Minh, Y. C., Irvine, W. M., McGonagle, D., and Ziurys, L. M. (1990). Observations of the H<sub>2</sub>S toward OMC-1. *ApJ*, 360:136–141.
- Montaigne, H., Geppert, W., Semaniak, J., Osterdahl, F., Hellberg, F., Thomas, R., Ugglas, M. a., Roberts, H., Millar, T., Zhaunerchyk, V., Kaminska, M., Al-Khallili, A., Kallberg, A., and Larsson, M. (2005). Dissociative recombination of the thioformyl (HCS<sup>+</sup>) and carbonyl sulfide (OCS<sup>+</sup>) cations. *ApJ*, 631:653–659.
- Mousavipour, S. H., Namdar-Ghanbari, M. A., and Sadeghian, L. (2003). A theoretical study on the kinetics of hydrogen abstraction reactions of methyl or hydroxyl radicals with hydrogen sulfide. *The Journal of Physical Chemistry A*, 107(19):3752–3758.
- Neufeld, D. A., Wolfire, M. G., and Schilke, P. (2005). The Chemistry of Fluorine-bearing Molecules in Diffuse and Dense Interstellar Gas Clouds. *ApJ*, 628:260–274.
- Nicholas, J. E., Amodio, C. A., and Baker, M. J. (1979). Kinetics and mechanism of the decomposition of H<sub>2</sub>S, CH<sub>3</sub>SH and (CH<sub>3</sub>)<sub>2</sub>S in a radio-frequency pulse discharge. *Journal of the Chemical Society, Faraday Transactions 1: Physical Chemistry in Condensed Phases*, 75:1868–1875.
- Nicolas, C., Shu, J., Peterka, D. S., Hochlaf, M., Poisson, L., Leone, S. R., and Ahmed, M. (2006). Vacuum ultraviolet photoionization of C<sub>3</sub>. *Journal of the American Chemical Society*, 128(1):220–226.
- Oya, Y., Sakai, N., López-Sepulcre, A., Watanabe, Y., Ceccarelli, C., Lefloch, B., Favre, C., and Yamamoto, S. (2016). Infalling-Rotating Motion and Associated Chemical Change in the Envelope of IRAS 16293-2422 Source A Studied with ALMA. *ApJ*, 824:88.
- Palumbo, M. E., Geballe, T. R., and Tielens, A. G. G. M. (1997). Solid Carbonyl Sulfide (OCS) in Dense Molecular Clouds. *ApJ*, 479:839–844.
- Peng, J., Hu, X., and Marshall, P. (1999). Experimental and ab initio investigations of the kinetics of the reaction of H atoms with H<sub>2</sub>S. *The Journal of Physical Chemistry A*, 103(27):5307–5311.
- Penzias, A. A., Solomon, P. M., Wilson, R. W., and Jefferts, K. B. (1971). Interstellar Carbon Monosulfide. *ApJL*, 168:L53.
- Petrie, S. (1996). Formation of interstellar CCS and CCCS: a case for radical/neutral chemistry? *Monthly Notices of the Royal Astronomical Society*, 281(2):666–672.

- Plume, R., Jaffe, D. T., Evans, II, N. J., Martín-Pintado, J., and Gómez-González, J. (1997). Dense Gas and Star Formation: Characteristics of Cloud Cores Associated with Water Masers. *ApJ*, 476:730–749.
- Podio, L., Codella, C., Gueth, F., Cabrit, S., Bachiller, R., Gusdorf, A., Lee, C.-F., Lefloch, B., Leurini, S., Nisini, B., and Tafalla, M. (2015). The jet and the disk of the HH 212 low-mass protostar imaged by ALMA: SO and SO<sub>2</sub> emission. *A&A*, 581:A85.
- Prasad, S. S. and Tarafdar, S. P. (1983). UV radiation field inside dense clouds - Its possible existence and chemical implications. *ApJ*, 267:603–609.
- Quénard, D., Bottinelli, S., Caux, E., and Wakelam, V. (2018a). 3D modelling of HCO<sup>+</sup> and its isotopologues in the low-mass proto-star IRAS16293-2422. *MNRAS*, 477:5312–5326.
- Quénard, D., Jiménez-Serra, I., Viti, S., Holdship, J., and Coutens, A. (2018b). Chemical modelling of complex organic molecules with peptide-like bonds in star-forming regions. *MNRAS*, 474:2796–2812.
- Rice, B. M., Cartland, H. E., and Chabalowski, C. F. (1993). Ab initio potential energy surface for the H + OCS reaction. *Chemical physics letters*, 211(4-5):283–292.
- Rice, B. M. and Chabalowski, C. F. (1994). Ab initio potential energy surface for H + OCS reactions: Extended basis sets and correlation treatment. *The Journal of Physical Chemistry*, 98(38):9488–9497.
- Ruaud, M., Loison, J. C., Hickson, K. M., Gratier, P., Hersant, F., and Wakelam, V. (2015). Modelling complex organic molecules in dense regions: Eley-Rideal and complex induced reaction. *MNRAS*, 447:4004–4017.
- Ruaud, M., Wakelam, V., and Hersant, F. (2016). Gas and grain chemical composition in cold cores as predicted by the Nautilus three-phase model. *MNRAS*, 459:3756–3767.
- Ruffle, D. P., Hartquist, T. W., Caselli, P., and Williams, D. A. (1999). The sulphur depletion problem. *MNRAS*, 306:691–695.
- Sakai, N., Sakai, T., Hirota, T., Watanabe, Y., Ceccarelli, C., Kahane, C., Bottinelli, S., Caux, E., Demyk, K., Vastel, C., Coutens, A., Taquet, V., Ohashi, N., Takakuwa, S., Yen, H.-W., Aikawa, Y., and Yamamoto, S. (2014). Change in the chemical composition of infalling gas forming a disk around a protostar. *Nature*, 507:78–80.
- Schöier, F. L., Jørgensen, J. K., van Dishoeck, E. F., and Blake, G. A. (2002). Does IRAS 16293-2422 have a hot core? Chemical inventory and abundance changes in its protostellar environment. *A&A*, 390:1001–1021.
- Scott, G. B., Milligan, D. B., Fairley, D. A., Freeman, C. G., and McEwan, M. J. (2000). A selected ion flow tube study of the reactions of small C<sub>m</sub>H<sub>n</sub><sup>+</sup> ions with O atoms. *The Journal of Chemical Physics*, 112(11):4959–4965.

- Sen, A., Anicich, V., and Federman, S. (1992). Formaldehyde reactions in dark clouds. *The Astrophysical Journal*, 391:141–143.
- Shackleford, W., Mastrup, F., and Kreye, W. (1972). Excitation and quenching of CO fourth positive chemiluminescence due to reactions involving C<sub>2</sub>O. *The Journal of Chemical Physics*, 57(9):3933–3944.
- Shalabiea, O. M. (2001). The effect of the initial elemental abundance on gas-grain chemical models. *A&A*, 370:1044–1055.
- Shannon, R. J., Cossou, C., Loison, J.-C., Caubet, P., Balucani, N., Seakins, P. W., Wakeham, V., and Hickson, K. M. (2014). The fast C (3P) + CH<sub>3</sub>OH reaction as an efficient loss process for gas-phase interstellar methanol. *Rsc Advances*, 4(50):26342–26353.
- Smith, D., Spanel, P., and Mayhew, C. A. (1992). A selected ion-flow tube study of the reactions of O<sup>+</sup>, H<sup>+</sup> and HeH<sup>+</sup> with several molecular gases at 300 K. *International journal of mass spectrometry and ion processes*, 117:457–473.
- Smith, R. G. (1991). A search for solid H<sub>2</sub>S in dense clouds. *MNRAS*, 249:172–176.
- Snow, T. P. and McCall, B. J. (2006). Diffuse Atomic and Molecular Clouds. *Annual Review of Astronomy and Astrophysics*, 44:367–414.
- Sofia, U. J., Cardelli, J. A., and Savage, B. D. (1994). The abundant elements in interstellar dust. *ApJ*, 430:650–666.
- Sutton, E. C., Peng, R., Danchi, W. C., Jaminet, P. A., Sandell, G., and Russell, A. P. G. (1995). The distribution of molecules in the core of OMC-1. *ApJS*, 97:455–496.
- Taquet, V., López-Sepulcre, A., Ceccarelli, C., Neri, R., Kahane, C., and Charnley, S. B. (2015). Constraining the Abundances of Complex Organics in the Inner Regions of Solar-type Protostars. *ApJ*, 804.
- Tiee, J., Wampler, F., Oldenberg, R., and Rice, W. (1981). Spectroscopy and reaction kinetics of HS radicals. *Chemical physics letters*, 82(1):80–84.
- Tieftrunk, A., Pineau des Forets, G., Schilke, P., and Walmsley, C. M. (1994). SO and H<sub>2</sub>S in low density molecular clouds. *A&A*, 289:579–596.
- van der Tak, F. F. S. (2004). Hot Molecular Cores and High Mass Star Formation. In Burton, M. G., Jayawardhana, R., and Bourke, T. L., editors, *Star Formation at High Angular Resolution*, volume 221 of *IAU Symposium*, page 59.
- Vaytet, N., Audit, E., Dubroca, B., and González, M. (2012). A Numerical Model for Multigroup Radiation Hydrodynamics. 459:180.
- Vaytet, N., Chabrier, G., Audit, E., Commercon, B., and Masson, J. (2013). Simulations Of Protostellar Collapse Using Multigroup Radiation Hydrodynamics.

- Vaytet, N. and Haugbolle, T. (2017). A grid of one-dimensional low-mass star formation collapse models. *A&A*, 598:A116.
- Vidal, T. H. G., Loison, J.-C., Jaziri, A. Y., Ruaud, M., Gratier, P., and Wakelam, V. (2017). On the reservoir of sulphur in dark clouds: chemistry and elemental abundance reconciled. *MNRAS*, 469:435–447.
- Vidal, T. H. G. and Wakelam, V. (2018). A new look at sulphur chemistry in hot cores and corinos. *MNRAS*, 474:5575–5587.
- Viti, S., Caselli, P., Hartquist, T. W., and Williams, D. A. (2001). Chemical signatures of shocks in hot cores. *A&A*, 370:1017–1025.
- Wakelam, V., Bron, E., Cazaux, S., Dulieu, F., Gry, C., Guillard, P., Habart, E., Hornekær, L., Morisset, S., Nyman, G., Pirronello, V., Price, S. D., Valdivia, V., Vidal, G., and Watanabe, N. (2017). H<sub>2</sub> formation on interstellar dust grains: The viewpoints of theory, experiments, models and observations. *Molecular Astrophysics*, 9:1–36.
- Wakelam, V., Caselli, P., Ceccarelli, C., Herbst, E., and Castets, A. (2004a). Resetting chemical clocks of hot cores based on S-bearing molecules. *A&A*, 422:159–169.
- Wakelam, V., Castets, A., Ceccarelli, C., Lefloch, B., Caux, E., and Pagani, L. (2004b). Sulphur-bearing species in the star forming region L1689N. *A&A*, 413:609–622.
- Wakelam, V. and Herbst, E. (2008). Polycyclic Aromatic Hydrocarbons in Dense Cloud Chemistry. *ApJ*, 680:371–383.
- Wakelam, V., Herbst, E., Loison, J.-C., Smith, I. W. M., Chandrasekaran, V., Pavone, B., Adams, N. G., Bacchus-Montabonel, M.-C., Bergeat, A., Béroff, K., Bierbaum, V. M., Chabot, M., Dalgarno, A., van Dishoeck, E. F., Faure, A., Geppert, W. D., Gerlich, D., Galli, D., Hébrard, E., Hersant, F., Hickson, K. M., Honvault, P., Klippenstein, S. J., Le Picard, S., Nyman, G., Pernot, P., Schlemmer, S., Selsis, F., Sims, I. R., Talbi, D., Tennyson, J., Troe, J., Wester, R., and Wiesenfeld, L. (2012). A KInetic Database for Astrochemistry (KIDA). *ApJS*, 199:21.
- Wakelam, V., Herbst, E., and Selsis, F. (2006). The effect of uncertainties on chemical models of dark clouds. *A&A*, 451:551–562.
- Wakelam, V., Hersant, F., and Herpin, F. (2011). Sulfur chemistry: 1D modeling in massive dense cores. *A&A*, 529:A112.
- Wakelam, V., Loison, J.-C., Herbst, E., Pavone, B., Bergeat, A., Béroff, K., Chabot, M., Faure, A., Galli, D., Geppert, W. D., Gerlich, D., Gratier, P., Harada, N., Hickson, K. M., Honvault, P., Klippenstein, S. J., Le Picard, S. D., Nyman, G., Ruaud, M., Schlemmer, S., Sims, I. R., Talbi, D., Tennyson, J., and Wester, R. (2015a). The 2014 KIDA Network for Interstellar Chemistry. *ApJS*, 217:20.

- Wakelam, V., Loison, J.-C., Hickson, K. M., and Ruaud, M. (2015b). A proposed chemical scheme for HCCO formation in cold dense clouds. *MNRAS*, 453:L48–L52.
- Wakelam, V., Smith, I., Herbst, E., Troe, J., Geppert, W., Linnartz, H., Öberg, K., Roueff, E., Agúndez, M., Pernot, P., et al. (2010). Reaction networks for interstellar chemical modelling: improvements and challenges. *Space science reviews*, 156(1-4):13–72.
- Wakelam, V., Vastel, C., Aikawa, Y., Coutens, A., Bottinelli, S., and Caux, E. (2014). Chemical modelling of water deuteration in IRAS16293-2422. *MNRAS*, 445:2854–2871.
- Woods, P. M., Occhiogrosso, A., Viti, S., Kaňuchová, Z., Palumbo, M. E., and Price, S. D. (2015). A new study of an old sink of sulphur in hot molecular cores: the sulphur residue. *MNRAS*, 450:1256–1267.
- Woon, D. E. and Herbst, E. (2009). Quantum chemical predictions of the properties of known and postulated neutral interstellar molecules. *The Astrophysical Journal Supplement Series*, 185(2):273.
- Yoshimura, M., Koshi, M., Matsui, H., Kamiya, K., and Umeyama, H. (1992). Non-arrhenius temperature dependence of the rate constant for the  $\text{H} + \text{H}_2\text{S}$  reaction. *Chemical physics letters*, 189(3):199–204.
- Zhang, X., Zou, S., Harding, L. B., and Bowman, J. M. (2004). A global ab initio potential energy surface for formaldehyde. *The Journal of Physical Chemistry A*, 108(41):8980–8986.